Università degli Studi di Genova

Scuola di Dottorato in Scienze e Tecnologie per l'Informazione e la Conoscenza

Corso di Dottorato di Ricerca in Fisica

XXXI Ciclo

Transport properties at the boundaries of Fermi liquid: iron-based and high-Tc superconductors

Martina Meinero

Tutor: Prof. ssa Marina Putti

Table of contents

Introduction

The discovery of copper-oxide high temperature (high-T_c) superconductors in the mid-eighties [1] represented an exceptional breakthrough in condensed matter physics. All of a sudden, using the cheap and abundant liquid nitrogen as cryogen was enough to benefit the exciting properties of superconductors, ranging from transport of electric currents without dissipation to maglev trains to the production of sensitive magnetometers. The rise in the maximum T_c during the first decade of high-T_c research was impressive: high-T_c superconductors have been observed with transition temperatures as high as 138 K, by far exceeding the maximum T_c~40 K predicted for "ordinary" metallic superconductors. Since then, many theories tried to explain such a high T_c and which is the mechanism mediating the Cooper pairing but none revealed exhaustive, leaving this two questions still unanswered.

Despite this slowdown, the field continued to develop, sustained by the realization that the "strange" metallic state out of which high-T_c superconductivity emerges is unlike any other that had been seen before. Indeed, the origin of electron pairing, the normal state pseudogap and the strange metal phase of cuprates are cornerstones of modern condensed matter physics. Yet the stark failure to describe strange metals with conventional theories has led to a consensus that they are fundamentally new states of matter that require an entirely new theoretical framework [2].

Before the discovery of superconductivity in the iron pnictides in 2006 [3], the high-T_c cuprates were considered a class apart. The former's discovery was no less surprising and seemed to confirm that the guiding

principles for optimization of superconductivity developed between 1960s and 1970s, were now obsolete. According to these principles, superconductivity had to be searched in high (cubic) symmetry materials, containing no oxygen and with no neighboring magnetic or insulating behavior. These rules not only have been proved incorrect but also their exact opposite seemed to be true: indeed, in both cuprates and pnictides, superconductivity was now observed in oxide materials with low dimensionality, close to an insulating state and/or magnetic order [4].

Beyond any doubt, there are many striking similarities between cuprates and pnictides. Structurally, they are low dimensional (almost 2D) materials and this feature is also reflected in their electronic properties. Besides, their phase diagrams look quite akin: superconductivity arises at doping concentrations close to a stable antiferromagnetic ground state, while T_c itself is dome shaped, falling away as either system is doped and becomes more itinerant. In addition, near optimum doping (the doping which corresponds to the maximum T_c), many normal-state properties of both cuprates and pnictides exhibit a marked deviation from conventional Fermi liquid and this "strange" behavior seems to originate from a magnetic quantum critical point (QCP), where the magnetic order is tuned to zero by a non-thermal parameter such as chemical composition or pressure. If and to what extent this QCP relates to unconventional superconductivity is a still pending issue.

It is important to notice that there exist important differences too. Whereas in cuprates the essential physics is captured by a single Cu d orbital hybridized with the oxygen p states, the pnictides have six electrons occupying the nearly degenerate 3d Fe manifold, implying that the Fe-based superconductors (IBS) are characterized by a multi-

orbital multi-band nature, which contrasts with the effective single-band nature of the cuprates [5]. Furthermore, while strong electronic correlations have played an important role in cuprates (they are doped Mott insulators), the IBS are properly classified as moderately correlated (Hund) semi-metals with regions of the phase diagram where the Fermi liquid picture is still valid, despite the complexity of treatment for a multi band system [6].

This manuscript is focused on the study of the transport properties of $BaFe_2As_2$ - a pnictide parent compound of the so called 122 family - and of $Bi_2Sr_2CuO_{6-x}$ (Bi-2201) - an optimal doped cuprate of the so called 2201 family. The principal aims of this work are: (i) to gather information on the electronic band structure of the pnictide parent compound by extracting meaningful quantities (the Peltier coefficients) which let disentangle the main transport mechanisms into play, despite the complexity of the multi-band nature of these compounds; (ii) to investigate the strange metal phase of cuprates in view of new approaches and formulae developed in the context of emerging holographic theories by the theoretical group of Prof. N. Magnoli of the Department of Physics in Genova. In order to carry out these studies, I performed the complete experimental characterization of the transport properties (namely resistivity, magnetoresistance, Hall effect, Seebeck and Nernst effect) on high-quality single crystals of $BaFe_2As_2$ and Bi-2201 as a function of temperature and magnetic field. The measurements on $BaFe_2As_2$ have been mainly performed at the Department of Physics of the University of Genova and transport characterization in high magnetic fields have been carried out at the international facility High Field Magnet Laboratory (HFML) of Nijmegen (NL). The measurements on Bi-2201 have been performed at the IFW Dresden (DE) and this activity has been rewarded and

supported with a DAAD Scholarship, Research Grants Award – Short-term grants, 2017 (57314023).

This thesis is divided into four chapters, whose contents are summarized in the following.

Chapter 1 consists of a general introduction to cuprates and iron-based superconductors. After a brief introduction to the concept of "strange metal" and "quantum criticality", it is proposed a description of the crystal and electronic structure, the phase diagram and the transport properties of cuprates and pnictides, particularly focussing on the 122 family.

Chapter 2 is devoted to a formal definition of the electric and thermoelectric transport properties which is given in terms of transport coefficients. Their expressions are presented both in a semi-classical Boltzmann approach and in a holographic scenario.

In Chapter 3 I show that the simultaneous analysis of magneto-electric and magneto-thermoelectric transport properties of a $BaFe_2As_2$ high quality single crystal, for different magnetic field directions up to 30 T, let extract the Peltier tensor coefficients α_{xx}, α_{xy} and α_{xz}. The large α_{xy} and α_{xz} values and their field dependence provide evidence of the presence of a high mobility band, compatible with a Dirac dispersion band, crossing the Fermi level and suggest a possible 3-dimensional nature of the Dirac Fermions.

In Chapter 4 I present the resistivity, magnetoresistance, Hall effect, longitudinal and transverse thermal conductivity, Seebeck and Nernst effect of a single crystal of Bi-2201. The data are first analysed in the

framework of the semi-classical Boltzmann approach and then compared to the holographic theory.

For completeness four Appendices have been inserted to give further details on the anisotropy of transport properties of $BaFe_2As_2$ both in-plane (Appendix B) and out-of-plane (Appendix A), the magnetic susceptibility measurement on Bi-2201 (Appendix D) and the experimental techniques (Appendix C).

1 The Fermi liquid breakdown: high-T_c superconductors

The Fermi liquid theory has been tremendously successful in explaining almost all metallic state in nature. However, the first big breakdown of this theory came in the mid-80s, with the discovery of high temperature (high-T_c) superconductivity [1]. Whereas "ordinary" metallic superconductors usually have T_c below 40 K [7], high-T_c superconductors have been observed with T_c as high as 138 K [8]. Until 2008, only compounds of copper and oxygen, the so called "cuprates", were believed to have high-T_c superconductors properties but since the discovery of superconductivity below 26 K in fluorine doped LaFeAsO [9], several iron-based compounds (IBS) are now known to be superconducting at high temperatures.

Moreover, in these particular materials both the transport properties of the non-superconducting phase and the superconducting pairing mechanism differ significantly from those predicted by the Fermi liquid and the Bardeen-Cooper-Schrieffer (BCS) theory, respectively. In particular, it is known that in these two family of superconductors the Cooper pairing mechanism is not mediated by phonons (as predicted by the BCS) and they are therefore known as *unconventional* superconductors. Furthermore, their phase diagrams (graphical representations of the physical states as a function of temperature and pressure/chemical doping) show many similarities. Indeed,

superconductivity in both the cuprates and the IBS is close to antiferromagnetism (AFM) and appears in a dome-shaped region upon doping the so called non superconductive *parent compounds*. Finally, near optimum doping (the doping which corresponds to the maximum T_c), many normal-state properties exhibit a marked deviation from conventional Fermi liquid behavior and this region is known as “strange metal” phase.

This chapter is devoted to a general introduction to cuprates and IBS. After a brief introduction to the concept of “strange metal” and “quantum criticality”, it is proposed a description of the crystal and electronic structure, the phase diagram and the transport properties of cuprates in section 2 and IBS (particularly focussing on the 122 family) in section 3.

1.1 Strange metals and quantum criticality

One of the milestones in condensed matter physics is the Landau Fermi liquid (FL) theory, which describes the vast majority of the known states of matter, like normal metals, semi-conductors, superconductors and superfluids. The basic assumption from which the phenomenological Landau theory starts is that the qualitative picture for non-interacting Fermi gas persists for a generic interacting fermionic system, also in presence of interactions between fermions. Specifically, the basic Landau's starting assumptions are:

- There exists a Fermi surface which characterizes the ground state of a generic interacting fermionic system. In momentum space this surface lies at $k = k_F$, where k_F is called the Fermi momentum.

- Despite the possibly strong interactions among bare fermions, the low energy excitations near the Fermi surface nevertheless behave like a weakly interacting particles and holes, called collectively quasi-particles. They have the same charge as fundamental fermions and satisfy Fermi statistics. The fundamental fermion mass m is replaced by an effective mass m^* of the quasi-particle and it is in general different from m, due to renormalization by many-body interactions.

The concept of quasi-particle is extremely powerful and makes it possible to develop a general low energy theory, independently of the precise microscopic details of the system.
Despite the great success of the Landau FL theory in describing condensed matter systems, its first big breakdown came with the discovery of the high-temperature superconductivity [1].

More generally, the term *non-Fermi liquid*, also known as "strange metal", is used to describe a system which displays the breakdown of FL behavior. Interestingly, the strange metal regime occurs in many materials which show unconventional superconductivity such as cuprates and IBS but also heavy fermions and organics [10]. The strange metal transports in cuprates, as well as in IBS, have been the subject of intense study. In particular, the amazing similarity between the quantum-mechanical phase diagrams of cuprates and IBS reveal that both their superconductivities might be ascribed to the quantum critical fluctuations associated with a quantum critical point (QCP). Within the quantum-mechanical phase transition, the singular QCP at absolute zero produces a wide region of unusual behavior at a finite temperature, which displays a striking deviation from the conventional Fermi-liquid behavior [11].

The strange metal regime was recognized early on as one of the most mysterious aspect of the copper oxide phase diagram. The most basic difference between the strange metal and a conventional metal is the temperature-behaviour of the electrical resistivity ρ, both at high and low temperatures. In a normal metal, unless the metal melts first, ρ saturates at high temperatures when the mean free path l becomes of the order of the de Broglie wavelength λ. The notion of a maximum metallic resistivity compatible with a minimum mean free path $l_{min} \sim \lambda$ is known as the Mott-Ioffe-Regel (MIR) limit. In many highly resistive elements, alloys and intermetallic compounds, ρ becomes weakly T-dependent at high temperatures and it approaches a constant value ρ_{sat} in the region 100-200 μΩcm consistent with $l_{min} \sim \lambda$. The resistivity of the copper oxide strange metal can be linear in T from near T_c up to as high a temperature as measured [12], without any sign of saturation. In the process, ρ attains values between 1 and 10 mΩcm, more than one order of magnitude higher than ρ_{sat} of typical metals, corresponding to $l \ll \lambda$. Since this clearly invalidates conventional quasiparticle picture, the absence of resistivity saturation is swiftly acknowledged as a possible signature of novel non-Fermi liquid behaviour. Such non-saturating ρ has been registered in a wide range of strongly correlated systems and they collectively have come to be referred to as "bad metals" [13]. Furthermore, in Table 1 is summarized the temperature dependence of ρ predicted for a 3d metal within the FL scenario (ρ_{FL}). The coefficients in front of the powers of T are constants which depend on the metal under consideration. As already discussed, at high temperatures ρ is expected to saturate to ρ_{sat} due to the MIR limit whereas in the region $T \gg \Theta_D$ (Θ_D being the Debye temperature) the electron-phonon scattering mechanism largely dominates the transport. At very low T the scattering mechanisms are dominated by impurities.

However, in the transition region between $T \sim 0$ and $T \sim \Theta_D$, since the scattering rate of the electron-phonon processes decrease faster than that of electron-electron processes as the temperature is decreased, there may be a region in which ρ_{FL} is dominated by electron-electron interactions. Indeed, the T^2 scaling of ρ is considered a standard evidence of the presence of FL regime in the experimental measurements.

As we will discuss in the following, the strange metals strongly violate this prediction, being characterized by a resistivity (ρ_{SM}in Table 1) whose *T*-linear behaviour survives for all $T > T_C$.

	$T \ll \Theta_D$	$T \gg \Theta_D$	High T (MIR limit)
ρ_{FL}	$A_{imp}+B_{e,e}T^2+C_{e,ph}T^{3-5}$	$\mathcal{A}_{e,ph}T$	ρ_{sat}
ρ_{SM}	$\propto T$	$\propto T$	$\propto T$

Table 1: Temperature dependence of the electric resistivity predicted by the FL theory (ρ_{FL}) and measured in strange metals (ρ_{SM})

In the 1990s it was proposed that quantum criticality could explain the low-energy excitations of the strange metal. A quantum phase transition occurs when a continuous phase transition occurs at zero temperature as a function of a tuning parameter (like pressure or doping), where the corresponding quantum critical point (QCP) defines the boundary between the ordered (broken symmetry) and disordered quantum phases [14]. The peculiar aspect of a quantum critical theory is that the influence of the QCP extends over a wide regime in the T>0 region of

the phase diagram. This is properly the regime of quantum criticality, which is crucial for interpreting a wide variety of experiments. As described in [14, 15], at the QCP the electronic system behaves like a perfect fluid in which the relaxation time is universally determined by the absolute temperature in terms of the indetermination principle which is sometimes referred to as "Planckian dissipation" because it is a quantum effect independent of the material parameters [16]. Away from the QCP, the dissipation rate is much larger and it satisfies the inequality $\tau \geq {\hbar}/{k_B T}$. Remarkably, τ does not depend on physical parameters, but scales only with fundamental universal quantities, namely $\hbar$ and k_B. These observations suggest an interpretation of the phase diagrams of both cuprates (see section 2.2) and IBS (see section 3.2), where the strange metal is identified with the quantum critical wedge associated with a QCP under the superconducting dome near optimal doping.

1.2 Cuprates

The discovery of high-temperature superconductivity in the copper oxide perovskite $La_{2-x}Ba_xCuO_4$ [1] in 1986 ranks among the major scientific events of the twentieth century. As already mentioned, the superconducting transition temperatures in the copper oxides greatly exceed those of any previously known superconductor by almost an order of magnitude. Moreover, according to the theory of "conventional" superconductors, the copper oxides would have seemed the least likely materials in which to look for superconductivity. Indeed, the parent (undoped) compounds are insulating antiferromagnets and upon doping they become poor conductors that can hardly be classified as metals. Superconductivity and magnetism are typically antithetical

forms of order. After all, in conventional superconductors, magnetic impurities break Cooper pairs [17].

In the three decades since their discovery, much has been learned about the novel forms of quantum matter that are exhibited in these strong correlated electron systems. However, unresolved issues include the astonishing complexity of their phase diagram with many exotic phases such as pseudogap, charge density wave state and strange metal region, which is one of the topics of this work. In the following sections we will briefly outline the basic crystalline structure of cuprate superconductors, their phase diagram and electronic structure, to then focus on the anomalous transport properties which characterize the strange metal regime. In the following, we will refer to this family of HTS either with "cuprates" or "HTS".

1.2.1 Crystal and electronic structure

As a common property, all HTS have a layered perovskite structure that consists of alternating CuO_2 layers and insulating blocking layers that as a consequence of doping, provide charge carriers to the CuO_2 layers. This structure causes a large anisotropy in conducting and superconducting properties, since electrical currents are carried by the holes or the electrons throughout the CuO_2 layers. Even though this is the general scheme, the numbers of CuO_2 layers are different in different cuprate families.

For example, the bismuth (Bi) families of HTS, $Bi_2Sr_2CuO_{6+\delta}$ (Bi-2201), $Bi_2Sr_2CaCu_2O_{8+\delta}$ (Bi-2212), $Bi_2Sr_2Ca_2Cu_3O_{10+\delta}$ (Bi-2223) have respectively one, two and three CuO_2 layers, as shown in Figure 1a. In these families, doping can be controlled by adding extra oxygen in the Bi-O planes, by substituting rare-earth ions for Ca^{2+} ions or substituting

La^{3+} ions for Sr^{2+} ions. Other families of cuprates, such as $La_{2-x}Sr_xCuO_4$ (LSCO) and $YBa_2Cu_3O_{7-\delta}$ (YBCO) have one and two CuO_2 planes, respectively.

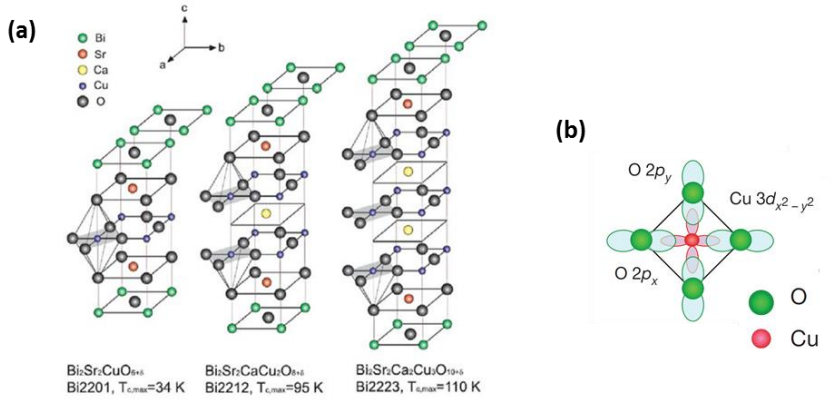

Figure 1: (a) Crystal structure of Bi-based families of HTS. Adapted from [18]. (b) Hybridization of a $3d_{x^2-y^2}$ hole on the copper sites (red) with planar-coordinated $2p_x$ and $2p_y$ oxygen orbitals (green). After [19].

The electronic structure of the universal Cu-O planes primarily involves hybridization of a $3d_{x^2-y^2}$ hole on the copper sites with planar-coordinated $2p_x$ and $2p_y$ oxygen orbitals (Figure 5b). The resulting two-dimensional energy dispersion can be expressed in tight-binding representation as:

$$\varepsilon(\boldsymbol{k}) = \epsilon_0 - 2t\left(\cos k_x + \cos k_y\right) + 4t'\left(\cos k_x \cdot \cos k_y\right) - 2t''\left(\cos 2k_x + \cos 2k_y\right)$$

At half-filling, with only nearest-neighbour (*t*) hopping, a diamond-like Fermi surface is expected. Inclusion of next-near neighbour (*t'*) hopping leads to a more rounded topology. Figure 2a sketches the CuO_2 plane with the principal hopping parameters *t*, *t*' and *t''*. Pavarini *et al* identified an intriguing correlation between T_c and the ratio *t'/t* for a

large number of cuprate families [20] Low-T_c cuprates like $La_{2-x}Sr_xCuO_4$ (LSCO) and $Bi_2Sr_{2-x}La_xCuO_6$ (Bi-2201) have a relatively low *t'/t*, whilst those with higher T_c values, such as $Bi_2Sr_2CaCu_2O_{8+\delta}$ (Bi-2212), $YBa_2Cu_3O_{7-\delta}$ (YBCO) and $Tl_2Ba_2CuO_{6+\delta}$ (Tl-2201), have much rounded FS geometries characteristic of the higher *t'/t* values. These predictions have largely been verified by extensive ARPES measurements [21]. The differences in topology are highlighted in Figure 2b and 2c, where representative 2D FS projections of LSCO and Tl-2201 respectively are shown for two different doping levels *p*=0.15 (near optimal doping) and 0.30 (beyond the superconducting dome), where *p* is the hole content per CuO_2 plane.

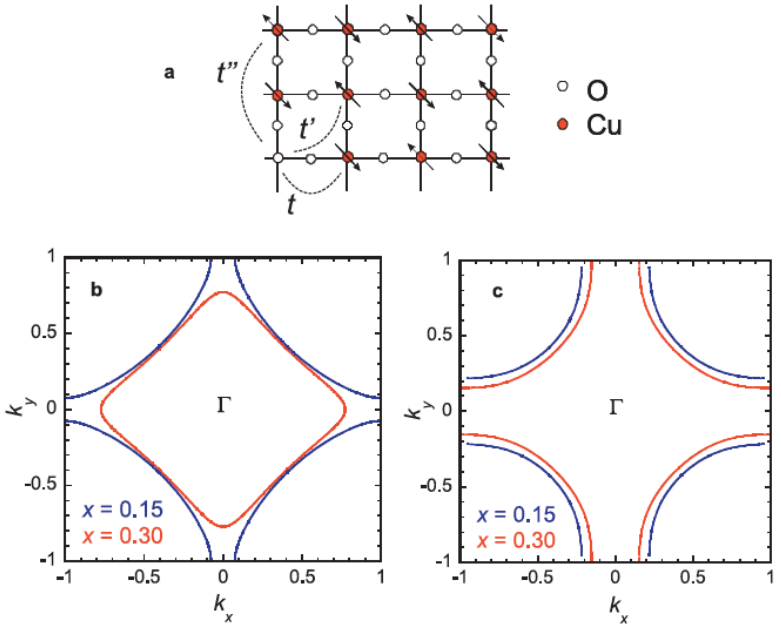

Figure 2: (a) Schematic figure of the CuO_2 plane showing the spin alignments of the Cu spins at half-filling with the basal plane and the three principal hopping parameters *t*, *t'* and *t''*. (b) Schematic 2D projection of the Fermi surface in $La_{2-x}Sr_xCuO_4$ for *p*=0.15 (*t'/t*=0.15) and 0.30 (*t'/t*=0.12). (c) Similar projections for $Tl_2Ba_2CuO_{6+\delta}$ for *p*=0.15 (*t'/t*=0.22) and 0.30 (*t'/t*=0.22). In all cases, *t''/t'*=-0.5. After [22]

1.2.2 Phase diagram of cuprates

Given the hybridation between the Cu $3d_{x^2-y^2}$ orbital with oxygen p orbitals (Figure 1b), the stoichiometric "parent" compound (Figure 3, zero doping) has nine *d* electrons (or one *d* hole). Therefore, the $d_{x^2-y^2}$ band is half-filled and each Cu atom has a spin ½. Since the on-site Coulomb repulsion *U* between $d_{x^2-y^2}$ electrons is stronger than the band width *W* (the kinetic energy of the electrons) in the cuprates, the electrons tend to avoid the double occupancy of the $d_{x^2-y^2}$ orbital and, at half-filling, the electrons are localized, producing the so called "Mott insulator". However, even a localized electron has a spin whose orientation remains a dynamical degree of freedom. Virtual hopping of these electrons produces, via the Pauli exclusion principle, an antiferromagnetic interaction between neighbouring spins. This, in turn, leads to a simple (Nèel) ordered phase below room temperature, in which there are static magnetic moments on the Cu sites with a direction that reverses from one Cu to the next. In the following, we will confine our discussion to hole-doped systems.

Hole doping rapidly suppresses the antiferromagnetic order. At a critical doping of p_{min}, superconductivity sets in, with a transition temperature that grows to a maximum at p_{opt}, then declines for higher dopings and vanishes for p_{max} (Figure 3). Materials with $p < p_{opt}$ are referred to as underdoped and those with $p > p_{opt}$ are referred to as overdoped. Generally, the superconducting transition temperature T_c for copper-oxide superconductors has a parabolic dependence on the concentration of charge carriers p with a maximum $T_{c,max}$ at optimal doping p_{opt} [23]. A universal relation between p and T_c, the so-called "bell shape" can be proposed:

$$T_c(p) = T_{c,max}[1 - \beta(p - p_{opt})^2],$$

where the parameters β and p_{opt} have the constant values of 0.82 and 0.16 respectively for a large number of compounds [24].

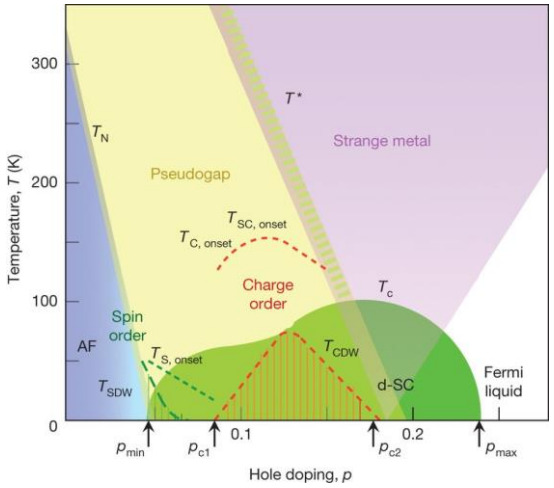

Figure 3: Temperature versus hole doping level for the copper oxides, indicating where various phase occur. The subscript "onset" marks the temperature at which the precursor order or fluctuations become apparent. $T_{S,onset}$ (dotted green line), $T_{c,onset}$ and $T_{SC,onset}$ (dotted red line for both) refer to the onset temperatures of spin-, charge and superconducting fluctuations, while T^* indicates the temperature where the crossover to the pseudogap regime occurs. The blue and green regions indicate fully developed antiferromagnetic order (AF) and *d*-wave superconducting order (d-SC) setting in at the Nèel and superconducting transition temperatures T_N and T_C, respectively. The red stripped area indicates the presence of fully developed charge order setting in at T_{CDW}. T_{SDW} represents the same for incommensurate spin density wave order. Quantum critical points for superconductivity and charge order are indicated by the arrows. After [19].

Unlike in conventional *s*-wave superconductors, the superconducting wavefunction in the copper oxides has *d*-wave symmetry, that is, it changes sign upon rotation by 90°. Associated with this "unconventional pairing" is the existence of zero energy (gapless) quasiparticle excitations at the lowest temperatures, which make even the thermodynamic properties entirely distinct from those of conventional superconductors (fully gapped) [19]. There is general

consensus that the pairing symmetry of the superconducting order parameter of hole-doped cuprates is predominantly $d_{x^2-y^2}$-like in the underdoped and optimally doped region [25,26]. In the heavily overdoped limit, on the other hand, a significant *s*-wave component in addition to the $d_{x^2-y^2}$ component has been revealed [27].

More unique to the copper oxides is the behaviour observed in a range of temperatures above T_c in what is referred to as the "pseudogap" regime. It is characterized by a substantial suppression of the electronic density of states at low energies that cannot be simple related to the occurrence of any form of broken symmetry. Although much about this regime is still unclear, convincing experimental evidence has emerged that there are strong and ubiquitous tendencies towards sorts of order or incipient order, including various forms of charge density-wave, spin-density-wave and electron-nematic order [19]. Superconducting fluctuations also have an important role in part of this regime, although to an extent that is still much debated. A long-standing question is whether, perhaps, pairs already form at the (very high) pseudogap temperature T* (Figure 3), while at a much lower temperature, the actual T_c, the phase locks to form the long-range ordered superconducting state. The structure of the pseudogap in momentum space was directly mapped by ARPES experiments at temperatures between T* and T_c, and found to crudely mimic the *d*-wave superconducting gap: the pseudogap is apparently only in the "antinodal" regions of the Brillouin zone (Figure 4) where the *d*-wave is largest [28, 29, 30]. This immediately suggests that at the very high pseudogap temperature T*, pairs already start to form, while phase fluctuations prohibit superconducting order until much lower temperatures are reached.

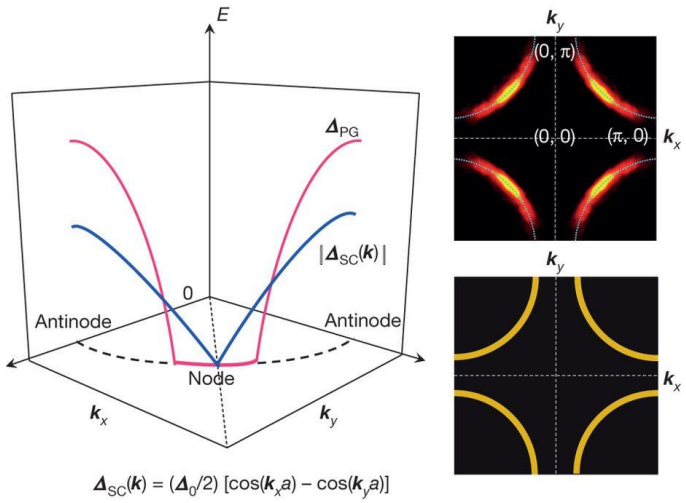

Figure 4: The large Fermi surface predicted by band theory is observed by ARPES and STS for overdopes compounds (bottom right). But once the pseudogap sets in, the antinodal regions of the Fermi surface near the Brillouin zone edge are gapped out, giving rise to Fermi arcs (top right). This is reflected (left) in the angle dependence of the energy *E* of the superconducting gap Δ_{SC} (blue line) and pseudogap Δ_{PG} (red line) as functions of the momenta k_x and k_y in one quadrant of the Brillouin zone around the underlying large Fermi surface (dashed curve), as revealed by ARPES and STS. Note the gapless region around the *d*-wave superconducting node for the pseudogap case that defines the Fermi arcs. After [19].

It is important to recognise that the strong electron repulsions that cause the undoped system to be an insulator (with an energy gap of 2 eV) are still the dominant microscopic interactions, even in optimally doped copper oxide superconductors. This has several general consequences. The resulting electron fluid is "highly correlated", in the sense that for an electron to move through the crystal, other electrons must shift to get out of its way. In contrast, for the Fermi liquid description of simple metals, the quasiparticles propagate freely through an effective medium defined by the rest of the electrons. The failure of the quasiparticle paradigm is most acute in the "strange metal" regime, that is, the state out of which the pseudogap and the superconducting phases emerge when the temperature is lowered [19].

1.2.3 In-plane transport properties in the strange metal phase

In the previous sections we noted that the typical critical T_c of cuprates is too high to be explained with the standard BCS theory. This is the first hint that the microscopic mechanisms governing the behaviour of these materials must be different from that described for the Fermi Liquid. The subject is important for a number of reasons. Just as in conventional superconductors, where the electron-phonon scattering processes that dominate the electrical resistivity provided an important clue to the pairing interaction, so an understanding of the normal state properties of high-T_c cuprates is widely regarded as a key step towards the elucidation of the pairing mechanism for high temperature superconductivity. Whilst this remains the ultimate goal, the anomalous transport behaviour of the cuprates themselves has become arguably the most studied phenomenon in the field of correlated electrons [31].

In this section, we will analyse the transport properties of cuprates in the strange metal phase. We will note that the transport properties deviate significantly from the Fermi Liquid prediction.

1.2.3.1 In-plane resistivity

The in-plane resistivity $\rho_{ab}(T)$ of hole-doped HTS shows a very systematic evolution with doping, that is summarized in Figure 5a, where a schematic phase diagram of p-type cuprates is reproduced together with the doping and temperature evolution of $\rho_{ab}(T)$.

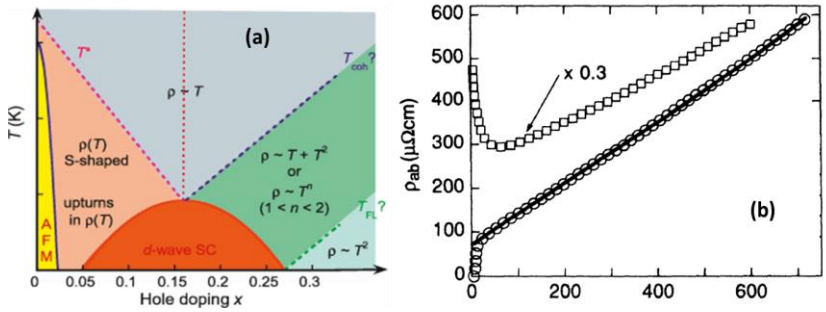

Figure 5: (a) Phase diagram of hole-doped cuprates mapped out in terms of the temperature and doping evolution of the in-plane resistivity $\rho_{ab}(T)$. The solid lines are the phase boundaries between the normal state and the superconducting or antiferromagnetic ground state. The dashed lines indicate crossovers in $\rho_{ab}(T)$ behaviour. The meanings of the labels T^*, T_{coh} and T_{FL} are explained in the text. After [32]. (b) $\rho_{ab}(T)$ measured in Bi-2201 crystals: a non-superconductor (empty squares) and a superconductor (empty circles) with T_C=6.5 K. After [12].

The solid lines are the phase boundaries between the normal state and the superconducting or antiferromagnetic ground state, whereas the dashed lines indicate crossovers in the $\rho_{ab}(T)$ behaviour, each of which may or may not be associated with a fundamental change in the nature of electronic states. Optimal doping is indicated by the vertical dotted line and the areas to the left (right) of this line are the underdoped (overdoped) regions of the phase diagram respectively.

In the underdoped (UD) cuprates, $\rho_{ab}(T)$ varies approximately linearly with temperature at high T, but as the temperature is lowered, $\rho_{ab}(T)$ deviates downward from linearity at $T = T^*$ (marked in Figure 5a and shown in Figure 6a for $Bi_2Sr_2CaCu_2O_{8+\delta}$ samples). In the more anisotropic cuprates such as LSCO [33] and Bi-2212 [34], it has proven difficult to distinguish between deviations from linearity due to genuine pseudo-gap effects and those due to para-conductivity fluctuations near T_c. As shown in Figure 6b for x=0.13 $La_{2-x}Sr_xCuO_4$ compound, at sufficiently low T, $\rho_{ab}(T)$ of UD cuprates develops an upturn,

suggestive of some form of (as yet unidentified) electronic localization. This upturn is characterized by a marked $\log(1/T)$ dependence [35]. The critical doping level p_{crit} at which these upturns occur differs amongst the various cuprate families [36,37] and its trend towards lower p_{crit} with increasing purity suggests that the onset of localization is in fact disorder driven.

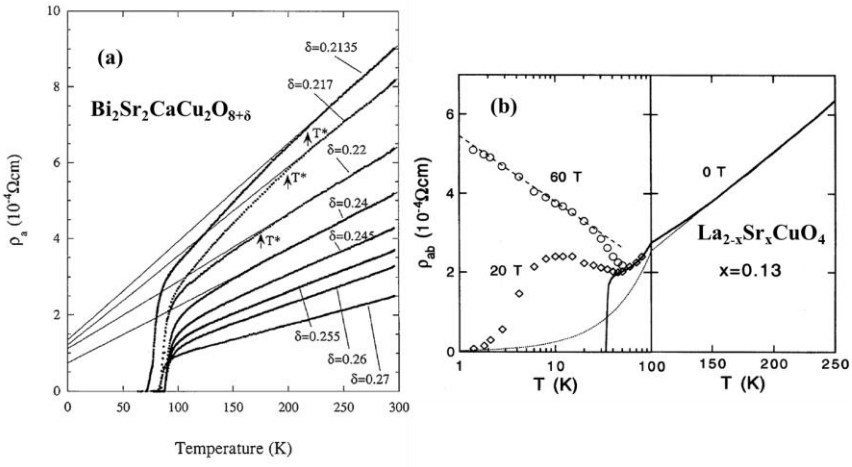

Figure 6: (a) In-plane resistivities ρ_a of $Bi_2Sr_2CaCu_2O_{8+\delta}$ (Bi-2212) single crystals versus temperature for various oxygen contents (δ). The solid straight lines, which are linear extrapolations of ρ_a at higher temperatures, are also shown as a guideline for the near optimally doped (δ=0.24) and underdoped (δ=0.22, 0.217 and 0.2135) samples. The temperatures T^* at which ρ_a deviates from T-linear behaviour are shown by arrows for the underdoped samples. After [34]. In-plane resistivity ρ_{ab} for a x=0.13 $La_{2-x}Sr_xCuO_4$ sample plotted vs linear T at high temperature and $\ln T$ at low temperature. Data are shown for B=0T (solid line), 20 T (diamonds), and 60 T (circles) with the logarithmic fit shown as a dashed line. The dotted line is the extrapolated linear-T dependence. After [35].

Optimally doped (OP) cuprates are characterized by a T-linear resistivity that survives for all $T > T_c$. Despite the large variations in (optimal) T_c and in the crystallography of individual cuprate families, T-linear resistivity is a universal feature at optimal doping, confirming that it is intrinsic to the CuO_2 planes. Figure 5b shows the temperature

dependence of $\rho_{ab}(T)$ for two Bi-2201 crystals, one non-superconducting (empty squares) and one superconducting (empty circles). The superconducting sample shows a strikingly linear-in-temperature $\rho_{ab}(T)$ from just above T_C up to 700 K [12] and it is also evident the violation of the MIR limit. In low-T_C OP cuprates, where the superconductivity can be destroyed by large magnetic fields, the *T*-linear $\rho_{ab}(T)$ has been found to cross over to a higher power *T* dependence, eventually saturating at some residual value [36,37]. Moreover, Ando *et al* showed that the region of strict *T*-linearity (in the normal state) is rather narrow, concentrated at or around optimal doping [38]. This confinement of the *T*-linear resistivity to a narrow composition range near optimal doping is often regarded as a signature of quantum criticality, as demonstrated in heavy-fermion compounds [39].

On the overdoped (OD) side, $\rho_{ab}(T)$ contains a significant supralinear contribution that can be interpreted either as a sum of two components, one *T*-linear, the other quadratic, or a single power law T^n where *n* varies smoothly from 1 at optimal doping to 2 at the SC/non-SC boundary on the OD side [40,41,42]. At sufficiently high *T* however, $\rho_{ab}(T)$ becomes *T*-linear once more. This crossover temperature is marked in Figure 5a as a coherence temperature T_{coh}, in line with the suggestion from ARPES community that the onset of *T*-linear resistivity coincides with the loss of the quasiparticle (coherence) peak in the energy dispersion curves [43]. The crossover to purely quadratic $\rho_{ab}(T)$, characteristic of a correlated Fermi liquid (FL) is only observed beyond the superconducting dome. The dashed line marked T_{FL} in Figure 5a represents the crossover to strictly T^2 resistivity, and, whilst its nomenclature hints at conventional FL behaviour, quantum

oscillations, the classic signature of a FL, have never been observed in this region of the phase diagram [32].

1.2.3.2 In-plane Hall coefficient

The Hall coefficient R_H of hole-doped cuprates is generally positive, as expected for single-band metals where R_H should reflect the sign of the charge carriers. However, equally striking to the *T*-linear resistivity, is the doping and temperature dependence of the in-plane R_H, decreasing in magnitude in some cases as fast as $1/T$ [44]. This behaviour is shown by data on LSCO in [45], which spans the entire (hole doped) phase diagram from the Mott-insulator to the non-superconducting metal. These data are reproduced in Figure 6a and 6b for UD and OD LSCO respectively [45]. At optimal doping ($x\sim0.15$), R_H is found to vary approximatively as $1/T$ over a wide temperature range, in apparent violation of conventional FL theory, which in a single band scenario predicts R_H to depend only on the number of carriers in the metal [46] and should be therefore constant in temperature.

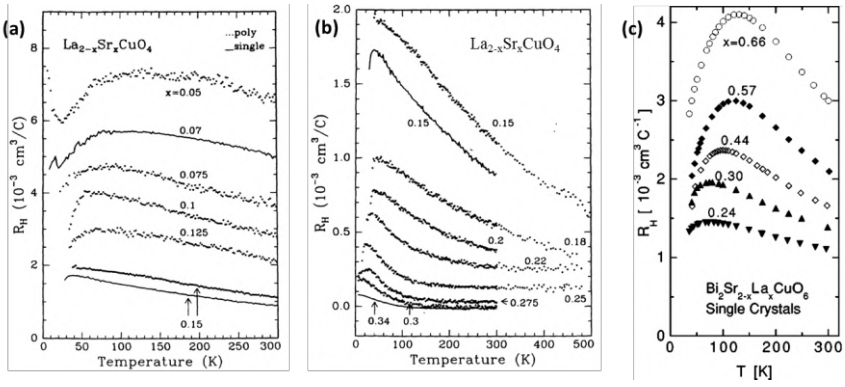

Figure 7: (a) and (b) The temperature dependence of R_H for $La_{2-x}Sr_xCuO_4$ with $0<x<0.35$. Solid lines denote single crystal data; dots denote polycrystalline data. After [45]. (c) Temperature dependence of R_H of the BLSCO crystals. After [47].

Figure 7c shows the temperature dependence of R_H for five samples of La-doped Bi-2201. A clear evolution of R_H with *x* is observed; the change in the magnitude of R_H at 300 K suggests that the carrier concentration is actually reduced roughly by a factor 3 upon increasing *x* from 0.24 to 0.66 [47]. It is worth noting that the ratio of the maximum R_H to the R_H at 300 K is always around 1.4 for all *x* values, indicating that the *T* dependence of R_H is not weakened with *x*.

The relevance of the Hall coefficient as a gauge of carrier density and its evolution with temperature, particularly in the hole-doped cuprates, was challenged by the discovery that the inverse Hall angle $\cot\vartheta_H (= \rho_{ab}/R_H B)$ had a unique and distinct *T* dependence on its own [48]. In marked contrast to the *T*-linear resistivity (at optimal doping), $\cot\vartheta_H$shows a quadratic *T* dependence over a remarkably broad temperature range. In OP LSCO, for example, $\cot\theta_H(T) \sim A + BT^2$ between 50 and 400 K (Figure 7a) [45], whilst $\rho_{ab} \propto T$ up to 1000 K [49]. This implicit "separation of lifetimes" is a classical hallmark of the cuprates, and has led theorists to develop a number of radical ideas beyond conventional Fermi-liquid theory. Finally, whilst the T^2 dependence of $\cot\theta_H(T)$ holds for a wide range of doping in most cuprates, it is not the case for the Bi-based cuprates Bi-2212 and Bi-2201. In these systems, the power exponent of $\cot\theta_H(T)$ is closer to 1.75 than 2 [47,50]. Detailed transport studies of both crystalline and thin-film samples of Bi-2212 and Bi-2201 have shown in fact that $\cot\theta_H(T) \sim A + BT^{\alpha}$ with α steadily decreasing from ~ 2 to $\sim 1.6 - 1.7$ as one moves from the UD to the OD regime [47,50]. Figure 7b shows the plot of $\cot\theta_H$ vs T^2 for five samples of La-doped Bi-2201. Only the data for $x = 0.66$ can be fitted with a straight line in this plot, indicating that the T^2 law of $\cot\theta_H$ can be found in Bi-2201 but only in this UD sample. This variable power law behaviour in $\cot\theta_H(T)$ reveals a high

level of complexity in the phenomenology of normal state transport in HTS that has yet to be properly addressed.

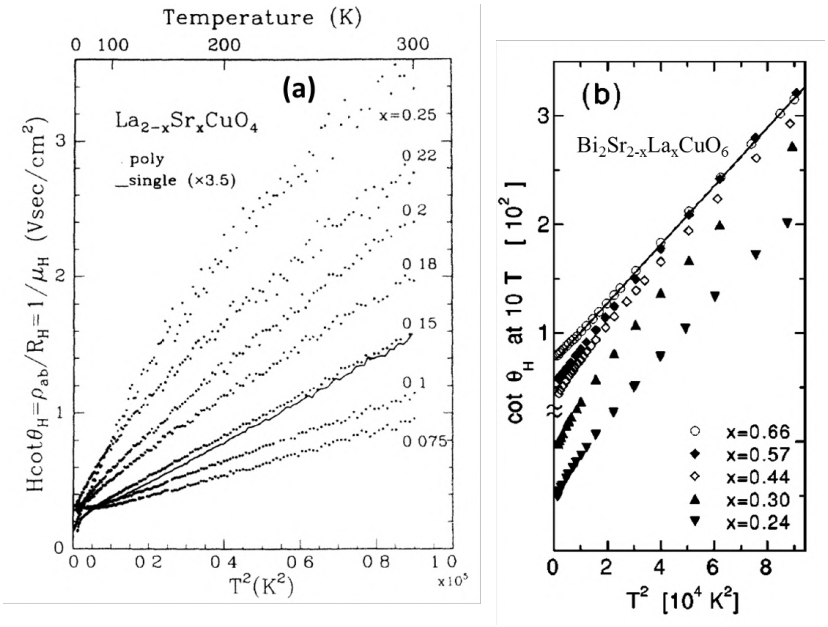

Figure 8: (a) $\cot\theta_H$ multiplied by the magnetic field H as a function of T^2 for $La_{2-x}Sr_xCuO_4$ with $0.075 \leq x \leq 0.25$. Solid lines denote single-crystal data; dots denote polycrystalline data. After [45]. (b) Plot of $\cot\theta_H$ vs T^2 for five samples of $Bi_2Sr_{2-x}La_xCuO_6$ (the data for $x = 0.30$ and 0.24 are shifted down by 50 and 100, respectively, to avoid congestion). The solid line is a fit to the $x = 0.66$ data. After [47].

1.2.3.3 In-plane magnetoresistance

The in-plane magnetoresistance MR of cuprates is small ($\sim 10^{-3}$) and depends on B^2. Figure 8a shows the field dependence of the in-plane resistivity ρ for YBCO when the magnetic field is applied out of plane ($B \parallel c$), perpendicularly to the in-plane electric current ($J \parallel ab$). At all temperatures, ρ increases as B^2 (positive MR) with a curvature that changes rapidly with T [52]. Classically, the transverse MR arises from "bending" of the electron trajectory by the Lorentz force (see Chapter

2). Figure 8b shows a typical example of the in-plane MR of LSCO under three different magnetic field orientations: ($B \parallel c$, $B \parallel J$), ($B \parallel ab$, $B \perp J$), and ($B \parallel c$, $B \perp J$). An appreciable amount of MR can be seen only for the $B \parallel c$ configuration, i.e., transverse MR with field parallel to the *c* axis. The negligibly small longitudinal MR (the Lorentz force is absent in this geometry) indicates that the orbital part dominates the transverse MR. The dominant orbital contribution is observed over the entire temperature range [51].

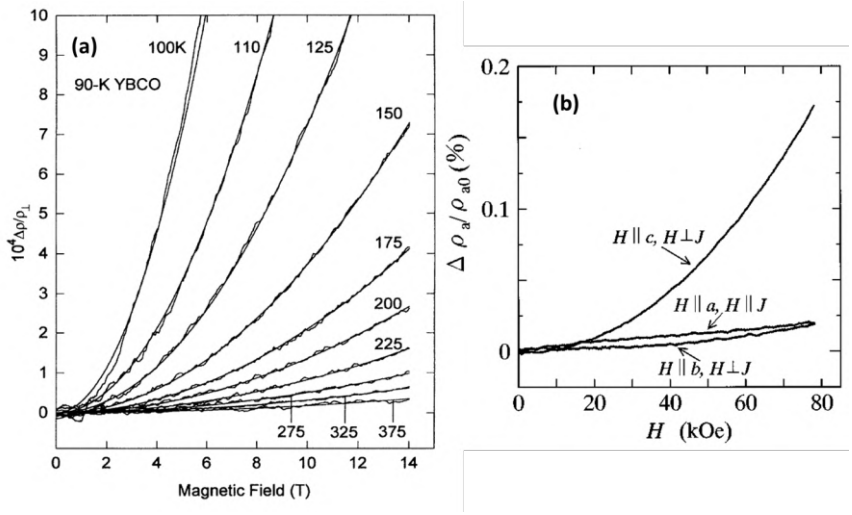

Figure 9: (a) Variation of the resistivity with field for a twinned 90-K $YBa_2Cu_3O_{7-\delta}$ crystal in the transverse geometry $B \parallel c, J \perp c$, at selected temperatures. Smooth lines are fits by $\Delta\rho/\rho = aB^2$. After [52]. (b) In-plane magnetoresistance of $La_{2-x}Sr_xCuO_4$ crystal as a function of magnetic field at T=60 K, with various field orientations $B \parallel c$, $B \parallel J \parallel ab$, $B \perp J \parallel ab$. After [51].

According to Boltzmann transport theory, the orbital transverse magnetoresistance (MR) of a metal $\Delta\rho/\rho \propto (\omega_C\tau_{tr})^2$ where ω_c is the cyclotron frequency and τ_{tr} the transport lifetime. If the only effect of a change of temperature or of a change of purity of the metal is to alter $\tau_{tr}(k)$ to $\lambda\tau_{tr}(k)$, where λ is not a function of k, then $\Delta\rho/\rho$ is unchanged if B is changed to B/λ. Thus the product $\Delta\rho \cdot \rho (= \Delta\rho/\rho \cdot \rho^2)$ is independent of τ_{tr} and a plot of $\Delta\rho/\rho$ versus $(B/\rho)^2$ is expected

to fall on a straight line with slope that is independent of T (provided that the carrier concentration remains constant). This relation, known as Kohler's rule, is obeyed in a large number of standard metals, including those with two types of carriers, provided that changes in temperature or purity simply alter $\tau_{tr}(k)$ by the same factor. In HTS, however, the conventional Kohler's rule is strongly violated; instead of data collapsing onto a single curve, there is a marked increase in the slope with decreasing temperature, as illustrated in the left panel of Figure 10 for UD YBCO [52]. Remarkably, this progression continues up to 350 K (see inset).

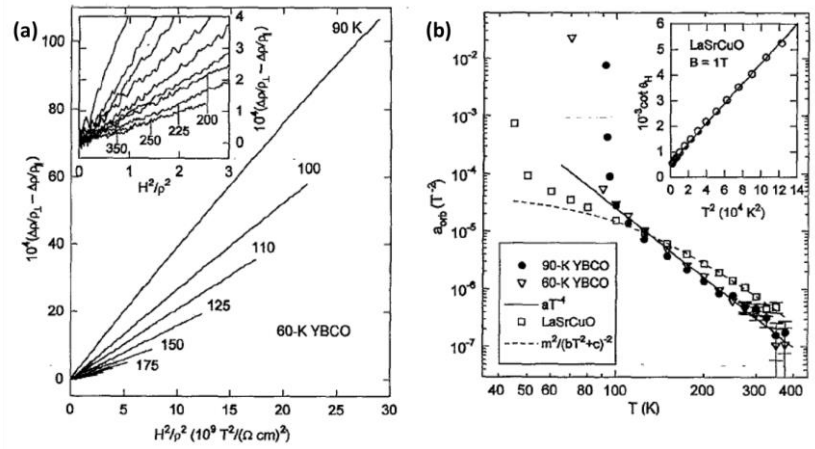

Figure 10: (a) Kohler plot for underdoped $YBa_2Cu_3O_{6.6}$ at intermediate (main) and high (inset) temperatures. (b) Temperature dependence of the orbital part of the magnetoresistance in $YBa_2Cu_3O_{6.6}$, optimally doped $YBa_2Cu_3O_7$ and $La_{1.85}Sr_{0.15}CuO_4$. The inset shows $\cot\theta_H$ versus T^2 in OP LSCO. After [52].

Progress towards understanding this anomalous behaviour came in the form of modified Kohler's rule suggested by Ong and co-workers [52]. They found that the in-plane orbital MR $\Delta\rho/\rho(T)$ follows the T dependence of $tan^2\theta_H$ in both YBCO and LSCO much more closely than ρ_{ab}^2. These behaviours allow them to introduce the following

phenomenological modified Kohler's rule $\Delta\rho/\rho \propto tan^2\theta_H$, which seems to be satisfied (at least in the under-doped and optimally doped region of the phase diagram) as one can see in Figure 9b. Intriguingly, both in over-doped non-superconducting LSCO [52] and in the pseudogap phase of $HgBa_2CuO_{4+\delta}$ (Hg1201) [53], conventional Kohler's scaling is seemingly recovered.

1.2.3.4 Seebeck effect

Within a simple picture of conventional metals, the thermopower is expected to be approximatively linear in temperature, with sufficiently pure metals showing a substantial "phonon drag" peak around $\theta_D/5$-$\theta_D/4$ (where θ_D is the Debye temperature). The thermopower $S(T)$ of the HTS cuprates, differs from this simple behaviour. The temperature dependence is most often linear in those materials, but the zero temperature extrapolated value (S_0) is nonzero [54,55,56]. These features are typified by the results [55] for $Bi_2Sr_{2-x}La_xCuO_{6+z}$ (La-doped Bi-2201), shown in Figure 11.

The temperature and doping dependence of S for the sample with $x > 0.4$ are linear in *T* with a negative slope (Figure 11a) and a positive S_0 (Figure 11b). S_0 having a large positive value at large *x* falls to zero at $x \sim 0.4$. Lowering *x* further below 0.4, S_0 becomes negative. Furthermore, as shown in Figure 10a, there is a systematic shift with increasing concentration of holes on the CuO_2 planes. It has caused some confusion that the shift is towards more negative values with increasing hole concentration (an increase in the La concentration in La-doped Bi-2201 leads to a smaller density of holes in the CuO_2 planes), in the opposite sense that implied by the simple expectation that the thermopower has the carrier sign. This expectation is not to be trusted, for even in some simple metals (e.g., the noble metals) the sign of the

thermopower differs from that of the carriers [57]. Indeed, the calculated band structure of the hole-doped $YBa_2Cu_3O_7$ (Y123), has been shown to lead to a negative thermopower [58].

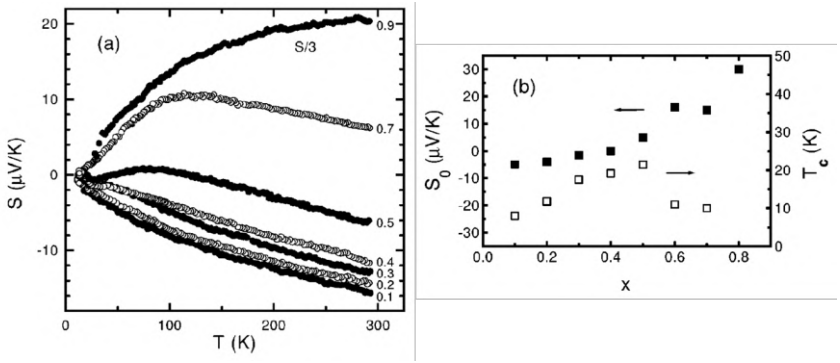

Figure 11: (a) Temperature dependence of the thermopower of $Bi_2Sr_{2-x}La_xCuO_{6+z}$. The numbers near the curves denote the lanthanum concentration *x*. The magnitude of the thermopower of the sample with *x*=0.9 is scaled down. (b) Shows the La-concentration dependence of the zero-offset thermopower S_0 (solid squares) and the superconducting transition temperature T_c (open squares). After [55].

The shift of $S(T)$ with doping is so nearly universal in these materials that it has been used as a gauge of the hole concentration. Orbetelli *et al*. [59] pointed out that the $S(290\ \mathrm{K})$ in a number of cuprates drops on a "universal" curve when it is plotted as a function of T_c/T_c^{max}. They suggested, as a consequence of the $S(290\ \mathrm{K})$ vs T_c/T_c^{max} plot, that the value of $S(290\ \mathrm{K})$ can be used as a measure for the p by additionally employing an empirical relation $T_c/T_c^{max} = 1 - 82.6(p - 0.16)^2$ reported by Presland *et al*. [60]. Although physical interpretation of the relation between $S(290\ \mathrm{K})$ and T_c/T_c^{max} has not been well established, $S(290\ \mathrm{K})$ has been often used to estimate unknown "p" in HTS according to Orbetelli's relation. Indeed, this approach has been successfully used in ref. [61] and ref. [62]. However, this relation was reported invalid for some superconductors such as LSCO [63,64], La-

doped BSCO [65], Pb,La-doped BSCO [66] and BSCO [56]. Figure 11a shows T_c/T_c^{max} of Pb,La-doped BSCO plotted as a function of $S(290\,K)$ together with data reported for other cuprates. The "universal" curve of T_c/T_c^{max} vs $S(290\,K)$ proposed by Orbetelli *et al*., [59] is superimposed by the dashed line [66]. Figure 11b shows the same T_c/T_c^{max} plot for non-substitute Bi-2201 and La-doped Bi-2201 [56].

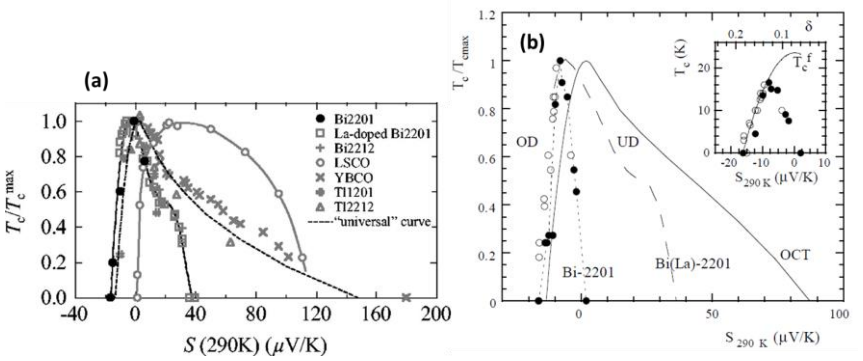

Figure 12: (a) T_c/T_c^{max} as a function of $S(290\,K)$ in $(Bi,Pb)_2(Sr,La)_2CuO_{6+\delta}$ (Pb,La-doped Bi-2201). The data for various cuprates of $Bi_2Sr_{2-z}La_zCuO_{6+\delta}$ (La-doped Bi-2201), $Bi_2Sr_2Ca_{1-x}Nd_xCu_2O_y$ (Bi-2212), $La_{2-x}Sr_xCuO_4$ (LSCO), $YBa_2Cu_3O_y$ (YBCO), $Tl_{0.5}Pb_{0.5}Sr_{2-x}La_xCuO_5$ (Tl-1201), and $Tl_2Ba_2Ca_{1-x}Y_xCu_2O_{8+y}$ (Tl-2212) are superimposed. The "universal" curve proposed by Orbetelli *et al.*, [59] is shown by the dashed line. The solid lines are drawn for the guide to the eye, which clearly show that T_c/T_c^{max} vs $S(290\,K)$ in Bi-2201, La-doped Bi-2201 and LSCO obviously possess data far from the "universal" curve. After [66]. (b) Comparison of T_c/T_c^{max} vs $S(290\,K)$ between non-substituted Bi-2201 films (closed circles) and ceramics (open circles) and La-doped Bi-2201 single crystal (dashed line). The Orbetelli relation is shown by the solid line. Inset: estimation of the fictitious $T_{c,max}^{f}$ value from the phenomenological law [60] with $p(S_{290\,K})$ (solid line). After [56].

Although Figure 12 shows appropriate consistency at negative $S(290\,K)$, the relation between T_c/T_c^{max} and $S(290\,K)$ for the Bi-2201, obviously deviates from the "universal curve". These experimental facts strongly indicate that the "univesal" curve proposed by Orbetelli *et al*., [59] may not be universally valid.

Finally, although the high-temperature behaviour of cuprates near optimal doping is described as $S \sim -bT + a$, with a, b constant (sometimes, with logarithmic corrections). However, the data considered in such fits is over a relatively restricted temperature range, below room temperature. Data over a larger temperature range in YBCO and LSCO clearly show a positive, upwards curvature to the temperature dependence of *S* at large temperatures [64,67].

1.2.3.5 Nernst effect

Given that in conventional metals the magnitude of the Nernst effect is usually in the nV $K^{-1}T^{-1}$ range [68], the enhanced Nernst effect in both cuprates and IBS in the hundreds of nV $K^{-1}T^{-1}$ range is surprising and could suggest a common relationship between high Nernst effect and unconventional superconductivity. Indeed, a large Nernst signal e_N extending from below T_c to a broad interval above has been detected in many hole-doped cuprates. The results have been interpreted considering that the observed e_N is the sum of a normal term due to the charge carriers (e_N^n) and an anomalous contribution (e_N^a), which, below T_c, is universally ascribed to the presence of superconducting vortices (e_N^s, see Chapter 2). An important point is that e_N^n must decrease to zero as $T \rightarrow 0$ because it is a carrier-entropy current. By contrast, e_N^s strongly diverges for $T \rightarrow T_c$ so that $e_N \sim e_N^s$ in the superconducting state. However, an enhanced e_N has been observed up to a certain $T_{onset} > T_c$ that depends on the material and is up to 50-100 K above T_c in $La_{2-x}Sr_xCuO_4$[69].The notion that vortices of whatever origin can be detected 50-100 K *above* T_C remains a surprising topic [70]. Hence, it is common to refer to the region between T_c and T_{onset} generically as a "fluctuation" regime. The important point of whether this regime corresponds to magnetic vortices or is caused by excitations in a strong

correlated state is at present open and several models interpreting the Nernst results strictly in terms of quasiparticles have appeared [71,72].

For the purpose of determining the onset temperature T_{onset} of e_N^s, however, the normal term has to be carefully resolved. This involves measuring the thermopower, Hall angle and resistivity in addition to e_N. This procedure has been described in detail in [73].

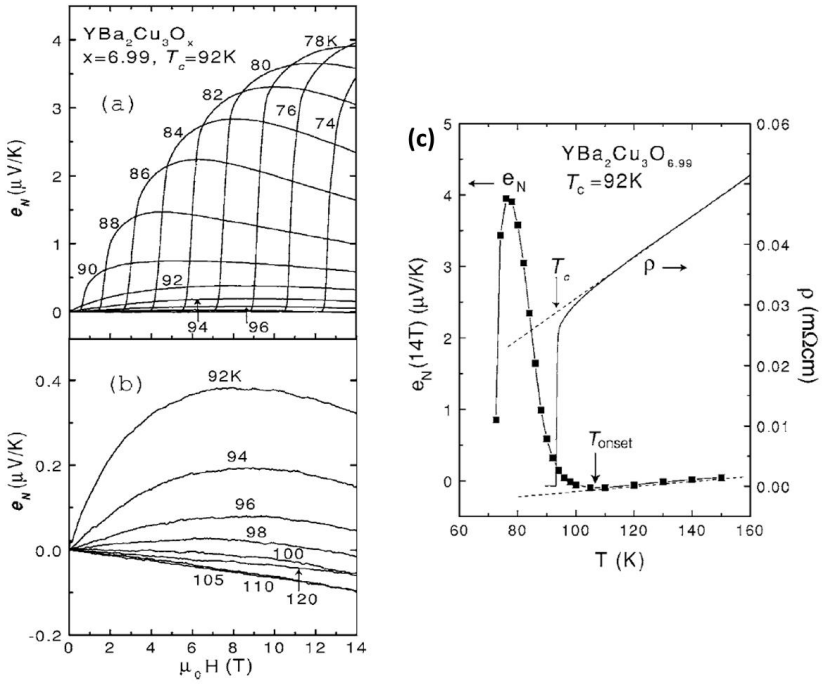

Figure 13: Curves of the Nernst signal e_N vs B measured in slightly OD YBCO (T_C = 92 K) at temperatures below T_C (a) and above T_C (b). Below T_C, e_N rises neatly vertically at the melting field B_m. Above T_C (b), the negative B-linear contribution of the qp term e_N^n becomes quite apparent. (c) Temperature dependence of e_N measured at 14 T compared with the resistivity ρ measured on OD YBCO. The onset temperature T_{onset} and T_C are indicated bu arrows. The dashed line indicates the negative qp contribution. After [70].

Figure 13a displays the traces of e_N versus B at fixed T, in a slightly OD crystal of $YBa_2Cu_3O_y$ (YBCO) with T_C = 92 K. As vortices start to

move, e_N rises vertically. The signal reaches a broad maximum and then decreases slowly. As T rises above T_c, the maximum values of $e_N(T)$ decrease markedly and the profile become broader (Figure 13b).

However, an abrupt transition is not observed in the Nernst signal. Instead, it retains its nonlinearity up to $\sim$ 105 K. Above 110 K, the curve of e_N is linear in B with a slope that changes mildly with T, which is commonly identified with e_N^n. To show the fluctuation regime more clearly, Figure 13c reports the T dependence of e_N measured ad 14 T together with its zero-field electric resistivity ρ. Clearly, e_N deviates from the normal background at $\sim$ 107 K, or 15 K above $T_c = 92$ K. Similar measurements on OP bilayer $Bi_2Sr_2CaCu_2O_{8+\delta}$ (Bi-2212, $T_c =$ 91 K) are shown in Figure 14a and 14b. The first shows that, near T_c, e_N displays a nonanalytic B dependence in weak B and above T_c, e_N rapidly becomes much smaller in amplitude. The latter displays the T dependence of e_N measured at 14 T together with the Meissner signal measured at 10 Oe in a superconducting quantum interference device (SQUID) magnetometer. The onset temperature T_{onset} of the vortex-Nernst signal is $\sim$ 125 K, or 30 K above T_c. The tri-layer cuprate $Bi_2Sr_2Ca_2Cu_3O_{10+\delta}$ (Bi-2223) also shows similar extension of the Nernst signal above its $T_c = 109$ K and the overall behaviour of e_N vs B is strikingly similar to that of the bilayer system with the Nernst onset temperature around 135 K, ~25 K above T_c [70].

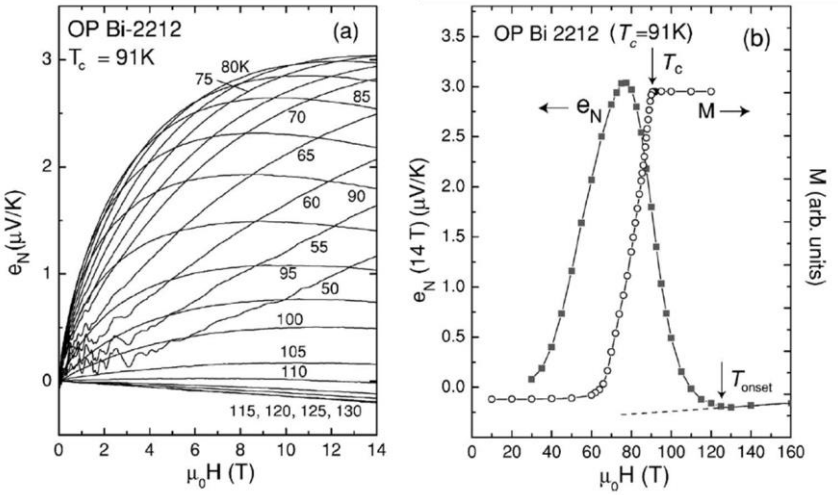

Figure 14: (a) The Nernst signal $\boldsymbol{e_N}$ vs *B* in OP Bi-2212 ($\boldsymbol{T_C}$ = 91 K) at temperatures 50-130 K. The oscillations in $\boldsymbol{e_N}$ are reproducible and may be caused by plastic flow of the vortices. (b) The *T* dependence of $\boldsymbol{e_N}$ measured at 14 T (solid squares) and the Meissner curve (magnetization *M* measured at *B*=10 Oe) in OP Bi-2212. The dashed line indicates the estimated negative normal contribution. After [70].

1.2.3.6 Thermal conductivity

The most characteristic feature of the thermal conductivity κ for a vast majority of cuprates is a sharp rise in the thermal conductivity which sets in at T_c and which culminates in a peak near $T_c/2$. This feature is illustrated in Figure 15 for a representative set of data on YBCO (a) and Bi-2223 *c*-oriented tape (b). A hint of an increase in $\kappa(T)$ as the temperature of a superconductor falls below T_c was seen already in 1950 in a rare case when T_c of a conventional superconductor was high enough and the material had a large lattice thermal conductivity [74]. The issue was pursued theoretically by Geilikmann and Kresin [75] and by Bardeen, Rickayzen and Tewordt in what is referred to as the BRT theory [76]. The essential point of this theory is the realization that as the electrons condense and the electronic thermal conductivity rapidly

vanishes below T_c, the mean-free path of phonons may increase to such an extent that the lattice thermal conductivity more than compensates for the loss of the electronic contribution. A prerequisite for this to happen is a modest electron-phonon interaction and a lattice thermal conductivity κ_{ph} which is non-negligible in comparison to the electronic thermal conductivity κ_{el} in the normal state. Resistivity measurements in conjunction with the Wiedemann-Franz law have clearly established that κ_{ph} is the dominant contribution, accounting for typically 90% of the normal-state total thermal conductivity in sintered samples and at least 50% of the heat conductivity in single crystals. For example, Figure 15b shows that the normal-state κ_{el} of a Bi-2223 c-oriented tape, estimated using the WF law, is nearly a constant curve [κ_{el}~9 mW(cm K)$^{-1}$], whose value is about 22% of κ [77].

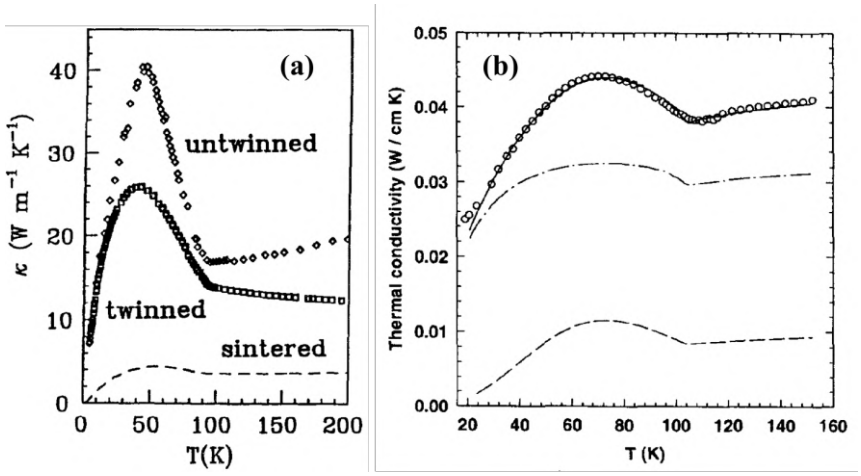

Figure 15: (a) Thermal conductivity of sintered, twinned and untwinned (a-direction) samples of YBCO. After [78]. (b) κ_{ph} (dotted-dashed line) and κ_{el} (dashed line) estimated assuming that both electrons and phonons contribute to the peak of κ (circles); best fit function (solid line) resulting from the sum of κ_{el} and κ_{ph}. After [77].

Other examples that in high-T_c cuprates κ_{ph} can be of the same order of magnitude as κ_{el} are reported in single crystals of YBCO [79] and $Bi_2Sr_2YCu_2O_8$ [80]), or even 10-100 times larger in polycrystalline samples of $REBa_2Cu_3O_7$ [81]. Although some attempts have been performed (e.g. in doped La_2CuO_4 [82]), due to a lack of solid theoretical model to compare it is almost impossible to subtract κ_{ph} and to analyse the pure κ_{el}; then the study of κ is not very helpful to understand the electronic properties of strange metals. A more interesting quantity is the thermal Hall conductivity κ_{xy} which measures the transverse response to an applied longitudinal thermal gradient when the system is immersed in an external magnetic field perpendicular to the plane (see Chapter 2). As a transverse contribution, κ_{xy} is almost unaffected by phonons and allows to measure directly the "Hall" Lorentz number $\mathcal{L}_{xy} = \kappa_{xy}/T\sigma_{xy}(e/k_B)^2$.

The thermal Hall conductivity κ_{xy} was studied for the OP YBCO (T_c~92.5 K) in [83] and [84]. Figure 14a displays the *B* dependence of κ_{xy} at selected temperatures from 95 to 320 K. As shown in Figure 14b (open symbols), the *T* dependence of κ_{xy}/B is well-fitted to $T^{-1.2}$. The calculated value of $\mathcal{L}_{xy}$ varies linearly with *T* (solid circles in Figure 14b) and its value from 95 to 320 K is significantly smaller than $\mathcal{L}$.

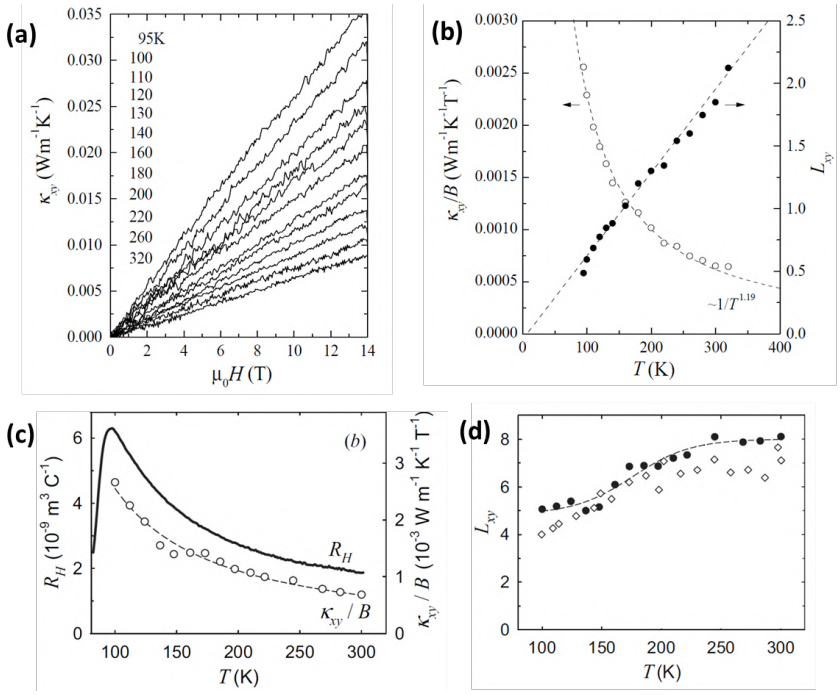

Figure 16: (a) The field dependence of κ_{xy} measured in untwinned $YBa_2Cu_3O_{6.95}$ at selected T. Each trace is in sequence with values of T indicated. After [83]. (b) The T dependence of the Hall-Lorentz number $\mathcal{L}_{xy}$ (solid circles) in untwinned $YBa_2Cu_3O_{6.95}$. Linear extrapolation of $\mathcal{L}_{xy}$ (broken line) shows that it attains the Sommerfield value $\pi^2/3$ near 500 K. The open circles represent the weak-field values of κ_{xy}/B derived from (a) (fit to curve $1/T^{1.19}$ is shown. After [83]. (c) Hall coefficient (solid line and left axis) and κ_{xy}/B (open points and right axis) for the $YBa_2Cu_3O_{6.95}$ crystal; the dashed line shows a function $aT^{-1.2}$ being the best power fit to the experimental points. After [84]. (d) Temperature dependence of $\mathcal{L}_{xy}$ (closed points) for the $YBa_2Cu_3O_{6.95}$ crystal; the dashed line is a guide for the eye. For comparison, values of $\mathcal{L}_{xy}$ (open diamonds) obtained for OP $EuBa_2Cu_3O_7$ single crystal are also depicted. Adapted from [84].

Aside from the overall suppressed scale, the nominally T-linear dependence of $\mathcal{L}_{xy}$ is also unusual. An extrapolation (broken line in Figure 14b) shows that it intersects the Sommerfield value near 500 K. These features seem incompatible with dominant electron-phonon scattering [83]. Figure 14c shows the temperature dependence of the Hall coefficient R_H and κ_{xy} of the sample measured in [84]. The

absolute values of κ_{xy} and its temperature dependence are almost identical to those obtained in [83]. The experimental data are fitted to the function $\kappa_{xy}/B \sim T^{\alpha}$ with α=-1.2, in agreement with the exponent obtained in [83]. The two paper, however, disagree in the prediction of $\mathcal{L}_{xy}$. Figure 14d shows the temperature dependence of $\mathcal{L}_{xy}$ obtained in [84]. The results show a large enhancement of $\mathcal{L}_{xy}$ above $\mathcal{L}$ value and a weak temperature dependence. The discrepancy between the two paper is not yet fully understood but it could be due to the different amounts of impurities existing in the two crystals used in [83], one for σ_{xy} and the second for κ_{xy} measurements [84]. However both papers agree in saying that the Wiedemann-Franz law seems to be strongly violated in these materials.

1.3 Iron-based superconductors

The existence of high-temperature superconductivity in Fe-based compounds was surprising, since historically magnetism has always been considered an antagonist of superconductivity.

After the discovery of fluorine-doped LaFeAsO compounds [9], new samples were synthetized by changing rare earth (RE=Nd, Pr, Sm, Ce, Gd, Tb, Dy) [85]. These compounds with chemical formula REFeAsO belong to a family which has been indicated with 1111. Apart from F-doping, also H-doping under pressure on the O site [86] and creating O-vacancies [87], the superconductivity appear in the 1111 family.
The discovery of the 122 family [88, 89, 90] with general formula AFe_2As_2 (A=Ca, Ba, Sr) resulted particularly interesting due to the possibility of growing big single crystals. The superconductivity in the 122 family can be induced either by hole doping on the site of Ba with

K or by electron doping on the site of Fe with Ni, Rh, Ir, Pd or through substitution of Ru or Co on the site of Fe and P on the site of As [85], generating multiple phase diagrams as shown in the following sections.
The simplest family in terms of crystalline structure is the 11 with chemical formula $Fe_{1+y}Te_{1-x}Se_x$. The so called α-phase of the FeSe is itself a superconductor with T_c of 8K that rises up to 37 K under pressure [91] and up to 100K in FeSe monolayer [92]. Instead the pure FeTe exhibits an antiferromagnetic transition. For x=0.5 T_c rises up to 16 K in bulk samples and 22 K in thin films [93]. Among the family of IBS, the 111 does not require any chemical doping to show superconductivity. Indeed stoichiometric LiFeAs and Na1-xFeAs compounds have Tc of 18 and 12-25 K respectively [85].
The 1111, 122, 11 and 111 families are the most studied so far, however there exist other IBS families with more complex crystalline structures. The so-called 32522 and 42622 families are characterized by the presence of a perovskite block layer as charge reservoir [94,95], whereas in the 1038 and 1048 families the role of charge reservoir is played by PtnAs8 layers [96]. Finally, a new family called 112 has been discovered with formula $Ca_{1-x}RE_xFeAs_2$ with T_c up to 43K in compounds with partial substitution of Sb on the site of As [97].

In the following section I will present more in details the crystal structure and the phase diagram of the IBS, focusing in particular to the 122 family which has been experimentally studied in this work of thesis.

1.3.1 Crystal and electronic structure

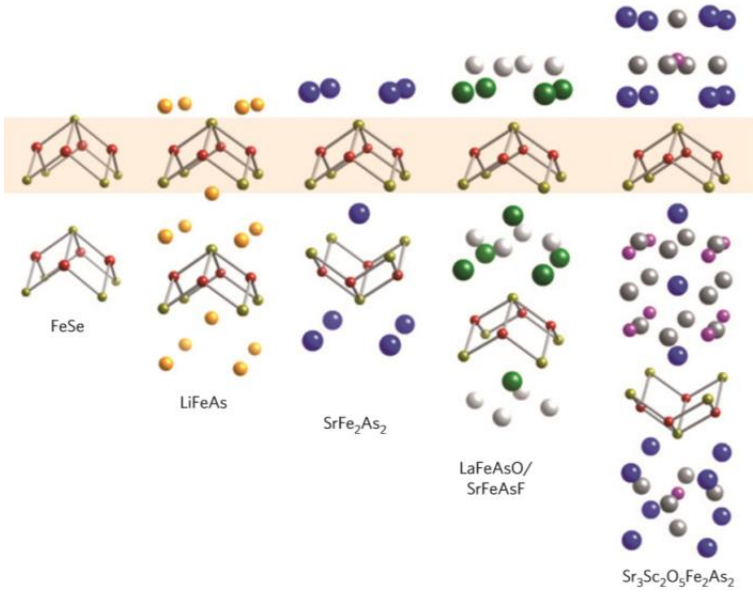

Figure 17: Crystalline structures of the most studied families of IBS. From left to right: 11-family, 111-family, 122-family, 1111-family, 32522-family. The orange band highlights the Fe-As layer. Figure from Ref. [98]

In Figure 17 the crystalline structures of the five main families of IBS are shown. All the families contain a common building block of square lattice of Fe^{2+} ions which takes tetrahedral coordination with pnictide *Pn* (P or As) or chalcogenide (S, Se or Te) elements. The ions are staggered above and below the iron lattice to form a chequerboard pattern that doubles the unit cell size. These slabs are either simply stacked together, as in FeSe, or are separated by spacer layers, called blocking layers, using alkali, alkaline-earth, rare-earth oxide/fluoride (for example, LaO or SrF) or more complicated perovskite-type combinations (for example, $Sr_3Sc_2O_5$). The blocking layers provide a quasi-two-dimensional character with the FeAs layers, whereas the

FeAs-type layer itself is held together by a combination of covalent (that is, Fe-As) and metallic (that is, Fe-Fe) bonding [98].

In order to gain a more physical understanding of superconductivity and its dependence on the structure and doping in the iron-based materials, knowledge of their electronic structure is indispensable. Already early ab initio calculations have shown that the low-energy band structure of these compounds is formed predominantly by Fe-3d orbitals, very weakly hybridized with As-4p orbitals, which commonly produce a rather complex Fermi surface with up to five sheets of different electronic character [99,100]. These calculations further reveal that, as can be expected from their layered crystalline structure, in the PM state, the iron-based materials possess a quasi-two dimensional Fermi surface (FS) (see Figure 18), with three cylinders centred at the point Γ and two at the M point. They seemingly show very good nesting (good geometrical overlap of superimposed portions of the Fermi surface upon shifting of a vector known as "nesting vector") between the hole-like and electron-like FS sheets in the centre and in the corner of the Brillouin zone, respectively (see Figure 18b). This would enhance susceptibility to electronic instabilities leading to the corresponding reconstruction of the Brillouin zone. Neutron-scattering measurements have indeed identified long-range antiferromagnetic order at low temperatures in the overwhelming majority of the parent (undoped) iron-based materials at a wave vector consistent with the nesting vector predicted by theoretical calculations [101,102] (with very few exceptions such as, e.g., LiFeAs superconductor possessing no magnetism or nesting [103] and FeTe, in which the antiferromagnetic wave vector is different from the nesting vector [104]).

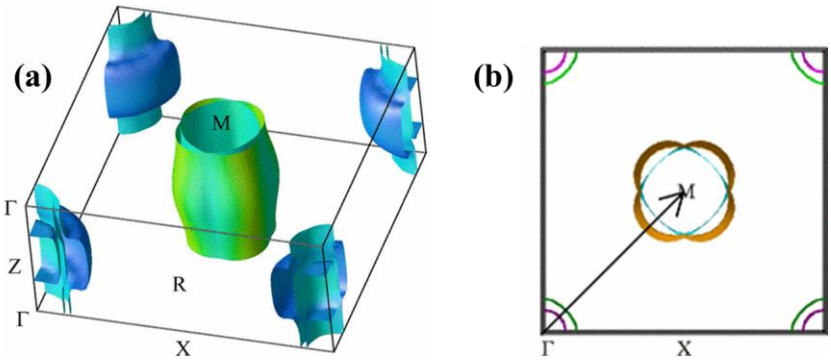

Figure 18: (a) Fermi surface of LaFeAsO calculated in local density approximation. The shading indicates different velocities [darker (blue) is low velocity]. After [99]. (b) Calculated Fermi surface of $LaFeAsO_{1-x}F_x$ with x=0.10. The only 3D parts are the far ends of the electron cylinders around *M*. The arrow represents the nesting vector. After [109].

It is important to note that, although the nesting scenario seemed to provide a plausible explanation for the observed ground state of the parent and superconducting iron-based materials at the dawn of their era [101,114,104], extensive angle-resolved photoemission experiments have revealed an unusual propeller-like shape of the electron sheets of the FS located in the corners of the Brillouin zone in a number of iron-based compounds [105], with no significant nesting between the electron- and hole-like sheets of the FS. These observations appear to challenge the importance of nesting and instead emphasize the role of the orbital character of the FS for superconducting pairing [106], therefore, lending some support to theories of orbital-fluctuation-mediated pairing [107,108].

In any case, the fermiology shown in Figure 18a imposes strong constraints on the superconductivity. Ab initio calculations show that the electron-phonon interaction is too small to account for the superconducting transition temperatures found in these compounds [109, 110,111]. On the other hand, the small FS (Figure 18a) are readily

compatible with a pairing state with weak variations of the order parameter within the sheets but with a π phase shift between electron and hole cylinders. In particular, nesting-enhanced antiferromagnetic spin fluctuations, though repulsive in the singlet channel, would nevertheless be strongly pairing provided that the order parameter on the two sets of the FSs have opposite signs. Although the order parameter of IBS has not been settled with consensus, this "$s_{\pm}$" superconducting state (shown in Figure 19) is both consistent with experimental observations and most favoured by spin fluctuations in these systems.

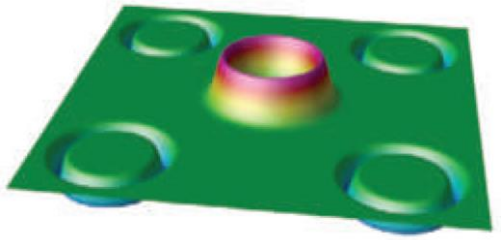

Figure 19: A schematic representation of the superconducting order parameter $\boldsymbol{s}\pm$, as is thought to be the case in iron-based superconductors. After [112].

1.3.2 Phase diagram and strange metal phase of 122 family

The phase diagrams of different classes of IBS have been extensively compared in previous reviews on the topic [85,113,114]. Here we would like to focus on the 122 family, which accepts different possible type of doping and widely thought to capture the main traits of all IBSs. As shown in Figure 20, similar behaviour can be observed considering the phase diagrams for both $Ba_{1-x}K_xFe_2As_2$ (hole doping) and $Ba(Fe_{1-x}Co_x)_2As_2$ (electron doping). Both systems share the same $BaFe_2As_2$ parent compound which exhibits both a structural phase transition (from the room temperature tetragonal *I4/mmm* space group to the low temperature orthorhombic *Fmmm* space group [140]) and the magnetic

transition to a long range ordered antiferromagnetic (AFM) state, associated to a spin-density wave (SDW) order. In the 122 parent compounds both the structural and magnetic phase transitions occur at the same temperature [115, 116]. Doping with either K [116, 117] and Co [118,119,120] causes a suppression of the structural and SDW transition. The isoelectronic substitution of P ions on the As site gives the same phase diagram of the electron doped compounds [121] (Figure 20).

As can be seen in Figure 20, the AFM and superconducting regions of the phase diagram overlap significantly at low doping levels, raising the question of how these two phases coexist with each other. Recently, experimental evidence in favour of microscopic phase coexistence in $Ba_{1-x}K_xFe_2As_2$ as well as in $Ba(Fe_{1-x}Ru_x)_2As_2$ single crystals of sufficiently high quality has emerged [129,122,123,124], proving that phase separation is an extrinsic effect, at least in the 122 iron pnictides.

Such coexistence of superconductivity and AFM suggests the occurrence of an antiferromagnetic QCP [125,126,127] underneath the superconducting dome. With the exception of very few compounds (such as 1111-type materials and $EuFe_2As_2$), the superconducting transition temperature is maximized close to the zero-temperature end point of the antiferromagnetic/structural phase transition line underneath the superconducting dome, at which the long-range antiferromagnetic order continuously disappears and the corresponding antiferromagnetic spin fluctuations are expected to be strongest.

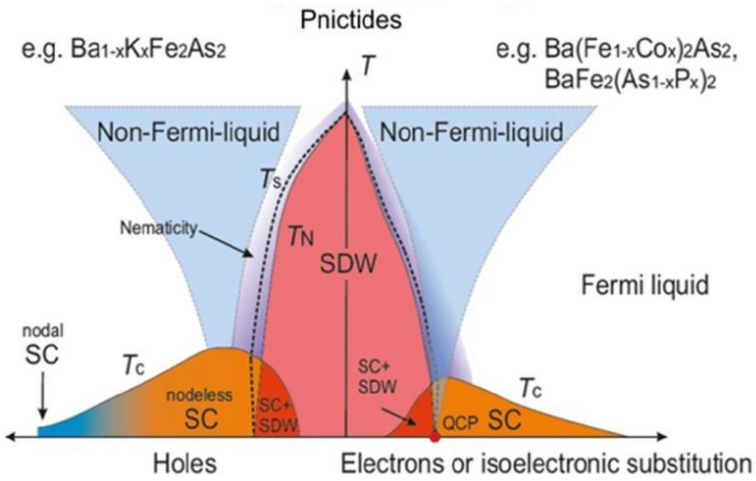

Figure 20: Phase diagram of the electron- and hole-doped 122 family of iron based superconductors. Superconductivity in otherwise non-superconducting antiferromagnetic parent compounds can be induced by doping charge carriers of either sign, which results in a weakening of the itinerant antiferromagnetic phase (pink) and appearance of a dome-shaped superconducting phase region (orange) with coexistence of superconducting and antiferromagnetic phase at certain doping levels. On the hole-doped side of the phase diagram, e.g. $Ba_{1-x}K_xFe_2As_2$ series of compounds, superconductivity has been found to occur continuously up to the complete substitution of potassium for barium [128,129], with a crossover (possibly phase transition) [130] from a nodeless superconducting order parameter in the underdoped, optimally doped and slightly overdoped regions of the phase diagram [131,132,133,134] to a nodal one in the extremely overdoped regime [135,136,137]. Nematic and non-Fermi liquid regions are discussed in the text. Figure adapted from ref. [138].

This observation immediately suggested that in addition to nesting-enhanced antiferromagnetic spin fluctuations discussed in the previous section, also quantum-critical fluctuations of the antiferromagnetic order parameter may mediate superconductivity in IBS, similarly to the mechanism proposed for their high-temperature copper-based [125,126,139] and heavy-fermion counterparts [140].

Figure 21 shows the doping evolution of $\rho(T)$ for the three systems, Co-, P-, and K-Ba122. With Co doping, the temperature dependence changes from T linear to T^2 in the overdoped, non-superconducting region. As in the case of Co-Ba122, the T dependence of $\rho(T)$ gradually

changes from T-linear to T^2 with P doping. The doping evolution of $\rho(T)$ in K-Ba122 is quite different to the Co- and P-doping cases: at low temperatures and at any doping level, the resistivity rapidly decreases with decreasing temperature, showing the T^2 dependence of typical Fermi liquid, whereas it shows a clear tendency for saturation in the high-temperature PM phase. Indeed, a T-linear contribution to $\rho(T)$ is still present for K-doping, but it is less evident than in the Co- and P-doping cases. Furthermore, the presence of a QCP was suggested for P-Ba122 at $x\sim0.3$ [141, 142], where $\rho(T)$ is perfectly linear (Figure 21b) and the effective mass m^* estimated from de Haas oscillations increases from the overdoped region towards $x\sim0.3$ [142]. Unfortunately, it is not clear whether the QCP scenario is applicable to Co and K doping or if the source of T-linear carrier scattering may come from x-dependent coupling with some bosonic excitations, such as antiferromagnetic spin fluctuations (marginal Fermi liquid) [143].

However, as already discussed for cuprates, the non-Fermi-liquid linear $\rho(T)$ appears in a funnel-shaped region of the phase diagram (Figure 20) and, at least for P-Ba122, it originates from the QCP.

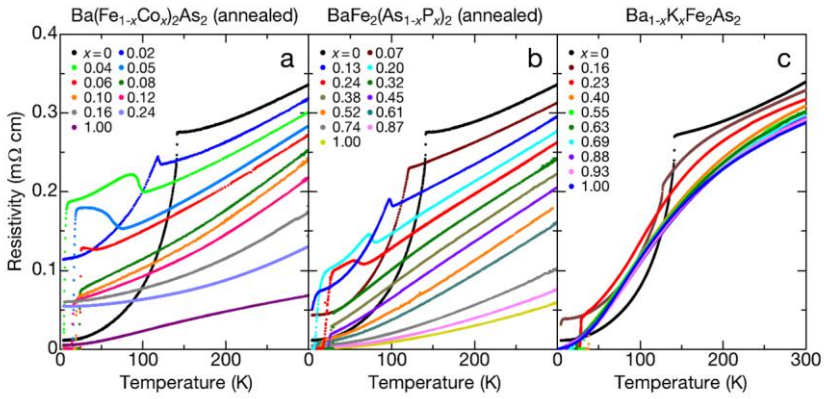

Figure 21: Doping evolution of temperature dependence of the in-plane resistivity for (a) Co-Ba122, (b) P-Ba122, and (c) K-Ba122. After [144].

Recent experiments have further demonstrated the existence of a *nematic* electronic state, which spontaneously breaks the four-fold rotational symmetry of the underlying lattice and induces the structural transition in several materials of the 122 type [145,146,147]. Whether the nematic order parameter is driven by spin-nematic or orbital fluctuations remains unclear [148,149,150,151]; this suggests an intimate interplay of spin and orbital degrees of freedom in the IBS.

1.3.3 Dirac cones in 122 parent compounds

In the SDW phase of 122 parent compounds, the magnetic order reconstructs the quasi-2D Fermi surface of the PM state (Figure 19a) into smaller more three-dimensional pockets (Figure 19b). Out of three cylinders centred at the Γ point, one remains in the SDW phase, whereas the other cylinders reconstruct into a more three-dimensional pockets. In the SDW state, there are two inequivalent directions between Γ and M, named M and M', pointing along the antiferromagnetic and ferromagnetic directions of the Fe-Fe bonds, respectively (see Figure 19b).

Figure 19c shows that a crossing of two bands occurs very near the Fermi level, hence the pocket is electron-like. In Figure 19b the same tiny pockets are marked by blue arrows, to show that it has indeed the shape of a Dirac cone. There are two such symmetry-related Dirac cones in the Γ plane and two in the Z plane. Note that these cones appear only in the path from Γ to M (antiferromagnetic direction) and not in Γ and M'.

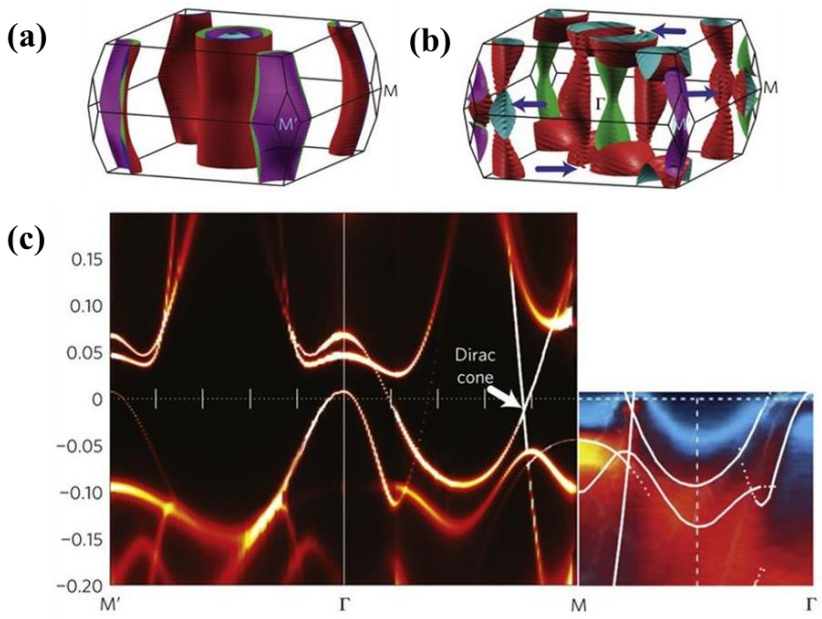

Figure 22: Fermi surface of $BaFe_2As_2$ in the PM state (a) and in the SDW state, plotted in the PM Brillouin zone (b). Blue arrows mark the position of the Dirac cones. (c) Momentum-resolved electronic spectra of BaFe2As2 in the Γ plane along the path M'-Γ-M-Γ in the SDW phase. The path M'-Γ-M (left-hand part) is the result of DFT+DMFT calculations [153], whereas the path M-Γ (right-hand part) has been measured by ARPES technique [155]. A crossing of two bands occurs very near the Fermi level between Γ and M, at three-quarters of the distance, marked by a white arrow. Figure adapted from [153].

The parent compounds of the IBS represent one of the rare 3D crystal solid systems in which DF are claimed to exist in a magnetic ground state [98,159]. Theoretical calculations in the AFM state [152,153] show the presence of topologically protected Dirac cones with linear energy-momentum dispersion carrying the same chirality. Indeed, DF have been experimentally revealed in $BaFe_2As_2$ by angle resolved photoemission spectroscopy (ARPES) measurements [154,155], linear magnetoresistance [156, 157, 158] and by very recent infrared studies [159].

1.3.4 Transport properties of 122 parent compounds

In the parent compounds of the 122 family of IBS, AFe$_2$As$_2$ (A=Ca, Sr, Ba), the magneto-structural transition which occurs at T_{SDW} and the formation of Dirac cones below T_{SDW} remarkably influence the transport properties. Furthermore, the availability of mm-size single crystals of 122 compounds allows better quality and finer measurements, with the further possibility of investigating anisotropy. In the next paragraphs we will review the transport properties of the parent compounds of the 122 family, focusing on those features considered as fingerprints of DF.

1.3.4.1 Electric resistivity

Figure 23 shows temperature-dependent in-plane resistivity of the parent compounds AFe$_2$As$_2$ (A=Ba, Ca, Sr). At high temperatures the curves are almost linear in temperature and in all cases the resistivity values are in the range of hundreds of μΩ cm. SrFe$_2$As$_2$ has the highest resistivity, while BaFe$_2$As$_2$ and CeFe$_2$As$_2$ show similar values. Upon cooling, the resistivity decreases and an abrupt change of regime is observed around the magneto-structural transition. Indeed, a steep decrease is observed in SrFe$_2$As$_2$ and in BaFe$_2$As$_2$, preceded by a small peak in CeFe$_2$As$_2$. T_{SDW} is maxima for Sr (205 K), followed by Ca (173 K) and Ba (138 K). At lower temperatures the curves exhibit metallic behaviour [160].

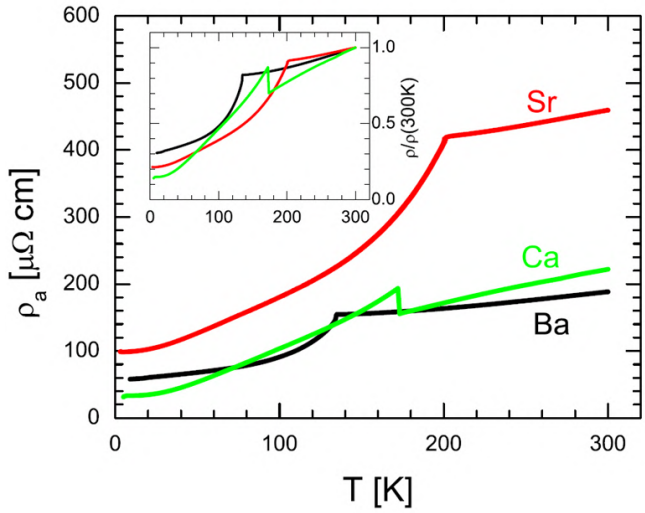

Figure 23: Temperature dependence of the in-plane resistivity for $CaFe_2As_2$ (green line), $SrFe_2As_2$ (red line) and $BaFe_2As_2$ (black line). The inset shows the same data normalized by the resistivity values at 300 K. After [160].

1.3.4.2 Hall effect

In Figure 24a are reported Hall coefficient R_H curves as a function of temperature of the parent compounds AFe_2As_2 (A=Ba, Ca, Sr). They show remarkably similar shapes, signs and magnitudes for the four samples.

At high temperatures all the R_H values are very small ($\sim -10^{-9}$ m^3/C) and weakly temperature dependent, suggesting that in this regime electron-type and hole-type carriers are virtually compensated and give rise to a small R_H. In particular, above T_{SDW}, R_H of $CeFe_2As_2$ rises slightly in modulus and then becomes constant whereas the other two compounds show a linear increase in R_H up to 300 K. In correspondence of T_{SDW} all the curves show an anomaly but only for $CaFe_2As_2$ and the higher purity $SrFe_2As_2$ (Sr(I)) crystal there is a region where $R_H>0$, suggesting a different balance between electron and hole contributions

here. Below T_{SDW}, similarly for all the samples, R_H curves increase in magnitude and are negative in sign. This suggests that a carrier condensation occurs in correspondence of the opening of the SDW gap due to Fermi structure reconstruction, and that at low temperature transport is dominated by electron type carriers.

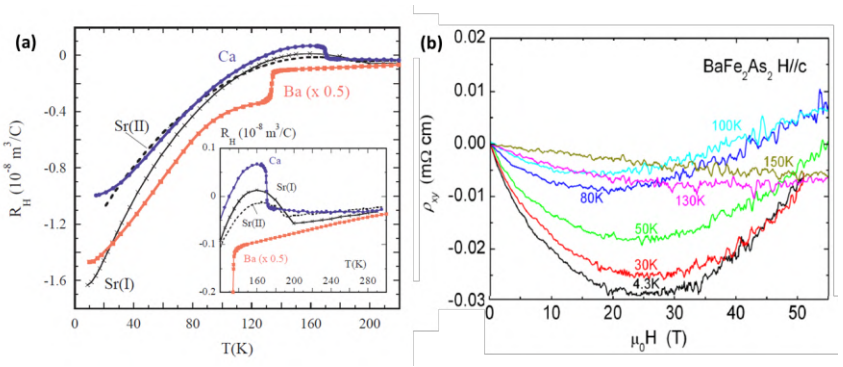

Figure 24: (a) Temperature dependence of the Hall coefficient R_H for single crystal of AFe_2As_2 (A=Ba, Ca, Sr). The inset shows the transitions and the high temperature region on an expanded scale. After [161]. (b) The Hall resistivity ρ_{xy} versus magnetic field up to 50 T of $BaFe_2As_2$.

Figure 24b shows the magnetic field dependence of the Hall resistivity ρ_{xy} for a $BaFe_2As_2$ single crystal, taken at several temperatures at fields up to 50 T [162]. $\rho_{xy}(B)$ shows basically *B*-linear dependence above T_{SDW} and a deviation from the *B*-linearity becomes apparent at T below T_{SDW}. In [162] it is reported that this sublinear *B* dependence of Hall resistivity persists up to 50 T and has been ascribed to the multiband nature of $BaFe_2As_2$.

1.3.4.3 Magnetoresistance

Figure 23 shows the *B* dependence of the magnetoresistance (MR) and its derivative with respect to *B*. In particular, Figure 23a and 23b refer to an as grown crystal of $BaFe_2As_2$ [163]. Figure 23c and 23d are instead relative to a $SrFe_2As_2$ as grown crystal [164].

The magnitude of MR is defined as $\Delta\rho_{ab}(B)/\rho_{ab}(B=0) = [\rho_{ab}(B) - \rho_{ab}(B=0)]/\rho_{ab}(B=0)$, where $\rho_{ab}(B=0)$ is the in-plane resistivity at zero field and $\rho_{ab}(B)$ is the resistivity at an applied field. In all cases, MR is negligible in the PM phase and rapidly increases below T_{SDW}. MR of the as grown crystals is 14% at B=7 T and T=5 K in the case of $BaFe_2As_2$ (Figure 23a) whereas it overcomes 30% at B=8T and 40 K for $SrFe_2As_2$ (Figure 23c). In all cases, a *B* linear contribution is present in the MR, more clearly seen in the *B* dependence of its derivative dMR/dB (Figures 23b,d), which shows a crossover from $MR \propto B^2$ to $MR \propto B$. A similar behaviour in the MR has also been measured in the parent compounds of the 1111 family [165]. *B* linear MR is anomalous since, at low *B*, MR $\propto(\mu_M B)^2$, where μ_M is the mobility, and MR saturates at high fields where $\mu_M B > 1$ [166]. The nonsaturating linear MR has been ascribed to a quantum transport of Dirac-cone states [157] based on a model proposed by Abrikosov [167].

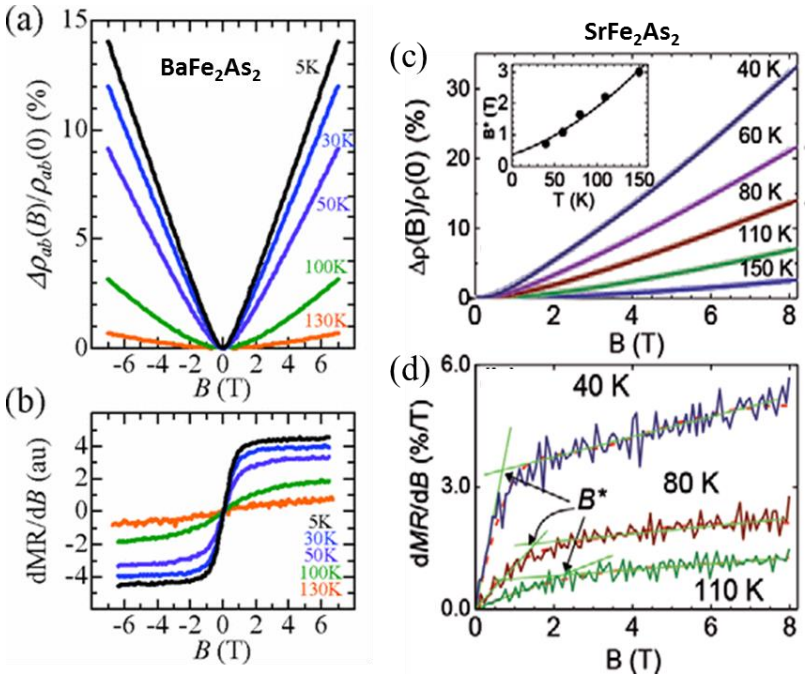

Figure 25: Magnetic field dependence of the magnetoresistance (MR, $\Delta\rho_{ab}(B)/\rho_{ab}(B=0)$) (a) and its field derivative (dMR/dB) (b) for the twinned as-grown $BaFe_2As_2$ crystal taken at several temperatures. After [163]. (c) Magnetoresistance and (d) its derivative for the $SrFe_2As_2$ crystal. The solid lines in (d) show high- and low-field extrapolations and the method to estimate the crossover field B*(T). B*(T) is plotted in the inset to (c). After [164].

1.3.4.4 Seebeck effect

In Figure 24 we present Seebeck curves of different 122 parent compounds collected from literature [168], namely $BaFe_2As_2$ [169,170,171], $CaFe_2As_2$ [172,173] and $EuFe_2As_2$ [174,175].

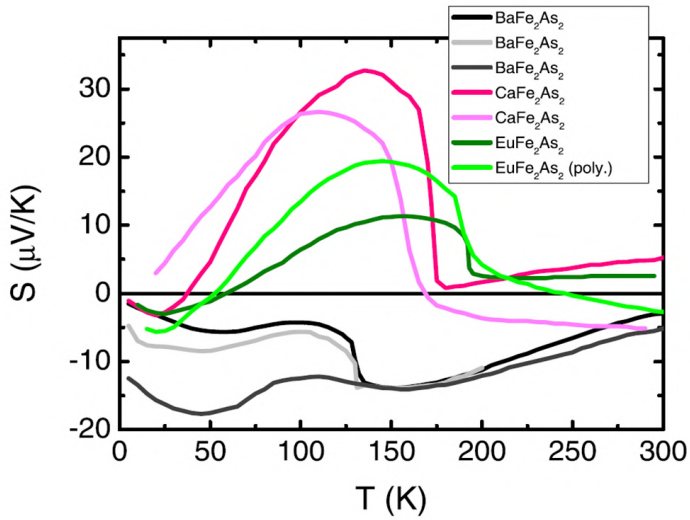

Figure 26: Seebeck coefficient curves of AFe$_2$As$_2$ (A=Ba, Ca, Eu) samples taken from [169-175]. All the samples are single crystals except for the polycrystal of [175]. After [168].

It can be clearly seen that the Seebeck effect curves of samples with the same composition may depart significantly below T_{SDW}, especially $BaFe_2As_2$ single crystals. However, an appreciable spread is also observed in the temperature range above T_{SDW}. This suggests that 122 parent compounds are very close to compensation and the multiband transport properties are very sensitive to the contribution of each band. In all cases, *S* curves undergo an abrupt jump at the magneto-structural transition toward more positive *S* values and exhibit non monotonic behaviour in the low temperature SDW state, where they are characterized by a broad maximum below T_{SDW} at temperatures between 100 K and 150 K and a minimum between 20 K and 50 K, before eventually vanishing at the lowest temperatures. In the high temperature regime above T_{SDW}, the *S* curves are featureless and very small in value. Furthermore, there is some systematic variability depending on the alkaline earth metal, either Ba, Ca or Eu, both above

and below T_{SDW}. The Seebeck of $BaFe_2As_2$ is negative in the whole temperature range. Instead, for the other parent compounds $CaFe_2As_2$ and $EuFe_2As_2$, the Seebeck curves become positive in the low temperature regime. It appears that the smaller is the ionic radius of the alkaline earth metal, the larger is the hole (positive) contribution to transport with respect to the electron (negative) contribution.

The dramatic upturn of *S* at the transition must be related to the structural transition, not to the magnetic transition, as demonstrated under an applied pressure that splits the two transitions [169]. The *S* upturn must be attributed to a steep increase of the hole contribution, related to the reconfiguration of electronic structure and appearance of a hole-like band at the structural transition. This scenario is consistent with the one extracted from ARPES measurements [176].

1.3.4.5 Nernst effect

The parent compounds of IBS show an enhanced Nernst effect. In this case, as discussed above, in the iron pnictides Fermi surface reconstructions related to formation of Fermi surface pockets with Dirac dispersion, could yield enhancement of the Nernst coefficient. In Figure 10, the Nernst coefficients υ measured on single crystals of 122 parent compounds, namely $EuFe_2As_2$ and $CaFe_2As_2$, taken from [174] and [172] respectively, are shown. In $EuFe_2As_2$, υ is positive in the whole temperature range, undergoes a jump at T_{SDW}=191 K, which correlates with the sharp increase in absolute value of *S*, and becomes anomalously large below T_{SDW}, reaching around 600 nV $K^{-1}T^{-1}$. The properties of $EuFe_2As_2$ can be interpreted by considering the presence of Dirac fermions at the Fermi surface. Indeed, experimental curves of Hall resistance R_H, *S* and υ are well reproduced by the phenomenological two-band model developed in [152], where a hole

band with conventional energy spectrum and an electron band with linear energy spectrum are assumed. The Nernst coefficient in $CaFe_2As_2$ also shows a sharp increase below T_{SDW}, and an overall behaviour qualitatively very similar to $EuFe_2As_2$.

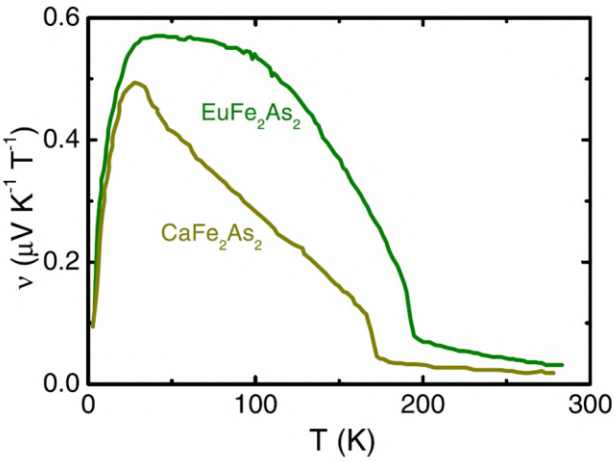

Figure 27: $\nu(T)$ curves measured in 122 parent compounds $EuFe_2As_2$ [174] and $CaFe_2As_2$ [172] single crystals.

References

[1] J.G. Bednorz & K.A.Z. Müller, Physik B, Condensed Matter (1986)
[2] N. E. Hussey *et al.*, *Rep. Prog. Phys.* **81** 052501 (2018)
[3] Y. Kamihara, H. Hiramatsu, M. Hirano, R. Kawamura, H. Yanagi, T. Kamiya and H. Hosono, *J. Am. Chem. Soc.* 128, 10012 (2006)
[4]I. I. Mazin, *Nature* **464**, 183 (2010)
[5] M. Yi, Y. Zhang, Z.-X. Shen, and D. Lu, Role of the orbital degree of freedom in iron-based superconductors, Npj Quantum Mater. 2, 57 (2017).
[6] Qazilbash, M. M. *et al. Electronic correlations in the iron pnictides*. *Nature Phys.* **5** 1–4 (2009).
[7] M. Tinkham "Introduction to Superconductivity", Dover Publications, ISBN: 9780486134727 (2004)
[8] P. Dai, B.C. Chakoumakos, G.F. Sun, K.W. Wong, Y. Xin, D.F. Lu, Physica C 243, 201 (1995)
[9] Y. Kamihara, T. Watanabe, M. Hirano, and H. Hosono, *J. Am. Chem. Soc.*, 2008, 130 (11), pp 3296–3297
[10] Bruin *et al*., "Similarity of Scattering Rates in Metals Showing T-Linear Resistivity", *Science* 339, 6121 (2013)
[11] *Laliberté F et al 2011 Nat. Commun. **2** 432*
[12] Martin, S., Fiory,A. T., Fleming, R. M.,Schneemeyer, L. F.&Waszczak, J. V. Phys.Rev.B41, 846–849 (1990)
[13]N. E. Hussey, K. Takenaka & H. Takagi Universality of the Mott–Ioffe–Regel limit in metals, Philosophical Magazine, 84:27, 2847-2864 (2004)
[14] Sachdev, S. Quantum Phase Transitions (Cambridge Univ. Press, 1999)
[15] S. A. Hartnoll, Nature Phys., vol. 11, p. 54, (2015)
[16] Zaanen, J., Nature 430,512–513 (2004)
[17] A. A. Abrikosov and L. P. Gor'kov, *Sov. Phys. JETP* **12**, 1243 (1961)
[18] M. Hashimoto, Thesis: "Photoemission Study of Single-Layer Cuprate High-Temperature Superconductors" (2007)
[19] B. Keimer, S. A. Kivelson, M. R. Norman, S. Uchida & J. Zaanen, Nature volume 518, pages 179–186 (2015)
[20] Pavarini E, Dasgupta I, Saha-Dasgupta T, Jepsen O and Andersen O K 2001 Phys. Rev. Lett. 87 047003
[21] Tanaka K et al 2004 Phys. Rev. B 70 092503
[22] N. E. Hussey, J. Phys: Condens. Matter 20, 123201 (2008)
[23] M. R. Presland, J. L. Tallon, R. G. Buckley, R. S. Liu, N. E. Flower, Physica C 176, 95 (1991)

[24] J. L. Tallon, C. Bernhard, H. Shaked, R. L. Hitterman, J. D. Jorgensen, Phys. Rev. B 51, 12911 (1995)
[25] D. J. VanHarlingen, Rev. Mod. Phys. 67, 515 (1995)
[26]C. C. Tsuei and J. R. Kirtley, Rev. Mod. Phys. 72, 969 (2000)
[27] N. C. Yeh, C. T. Chen, G. Hammerl, J. Mannhart, A. Schmehl, C.W. Schneider, R. R. Schulz, S. Tajima, K. Yoshida, D. Garrigus, et. al., Phys. Rev. Lett. 87, 087003 (2001)
[28] 57. Marshall, D. S. et al. Unconventional electronic structure evolution with hole doping in Bi2Sr2CaCu2O81d: angle-resolved photoemission results. Phys. Rev. Lett. 76, 4841–4844 (1996)
[29] Ding, H. et al., Nature 382, 51–54 (1996)
[30] Loeser, A. G. et al., Science 273, 325–329 (1996)
[31] Zaanen J., et al., Nat. Phys. 2 138 (2006)
[32] N. E. Hussey, "Phenomenology of the normal state in-plane transport properties of high-T_c cuprates," J. Phys: Condens. Matter 20 (2008) 123201.
[33]T. Nakano, N. Momono, M. Oda and M. Ido, J. Phys. Soc. Japan 67, 2622 (1998)
[34]T. Watanabe, T. Fujii and A. Matsuda, Phys. Rev. Lett. 79, 2113 (1997)
[35] Y. Ando, G. S. Boebinger, A. Passner, T. Kimura and K. Kishio, Phys. Rev. Lett. 75, 4662 (1997)
[36] G. S. Boebinger et al. , Phys. Rev. Lett. 77, 5417 (1995)
[37] S. Ono, Y. Ando, T. Murayama, F. F. Balakirev, J. B. Betts and G. S. Boebinger, Phys. Rev. Lett. 85, 638 (2000)
[38] Ando Y., Komiya S., Segawa K., Ono S. and Kurita Y., Phys. Rev. Lett. 93 267001 (2004)
[39] Custers J., *et al*., Nature 424 524 (2003)
[40] Manako T., Kubo Y. and Shimakawa Y., Phys. Rev. B 46 11019 (1992)
[41] Mackenzie A P, Julian S R, Sinclair D C and Lin C T Phys. Rev. B 53 5848 (1996)
[42] Naqib S. H., Cooper J. R., Tallon J. L. and Panagopoulos C., Physica C 387 365 (2003)
[43] Kaminski A, Rosenkranz S, Fretwell H M, Li Z Z, Raffy H, Randeria M, Norman M R and Campuzano J C Phys. Rev. Lett. 90 207003 (2003)
[44] N. P. Ong, in Physical Properties of High Temperature Superconductors, edited by D. M. Ginsberg (World Scientific, Singapore, 1990), Vol. 2, p. 459.
[45] H. Y. Hwang, B. Batlogg, H. Takagi, H. L. Kao, J. Kwo, R. J. Cava, J. J. Krajewski, and W. F. Peck Jr. , Phys. Rev. Lett. 72, 2636 (1994)

[46] A. A. Abrikosov, Fundamentals of the Theory of Metals (North-Holland, 1988)
[47] Yoichi Ando and T. Murayama, Phys. Rev. B 60, R6991(R) (1999)
[48] T. R. Chien, Z. Z. Wang, and N. P. Ong, Phys. Rev. Lett. 67, 2088 (1991)
[49] Gurvitch M. and Fiory A. T., Phys. Rev. Lett. 59 1337 (1987)
[50] Konstantinovic Z., Li Z. Z. and Raffy H., Phys. Rev. B 62 R11989 (2000)
[51] Kimura, S. Miyasaka, H. Takagi, K. Tamasaku, H. Eisaki, S. Uchida, K. Kitazawa, M. Hiroi, M. Sera, and N. Kobayashi, Phys. Rev. B 53, 8733 (1996)
[52] Harris J M, Yan Y F, Matl P, Ong N P, Anderson P W, Kimura T and Kitazawa K Phys. Rev. Lett. 75 1391 (1995)
[53] M. K. Chan, M. J. Veit, C. J. Dorow, Y. Ge, Y. Li, W. Tabis, Y. Tang, X. Zhao, N. Barišić, and M. Greven, Phys. Rev. Lett. 113, 177005 (2014)
[54] C. R. Varoy, H. J. Trodahl, R. G. Buckley, and A. B. Kaiser, Phys. Rev. B 46, 463 (1992)
[55] Mu-Yong Choi and J. S. Kim, Phys. Rev. B 59, 192 (1999)
[56] Z. Konstantinović, G. Le Bras, A. Forget, D. Colson, F. Jean, G. Collin, Z. Z. Li, H. Raffy and C. Ayache, Europhys. Lett., 62 (2), pp. 257–263 (2003)
[57] F. J. Blatt, P. A. Schroeder, C. Foiles, and D. Greig, Thermoelectric Power of Metals (Plenum, New York, 1976)
[58] P. B. Allen, W. E. Pickett, and H. Krankauer, Phys. Rev. B 37, 7482 (1988); Y. Kubo, J. Supercond. 7, 1 (1994)
[59] S. D. Obertelli, J. R. Cooper, and J. F. Talion, Phys. Rev. B 46, 14 928 (1992)
[60] M. R. Presland, J. L. Tallon, R. G. Buckley, R. S. Liu, and N. E. Flower, Physica C 176, 95 (1991)
[61] M. Putti, D. Marré, I. Pallecchi, P. G. Medaglia, A. Tebano, and G. Balestrino, Phys. Rev. B 69, 134511 (2004)
[62] M. Salluzzo, G. M. de Luca, D. Marrè, M. Putti, M. Tropeano, U. Scotti di Uccio, and R. Vaglio
Phys. Rev. B 72, 134521 (2005)
[63] M. V. Elizarova and V. E. Gasumyants, Phys. Rev. B 62, 5989 (2000)
[64] T. Nishikawa, J. Takeda, and M. Sato, J. Phys. Soc. Jpn. 63, 1441 (1994)
[65] Y. Ando, Y. Hanaki, S. Ono, T. Murayama, K. Segawa, N. Miyamoto, and S. Komiya, Phys. Rev. B 61, R14956 (2000)

[66] Takeshi Kondo, Tsunehiro Takeuchi, Uichiro Mizutani, Takayoshi Yokoya, Syunsuke Tsuda, and Shik Shin, Phys. Rev. B 72, 024533 (2005)
[67] J. S. Kim, B. H. Kim, D. C. Kim, and Y.W. Park, Ann. Phys. 13, 43 (2004)
[68] K. Behnia, J. Phys.: Condens. Matter 21 113101 (2009)
[69]Z. A. Xu, N. P. Ong, Y. Wang, T. Kageshita, and S. Uchida, Nature (London) 406, 486 (2000).
[70]Yayu Wang, Lu Li, and N. P. Ong, Phys. Rev. B 73, 024510 (2006)
[71] A. S. Alexandrov and V. N. Zavaritsky, Phys. Rev. Lett. 93, 217002 (2004)
[72] S. Tan and K. Levin, Phys. Rev. B 69, 064510 (2004)
[73] Y. Wang, Z. A. Xu, T. Kakeshita, S. Uchida, S. Ono, Y. Ando, and N. P. Ong, Phys. Rev. B 64, 224519 (2001)
[74] K. Mendelsshon and J. Olsen, Proc. Phys. Soc. A 63, 2 (1950)
[75] B.T. Geilikman and V.Z. Kresin, Sov. Phys. Doklady 3, 116 (1958); Sov. Phys. JETP 9, 1385 (1959)
[76] J. Bardeen, G. Rickayzen and L. Tewordt, Phys. Rev. 113, 982 (1959)
[77] S. Castellazzi, M.R. Cimberle, C. Ferdeghini, E. Giannini, G. Grasso, D. Marrè, M. Putti, A.S. Siri, Physica C: Superconductivity, 273, 3–4 (1997)
[78] C. Uher, Y. Liu, J. F. Whitaker, Journal of Superconductivity 7, 2, 323-329 (1994)
[79] Peacor S. D., Richardson R. A., Nori F. and Uher C., Phys. Rev. B, 44 9508 (1991)
[80] Allen P. B., Du X., Mihaly L. and Forro L., Phys. Rev. B, 49 9073 (1994)
[81] Ikebe M., Fujishiro H., Nakasato K. and Noto K., Physica C, 263 309 (1996)
[82] C. Hess, B. Büchner, U. Ammerahl, and A. Revcolevschi, Phys. Rev. B 68, 184517 (2003)
[83] Y. Zhang, N. P. Ong, Z. A. Xu, 1, K. Krishana, R. Gagnon and L. Taillefer, Phys. Rev. Lett. 84, 10 (2000)
[84] M. Matusiak, K. Rogacki and B. W. Veal, EPL 88 47005 (2009)
[85] M.D. Lumsden & A.D. Christianson, J. Phys. Condens. Matter 22, 203203 (2010)
[86] Iimura S. et al., Nat Comm 3 943 (2012)
[87] Ren Z.A. et al., Eur. Phys. Lett. 83 17002 (2008)
[88]M. Rotter, M. Tegel, and D. Johrendt, Phys. Rev. Lett. 101, 107006 (2008)
[89]Parasharam Maruti Shirage *et al.*, *Appl. Phys. Express* 1 081702 (2008)

[90] K. Sasmal, B. Lv, B. Lorenz, A. M. Guloy, F. Chen, Y.-Y. Xue, and C.-W. Chu, Phys. Rev. Lett. 101, 107007 (2008)
[91] Mizuguchi Y. Et al., Appl. Phys. Lett 93, 152505 (2008)
[92] Ge J.-F. et al., Nat. Mat. 15, 285-289 (2015)
[93] Bellingeri E. et al., Appl. Phys. Lett. 96, 102512 (2012)
[94] Ma Y. Et al., Sup. Sci. And Tech. 25.11 p. 113001 (2012)
[95] Ogino H. et al., Applied Physics Express 3.6 p. 063103 (2010)
[96] T.P. Ying et al., Scientific Reports 2, 426 (2012)
[97] Kudo K. Et al., Journal of the Physical Society of Japan 83, 025001 (2014)
[98] Paglione J. Et al., Nat. Phys. 6.9, pp. 645-658 (2010)
[99] D. J. Singh and M.-H. Du, Phys. Rev. Lett. 100, 237003 (2008)
[100] I.I. Mazin and J. Schmalian, Physica C 469 614-27 (2009)
[101] Johnston D C 2010 Adv. Phys. 59 803
[102] Stewart G R 2011 Rev. Mod. Phys. 83 1589–652
[103] Borisenko S V et al 2010 Phys. Rev. Lett. 105 067002
[104] Dai P, Hu J and Dagotto E 2012 Nature Phys. 8 709–18
[105] Zabolotnyy V B et al 2009 Nature 457 569–72
[106] Evtushinsky D V et al 2014 Phys. Rev. B 89 064514
[107]Kontani H and Onari S 2010 Phys. Rev. Lett. 104 157001
[108] Saito T, Onari S and Kontani H 2011 Phys. Rev. B 83 140512
[109]I. I. Mazin, D. J. Singh, M. D. Johannes, and M. H. Du, Phys. Rev. Lett. 101, 057003 (2008)
[110] Boeri L, Dolgov O V and Golubov A A 2008 Phys. Rev. Lett. 101 026403
[111] Boeri L, Calandra M, Mazin I I, Dolgov O V and Mauri F Phys. Rev. B 82 020506 2010
[112] I. I. Mazin, Nature 464, 183-186 (2010)
[113]Johnston D C 2010 Adv. Phys. 59 803
[114]Stewart G R 2011 Rev. Mod. Phys. 83 1589–652
[115] Huang Q et al., Phys. Rev. Lett. 101, 257003 (2008)
[116]Kofu M. et al., New J. Phys. 11, 055001 (2009)
[117]Chen H. et al., Europhys. Lett. 85, 17006 (2009)
[118]Chu. J. H. et al., Phys. Rev. B 79, 014506 (2009)
[119]Wang X. F.et al., New J. Phys. 11, 045003 (2009)
[120]Ni N. et al., Phys. Rev. B 78, 214515 (2008)
[121]Jiang. S. et al., J. Phys. Condens. Matter 21, 382203 (2009)
[122]Li Z, Zhou R, Liu Y, Sun D L, Yang J, Lin C T and Zheng G-q Phys. Rev. B 86 180501 (2012)
[123]Munevar J, Micklitz H, Agüero J, Tan G, Zhang C, Dai P and Baggio-Saitovitch E Phys. Rev. B 88 184514 (2013)
[124]Ma L, Ji G F, Dai J, Lu X R, Eom M J, Kim J S, Normand B and Yu W Phys. Rev. Lett. 109 197002 (2012)

[125]Sachdev S and Keimer B Phys. Today 64 29 (2011)
[126]Sachdev S 2011 Quantum Phase Transitions (Cambridge: Cambridge University Press)
[127]Shibauchi T, Carrington A and Matsuda Y Annu. Rev. Condens. Matter Phys. 5 113–35 (2014)
[128]Rotter M, Pangerl M, Tegel M and Johrendt D 2008 Angew. Chem. Int. Edn Engl 47 7949–52
[129]Avci S et al 2012 Phys. Rev. B 85 184507
[130]Maiti S and Chubukov A V 2013 Phys. Rev. B 87 144511
[131]Ding H et al 2008 Europhys. Lett. 83 47001
[132]Evtushinsky D V et al 2009 New J. Phys. 11 055069
[133]Evtushinsky D V et al 2009 Phys. Rev. B 79 054517
[134]Shan L, Wang Y-L, Gong J, Shen B, Huang Y, Yang H, Ren C and Wen H-H 2011 Phys. Rev. B 83 060510
[135]Reid J-P 2012 Phys. Rev. Lett. 109 087001
[136]Reid J-P 2012 Supercond. Sci. Technol. 25 084013
[137]Okazaki K et al 2012 Science 337 1314–7
[138]A Charnukha 2014 J. Phys.: Condens. Matter 26 253203
[139]Sachdev S 2003 Rev. Mod. Phys. 75 913–32
[140]Gegenwart P, Si Q and Steglich F 2008 Nature Phys. 4 186–97
[141] Shishido, H. et al., Phys. Rev. Lett. 104, 057008 (2010).
[142] Hashimoto, K. et al., Science 336, 1554–1557 (2012).
[143] Varma C M, Littlewood P B, Schmitt-Rink S, Abrahams E and Ruckenstein A E 1989 Phys. Rev. Lett. 63 1996–9
[144]Nakajima, M. et al., Sci. Rep. 4,5873; (2014)
[145]Chu J-H, Analytis J G, De Greve K, McMahon P L, Islam Z, Yamamoto Y and Fisher I R Science 329 824–6 (2010)
[146]Chu J-H, Kuo H-H, Analytis J G and Fisher I R Science 337 710–2 (2012)
[147]Kasahara S et al Nature 486 382–5 (2012)
[148]Fernandes R M, B.hmer A E, Meingast C and Schmalian J Phys. Rev. Lett. 111 137001 (2013)
[149]Kim Y K et al Phys. Rev. Lett. 111 217001 (2013)
[150]Fernandes R M, Chubukov A V and Schmalian J Nature Phys. 10 97–104 (2014)
[151]Wysocki A L, Belashchenko K D and Antropov V P Nature Phys. 7 485–9 (2010)
[152]T. Morinari, E. Kaneshita, and T. Tohyama, Phys. Rev. Lett. 105, 037203 (2010).
[153] Z. P. Yin, K. Haule e G. Kotliar, Nat Phys 7.4 (2011), pp. 294-297

[154] Y. Kim, H. Oh, C. Kim, D. Song, W. Jung, B. Kim, H. J. Choi, C. Kim, B. Lee, S. Khim, H. Kim, K. Kim, J. Hong, and Y. Kwon, Phys. Rev. B 83, 064509 (2011).
[155] P. Richard, K. Nakayama, T. Sato, M. Neupane, Y.-M. Xu, J. H. Bowen, G. F. Chen, J. L. Luo, N. L. Wang, X. Dai, Z. Fang, H. Ding, and T. Takahashi, Phys. Rev. Lett. 104, 137001 (2010).
[156] I. Pallecchi, F. Bernardini, F. Caglieris, A. Palenzona, S. Massidda and M. Putti, Eur. Phys. J.B 86: 338 (2013)
[157] K. K. Huynh, Y. Tanabe and K. Tanigaki, Phys. Rev. Lett. 106, 217004 (2011)
[158] I. Pallecchi, F. Bernardini, M. Tropeano, A. Palenzona, A. Martinelli, C. Ferdeghini, M. Vignolo, S. Massidda, and M. Putti, Phys. Rev. B 84, 134524 (2011)
[159] Z.-G. Chen, Luyang Wang, Yu Song, Xingye Lu, Huiqian Luo, Chenglin Zhang, Pengcheng Dai, Zhiping Yin, Kristjan Haule, and Gabriel Kotliar, Phys. Rev. Lett. 119, 096401 (2017).
[160] M. A. Tanatar, N. Ni, G. D. Samolyuk, S. L. Bud'ko, P. C. Canfield, and R. Prozorov Phys. Rev. B 79, 134528 (2009)
[161]C. L. Zentile, J. Gillett, S. E. Sebastian, and J. R. Cooper, arXiv:0911.1259
[162] H. Q. Yuan, L. Jiao, F. F. Balakirev, J. Singleton, C. Setty, J. P. Hu, T. Shang, L. J. Li, G. H. Cao, Z. A. Xu, B. Shen, and H. H.Wen, e-print arXiv:1102.5476.
[163]S. Ishida, T. Liang, M. Nakajima, K. Kihou, C. H. Lee, A. Iyo, H. Eisaki, T. Kakeshita, T. Kida, M. Hagiwara, Y. Tomioka, T. Ito, and S. Uchida, Phys. Rev. B 84, 184514 (2011).
[164]S. V. Chong et al, EPL 104 17002 (2013)
[165]I. Pallecchi, F. Bernardini, F. Caglieris, A. Palenzona, S. Massidda and M. Putti, Eur. Phys. J.B 86: 338 (2013)
[166] J.M. Ziman, Principles of the Theory of Solids, (Cambridge University Press, 1972)
[167] A. A. Abrikosov, Phys. Rev. B 58, 2788 (1998).
[168] I. Pallecchi, F. Caglieris and M. Putti, Supercond. Sci. Technol. 29 073002 (32pp) (2016)
[169] Arsenijevic S, Gaál R, Sefat A S, McGuire M A, Sales B C, Mandrus D and Forró L, Phys. Rev. B 84 075148 (2011)
[170] May A F, McGuire M A, Mitchell J E, Sefat A S and Sales B C, Phys. Rev. B 88 064502 (2013)
[171] Yan Y J, Wang X F, Liu R H, Chen H, Xie Y L, Ying J J and Chen X H, Phys. Rev. B 81 235107 (2010)
[172] Matusiak M, Bukowski Z and Karpinski J, Phys. Rev. B 81 020510 (R) (2010)
[49] Wu G, Chen H, Wu T, Xie Y L, Yan Y J, Liu R H,

Wang X F, Ying J J and Chen X H 2008 J. Phys.: Condens. Matter 20 422201
[173] Wu G, Chen H, Wu T, Xie Y L, Yan Y J, Liu R H, Wang X F, Ying J J and Chen X H, J. Phys.: Condens. Matter 20 422201 (2008)
[174] Matusiak M, Bukowski Z and Karpinski J, Phys. Rev. B 83 224505 (2011)
[175] Ren Z, Zhu Z, Jiang S, Xu X, Tao Q, Wang C, Feng C, Cao G and Xu Z, Phys. Rev. B 78 052501 (2008)
[176] Liu C et al., Nat. Phys. 6 419 (2010)

2 Transport properties

Transport properties are the physical properties related to the flow of an electric ($\boldsymbol{j}$) or heat ($\boldsymbol{j^q}$) current in response to an applied electrochemical field $\boldsymbol{\varepsilon}$ or a temperature gradient $\boldsymbol{\nabla} T$.

In linear approximation, the currents are proportional to the external fields and the coefficients of these linear relations are known as *transport coefficients*. In this Chapter we will define the measurable transport properties (resistivity, Hall effect, thermal conductivity, Seebeck and Nernst effect) in terms of transport coefficients, introducing the phenomenological parameters which come into play in transport.

2.1 Transport coefficients

We consider an electrical and thermal conductor, where both heat and charge carriers can be transferred from a region to another. The current densities $\boldsymbol{j}$ and $\boldsymbol{j^q}$ are linearly related to the thermal gradient ∇T and the electrochemical field $\boldsymbol{\varepsilon} = \boldsymbol{E} + \boldsymbol{\nabla}\mu/e$, with $\boldsymbol{E}$ the electrical field and μ the chemical potential. These linear relations can be written in a matrix form [1]:

$$\begin{pmatrix} \boldsymbol{j} \\ \boldsymbol{j^q} \end{pmatrix} = \begin{pmatrix} \widehat{\boldsymbol{\sigma}} & \widehat{\boldsymbol{\alpha}} \\ T\widehat{\boldsymbol{\alpha}} & \widehat{\widehat{\boldsymbol{\kappa}}} \end{pmatrix} \begin{pmatrix} \boldsymbol{\varepsilon} \\ -\boldsymbol{\nabla} T \end{pmatrix} \tag{2.1}$$

We will generally consider the case of a *xy*-isotropic material on which an electrical and/or thermal current is applied along *x* and a magnetic field *B* is eventually applied along *z*. Under these assumptions, the

transport coefficients $\hat{\boldsymbol{\sigma}}$, $\hat{\boldsymbol{\alpha}}$ and $\hat{\bar{\boldsymbol{\kappa}}}$ are matrices, which, due to the Onsager reciprocity, assume the following form [2]:

$$\hat{\sigma} = \sigma_{xx}\hat{1} + \sigma_{xy}\hat{\varepsilon} \tag{2.2}$$

where $\hat{1}$ is the identity and $\hat{\varepsilon}$ is the antisymmetric tensor $\varepsilon_{ij} = -\varepsilon_{ji}$. $\hat{\sigma}$ is the electric conductivity matrix and analogous expressions hold for the Peltier conductivity matrix $\hat{\alpha}$ and the thermal conductivity matrix $\hat{\bar{\kappa}}$. In the following, we will express measurable transport properties (resistivity, Hall effect, thermal conductivity, Seebeck and Nernst effect) in terms of transport coefficients.

2.2 Transport coefficients in absence of magnetic field

In absence of the applied magnetic field, only the diagonal elements of $\hat{\sigma}$, $\hat{\alpha}$ and $\hat{\bar{\kappa}}$ are different from zero (eq. 2.2). In this condition, we formally define the electric resistivity, the thermal conductivity and the Seebeck coefficient.

2.2.1 Electric resistivity

Applying an electric field (with all the thermal gradients equal to zero), an electric current will flow along the same direction. If the electric field is applied along *x*, from eq. 2.1 we have:

$$\sigma_{xx} = \frac{j_x}{\varepsilon_x} = -\frac{j_x}{\nabla_x V} \tag{2.3}$$

where we introduced the electric potential V as $\varepsilon_x = -\nabla_x V$. Equation (2.3) defines the longitudinal electric conductivity σ_{xx}. Performing

experiments, it is common to apply a current density j_x to the sample and to measure the generated $\nabla_x V$. Therefore, it is convenient to introduce the longitudinal electric resistivity ρ_{xx}, defined as:

$$\rho_{xx} = -\frac{\nabla_x V}{j_x} = \frac{\varepsilon_x}{j_x} = \sigma_{xx}^{-1} \tag{2.4}$$

Equation 2.4 can be generalized to the matrix relation between $\hat{\sigma}$ and the electric resistivity matrix $\hat{\rho}$:

$$\hat{\rho} = \hat{\sigma}^{-1} \tag{2.5}$$

2.2.2 Seebeck effect

The Seebeck effect S is defined as the longitudinal electric field generated by the application of a thermal gradient under open circuit conditions. If a thermal gradient is applied along *x*, eq. 2.1 leads to the following relation:

$$j_x = \sigma_{xx}\varepsilon_x - \alpha_{xx}\nabla_x T = 0 \tag{2.6}$$

from which the Seebeck effect is defined as:

$$S = \frac{\varepsilon_x}{\nabla_x T} = \frac{\alpha_{xx}}{\sigma_{xx}} \tag{2.7}$$

Experimentally, S is measured by creating a thermal gradient $\nabla_x T$ along the sample and measuring the generated electric potential $\nabla_x V$ along the same direction. In terms of these two gradients, from eq. 2.7 we read:

$$S = -\frac{\nabla_x V}{\nabla_x T} \tag{2.8}$$

2.2.3 Thermal conductivity

If a thermal gradient is applied along x ($\nabla_x T$) under open circuit conditions ($j_x = 0$), from eq. 2.1 we read:

$$j_x = \sigma_{xx}\varepsilon_x - \alpha_{xx}\nabla_x T = 0 \tag{2.9}$$

$$j_x^q = T\alpha_{xx}\varepsilon_x - \bar{\kappa}_{xx}\nabla_x T \tag{2.10}$$

By applying the heat current j_x^q to the sample and measuring the generated thermal gradient $\nabla_x T$, we define the longitudinal thermal conductivity κ_{xx} as:

$$\kappa_{xx} = -\frac{j_x^q}{\nabla_x T} = \bar{\kappa}_{xx} - T\frac{\alpha_{xx}^2}{\sigma_{xx}} = \bar{\kappa}_{xx} - TS\alpha_{xx} \tag{2.11}$$

where the last equality follows from eq. 2.7. Equation 2.11 links the measured κ_{xx} to the coefficient $\bar{\kappa}_{xx}$ of the matrix $\hat{\bar{\kappa}}$ which appears in the transport equations 2.1[1].

[1] It is worth noting that $\kappa_{xx} \sim \bar{\kappa}_{xx}$ whenever the term $TS\alpha_{xx}$ is negligible with respect to κ_{xx}. In particular, if we estimate κ_{xx} from the Wiedemann-Franz law (see below) $\kappa_{xx} \sim T\sigma_{xx}L_0$ (L_0 =2.44× 10^{-8}WΩK^{-2} being the Lorenz number) and noting that $TS\alpha_{xx} = T\sigma_{xx}S^2$, it follows that $\kappa_{xx} \sim \bar{\kappa}_{xx}$ whenever $S^2 \ll L_0$. This condition is therefore satisfied in those materials whose S is up to tens of μV/K. On the other hand, it comes out that $\kappa_{xx} \sim \bar{\kappa}_{xx}$ by neglecting ε_x in eq. 2.7. Since $\varepsilon_x = S\nabla_x T$, it is equivalent to ignore the thermoelectric field from the start. We emphasize that its validity requires degenerate Fermi statistics and therefore the term $TS\alpha_{xx}$ is negligible for a metal. In semiconductors, $\kappa_{xx} \sim \bar{\kappa}_{xx}$ is not a good approximation to the correct result (eq. 2.8) [1].

2.3 Transport coefficients with applied magnetic field

In presence of an external magnetic field *B*, the electric charges are subjected to transverse forces which makes off-diagonal terms of $\widehat{\boldsymbol{\sigma}}$, $\widehat{\boldsymbol{\alpha}}$ and $\widehat{\widehat{\boldsymbol{\kappa}}}$ matrices being different from zero (eq. 2.2). In this case, there are a great many transport coefficients to account for. The tree 3×3 matrices, with 27 components, have still 18 independent terms when the Onsager relations are satisfied (eq. 2.2) [3]. Moreover, each coefficient depends on the magnitude and direction of the magnetic field and is only known from the Onsager relations that diagonal (off-diagonal) coefficients must be even (odd) functions of *B*. If we take *B* to be along *z*, we must have cylindrical symmetry along this axis. The matrices $\widehat{\boldsymbol{\sigma}}$, $\widehat{\boldsymbol{\alpha}}$ and $\widehat{\widehat{\boldsymbol{\kappa}}}$ then contain only 9 independent coefficients, namely their *xx*, *xy*, and *zz* components.

In the following we consider the effect of a magnetic field on the transport properties, when heat and/or charge current flows along *x* and *B* is applied along *z*.

2.3.1 Electric coefficients

Considering that the effect of *B* on the electrons is just the Lorentz force, we can write:

$$\boldsymbol{j} = \sigma_E \boldsymbol{\varepsilon} + \sigma_H \boldsymbol{B} \times \boldsymbol{\varepsilon} \tag{2.12}$$

where in an isotropic case σ_E and σ_H are just two scalar coefficients [3]. From eq. 2.12 we see that the current is related to the electric field by $\widehat{\boldsymbol{\sigma}}$ whose off-diagonal part is antisymmetric and proportional to $\boldsymbol{B}$. We can

rewrite eq. 2.12 in a more explicit form, supposing that $\boldsymbol{B}$ is applied along *z*, perpendicularly to the current j_x which flows along *x*:

$$\begin{pmatrix} j_x \\ 0 \\ 0 \end{pmatrix} = \begin{pmatrix} \sigma_E & -\sigma_H B_z & 0 \\ \sigma_H B_z & \sigma_E & 0 \\ 0 & 0 & 0 \end{pmatrix} \begin{pmatrix} \varepsilon_x \\ \varepsilon_y \\ 0 \end{pmatrix} \tag{2.13}$$

Equation 2.13 exploits the magnetic field dependence of σ_{xx} and σ_{xy}. In particular, at first order in *B*, $\sigma_{xx} \equiv \sigma_E$ which does not depend on *B*, whereas $\sigma_{xy} \equiv -\sigma_H B_z$ is *B*-linear. We can also invert eq. 2.13, to express the resistivity matrix $\hat{\rho}$ (eq.2.5):

$$\begin{pmatrix} \varepsilon_x \\ \varepsilon_y \\ 0 \end{pmatrix} = \frac{1}{\sigma_E^2 + \sigma_H^2 {B_z}^2} \begin{pmatrix} \sigma_E & \sigma_H B_z & 0 \\ -\sigma_H B_z & \sigma_E & 0 \\ 0 & 0 & 0 \end{pmatrix} \begin{pmatrix} j_x \\ 0 \\ 0 \end{pmatrix} \tag{2.14}$$

From eq. 2.14, the longitudinal electric resistivity (eq. 2.4) reads:

$$\rho_{xx} = \frac{\sigma_E}{\sigma_E^2 + \sigma_H^2 {B_z}^2} = \frac{\sigma_{xx}}{\sigma_{xx}^2 + \sigma_{xy}^2} \tag{2.15}$$

Furthermore, in presence of the magnetic field, it appears a transverse electric resistivity, defined as:

$$\rho_{xy} = \frac{\varepsilon_y}{j_x} = \frac{\sigma_H B_z}{\sigma_E^2 + \sigma_H^2 {B_z}^2} = \frac{\sigma_{xy}}{\sigma_{xx}^2 + \sigma_{xy}^2} \tag{2.16}$$

Where the last equality follows from eq. 2.14 and brings directly to the definition of the Hall coefficient:

$$R_H = \frac{\rho_{xy}}{B_z} = \frac{\sigma_H}{\sigma_E^2 + \sigma_H^2 {B_z}^2} \tag{2.17}$$

Another useful quantity to introduce is Hall angle θ_H, defined as:

$$\tan \theta_H = \frac{\sigma_{xy}}{\sigma_{xx}} = \frac{\rho_{xy}}{\rho_{xx}} = \frac{\sigma_H B_z}{\sigma_E} \tag{2.18}$$

where the last equality follows from eq. 2.15 and 2.16.

2.3.2 Transverse thermal conductivity

In zero magnetic field, the observed total thermal current $\boldsymbol{j^q}$ is parallel to the applied ∇T. In an external field perpendicular to ∇T, analogously to the electric case, the generated Lorentz force acts on $\boldsymbol{j^q}$ and makes off-diagonal terms of $\hat{\hat{\boldsymbol{\kappa}}}$ being different from zero. Considering the thermal gradient along *x* and the magnetic field parallel to *z*, from eq. 2.1 we have:

$$\begin{pmatrix} j_x^q \\ j_y^q \\ 0 \end{pmatrix} = T \begin{pmatrix} \alpha_{xx} & \alpha_{xy} & 0 \\ -\alpha_{xy} & \alpha_{xx} & 0 \\ 0 & 0 & 0 \end{pmatrix} \begin{pmatrix} \varepsilon_x \\ \varepsilon_y \\ 0 \end{pmatrix} - \begin{pmatrix} \bar{\kappa}_{xx} & \bar{\kappa}_{xy} & 0 \\ -\bar{\kappa}_{xy} & \bar{\kappa}_{xx} & 0 \\ 0 & 0 & 0 \end{pmatrix} \begin{pmatrix} \nabla_x T \\ \nabla_y T \\ 0 \end{pmatrix} \tag{2.19}$$

From eq. 2.19 we read:

$$j_y^q = -T\alpha_{xy}\varepsilon_x + T\alpha_{xx}\varepsilon_y + \bar{\kappa}_{xy}\nabla_x T - \bar{\kappa}_{xx}\nabla_y T = 0 \tag{2.20}$$

Where we set $j_y^q = 0$, since no heat current is made to flow along *y*. From eq. 2.20, we obtain:

$$\bar{\kappa}_{xy} = \bar{\kappa}_{xx}\frac{\nabla_y T}{\nabla_x T} + T\left(\alpha_{xy}\varepsilon_x - \alpha_{xx}\varepsilon_y\right) \tag{2.21}$$

As for the $B = 0$ case (section 2.2.2), we can approximate $\kappa_{xx} \sim \bar{\kappa}_{xx}$ by neglecting the thermoelectric field. It is worth noting that since now $B \neq 0$, it is reasonable that in order to approximate $\kappa_{xx} \sim \bar{\kappa}_{xx}$, it is necessary to neglect both ε_x and ε_y which correspond to the longitudinal and transverse thermoelectric field respectively. By doing so, we come to the expression for the transverse heat conductivity κ_{xy}:

$$\kappa_{xy} = \kappa_{xx}\frac{\nabla_y T}{\nabla_x T} \tag{2.22}$$

where κ_{xx} is the measured longitudinal thermal conductivity, $\nabla_x T$ is the longitudinal thermal gradient and $\nabla_y T$ is the transverse thermal gradient.

2.3.3 Seebeck effect

In presence of an external magnetic field along *z*, from eq. 2.1, the Seebeck coefficient defined in eq. 2.7 becomes:

$$S = \frac{\alpha_{xx}\sigma_{xx}+\alpha_{xy}\sigma_{xy}}{\sigma_{xx}^2+\sigma_{xy}^2} = \alpha_{xx}\rho_{xx} + \alpha_{xy}\rho_{xy} \tag{2.23}$$

where the last equality follows from eq. 2.15 and 2.16. Usually in metals $\sigma_{xx} \gg \sigma_{xy}$ and $\alpha_{xx} \gg \alpha_{xy}$. This makes the off-diagonal terms negligible, going back to eq. 2.7.

2.3.4 Nernst effect

The Nernst effect is defined as the appearance of an electric field transverse to the applied thermal gradient, in presence of a perpendicular external magnetic field. As for the Seebeck effect, it is measured under open circuit conditions. Let's consider a thermal gradient along *x* ($\nabla_x T$) when a magnetic field is applied along *z*. From eq. 2.1, neglecting the transverse thermal gradient $\nabla_y T$ we read:

$$j_x = \sigma_{xx}\varepsilon_x + \sigma_{xy}\varepsilon_y - \alpha_{xx}\nabla_x T = 0 \tag{2.24}$$

$$j_y = \sigma_{xx}\varepsilon_y - \sigma_{xy}\varepsilon_y + \alpha_{xy}\nabla_x T = 0 \tag{2.25}$$

From Eq. 2.24 we get:

$$\varepsilon_x = \frac{\alpha_{xy}}{\sigma_{xy}}\nabla_x T + \frac{\sigma_{xx}}{\sigma_{xy}}\varepsilon_y \tag{2.26}$$

which can be substituted in Eq. 2.25 to obtain:

$$\varepsilon_x = \frac{\alpha_{xy}}{\sigma_{xy}} \nabla_x T + \frac{\sigma_{xx}}{\sigma_{xy}} \varepsilon_y \tag{2.27}$$

The Nernst coefficient is then defined as[2]:

$$N = -\frac{\varepsilon_y}{\nabla_x T} = -\frac{\alpha_{xx}\sigma_{xy} - \alpha_{xy}\sigma_{xx}}{\sigma_{xx}^2 + \sigma_{xy}^2} = -\alpha_{xx}\rho_{xy} + \alpha_{xy}\rho_{xx} \tag{2.28}$$

where the last equality follows from eq. 2.15 and 2.16.

Furthermore, from eq. 2.28 and 2.23 we obtain:

$$N = \frac{\alpha_{xy}}{\sigma_{xx}} - S\frac{\sigma_{xy}}{\sigma_{xx}} \tag{2.29}$$

2.4 The Peltier coefficients α_{xx} and α_{xy}

By combining the electric resistivity coefficients ρ_{xx}, ρ_{xy} and the thermoelectric coefficients S and N, the thermoelectric conductivities α_{xx} and α_{xy} are derived by solving Eq. 2.23 and Eq. 2.28 for α_{xx} and α_{xy}:

$$\alpha_{xx} = \frac{S\rho_{xx} - N\rho_{xy}}{\rho_{xx}^2 + \rho_{xy}^2} \tag{2.30}$$

$$\alpha_{xy} = \frac{S\rho_{xy} + N\rho_{xx}}{\rho_{xx}^2 + \rho_{xy}^2} \tag{2.31}$$

[2] The Nernst coefficient has been defined according to the sign convention which regards the Nernst signal as positive if is it is consistent with superconducting vortex flow (see section 2.5.3).

Eq. 2.30 and 2.31 show that in order to extract α_{xx} and α_{xy}, both the electric resistivities ρ_{xx} and ρ_{xy} and the thermoelectric coefficients S and N must be experimentally measured.

2.5 Diffusive coefficients in semiclassical theory

We formally introduced the transport coefficients and in this section we will show their expressions within the semiclassical theory of conduction. We therefore refer to the case when the external fields (ε and ∇T introduced in section 2.1) are treated as a small perturbation on the equilibrium state of the many-particle system, eliciting a linear response, whose magnitude measures the corresponding transport coefficient.

The electric current density $\boldsymbol{j}$ and the heat current density $\boldsymbol{j^q}$ are expressed in terms of velocity v_n, energy ϵ_n, charge q_n and distribution function g_n of the *n*-th band [1]:

$$\boldsymbol{j} = \sum_n \int \frac{d\boldsymbol{k}}{4\pi^3} q_n \boldsymbol{v}_n g_n \tag{2.32}$$

$$\boldsymbol{j^q} = \sum_n \int \frac{d\boldsymbol{k}}{4\pi^3} [\epsilon_n - \mu] \boldsymbol{v}_n g_n \tag{2.33}$$

Furthermore, using the linearized Boltzmann equation, the distribution function at $B = 0$ in the presence of a uniform static electric field and temperature gradient becomes:

$$g = g_0 + \tau \left(-\frac{\partial f}{\partial \epsilon}\right) \boldsymbol{v} \cdot \left[-e\boldsymbol{\varepsilon} + \frac{\epsilon - \mu}{T}(-\boldsymbol{\nabla} T)\right] \tag{2.34}$$

where g_0 corresponds to the Fermi-Dirac distribution at the equilibrium, f is the Fermi function and τ is the scattering time. Putting eq. 2.34 in

eq. 2.32, 2.33 and defining the matrices $\boldsymbol{L}^{ij}$ we obtain the relations which link $\boldsymbol{j}$ and $\boldsymbol{j^q}$ to the fields $\boldsymbol{\varepsilon}$ and $\boldsymbol{\nabla} T$:

$$\boldsymbol{j} = \boldsymbol{L}^{11}\boldsymbol{\varepsilon} + \boldsymbol{L}^{12}(-\boldsymbol{\nabla} T) \tag{2.35}$$

$$\boldsymbol{j^q} = \boldsymbol{L}^{21}\boldsymbol{\varepsilon} + \boldsymbol{L}^{22}(-\boldsymbol{\nabla} T) \tag{2.36}$$

where the matrices $\boldsymbol{L}^{ij}$ are defined in terms of the integral:

$$\boldsymbol{\mathcal{L}}^{(\alpha)} = e^2 \int \frac{d\boldsymbol{k}}{4\pi^3}\left(-\frac{\partial f}{\partial \epsilon}\right)\tau \boldsymbol{v}(\boldsymbol{k})\boldsymbol{v}(\boldsymbol{k})(\epsilon - \mu)^{\boldsymbol{\alpha}} \tag{2.37}$$

by

$$\boldsymbol{L}^{11} = \boldsymbol{\mathcal{L}}^{(0)} = \hat{\sigma} \tag{2.38}$$

$$\boldsymbol{L}^{21} = T\boldsymbol{L}^{12} = -\frac{1}{e}\boldsymbol{\mathcal{L}}^{(1)} = T\hat{\alpha} \tag{2.39}$$

$$\boldsymbol{L}^{22} = \frac{1}{e^2 T}\boldsymbol{\mathcal{L}}^{(2)} = \bar{\kappa} \tag{2.40}$$

where the last equality follows from comparing eq. 2.35, 2.36 with eq. 2.1.

From eq. 2.37 and eq. 2.38, we obtain the expression for the conductivity matrix $\hat{\sigma}$ (for $B = 0$):

$$\hat{\sigma} = e^2 \int \frac{d\boldsymbol{k}}{4\pi^3}\tau(\epsilon(\boldsymbol{k}))\boldsymbol{v}(\boldsymbol{k})\boldsymbol{v}(\boldsymbol{k})\left(-\frac{\partial f}{\partial \epsilon}\right) \tag{2.41}$$

Since the integrands in $\boldsymbol{\mathcal{L}}^{(1)}$ and $\boldsymbol{\mathcal{L}}^{(2)}$ have factors that vanish when $\epsilon = \mu$, to evaluate them one must retain the first temperature correction

in the Sommerfeld expansion[3]. When this is done from eq. 2.39 and 2.40, one finds:

$$\boldsymbol{L}^{12} = \hat{\alpha} = -\frac{\pi^2}{3e} k_B^2 T \frac{\partial}{\partial \epsilon} \hat{\sigma}\Big|_{\epsilon=\epsilon_F} \tag{2.42}$$

$$\boldsymbol{L}^{22} = \hat{\bar{\kappa}} = \frac{\pi^2}{3} \frac{k_B^2 T}{e^2} \hat{\sigma} \tag{2.43}$$

where k_B,e and ϵ_F are respectively the Boltzmann constant, the charge of the carrier and the Fermi energy. Eq. 2.42 and 2.43 are of particular importance. The first expresses a cornerstone relation between $\hat{\sigma}$ and $\hat{\alpha}$ and it is called the Mott relation, whereas the second is the well-known Wiedemann-Franz law. We will discuss these two relations in following sections.

2.5.1 Drude conductivity and Hall effect

Recalling that $\boldsymbol{v}(\boldsymbol{k}) = \frac{1}{\hbar}\frac{\partial \epsilon(\boldsymbol{k})}{\partial \boldsymbol{k}}$, it is possible to write $\boldsymbol{v}(\boldsymbol{k})\left(-\frac{\partial f}{\partial \epsilon}\right) = -\frac{1}{\hbar}\frac{\partial}{\partial \boldsymbol{k}} f(\epsilon(\boldsymbol{k}))$ and integrating by parts [1], eq. 2.34 becomes:

$$\hat{\sigma} = e^2 \tau(\epsilon_F) \int_{\substack{\text{occupied} \\ \text{levels}}} \frac{d\boldsymbol{k}}{4\pi^3} \mathbf{M}^{-1}(\boldsymbol{k}) \tag{2.44}$$

where $\mathbf{M}^{-1}(\boldsymbol{k}) \equiv \frac{1}{\hbar}\frac{\partial}{\partial \boldsymbol{k}} \boldsymbol{v}(\boldsymbol{k})$ is the effective mass tensor. In the approximation $\mathbf{M}^{-1}{}_{\mu\nu} = (1/m^*)\delta_{\mu\nu}$ independent of $\boldsymbol{k}$ for all occupied levels in the band, then eq. 2.44 reduces to the Drude conductivity:

$$\sigma_E = \frac{ne^2\tau}{m^*} = ne\mu \tag{2.45}$$

[3] $\int_{-\infty}^{\infty} H(\epsilon) f(\epsilon) d\epsilon = \int_{-\infty}^{\mu} H(\epsilon) d\epsilon + \frac{\pi^2}{6}(k_B T)^2 H'(\mu) + O(k_B T)^4$, where $f(\epsilon)$ is the Fermi-Dirac function and $H(\epsilon)$ vanishes as $\epsilon \to -\infty$ and diverges no more than some powers of ϵ as $\epsilon \to +\infty$.

where we defined the mobility of the carrier:

$$\mu = e\tau/m^* \tag{2.46}$$

In presence of an external magnetic field the off-diagonal elements of $\hat{\sigma}$ will be different from 0 and, at first order in *B*, we have [12]:

$$\sigma_H = \sigma_H \mu = ne\mu^2 \tag{2.47}$$

Putting. Eq. 2.46 and 2.47 in eq. 2.17 (which, at first order in *B* becomes $R_H \sim \frac{\sigma_H}{\sigma_E^2}$) we read the expression for the single-band Hall coefficient:

$$R_H = \frac{1}{ne} \tag{2.48}$$

which is inversely proportional to the density of carriers n and its sign depends on the sign of the carriers (e is the charge of the carrier with its sign).

Furthermore, substituting eq. 2.46 and 2.47 into eq. 2.18, we get the expression for the tangent of the Hall angle:

$$\tan\theta_H = \mu\, B = \omega_c \tau \tag{2.49}$$

where in the last equality we defined the cyclotron frequency ω_c, depending on the magnetic field B and the effective mass m^*.

2.5.2 Diffusive Seebeck

From eq. 2.42 we read the relation between the diagonal components of $\hat{\sigma}$ and $\hat{\alpha}$:

$$\alpha_{xx} = -\frac{\pi^2}{3e} k_B^2 T \frac{\partial}{\partial \epsilon} \sigma_{xx}|_{\epsilon=\epsilon_F} \tag{2.50}$$

and using the definition of the S in zero magnetic field (eq. 2.7) we get:

$$S^{(e/h)} = (-/+)\frac{\pi^2}{3}\frac{k_B}{e}k_B T\left.\frac{\partial \ln \sigma_{xx}^{(e/h)}}{\partial \epsilon}\right|_{\epsilon=\epsilon_F} \tag{2.51}$$

Considering the Drude expression of the conductivity (eq. 2.45), it is possible to express S in terms of charge carrier densities n, scattering times τ and effective masses m^*:

$$S^{(e/h)} = (-/+)\frac{\pi^2}{3}\frac{k_B^2 T}{e}\left(\frac{1}{n_{e/h}}\frac{dn_{e/h}}{d\epsilon} + \frac{1}{\tau_{e/h}}\frac{d\tau_{e/h}}{d\epsilon} - \frac{1}{{m^*}_{e/h}}\frac{d{m^*}_{e/h}}{d\epsilon}\right)\Bigg|_{\epsilon=\epsilon_F} \tag{2.52}$$

which explicitly identifies the Seebeck effect as a powerful tool to get information about the scattering mechanisms and the band structure.

Considering the elastic scattering with impurities as the dominant mechanism, it is possible to assume m^* and the mean free path l as energy independent[4].

For a 3D system with a parabolic band, $\epsilon_F = \hbar^2/2m^*(3\pi^2 n)^{2/3}$ and

$$\left.\frac{\partial n}{\partial \epsilon}\right|_{\epsilon=\epsilon_F} = \frac{3}{2}\frac{n}{\epsilon_F} \tag{2.53}$$

Putting eq. 2.53 into eq. 2.52, in the elastic scattering limit, we get the 3D Mott expression for S:

$$S_{3D}^{(e/h)} = (-/+)\frac{1}{3}\frac{\pi^2}{e}\frac{k_B^2 T}{\epsilon_F} \tag{2.54}$$

[4] If we rewrite the scattering time as $\tau = l/v_F$ (where $v_F = \sqrt{2\epsilon_F/m^*}$ for a parabolic band), to consider l as energy independent is equivalent to assume $\tau \sim \epsilon^{-1/2}$. Therefore, $\left.\frac{d\tau}{d\epsilon}\right|_{\epsilon=\epsilon_F} = -\frac{1}{2}\frac{\tau}{\epsilon_F}$.

In 2D, the Fermi energy is simply expressed in terms of n: $\epsilon_F = \pi\hbar^2 n_{2D}/m^*$, where $n_{2D} = n \cdot c_{axis}$, from which we immediately obtain:

$$\left.\frac{\partial n_{2D}}{\partial \epsilon}\right|_{\epsilon=\epsilon_F} = \frac{n_{2D}}{\epsilon_F} \tag{2.55}$$

Putting eq. 2.55 in eq. 2.52, in the elastic scattering limit, we obtain the 2D Mott expression for S:

$$S_{2D}{}^{(e/h)} = (-/+)\frac{1}{6}\frac{\pi^2}{e}\frac{k_B^2 T}{\epsilon_F} \tag{2.56}$$

Eq. 2.56 is derived assuming a parabolic dispersion relation of the energy. We can extend Eq. 2.56 to a band with linear dispersion relation $\epsilon(k)$. In this case, the Fermi energy is expressed in terms of the Fermi velocity v_F and the 2D carrier density n_{2D} as $\epsilon_F = \hbar v_F\sqrt{2\pi n_{2D}}$, while assuming l as energy-independent, bringing to the following equations:

$$\left.\frac{\partial n_{2D}}{\partial \epsilon}\right|_{\epsilon=\epsilon_F} = 2\frac{n_{2D}}{\epsilon_F}, \qquad \left.\frac{\partial \tau}{\partial \epsilon}\right|_{\epsilon=\epsilon_F} = -\frac{\tau}{\epsilon_F} \tag{2.57}$$

It follows that Eq. 2.56, in case of linear $\epsilon(k)$, becomes:

$$S^{(e/h)} = (-/+)\frac{1}{3}\frac{\pi^2}{e}\frac{k_B^2 T}{\epsilon_F} \tag{2.58}$$

It is worth to notice that eq. 2.54, 2.56 and 2.58 simply differ for a pre-factor (1/3 or 1/6) keeping the same (linear) *T*-dependence.

Considering the expression of the electronic specific heat of a degenerate electron gas with carrier density n:

$$C_e = \frac{n\pi^2}{3}\frac{k_B^2}{\epsilon_F}T \tag{2.59}$$

the diffusive Seebeck contribution can be written as:

$$S = \frac{C_e}{ne} \tag{2.60}$$

Eq. 2.60 shows that S can be interpreted as the average entropy carried by an electron in the material.

We remark that the discussed S is the diffusive contribution to the Seebeck effect, due to the diffusion of charge carriers as a consequence of $\nabla_x T$. As for the longitudinal thermal conductivity, different physical mechanisms could contribute to the Seebeck signal other than diffusive motion of carriers, such as *phonon drag* and *magnon drag*. This concepts will be developed contextually to the data analysis in the following Chapters.

2.5.3 Diffusive Nernst and vortex-Nernst contribution

The low temperature Nernst coefficient can be evaluated in analogy with the Seebeck coefficient. Since this effect is measured under an applied magnetic field, we need to take into account the off-diagonal elements of the Mott relation (Eq. 2.42):

$$\alpha_{xy} = -\frac{\pi^2}{3e} k_B^2 T \frac{\partial}{\partial \epsilon} \sigma_{xy}\Big|_{\epsilon=\epsilon_F} \tag{2.61}$$

In the approximation $\sigma_{xx} \gg \sigma_{xy}$, eq. 2.28 becomes:

$$N \approx \frac{\alpha_{xy}\sigma_{xx} - \alpha_{xx}\sigma_{xy}}{\sigma_{xx}^2} \tag{2.62}$$

Putting eq. 2.50 and 2.61 into eq. 2.62 and noting that $\frac{\partial}{\partial \epsilon} \tan \theta_H = \frac{1}{\sigma_{xx}} \frac{\partial \sigma_{xy}}{\partial \epsilon} - \frac{\sigma_{xy}}{\sigma_{xx}^2} \frac{\partial \sigma_{xx}}{\partial \epsilon}$, the Nernst coefficient can be expressed as:

$$N^{(e/h)} = -\frac{\pi^2}{3}\frac{k_B}{e}k_B T \left.\frac{d\tan\theta_H^{(e/h)}}{d\epsilon}\right|_{\epsilon=\epsilon_F} \tag{2.63}$$

Such an expression directly linking the Nernst effect to the energy derivative of the Hall angle was first put forward by Oganesyan and Ussishkin [4].

Using eq. 2.49, assuming that the scattering time is the only energy-dependent component of the Hall angle, an alternative expression for equation 2.63 would be:

$$N^{(e/h)} = -B\frac{\pi^2}{3}\frac{k_B^2 T}{m^*}\left.\frac{d\tau^{(e/h)}}{d\epsilon}\right|_{\epsilon=\epsilon_F} \tag{2.64}$$

The simplest approximation is to assume that the Hall angle does not depend on energy in the vicinity of the Fermi energy. This assumption would lead to a strictly zero Nernst response, which from eq. 2.29 implies:

$$\frac{\alpha_{xy}}{\alpha_{xx}} = \frac{\sigma_{xy}}{\sigma_{xx}} \tag{2.65}$$

Eq. 2.65 formalizes the so-called Sondheimer's cancelation [5].

Therefore, in a single band scenario, the finite Nernst response observed in real metals requires an energy-dependent Hall angle (equivalently energy dependent mobility μ). In the case of elastic impurity scattering, analogously to the Seebeck effect, from eq. 2.64 we get:

$$N^{(e/h)} = B\frac{\pi^2}{3}\frac{k_B^2 T}{e}\frac{\mu}{\epsilon_F} \tag{2.66}$$

where we introduced μ (eq. 2.46). From eq. 2.66 it emerges that the Nernst coefficient, unlike the Seebeck coefficient, is not intrinsically related to the sign of a charge and it is directly proportional to the

mobility of the charge carriers. Therefore, in a single band scenario, the necessary ingredients for an enhanced Nernst signal is a large μ and small Fermi energy.

Up to now transport in the normal state has been considered, however superconducting state introduces additional mechanisms that contribute to the Nernst effect [6]. When a type-II superconductor is placed in a magnetic field B, this partially penetrates into the superconductor in a form of the so called Abrikosov vortices, each of which carries one quantum of magnetic flux $\Phi_0 = h/2e$ such as $B = n\Phi_0$ where n the density of the vortices [7]. They consist of a normal (non-superconducting) core, surrounded by superconducting currents circulating externally to it. In the presence of B, the temperature gradient ∇T, drives the vortices to the cooler end of the sample, because a normal vortex core has a finite amount of entropy relative to the zero-entropy condensate [8,9]. By the Josephson effect, the vortex motion generates an electric field $\boldsymbol{E} = \boldsymbol{B} \times \boldsymbol{v}$ that lies perpendicular to both the vortex velocity $\boldsymbol{v}$ and $\boldsymbol{B}$ and it is detected as the vortex Nernst signal. We already discussed that the sign of the Nernst signal is not intrinsically related to the sign of a charge. Fortunately, the Josephson equation, which dictates $\boldsymbol{E}$ parallel to $\boldsymbol{B} \times (-\boldsymbol{\nabla} T)$, provides a sign convention for the Nernst experiment [10]. We regard the Nernst signal as positive if it is consistent with vortex flow. Therefore, the observed Nernst signal N of a type-II superconductor below T_C is the sum of the vortex (N_s) and normal charge-carriers (N_n) terms ($N = N_s + N_n$). It is worth noting that N_s reflects the *primary* response of vortices to an applied gradient, while N_n is a relatively feeble off-diagonal response that is further attenuated by the Sondheimer cancelation (eq. 2.65) [10]. This let understand why the Nernst experiment is so useful for detecting vortex motion.

Another point to be considered is that N_n is linear in B (eq. 2.66), whereas N_s is intrinsically strongly nonlinear in B, showing a characteristic profile of a "tilted hill" associated with vortex motion [11].

2.5.4 The Wiedemann-Franz law

Eq. 2.43 is a relation between thermal and electrical conductivities known as the Wiedemann-Franz (WF) law, which states that the ratio of the thermal to the electrical conductivity of a great number of metals is directly proportional to the temperature, with a proportionality constant which is to a fair accuracy the same for all metals. At given temperature, the WF law can be written as:

$$\kappa_{el} = L\,\sigma T \tag{2.67}$$

where κ_{el} is the electronic thermal conductivity, σ is the electrical conductivity, k_B is Boltzmann constant and L is the Lorenz number that in Boltzmann transport theory is equal to the Sommerfeld value $L_0=\frac{\pi^2}{3}\left(\frac{k_B}{e}\right)^2=2.44\times10^{-8}\mathrm{W\Omega K^{-2}}$ if the mean free paths for transport of charge and entropy are identical. Eq. 2.67 holds whenever the scattering is *elastic* [12]. Indeed, in all conventional metals, the observed L is close to L_0 for low T, where the impurity scattering dominates and for $T > \theta_D$ (θ_D being the Debye temperature of the metal). However, below ~273 K [1], the observed L falls significantly below L_0, implying that the heat current is more strongly scattered relative to the charge current. Because L compares directly the charge and entropy currents, it has contributed strongly to the understanding of how the two currents are affected by distinct scattering processes in conventional metals [12].

It is worth to notice that in eq. 2.67 it appears the electron contribution to the thermal conductivity. The measured total longitudinal thermal conductivity κ is the sum of the electronic (κ_{el}) and phonon (κ_{ph}) components $\kappa = \kappa_{el} + \kappa_{ph}$, and the contribution of each component has to be determined. In conventional metals electrons carry most of the heat, so the phonon contribution to κ can be in many cases neglected. However, in conductors with relatively small carrier densities, κ_{ph} is often much larger than κ_{el}. Therefore, in conventional metals one may use the WF law (with $L = L_0$) to evaluate κ_{el} with negligible error, whereas in conductors with relatively small carrier densities, another experimental approach is needed to evaluate κ_{el}.

The thermal Hall effect (section 2.3.2) provides a rather efficient way to screen out the phonon heat current (even when it is dominant) because whereas in zero magnetic field the observed total thermal current is parallel to the applied temperature gradient ∇T, in an external field perpendicular to ∇T, the Lorenz force acts only on the electronic component of the heat current, considering that phonons are not deviated by the field. By forming the ratio in Eq. 2.67 with κ_{xy} and the electrical Hall conductivity σ_{xy}, it is possible to write:

$$\kappa_{xy} = L_{xy}\sigma_{xy}T \tag{2.68}$$

where L_{xy} is the "Hall" Lorenz number which is regarded as a direct source of information about the electronic heat current [13].

2.5.5 Single band magnetoresistance

We now turn to the second-order effects in *B*. The (low) field Drude conductivity components (eq. 2.45 and eq. 2.47) must be replaced by the expressions of σ_E and σ_H at order B^2. Indeed, it is worth to notice that the second order effects are often non-negligible in actual measurements, causing also in-diagonal terms of eq. 2.13 being field-dependent. For example, a B^2 dependence of the longitudinal resistivity ρ_{xx} (caused by the cyclotron motion of charge carriers) is observable in many cases (see section 2.6.1). Considering one-band system with carrier density n and mobility μ when an external magnetic field *B* is applied, at second order in B, the Boltzmann-Drude expressions for the conductivity tensor read [3]:

$$\sigma_E(B) = ne\mu/(1+\mu^2B^2) \tag{2.69}$$

$$\sigma_H(B) = ne\mu^2/(1+\mu^2B^2) \tag{2.70}$$

The application of a magnetic field usually alters the electrical resistance of a metal and this phenomenon is known as *magnetoresistance*. Turning back to eq. 2.12, it is possible to deduce a formula for the macroscopic conductivity, $\sigma_\perp$, when $\boldsymbol{B}$ is transverse to $\boldsymbol{j}$. This is the ratio of the current to the e.m.f. actually measured along the current axis [3], namely

$$\sigma_\perp = j^2/\boldsymbol{j}\cdot\boldsymbol{E} = \frac{\sigma_E^2+B^2\sigma_H^2}{\sigma_E} \tag{2.71}$$

Considering eq. 2.69 and 2.70, it follows that, for a single band, this yields precisely the same conductivity as in the absence of a magnetic

field[5]. Thus, in free-electron case, the transverse magnetoresistance vanishes identically. In section 2.6.1 we will show how this effect does not vanish in a two-band scenario.

It might be interesting to note that putting eq. 2.69 and eq. 2.70 in eq. 2.17, we get $R_H = \frac{1}{ne}$, which is the same result obtained in the low field limit (eq. 2.48).

2.5.6 Semi-classical Peltier coefficients α_{xx} and α_{xy}

Although a quantitative expression of α_{xx} and α_{xy} in terms of microscopic parameters is challenging, in a single-band scenario, at order B^2, it can be obtained from Eq. 2.42 that:

$$\alpha_{xx}(B) = A\mu/(1+\mu^2B^2) \tag{2.72}$$

$$\alpha_{xy}(B) = A'\mu^2B/(1+\mu^2B^2) \tag{2.73}$$

where $A = c\pi^2k_B^2Tn/\epsilon_F$ and $A' = c'\pi^2k_B^2Tn/\epsilon_F$ with k_B being the Boltzmann constant, ϵ_F the Fermi energy, c and c' coefficients of order unity depending on the dimensionality of the system [2] and on the details of the energy dependence of σ_{xx} and σ_{xy} respectively [14]. Without providing a quantitative description, Eq. 2.72 and 2.73 give a quantitative understanding of the particular conditions from which sizeable α_{xx} and α_{xy} emerge. High μ and small ϵ_F are required, namely, tiny pockets in the Fermi surface with small effective masses can significantly contribute. Furthermore, it is noteworthy that the above formulation does not depend on the carrier sign, which means

[5] Putting eq. 2.64 and 2.65 into eq. 2.75, we get that $\sigma_\perp = \sigma_E(1+\mu^2B^2) = ne\mu$, which is the same conductivity as in the absence of a magnetic field.

that in the case of multiband materials contributions from hole- and electron-like pockets add up and the one coming from a band with high μ and small ϵ_F emerges.

2.6 Multiband transport

If both electron-like and hole-like carriers contribute to transport, the expressions for the electric and thermoelectric transport properties become:

$$\sigma_{xx} = \sigma_{xx}^{(e)} + \sigma_{xx}^{(h)} = \sigma_{xx}^{(tot)}, \qquad \sigma_{xy} = \sigma_{xy}^{(e)} + \sigma_{xy}^{(h)} = \sigma_{xy}^{(tot)} \tag{2.74}$$

$$\rho_{xx} = \frac{\sigma_{xx}^{(e)}+\sigma_{xx}^{(h)}}{\left(\sigma_{xx}^{(e)}+\sigma_{xx}^{(h)}\right)^2+\left(\sigma_{xy}^{(e)}+\sigma_{xy}^{(h)}\right)^2} = \frac{\sigma_{xx}^{(tot)}}{\left(\sigma_{xx}^{(tot)}\right)^2+\left(\sigma_{xy}^{(tot)}\right)^2} \tag{2.75}$$

$$\rho_{xy} = \frac{\sigma_{xy}^{(e)}+\sigma_{xy}^{(h)}}{\left(\sigma_{xx}^{(e)}+\sigma_{xx}^{(h)}\right)^2+\left(\sigma_{xy}^{(e)}+\sigma_{xy}^{(h)}\right)^2} = \frac{\sigma_{xy}^{(tot)}}{\left(\sigma_{xx}^{(tot)}\right)^2+\left(\sigma_{xy}^{(tot)}\right)^2} \tag{2.76}$$

$$S = \frac{\left(\alpha_{xx}^{(e)}+\alpha_{xx}^{(h)}\right)\left(\sigma_{xx}^{(e)}+\sigma_{xx}^{(h)}\right)+\left(\alpha_{xy}^{(e)}+\alpha_{xy}^{(h)}\right)\left(\sigma_{xy}^{(e)}+\sigma_{xy}^{(h)}\right)}{\left(\sigma_{xx}^{(e)}+\sigma_{xx}^{(h)}\right)^2+\left(\sigma_{xy}^{(e)}+\sigma_{xy}^{(h)}\right)^2} = \alpha_{xx}^{(tot)}\rho_{xx}^{(tot)} + \alpha_{xy}^{(tot)}\rho_{xy}^{(tot)} \tag{2.77}$$

$$N = \frac{-\left(\alpha_{xx}^{(e)}+\alpha_{xx}^{(h)}\right)\left(\sigma_{xy}^{(e)}+\sigma_{xy}^{(h)}\right)+\left(\alpha_{xy}^{(e)}+\alpha_{xy}^{(h)}\right)\left(\sigma_{xx}^{(e)}+\sigma_{xx}^{(h)}\right)}{\left(\sigma_{xx}^{(e)}+\sigma_{xx}^{(h)}\right)^2+\left(\sigma_{xy}^{(e)}+\sigma_{xy}^{(h)}\right)^2} = -\alpha_{xx}^{(tot)}\rho_{xy}^{(tot)} + \alpha_{xy}^{(tot)}\rho_{xx}^{(tot)} \tag{2.78}$$

where total electric conductivity $\sigma_{ij}^{(tot)}$ and Peltier conductivity $\alpha_{ij}^{(tot)}$ are given by the algebraic sum over different bands. The definition of the total electric resistivity $\rho_{ij}^{(tot)}$ follows from substituting σ_{ij} and α_{ij} with $\sigma_{ij}^{(tot)}$ and $\alpha_{ij}^{(tot)}$in eq. 2.15 and eq. 2.16. Remarkably, Eq. 2.77 and Eq. 2.78 have the same structure as Eq. 2.23 and Eq. 2.28, respectively. This means that the multiband expressions for S and N are the same as the single-band ones, provided that the single transport coefficients are simply replaced by the sum over the different bands.

2.6.1 Magnetoresistance and Kohler's rule

It is easy enough to show, for example, that the transverse magnetoresistance need not to vanish if we had a two-band system. In this case, putting eq. 2.74 into eq. 2.71, and we get:

$$\sigma_{\perp} = \frac{(\sigma_{xx}^{(tot)})^2+(\sigma_{xy}^{(tot)})^2}{(\sigma_{xx}^{(tot)})} = \sigma_1 + \sigma_2 - \frac{\sigma_1\sigma_2(\mu_1-\mu_2)^2B^2}{\sigma_1(1+\mu_1^2B^2)+\sigma_2(1+\mu_2^2B^2)} \tag{2.79}$$

where the last equality follows from defining $\sigma_1 = n_1e_1\mu_1$ and $\sigma_2 = n_2e_2\mu_2$ the zero-field conductivity of the electrons or holes. After some algebra this gives us [12]:

$$\frac{\Delta\rho}{\rho_0} = \frac{\rho_{xx}(B)-\rho_{xx}(0)}{\rho_{xx}(0)} = \frac{\sigma_1\sigma_2(\mu_1-\mu_2)^2B^2}{(\sigma_1+\sigma_2)^2+B^2(\mu_1\sigma_2+\mu_2\sigma_1)^2} \tag{2.80}$$

This formula illustrates the main features of the phenomenon of magnetoresistance. In first place, $\Delta\rho$ is essentially positive, and vanishes only if $\mu_1 = \mu_2$. This effect will not vanish if μ_1 and μ_2 are not equal. If we have an assembly of electrons and holes, then μ_1 and μ_2

will be of opposite sign and the effect would be correspondingly large. It is typical, also, that $\Delta\rho$ is proportional to B^2 for small fields, but that it tends to saturate at high fields. This sort of formula can be generalized to the case where we have many different types of carrier, all contributing separately to the current. In other words, we can deal with complicated Fermi surfaces, with different parts having different values of μ. The existence of magnetoresistance in metals is thus evidence for variation of μ, i.e. different values of effective mass, or perhaps a variation of τ, over the Fermi surface.

Supposing that both groups of carriers have the same value of τ, then $\frac{\Delta\rho}{\rho_0}$ comes out as a function only of τB. But τ itself will then be inversely proportional to the resistivity ρ_0: we can write

$$\frac{\Delta\rho}{\rho_0} = F\left(\frac{B}{\rho_0}\right) \tag{2.81}$$

where F is a function depending on the nature of the metal itself. Eq. 2.80 is known as *Kohler's Rule*. It is customary to analyse the classical orbital magnetoresistance using the Kohler plot [3]. The motivation in that from eq. 2.80 and 2.81 it follows that, in conventional metals, a plot of $\frac{\Delta\rho}{\rho_0}$ vs $\left(\frac{\Delta\rho}{\rho_0}\right)^2$ should fall on a straight line with a slope that is independent of T. However, this rule is only an approximation. It by no means follows that two different types of carriers have the same relaxation time, or even that their relaxation times stand in the same ratio whether they are being scattered by impurities or by phonons, at high temperatures or at low temperatures. Deviations from Kohler's rule are evidence that different types of scattering mechanism have different effects on different groups of carriers.

2.6.2 Ambipolar Hall and Nernst effect

From eq. 2.17 and 2.78, in low field limit, it is possible to obtain the expression of the Hall coefficient in terms of the mobilities of the electrons and holes [3]:

$$R_H = \frac{1}{e}\frac{n_e\mu_e^2 - n_h\mu_h^2}{(n_e\mu_e + n_h\mu_h)^2} \tag{2.82}$$

From eq. 2.82 we see that R_H will be a balance between contributions from electron-like carriers and hole-like carriers and the sign of R_H depends not only on the sign of the majority carrier but also on its relative mobility. However, from eq. 2.82 we expect R_H to be vanishing small in compensated materials.

On the other hand, eq. 2.78 displays how N can be enhanced by the existence of two types of carriers in the system. Indeed, since the signs of σ_{xy} and α_{xx} depend on the sign of the carriers, the validity of the cancellation (eq. 2.62) for each band does not lead to the cancellation of the numerator of eq. 2.78. In particular, the ambipolar Nernst signal is maximal when the bands are exactly compensated. This can be understood by thinking that charge carriers of opposite sign are driven by the thermal gradient along the same direction and thus are deflected along opposite directions by the magnetic field. On the contrary, for the Hall effect, charge carriers of opposite sign are driven by the electric field along opposite directions and thus are deflected along the same direction by the magnetic field. Hence, in compensated compounds, the Hall resistance vanishes, whereas the Nernst effect is magnified.

2.7 Transport coefficients in holographic magneto-transport

In Section 3.2.1 of Chapter 1, we introduced the strange metal phase of cuprates which is identified as the quantum critical wedge associated with a QCP under the superconducting dome near optimal doping. For strongly interacting systems one is faced with a paucity of theoretically controlled models. Indeed, several attempts to explain the experimental observations within some modified Fermi liquid framework had always provided unsatisfactory results (see [15] for a detailed review on the topic).

The idea that one can capture the basic ingredients of the physics of the strange metals by studying some sort of deformed strongly coupled conformal field theory has become one of the leading direction of research in this field. From the theoretical point of view, there exist very few tools which allow us to analyse the properties of these complicated theories. However, in the last decade new techniques developed in the context of string theory have acquired greater and greater relevance in the study of strongly correlated systems [16]. These techniques include the so called AdS/CFT (holographic) correspondence. In this section we will not focus on the technical aspects of theory, which are reported in [17]. We will rather report the in-plane transport coefficients calculated by means of holographic techniques for a strongly correlated system which do not conserve momentum. This has a direct impact on condensed matter studies where disorder, lattices or heavy degree of freedom exchange momentum with the light degreed of freedom responsible for transport. For a correlated material, in presence of an orthogonal magnetic field and of some generic mechanism of explicit momentum dissipation, the final outcome is:

$$\sigma_{xx}=\frac{\mathcal{E}+\mathrm{P}}{\tau}\frac{\rho^2+\sigma_Q\left(B^2\sigma_Q+\frac{\mathcal{E}+\mathrm{P}}{\tau}\right)}{B^2\rho^2+\left(B^2\sigma_Q+\frac{\mathcal{E}+\mathrm{P}}{\tau}\right)^2},\qquad \sigma_{xy}=\rho B\frac{\rho^2+\sigma_Q\left(B^2\sigma_Q+\frac{\mathcal{E}+\mathrm{P}}{\tau}\right)}{B^2\rho^2+\left(B^2\sigma_Q+\frac{\mathcal{E}+\mathrm{P}}{\tau}\right)^2},$$

(2.83)

$$\alpha_{xx}=\rho s\frac{\mathcal{E}+\mathrm{P}}{\tau}\frac{1}{B^2\rho^2+\left(B^2\sigma_Q+\frac{\mathcal{E}+\mathrm{P}}{\tau}\right)^2},\qquad \alpha_{xy}=sB\frac{\rho^2+\sigma_Q\left(B^2\sigma_Q+\frac{\mathcal{E}+\mathrm{P}}{\tau}\right)}{B^2\rho^2+\left(B^2\sigma_Q+\frac{\mathcal{E}+\mathrm{P}}{\tau}\right)^2},$$

(2.84)

$$\bar{\kappa}_{xx}=\frac{s^2T(B^2\sigma_Q+\frac{\mathcal{E}+P}{\tau})}{B^2\rho^2+\left(B^2\sigma_Q+\frac{\mathcal{E}+\mathrm{P}}{\tau}\right)^2},\qquad \bar{\kappa}_{xy}=\frac{B\rho s^2T}{B^2\rho^2+\left(B^2\sigma_Q+\frac{\mathcal{E}+\mathrm{P}}{\tau}\right)^2},$$

(2.85)

where T is the temperature, σ_Q is a characteristic (quantum critical) conductivity at zero charge density and $\mathcal{E}$, P, ρ and s are respectively the energy density, the pressure, the charge density and the entropy density of the electron plasma. These quantities follow the usual thermodynamical relation $\mathcal{E}+P=sT+\mu\rho$, where μ is the chemical potential. Finally, τ is the explicit momentum-dissipation rate. These results are amenable of direct experimental confirmation for an isotropic strongly coupled system in two spatial dimensions. At the phenomenological level it is easy to see that the six transport coefficients depend only on four parameters: two thermodynamical variables ρ and s and two dynamical parameters σ_Q and $\frac{\tau}{\mathcal{E}+P}$. Consequently, if the holographic picture is generically valid in a two dimensional strongly correlated material, just four phenomenological entries are needed to fully determine the transport properties of the system. This theoretical result is demanding for an experimental testing. One of the major problems in performing this kind of measurements in interesting strongly coupled materials, such as cuprates, is that, how

already discussed in the previous sections, certain transport coefficients are typically dominated by the effect of phonons, while we are interested in extracting just the electrons response. This is actually not the case for the electric conductivity, where the phonons are typically suppressed. In this case we get some phenomenological insight using the holographic result (eq. 2.83). It was noted in [18], indeed, that holography naturally solves the puzzle of the linear in temperature behavior of the resistivity and the concomitant T^2 scaling of the Hall angle in the strange metal phase of the cuprates. In fact, expanding σ_{xx} and σ_{xy} at low magnetic field, the electric conductivity follows an inverse Mathissen's rule, namely

$$\sigma_{xx} = \sigma_Q + \sigma_D, \qquad \text{with} \qquad \sigma_D = \frac{\rho^2 \tau}{\mathcal{E}+P}, \tag{2.86}$$

while the Hall angle does not depend on σ_Q

$$\tan\theta_H = \frac{\sigma_{xy}}{\sigma_{xx}} \sim \frac{B}{\rho}\sigma_D \tag{2.87}$$

Assuming that near the quantum critical region σ_Q is greater than the Drude contribution σ_D (we called it Drude contribution in analogy with eq. 2.45, since it is proportional to the square of the charge density and the scattering time), and imposing that $\sigma_Q \sim 1/T$ and $\sigma_D \sim 1/T^2$, we find the following scaling for the resistivity and the Hall angle:

$$\rho_{xx} \sim T, \qquad \tan\theta_H \sim 1/T^2 \tag{2.88}$$

Which are precisely the same scalings experimentally measured in most of the cuprates (see Chapter 1). Another reasonable assumption is that the charge density ρ is temperature independent, a condition that can be easily achieved in standard experimental set-ups. In order to determine the fourth parameter, a promising quantity to be measured is the Hall

thermal conductivity κ_{xy} which, as already explained in section 2.3.2, is almost unaffected by phonons. However, this quantity is very difficult to measure and currently there are very few measurements for cuprates [13,19]. It is worth to notice that imposing the scalings measured in [13,19] in the holographic theoretical prediction (2.83 and 2.85) leads to nontrivial agreement for some of the other transport coefficients of the cuprates, such as the magnetoresistance and the Hall Lorenz ratio, even though a more precise experimental characterization of the whole set of transport coefficients is needed in order to be conclusive on the agreement between holographic predictions and the scaling behaviour of these quantities in cuprates.

One of the goals of this work of thesis is to analyse the collected data in view of the holographic results, possibly clarifying if holography could be the answer to the vastly debated anomalies of the strange metals.

References

[1] N. W. Ashcroft, N. D. Mermin, *Solid State Physic, ,* Saunders College, Philadelphia (1976)
[2] A.A. Abrikosov, "Fundamentals of the Theory of Metals", North Holland (1988)
[3] J. M. Ziman, "Electrons and Phonons – The Theory of Transport Phenomena in Solids", Oxford at the Clarendon Press (1960)
[4] V. Oganesyan and I. Ussishkin Phys. Rev. B 70 054503 (2004)
[5] E. H. Sondheimer, Proc. R. Soc. London, Ser. A 193, 484 (1948)
[6]R. P. Huebener, Magnetic Flux Structures in Superconductors (Springer Series in Solid-State Sciences, vol 6) (Berlin: Springer) 1979
[7] M. Tinkham, "Introductio to Superconductivity – Second Edition", Dover Publications, New York (2004)
[8] F. A. Otter and P. R. Solomon, Phys. Rev. Lett. **16**, 681 (1966); A. T. Fiory and B. Serin, *ibid.* **19**, 227 (1967)

[9]R. P. Huebener and A. Seher, Phys. Rev. **181**, 701 (1969); **181**, 710 (1969); V. A. Rowe and R. P. Huebener, *ibid.* **185**, 666 (1969)
[10] Y. Wang, Z. A. Xu, T. Kakeshita, S. Uchida, S. Ono, Y. Ando, and N. P. Ong, Phys. Rev. B **64**, 224519 (2001)
[11]Yayu Wang, Lu Li, and N. P. Ong, Phys. Rev. B 73, 024510 (2006)
[12] J.M. Ziman, "Principles of the theory of Solids", Cambridge University Press, Cambridge (1964)
[13] Y. Zhang, N. P. Ong, Z. A. Xu, K. Krishana, R. Gangon and L. Taillefer, Phys. Rev. Lett., 84 2219 (2000)
[14] T. Liang, Q. Gibson, J. Xiong, M. Hirschberger, S. P. Koduvayur, R. J. Cava, and N. P. Ong, Nat. Comm. 4, 2696 (2013)
[15] A. Donos and S. A. Hartnoll, Nature Phys. 9 649 (2013)
[16] A. Amoretti, A. Braggio, N. Maggiore and N. Magnoli, Advances in Physics: X, 2:2, 409-427 (2017)
[17] A. Amoretti, Condensed Matter Applications of AdS/CFT: Focusing on Strange Metals (Springer Thesis, Cham, 2017).
[18] M. Blake and A. Donos, Phys. Rev. Lett., vol. 114, no. 2, p. 021601 (2015)
[19] M. Matusiak, K. Rogacki, and B. W. Veal, EPL, vol. 88, no. 4, p. 47005, (2009)

3 High field thermoelectric properties of $BaFe_2As_2$ parent compound

Thermoelectric properties, namely Seebeck and Nernst effects, have proven to be a powerful tool to investigate several aspects in condensed matter physics, like topology of the Fermi surface, the scattering mechanisms at play, the electronic band structure and phase transitions. However, the mutual entanglement of the electric and thermoelectric properties in diffusive transport equations we introduced in Chapter 2 is a well-established framework of condensed matter physics. Yet, the application of this formalism in its entirety to real materials is highly challenging and has not been thoroughly exploited so far.

In this Chapter we will show the complete transport properties characterization of a $BaFe_2As_2$ single crystal whose quality has been remarkably improved thanks to an annealing process (section 3.1 is devoted to the role of annealing in $BaFe_2As_2$). The temperature dependence of the transport properties is reported in section 3.2, whereas in section 3.5 and 3.6 we show the magneto-electric (up to 9T) and the magneto-thermoelectric (up to 30 T) transport properties, respectively. In section 3.7 we prove that the simultaneous analysis of all these properties for different magnetic field directions (shown in section 3.3), let extract the Peltier tensor coefficients α_{xx}, α_{xy} and α_{xz} which have been proven pivotal to disentangle the main transport

mechanism into play. We also provide evidence of the presence of a high mobility band, compatible with a Dirac dispersion band, crossing the Fermi level and we suggest a possible 3-dimensional nature of the Dirac Fermions.

Seebeck effect, magnetoresistance and Hall effect measurements were performed in the temperature range from 5 to 300 K and in magnetic fields up to 9 T using a Physical Property Measurement System (PPMS, Quantum Design). The temperature dependent volume magnetic susceptibility was measured by a commercial dc-SQUID magnetometer (MPMS2 by Quantum Design) in a temperature range from 4 to 300 K by applying a magnetic field of 3 T.
High magnetic field thermoelectric characterizations were performed up to 30 T at the High Field Magnet Laboratory (HFML) in Nijmegen (NL).

3.1 Role of annealing in $BaFe_2As_2$

In [1] it is reported that annealing remarkably improves transport properties in the ordered phase of $BaFe_2As_2$. Figure 1a shows temperature (T) dependence of the in-plane resistivity $\rho_{ab}(T)$ measured on twinned $BaFe_2As_2$ crystals annealed under various conditions. It is worth to notice that the annealing remarkably reduces the residual resistivity ratio RRR (defined as $\rho_{ab}(300K)/\rho_{ab}(5K)$) of a factor above 10 [2]. In general, the annealing process would remove crystal defects and lattice dislocations, which are possible scattering sources and can cause large residual resistivity and therefore a smaller RRR. Furthermore, as shown in Figure 1b, T_{SDW} increases from 136 K to 142 K and the phase transition becomes sharper probably because crystal

defects are removed and it helps to stabilize the orthorhombic lattice and magnetic ordering.

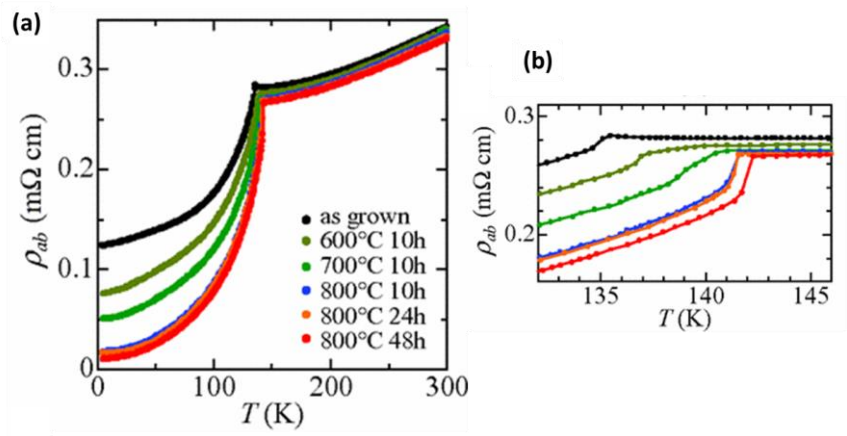

Figure 1: (a) Temperature dependence of the in-plane resistivity measured on twinned $BaFe_2As_2$ crystal before (as grown) and after annealing under various conditions shown in figure. (b) Enlarged view of (a) around the magneto-structural transition temperature. After [2].

Furthermore, the B dependence of $\rho_{xy}(B)$ for annealed crystal is shown in Figure 2b. In stark contrast to the as-grown crystal (Figure 2a), $\rho_{xy}(B)$ below T_{SDW} soon deviates from B linear dependence and exhibits nonmonotonic B dependence. Especially at T=5 K, $\rho_{xy}(B)$ changes its sign to positive above $B{\sim}4\,T$. It is natural to attribute this B dependence of $\rho_{xy}(B)$ to the multiple-carrier effect.

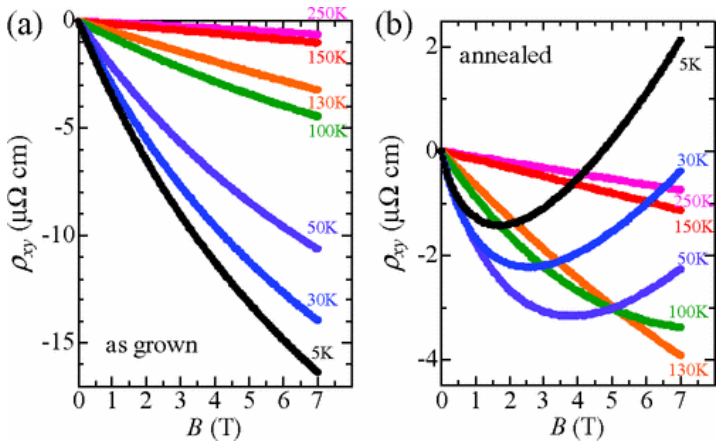

Figure 2: Magnetic field dependence of the Hall resistivity ρ_{xy} of twinned as grown (a) and annealed (b) $BaFe_2As_2$ crystals taken at several temperatures. After [2].

In the case of the annealed $BaFe_2As_2$ crystal (Figure 3b), the magnetoresistance MR reaches ~280% at B=7 T and T=5 K, which is by an order of magnitude larger than that of the as-grown crystal (reported in Figure 3a for comparison and already discussed in Chapter 1). In the annealed crystal, the linear MR, suggestive of a contribution from Dirac pockets, is superimposed to the semi-classical cyclotron contribution ($\propto B^2$) up to 7T. Observed large and quadratic MR gives evidence that other FS pockets have appreciable contribution to the charge transport in the ordered phase of the 122 parent compounds. Furthermore, considering that the magnitude of MR is a measure of carrier mobility, it should be greatly enhanced by the annealing, which is consistent with the increase of the RRR (Figure 1a) and the non-monotonic *B* dependence of ρ_{xy} (Figure 2b). All these features originate from the multiple-carrier contribution, which becomes clear as the sample quality is improved or as the carrier mobilities become higher.

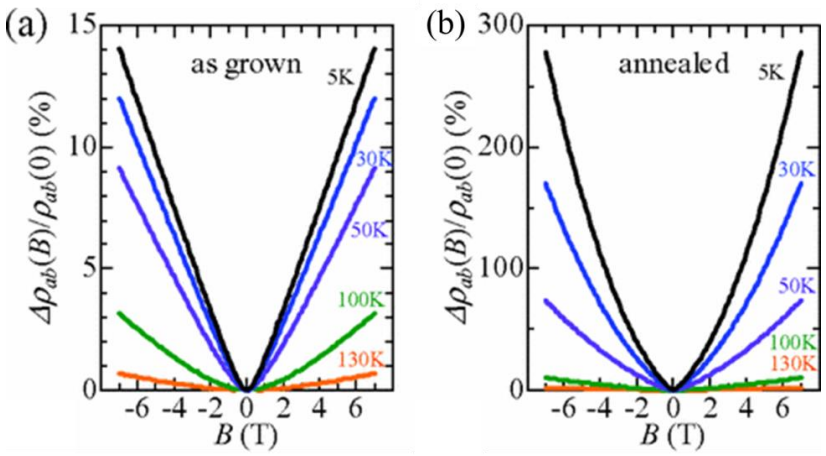

Figure 3: Comparison of the magnetic field dependence up to 7T of the magnetoresistance (MR, $\Delta\rho_{ab}(B)/\rho_{ab}(B=0)$) for as-grown (a) and annealed (b) $BaFe_2As_2$ crystals, taken at several temperatures. After [2].

3.2 The sample and its temperature characterization

As already discussed in Chapter 1, $BaFe_2As_2$ is one parent compound of the 122 family of IBS and the availability of mm-size single crystals makes this compound suitable for a complete characterization of all transport properties, with the further possibility of investigating the in-plane-out-of-plane anisotropy (see Appendix A for in-plane-out-of-plane properties of $BaFe_2As_2$). The $BaFe_2As_2$ single crystal was grown by the self-flux method, as described in [2]. The crystal was cut in a rectangular shape along the tetragonal [110] directions, which become the *a* or *b* axes in the orthorhombic phase if external uniaxial pressure is applied to the sample [3]. The crystal dimensions were 2.5×0.8×0.7 mm^3, with the shortest edge along the *c* axis. In the following we will use the notation *x*, *y* and *z* to indicate the geometrical sides of our slab-like sample (Figure 4).

In the parent compounds of the 122 family of IBS, the magneto-structural transition which occurs at T_{SDW} leads to the formation of twin domains of four types [4,5] which can be removed by applying uniaxial strain to the crystals [6]. When this is done, it is possible to investigate the in-plane anisotropy (i.e. the nematicity) of the 122 compounds. Since in the orthorhombic phase no external uniaxial pressure was applied to our the sample, the crystal presented the expected in-plane twin domains so that we cannot refer *x* and *y* to the orthorhombic *a* and *b* axis, whereas the *z* direction corresponds to the *c*-axis.

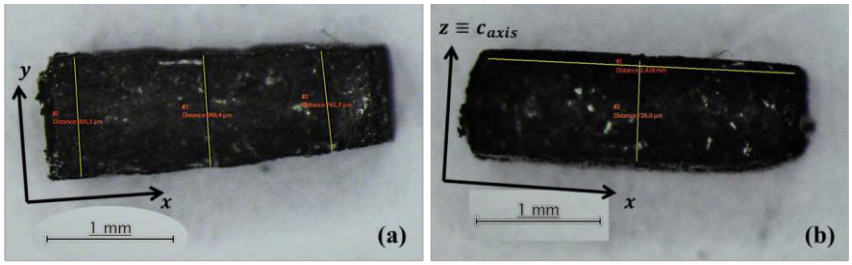

Figure 4: $BaFe_2As_2$ single crystal: *xy*-side (a) and *xz*-side (b). The *z* direction corresponds to the *c*-axis of the crystal.

The crystal was sealed into an evacuated quartz tube together with BaAs powders and annealed at 800 °C for 2 days. The good quality of the crystal was confirmed both by magnetic susceptibility χ_V measurement, reported in Figure 5, and electric resistivity, shown in Figure 6.

From room temperature χ_V decreases linearly with temperature showing the expected temperature behaviour for 1111 and 122 pnictide families in the PM state [7,8,9]. In correspondence of the magneto-structural transition from PM tetragonal to AFM orthorhombic structures, χ_V decreases abruptly in less than 2 K. The remarkable sharpness of this transition is a proof of the high quality of the crystal under test. It is

possible to determine precisely the transition temperature T_N by analysing the temperature behaviour of $d\chi_V(T)/dT$ (see the inset of Figure 1): T_N=140.5±0.6K where T_N and its uncertainty are defined as the temperature of the derivative peak and its half width respectively. Below such temperature a small spurious Curie-Weiss-like behaviour is detected.

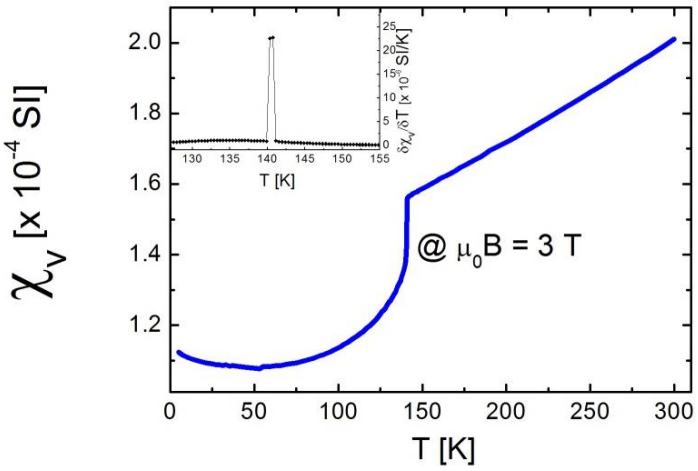

Figure 5: Volume susceptibility χ_V as a function of temperature from 4 to 300 K. Inset: first derivative of χ_V

Figure 6 shows the longitudinal electric resistivity ρ_{xx} in a temperature range between 2 and 320 K. $\rho_{xx}(T)$ shows typical temperature dependence so far reported for this compound. ρ_{xx} drops around T_N and shows residual resistivity of typically 0.02 mΩcm. The RRR is about 27. As discussed in section 3.1, the annealing process let notably enhance the RRR, which is around 3 in the as grown samples and assumes values as high as 30 in the annealed crystals.

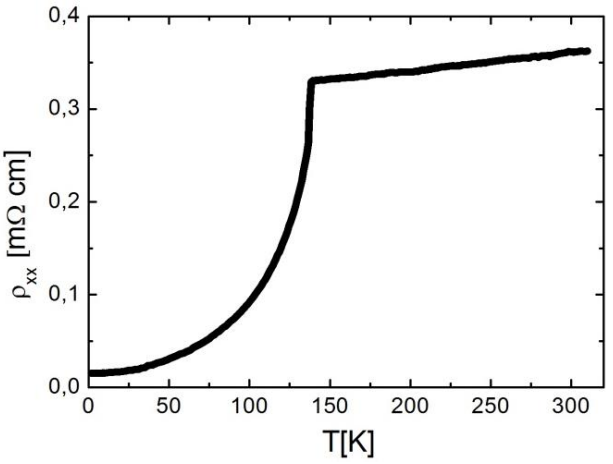

Figure 6: Electric resistivity ρ_{xx} as a function of temperature between 2 and 320 K.

For completeness, in the following we also report the temperature behavior of Hall effect, Seebeck and Nernst effect.

Figure 7 shows the in-plane Hall coefficient R_H as a function of temperature in the range 5-200 K, when B is applied $\|z$ (solid points) and $\|y$ (empty points). R_H values are determined from the slope of ρ_{xy}(B) (reported in Figure 12b) and ρ_{xz}(B) (reported in Figure 12d) for B going to zero. Above T_N, R_H is negative (positive) for $B\|z$ ($B\|y$). In both cases, for $T>T_N$, R_H is very small ($\sim$-0.6×10^{-9} m^3/C when $B\|z$ and $\sim$0.7×10^{-9} m^3/C when $B\|y$) and weakly temperature dependent, suggesting that in this regime electron-type and hole-type carriers are virtually compensated and give rise to vanishing small values of R_H. Below T_N, similarly for $B\|z$ and $B\|y$, R_H is negative and increases in magnitude with decreasing temperature. This suggests that in the AFM state transport is dominated by electron-type carriers and a carrier condensation occurs in correspondence of the opening of the SDW gap [10] in correspondence of the magneto/structural transition at T_N.

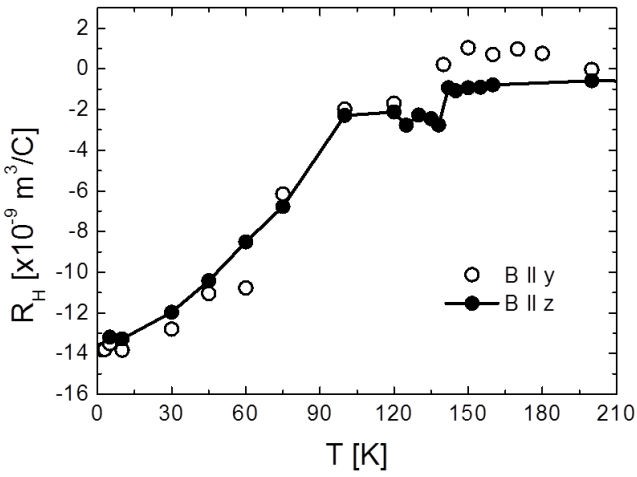

Figure 7: Temperature dependence of R_H when $B \| z$ (solid points) and $B \| y$ (empty points) from 4 to 200 K

Figure 8 shows the S_{xx} coefficients in the temperature range between 5 and 300 K in 0 T and 9 T magnetic fields, applied $\| z$ and $\| y$. At room temperature, zero field S_{xx} is negative and its absolute value increases linearly with decreasing temperature reaching the maximum value of about -8 μVK^{-1} around T=175 K. In correspondence with the structural/magnetic transition at T_N=140 K an abrupt change occurs, the signal strongly diminishes and crosses zero around T=120 K. For T=90 K, S_{xx} becomes negative again and it exhibits a broadened minimum centred around 40 K. This behavior is in substantial agreement with previous reports on $BaFe_2As_2$ [11,12,13,14].

No magnetic field dependence is detected in the paramagnetic state ($T>T_N$) whereas in the AFM state ($T<T_N$) we observe two different *B* behaviors when $B \| z$ or $B \| y$. In both cases the magnetic field tends to increase S_{xx} by up to 30% and 50% of the zero-field signal for $B \| z$ and $B \| y$ respectively. The main difference between the two curves is indeed the position of their negative maxima, which is around T=30 K and

T=50 K, respectively, revealing the possible competition of different mechanisms into play.

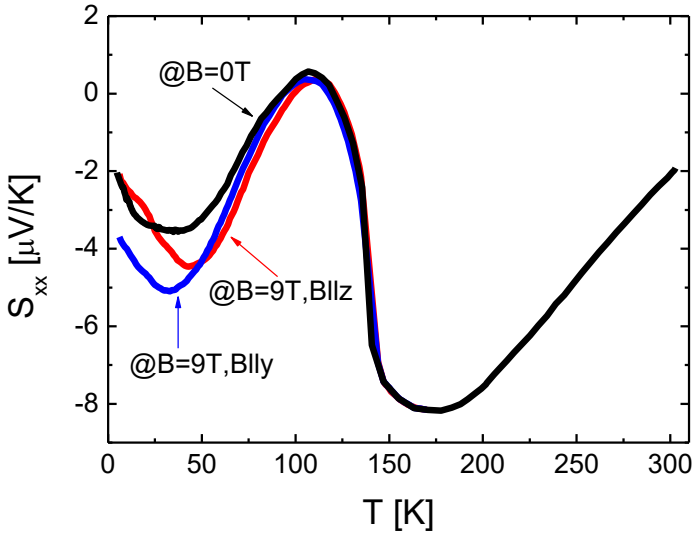

Figure 8: Seebeck effect measured from 5 to 300 K in a magnetic field of 0 T (black curve) and 9T ∥ z (red curve) and ∥ y (blue curve).

In Figure 9 we report the temperature dependence of the Nernst coefficient $\nu=N_{xy}/B$ from 4 to 300 K. ν is positive in the whole temperature range, undergoes a jump at T_N and grows below this temperature, reaching the value of 1 $\mu VK^{-1}T^{-1}$ at 50 K.

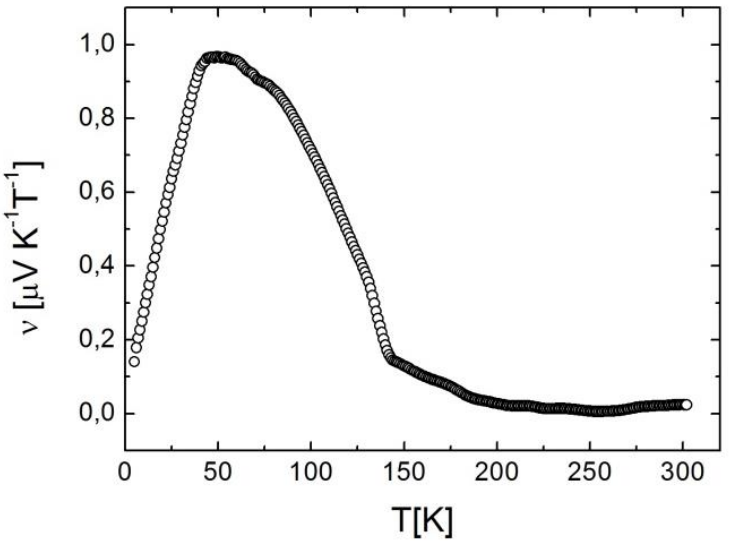

Figure 9: Temperature dependence of the Nernst coefficient ν between 4 and 300 K

3.3 Measurements setup

In order to probe the *B*-dependence of the thermoelectric coefficients, the measurements were performed using two different configurations, varying the orientation of *B*. Figure 10 shows the experimental set-up and a sketch of the measured quantities which allow obtaining the thermoelectric coefficients.

We performed all the measurements with both positive and negative *B* in order to separate the even and odd parts of the signal with respect to the magnetic field.

It is worth to notice that a partial detwinning by action of in-plane magnetic field has been observed in a Co-doped $BaFe_2As_2$ crystal [15]. A partial detwinning is therefore expected in our case when $B \| y$. We will discuss this point in the next paragraphs.

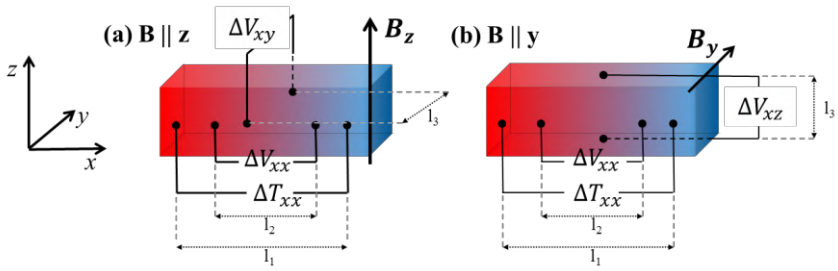

Figure 10: Thermoelectric measurements set up. A thermal gradient ΔT_{xx} was generated along x and a longitudinal voltage ΔV_{xx} was detected with B applied (a) along z and (b) along y. The Seebeck effect in both cases is defined as $S_{xx}= (\Delta V_{xx}/ \Delta T_{xx})(l_1/l_2)$. In (a), a transverse voltage ΔV_{xy} is detected along y and the Nernst effect is defined as $N_{xy}= (\Delta V_{xy}/ \Delta T_{xx})(l_1/l_3)$. In (b) a transverse voltage ΔV_{xz} is measured along z and the Nernst effect is defined as $N_{xz}= (\Delta V_{xz}/ \Delta T_{xx})(l_1/l_3)$.

3.4 High fields Seebeck and Nernst

In order to investigate this peculiar field dependence, we measured S_{xx} as a function of *B* up to 30 T for selected temperatures in the AFM regime. Figures 11a and 11c show $\Delta S_{xx}(B)=S_{xx}(B)-S_{xx}(0)$ with magnetic field applied $\|z$ or $\|y$, respectively. In Figure 11a, $\Delta S_{xx}(B)$ has an absolute value of the order of several μV/K at the largest field, is non-monotonic and presents a sign change from negative to positive which shifts to higher field with increasing temperature.

This trend completely changes for $B\|y$ (Figure 11c), where $\Delta S_{xx}(B)$ remains negative up to 30 T.

In Figures 114b and 11d we show the Nernst coefficients N_{xy} and N_{xz} measured up to 30 T for $B\|z$ and $B\|y$, respectively. The former varies almost linearly with magnetic field, reaching a maximum value of 30 μV/K (Figure 11b) at the maximum field, whereas the latter exhibits a slightly super-linear magnetic field dependence, reaching a maximum value of 13 μV/K (Figure 11e).

Before discussing in detail these data, we consider here the possible effects due to the partial detwinning expected for $B \| y$, particularly relevant for the present system because of the in-plane anisotropy of its Seebeck coefficient [16] (see Appendix B).

In our experimental configuration for $B \| y$ (see Figure 10b), the Seebeck coefficient is measured in the direction perpendicular to *B*. In agreement with ref. [15], with increasing field, more domains with the ortorhombic a-axis aligned perpendicular to the B direction would appear. Therefore, the contribution of S_a is expected to overcome the one of S_b (where S_b and S_a are the Seebeck coefficient along the *b* and the *a*-axis respectively) [16]. The in-plane Seebeck anisotropy in $BaFe_2As_2$ in the considered temperature range (T<80K), comes out to be around 43% with $|S_b|>|S_a|$. Thus, if the detwinning is dominant we should expect a decrease of the total measured S coefficient with increasing *B*: considering a change in the twin population of about 15% at 15 T [15], we estimated a reduction in the Seebeck effect with a maximum value of about 0.1 μV/K around 30 K. On the contrary, at the same temperature and field, we measure S as high as 1.5 μV/K, that is ten times higher than the expected value.

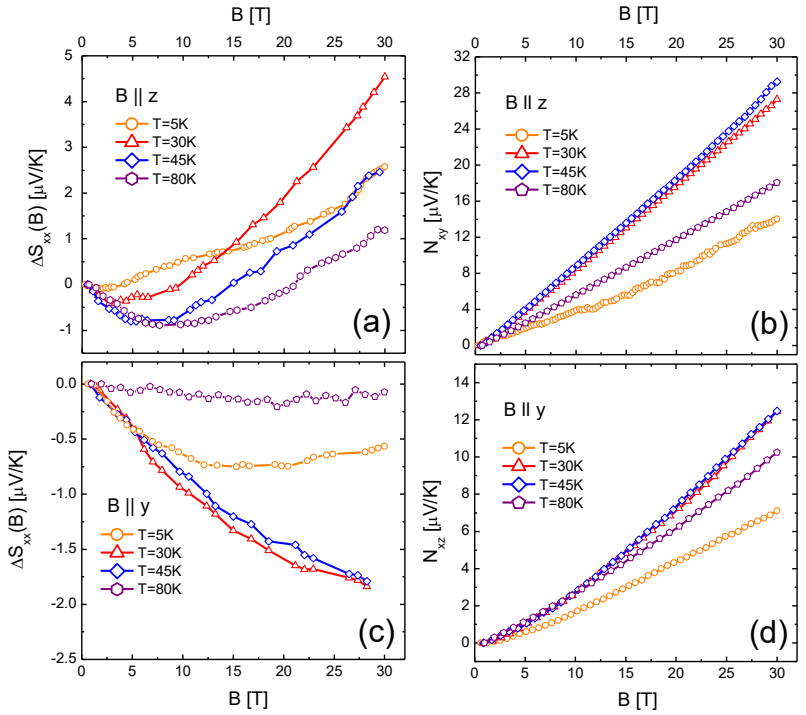

Figure 11: $\Delta S_{xx}(B)$ measured at T = 5,30,45,80 K for B up to 30 T applied $\|z$ (a) and $\|y$ (c). Nernst coefficients N_{xy} (b) and N_{xz} (d) measured at T = 5,30,45,80 K for B up to 30 T.

In the $B\|y$ configuration, the Nernst voltage is measured in z-direction (c-axis), as represented in Figure 10b. Therefore the detwinning should not influence this measurement.

3.5 Magnetoresistance and Hall effect up to 9 T

In Figure 12a and 12c we report the magnetoresistance $\Delta\rho/\rho=(\rho_{xx}(B)-\rho_{xx}(0))/\rho_{xx}(0)$ measured up to 9 T for $B\|z$ and $B\|y$, respectively. At T=5K, it reaches 160% for $B\|z$ and 130% for $B\|y$. In this case, the effect due to the detwinning for $B\|y$ is negligibly small and can be

evaluated as low as 0.7% at 4 K and 15 T[1]. For both the field directions the $\Delta\rho/\rho$ vs B curves cannot be described just by a quadratic term representing the classical contribution [17]. Instead, an additional linear term is needed, in agreement with previous reports [15,18,19]. In pnictides, this linear behavior has been attributed to the presence of Dirac cones in the band structure (see Chapter 1). In Figures 12b and 12d we show the magnetic field dependence of the Hall resistivities ρ_{xy} and ρ_{xz} measured up to 9 T for selected temperatures in the range 5-80K, for $B \| z$ and $B \| y$, respectively. R_H vs T (reported in the inset of Figure 12b), evaluated in the low field limit, appears to be similar in the two configurations. However, it is worth to notice that ρ_{xy} and ρ_{xz} B-dependences look pretty different, as one could expect for an anisotropic material [20]. ρ_{xy} soon deviates from B-linear dependence and shows a broad minimum below 9T. Remarkably, ρ_{xy} of a twin sample of literature ($BaFe_2As_2$ crystal annealed at 800°C for two days) measured up to 15T exhibits a change in sign above 9T [15]. In contrast to ρ_{xy}, ρ_{xz} shows only a slight sublinear B-dependence.

[1]Taking into account the in plane anisotropy of the resistivity which in ref. [2] is reported to be as low as 4% at 5K, similarly to the Seebeck coefficient, we evaluated that the detwinning effect at 5 K and 15 T is of the order of 0.7%.

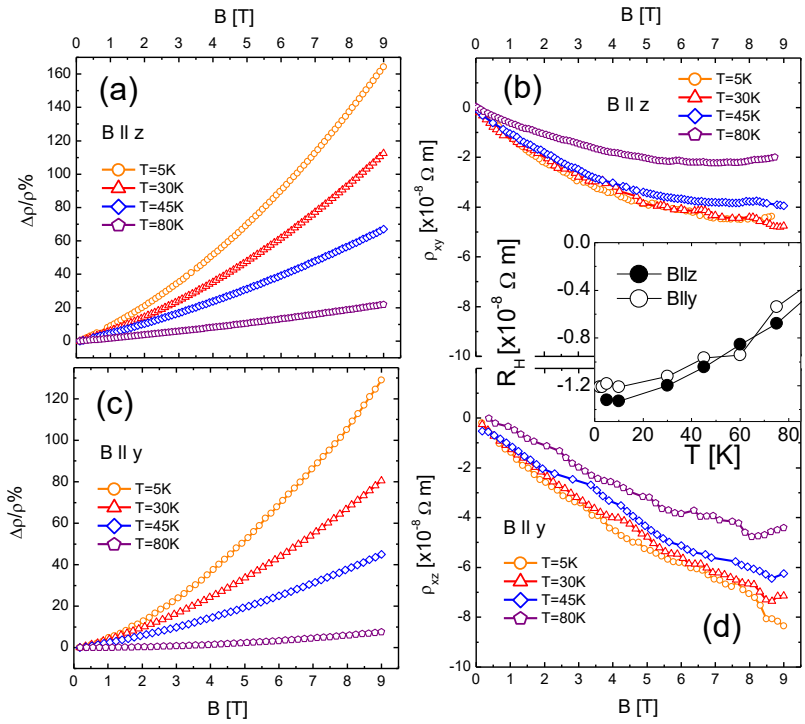

Figure 12: $\Delta\rho/\rho$% measured at T = 5,30,45,80 K for B up to 9 T applied ∥z (a) and ∥y (c). ρ_{xy} (b) and ρ_{xz} (d) measured at T = 5,30,45,80 K for B up to 9 T. Inset of (b): R_H vs T in the temperature range 0-80K when B is ∥z (filled dots) and ∥y (empty dots). R_H curves up to 250 K are reported in Figure 7.

3.6 Data analysis

In Chapter 2 we reported the diffusive Seebeck and Nernst coefficient when a thermal gradient is applied parallel to *x* and a magnetic field parallel to *z*. Extending these equations to a general case when the thermal gradient is applied along a generic *i* direction and *B* is applied along a *k* direction perpendicular to the *ij* plane, we get:

$$S_{ii} = \alpha_{ii}\rho_{ii} + \alpha_{ij}\rho_{ij} \quad (1)$$

$$N_{ij} = -\alpha_{ii}\rho_{ij} + \alpha_{ij}\rho_{ii} \quad (2)$$

Remarkably, equations (1) and (2) remain valid also for multi-band materials, where the single transport coefficients are replaced by the sum over different bands (see Chapter 2). Both S_{ii} and N_{ij} are composed of two terms. In the longitudinal S_{ii} coefficient (eq. (1)) the diagonal entries of $\hat{\rho}$ and $\hat{\alpha}$ multiply each other in the first term, while the off-diagonal ones combine together in the second term.

In the transversal N_{ij} coefficient (eq. (2)) diagonal and off-diagonal entries are mixed up. We recall that the off-diagonal entries represent the diffusive transverse transport coefficients, which rise up only in presence of a Lorentz force acting on charge carriers. If $B \neq 0$, in the great majority of the conducting materials $\rho_{ii} >> \rho_{ij}$ and $\alpha_{ii} >> \alpha_{ij}$, namely the longitudinal transport coefficients are much larger than their transverse counterparts. Hence, it is typically verified that $\alpha_{ii}\rho_{ii} >> \alpha_{ij}\rho_{ij}$ bringing a negligible contribution of the second term $\alpha_{ij}\rho_{ij}$ in eq. (1) to the Seebeck coefficient even in finite magnetic field [21]. Furthermore, in conventional metals, N_{ij} is usually very small (in the range of nVK^{-1}) due to Sondheimer's cancellation (see Chapter 2).

In addition, the transverse transport coefficients are *B*-linear in the low field limit ($\mu B << 1$, where μ is the charge carriers' mobility) whereas their longitudinal counterparts generally show a negligible *B*-dependence[2]. However, the term $\alpha_{ii}\rho_{ii}$ may have non-diffusive contributions with a sizeable *B*-dependence; among these, is the magnon drag contribution in magnetic materials [22,23,24].

[2]Given that $\rho_{xx}\alpha_{xx} \simeq \alpha_{xx}/\sigma_{xx} \propto 1/\sigma_{xx}\ (\partial\sigma_{xx}/\partial\varepsilon)|_{\varepsilon=EF} \propto (\partial \ln\sigma_{xx}/\partial\varepsilon)|_{\varepsilon=EF}$, in presence of a not negligible magnetoresistance, this term is not sizeably affected.

In the light of these considerations, the giant N_{ij} combined with a large field dependence of S_{ii} in the AFM phase of $BaFe_2As_2$ are the fingerprints of the strong departure from a conventional behavior. In the following we propose an analytical approach in order to single out the leading terms that cause anomalous contributions and identify the physical mechanisms that play a key role.

As already discussed in Chapter 2, by combining the experimental values of resistivity tensor entries, $\rho_{ii}(B)$ and $\rho_{ij}(B)$, and thermomagnetic coefficients, S_{ii} and N_{ij}, the Peltier coefficients α_{ii} and α_{ij} are derived by solving eq. (1) and (2) for α_{ii} and α_{ij}:

$$\alpha_{ii} = \frac{S_{ii}\rho_{ii} - N_{ij}\rho_{ij}}{\rho_{ii}^2 + \rho_{ij}^2} \tag{3}$$

$$\alpha_{ij} = \frac{S_{ii}\rho_{ij} + N_{ij}\rho_{ii}}{\rho_{ii}^2 + \rho_{ij}^2} \tag{4}$$

Note that according to our experimental setup (Figure 10), the subscript *i* is identified with *x* and *j* with *y* when $B \| z$, whereas *i* corresponds to *x* and *j* to *z* when $B \| y$.

In order to estimate α_{ii} and α_{ij} up to high fields, we extrapolated our magnetoresistance data (Figure 12a, 12c) up to 30 T assuming that no saturation occurs in that range, as it was observed up to 55 T for the same compound in ref. [25] and up to 30 T for a parent compound of the 1111 family in ref. [26].

Furthermore, since ρ_{xy} and ρ_{xz} show a not trivial *B*-dependence which does not discloses up to 9 T, it is not possible to univocally extrapolate our data (Figure 12b, 12d) up to 30 T.

3.6.1 Data analysis $B \| z$

Let's first focus on the $B \| z$ configuration, where we extrapolated up to 30 T the ρ_{xy} data measured up to 15 T in the twin sample of ref. [2] (Figure 13b). Figure 13a shows the interpolation of ρ_{xx} up to 30 T, when $B \| z$. The magnetoresistance $\Delta\rho/\rho\%$ at 30 T reaches values up to 1200% (Inset of Figure 13a).

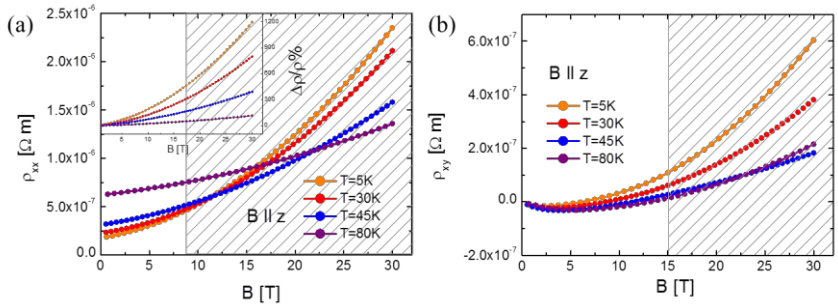

Figure 13: (a) Longitudinal resistivity data as a function of B at T=5,30,45,80 K extrapolated up to 30 T when $B \| z$. The Inset shows the resulting magnetoresistance $\Delta\rho/\rho\%$ which reaches 1200%. (b) Hall resistivity ρ_{xy} as a function of B at T=5,30,45,80 K. The experimental data measured up to 15 T are taken from Ref. [2] and extrapolated up to 30 T. Dashed areas indicate the extrapolated region.

In Figure 14, we show the results of our analysis for selected temperatures in the range 5–80K. In Figure 14a and 14b we compare the two terms in Eq. (1) and Eq. (2) which compose S_{xx} and N_{xy} respectively. Figure 14a compares the field dependence of $\alpha_{xx}\rho_{xx}$ with $\alpha_{xy}\rho_{xy}$ up to 30 T.

The $\alpha_{xx}\rho_{xx}$ curves look almost flat at all temperatures. This term would include magnon drag contribution, however in AFM materials, an external magnetic field strongly enhances the magnon drag contribution to S_{xx} only if it is applied as parallel to the easy-axis of the magnetic order, while its effect should be minimal if applied perpendicularly [23].

In case of $BaFe_2As_2$ the easy-axis lies in the *ab*-plane; this means that negligible contribution from the magnon drag is expected when $B \| z$.

On the contrary, $\alpha_{xy}\rho_{xy}$ vs *B*, after an initial decrease, increases rapidly with positive sign up to 30 T, emerging as the principal responsible for the large field dependence of S_{xx} in this measurement configuration. More in detail, the sign of $\alpha_{xy}\rho_{xy}$ is driven by the unusual change from negative to positive sign of ρ_{xy} at high *B* [2]. Since $|\rho_{xx}| > |\rho_{xy}|$ (Figure 13), the predominance of $\alpha_{xy}\rho_{xy}$ is induced by an anomalously high α_{xy}.

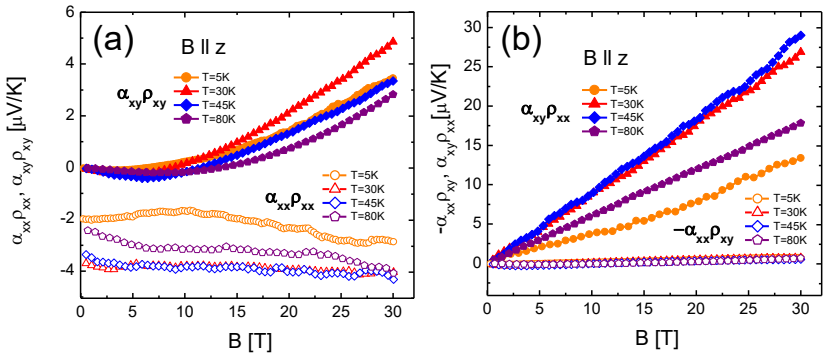

Figure 14: (a) $\alpha_{xy}\rho_{xy}$ (filled symbols) and $\alpha_{xx}\rho_{xx}$ (empty symbols) vs *B* up to 30 T for selected temperatures in the range 5-80 K. (b) $\alpha_{xy}\rho_{xx}$ (filled symbols) and $-\alpha_{xx}\rho_{xy}$ (empty symbols) vs *B* up to 30 T for selected temperatures in the range 5-80 K.

In Figure 14b the two terms which compose N_{xy} are plotted and it is evident that $|\alpha_{xy}\rho_{xx}| > |\alpha_{xx}\rho_{xy}|$, which is to say that $\alpha_{xy}\rho_{xx}$ is also responsible for the giant N_{xy}. Figure 15 reports the field dependence of α_{xy} estimated as in Eq. (4) up to 30 T for selected temperatures in the range 5K-80K. Remarkably, a non-monotonic behavior emerges: all the α_{xy}(B) curves exhibit a maximum which is shifted to higher fields with increasing temperature.

Although a quantitative expression of α_{xy} in terms of microscopic parameters is challenging, in Chapter 2 we saw that in a single-band scenario, from the Mott relation, it can be obtained the semi-classical expression for $\alpha_{xy}(B) = A'\mu^2 B/(1+\mu^2 B^2)$, with $A' = c'\pi^2 k_B^2 Tn/\epsilon_F$ (k_B being the Boltzmann constant, ϵ_F the Fermi energy and c' a coefficients of order unity).

We interpolate our $\alpha_{xy}(B)$ data using the semiclassical expression for $\alpha_{xy}(B)$ as fitting function (dashed black lines in Figure 15), finding a good agreement with the experimental data. We extract the mobility μ as a fit parameter, obtaining values up to 10^3 $cm^2V^{-1}s^{-1}$ at T=5K and a progressive decrease at higher temperatures (inset of Figure 15). This is in good agreement with the values of mobility obtained from the magnetoresistance analysis of $BaFe_2As_2$ in the semimetal scenario [19,27]. Remarkably, this average mobility is strongly reduced upon electron doping with the simultaneous suppression of the magnetic phase, as the Dirac cones develop [27].

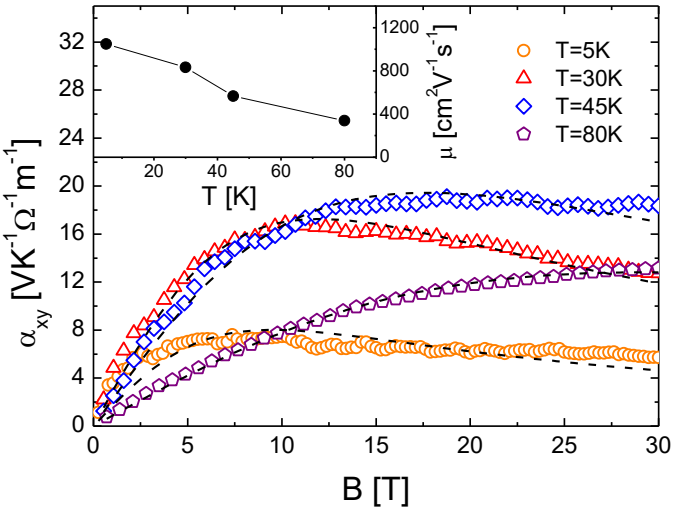

Figure 15: Magnetic field dependences up to 30 T in the temperature range 5-80K of α_{xy}. Dashed lines are the fitting curves of α_{xy} using Eq.(2.48). Inset: temperature dependence of carrier mobility μ obtained by the fitting.

Without providing a quantitative description, Eq. (5) gives a qualitative understanding of the particular conditions from which a sizeable α_{xy} emerges. High μ and small E_F are required, namely tiny pockets in the Fermi surface with small effective masses can significantly contribute. Furthermore, it is noteworthy that the above formulation does not depend on the carrier sign, which means that in case of multiband materials, contributions from hole-like and electron-like pockets add up and the one coming from a band with high μ and small E_F emerges.

Taking into account the Shubnikov de Haas (SdH) oscillations measured in a $BaFe_2As_2$ crystal [28], we can assume that for $B \| z$ the electron γ-pocket with the lowest effective mass gives the main contribution to α_{xy}. The γ-pocket carrier density has been estimated [28] 3×10^{19} cm^{-3} and considering the coefficient c~1, from the fit coefficients A at T=5,30,45 K we estimate E_F in the range ~11÷25 *meV*. Being aware that it only represents a qualitative approximation, it is interesting to notice that the proposed value for E_F comes out tiny and consistent with the size of the electron γ-pocket estimated from SdH oscillations [28]. Remarkably, this pocket has been located in a position of the band structure where Dirac cones with E_F in the range of ten *meV* has been experimentally confirmed by ARPES [29,30] and infrared studies [31] in the AFM phase of $BaFe_2As_2$.

Oganesyan predicted that in presence of Dirac cones, whose nodal point is close enough to the Fermi level (i.e. very small E_F), a giant Nernst coefficient can be determined by an anomalously high α_{xy} [32]. Moreover, Morinari demonstrated that the contribution of chiral Dirac fermions could be dominant in thermoelectric transport properties of iron-based parent compounds even if they are minor carriers [33]. Giant Nernst coefficient in the similar compounds $EuFe_2As_2$ and $CaFe_2As_2$

have indeed been reported [34,35]. All these evidences suggest that the giant α_{xy}, responsible for the large Nernst effect that we observe experimentally, is plausibly determined by the Dirac cone band, which indeed perfectly fulfils the required condition of high mobility and small Fermi energy.

3.6.2 Data analysis $B \| y$

We now turn to the $B \| y$ configuration. Figure 16a shows the interpolation of ρ_{xx} up to 30 T, when $B \| y$. The magnetoresistance $\Delta\rho/\rho$% at 30 T reaches values up to 1000% (inset of Figure 16a). The extrapolation of ρ_{xz} is less trivial. Indeed, we have experimental data of ρ_{xz} up to 9 T (Figure 12d), but we do not have any indication whether with increasing field it remains negative or changes in sign as ρ_{xy} does. Therefore, we tentatively extrapolate ρ_{xz} data from 9 T to 30 T using a polynomial of second and third order (Figure 16b) to take into account different magnetic field dependencies.

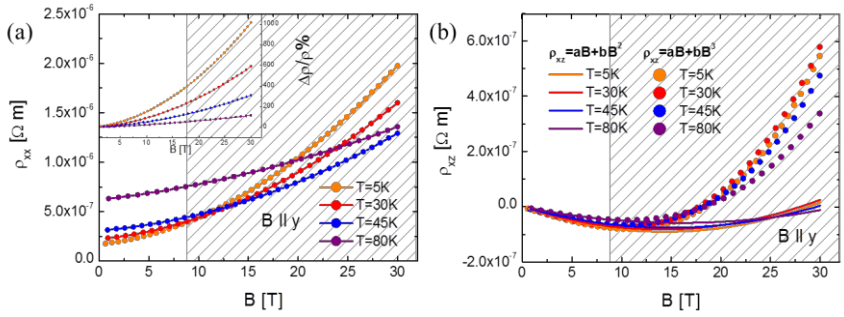

Figure 16: (a) Longitudinal resistivity data as a function of B at T=5,30,45,80 K extrapolated up to 30 T when $B \| y$. The Insets show the resulting magnetoresistance $\Delta\rho/\rho$% which reaches 1000%. (b) Hall resistivity ρ_{xz} as a function of B at T=5,30,45,80 K extrapolated up to 30 T with a polynomial of second (lines) and third (dots) order. Dashed areas indicate the extrapolated region.

In particular, the second order polynomial (lines in Figure 16b) simulates a non-monotonic *B*-dependence of ρ_{xz} which however does not change sign up to 30 T, whereas the third order polynomial (dots in Figure 16b) reproduces a sign change from negative to positive and this occurs at fields much higher than in the case of ρ_{xy}.

Let's first focus on the two terms composing N_{xz}. Figure 17a and 17b show the *B*-dependence of $-\alpha_{xx}\rho_{xz}$ and $\alpha_{xz}\rho_{xx}$ respectively. It is worth to notice that $-\alpha_{xx}\rho_{xz}$ is strongly influenced by the choice of the extrapolating polynomial for ρ_{xz} and we cannot conclude anything about its field dependence. However, since $-\alpha_{xx}\rho_{xz}$ is more than a factor 3 smaller than $\alpha_{xz}\rho_{xx}$ for all the considered temperatures and independently on the *B*-dependence of ρ_{xz}, we can reliably discuss $\alpha_{xz}\rho_{xx}$ versus *B*.

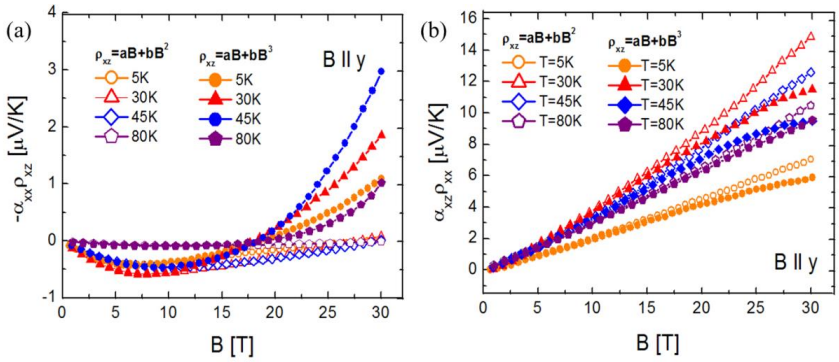

Figure 17: Magnetic field dependence of $-\alpha_{xx}\rho_{xz}$ (a) and $\alpha_{xz}\rho_{xx}$ (b) up to 30 T at T=5,30,45,80K, when ρ_{xz} is extrapolated up to 30 T using a polynomial of second (empty symbols) or third (filled symbols) order.

Figure 17b shows the magnetic field dependence of $\alpha_{xz}\rho_{xx}$ up to 30 T in the temperature range 5-80K when ρ_{xz} is extrapolated up to 30 T using a polynomial of second (empty symbols) or third (filled symbols) order. $\alpha_{xz}\rho_{xx}$ is almost unaffected by the polynomial's choice and in both cases

$\alpha_{xz}\rho_{xx}$ reaches values up to 12-14μV/K. Therefore, it is possible to conclude that this term determines the giant N_{xz} (Figure 3d), as already observed for $\alpha_{xy}\rho_{xx}$ with respect to N_{xy}.

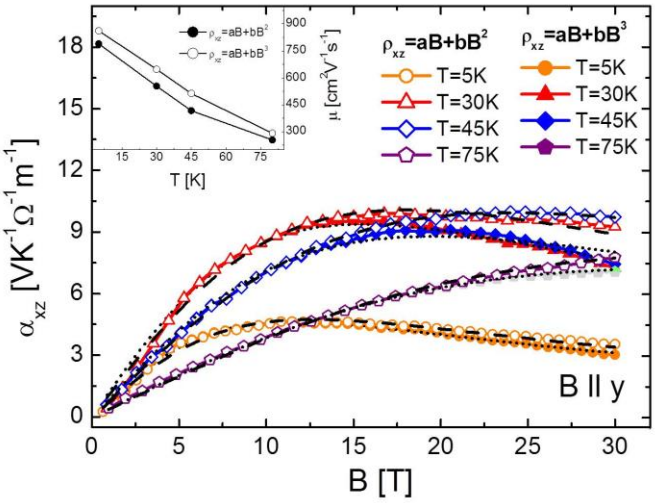

Figure 18: Magnetic field dependence up to 30 T in the temperature range 5-80 K of α_{xz} when ρ_{xz} is extrapolated up to 30 T using a polynomial of second (empty symbols) or third (filled symbols) order. Dashed and dotted lines are the fitting curves of α_{xz} using Eq. (2.48) when ρ_{xz} is extrapolated up to 30 T using a polynomial of second and third order respectively. Inset: temperature dependence of carrier mobility obtained by the fitting.

In Figure 18 we show the magnetic field dependence of α_{xz} up to 30 T in the temperature range 5-80K, for the two ρ_{xz} extrapolations. Comparing it with Figure 8 it is interesting to note that α_{xz} is a factor 2 smaller than α_{xy} and their magnetic field dependence is pretty similar, i.e. well described by Eq. (2.48). We interpolated our α_{xz} data using $\alpha_{xz}(B) = B\mu^2 B/(1+\mu^2 B^2)$ as fitting function (dashed and dotted lines in Figure 18) and we extracted the mobility μ as a fit parameter, obtaining values up to 825±35 $cm^2V^{-1}s^{-1}$ at T=5K and a progressive decrease by rising the temperature. Furthermore, the B-values resulting from the fitting are compatible with those previously obtained for $B \| z$.

In the $B \| y$ configuration, where cross-plane transport comes into play, we extract an effective carrier mobility which is slightly lower than for in-plane transport ($B \| z$), but still high enough to be compatible with a Dirac dispersion. This observation points to a possible 3-dimensional nature of DF in this compound, providing a clue in the still open issue of 2- or 3-dimensional character of DF in the parent compounds of iron-based superconductors, addressed both by theory [31,36,37] and experiments [31,38].

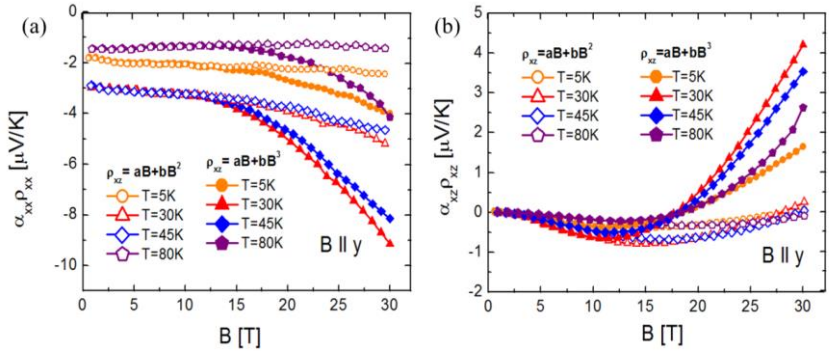

Figure 19: Magnetic field dependence of $\alpha_{xx}\rho_{xx}$ (a), $\alpha_{xz}\rho_{xz}$ (b) up to 30 T at T=5,30,45,80K, when ρ_{xz} is extrapolated up to 30 T using a polynomial of second (empty symbols) or third (filled symbols) order.

Comparing Figure 19a and 19b it is clear that the two terms composing S_{xx} are comparable (they differ for less than a factor 2) so that both $\alpha_{xx}\rho_{xx}$ and $\alpha_{xz}\rho_{xz}$ are strongly affected by the chosen *B*-dependence of ρ_{xz}. This uncertainty does not allow to disentangle the ΔS_{xx}vs B anisotropy observed for $B \| z$ and $B \| y$ (Figure 11a and 11c, respectively). Indeed, it may arise from a field dependence of the transverse resistivity ρ_{ij} which for $B \| z$ changes in sign above 9 T and for $B \| y$ it does not. This is consistent with the observation that a field

dependence of $\alpha_{xx}\rho_{xx}$ (Figure 19a) emerges for $B \parallel y$ if we assume a change of sign in ρ_{xz} (see Figure 16b).

Another possible anisotropic contribution comes from the magnon drag. In the AFM phase of iron-based parent compounds, antiferromagnetic magnons are expected to induce a measurable drag effect, which should influence the longitudinal term $\alpha_{xx}\rho_{xx}$ of S_{xx}, as it has already been observed in polycrystalline REFeAsO compounds [23,24]. Remarkably, the magnon drag contribution is expected to be anisotropic, since an external magnetic field is capable to strongly enhance the magnon drag contribution only if it is applied parallel to the easy-axis of the AFM order while its effect should be minimal if applied perpendicularly [23]. In case of $BaFe_2As_2$ the easy-axis lies in the *ab*-plane. This means that in our experiments no contribution from the magnon drag is expected when B∥z. This is consistent with the negligible field dependence of $\alpha_{xx}\rho_{xx}$ when $B \parallel z$ (Figure 14a). On the other hand, Figure19a shows that a field dependence of $\alpha_{xx}\rho_{xx}$ emerges for $B \parallel y$ if we assume a change of sign in ρ_{xz} (Figure 16b). Hence, we are not able to establish whether the observed ΔS_{xx} vs B anisotropy is determined by the different field dependence of ρ_{ij} or by a magnon drag mechanism, or else by both.

3.7 Remarks on this Chapter

We measured the longitudinal and transverse electrical and thermoelectric properties in magnetic fields up to 30T for two field directions in a $BaFe_2As_2$ single crystal.

By carrying out a simultaneous quantitative analysis of all these properties, which are mutually intertangled in the diffusive transport equations, we demonstrated the possibility of extracting information on

band structure and dispersion, as well as on multiple physical mechanisms into play other than diffusive motion of carriers. Indeed, the anomalous field dependence and the anisotropy of the thermoelectric properties turns out to be distinctive and reveal key features of microscopic mechanisms.

Specifically, we identified the presence of high mobility carriers, compatible with the existence of DF in the band structure, from the giant magnitude of the off-diagonal terms of the thermoelectric tensor α_{xy} and α_{xz}. Moreover, from the anisotropic thermoelectric response with respect to the direction of the applied field, we found possible evidence of the 3D nature of DF in $BaFe_2As_2$.

References

[1] C. R. Rotundu, et al., Phys. Rev. B 82, 144525 (2010)

[2] S. Ishida, T. Liang, M. Nakajima, K. Kihou, C. H. Lee, A. Iyo, H. Eisaki, T. Kakeshita, T. Kida, M. Hagiwara, Y. Tomioka, T. Ito, and S. Uchida, Phys. Rev. B 84, 184514 (2011).

[3] M. A. Tanatar, E. C. Blomberg, A. Kreyssig, M. G. Kim, N. Ni, A. Thaler, S. L. Bud'ko, P. C. Canfield, A. I. Goldman, I. I. Mazin, and R. Prozorov, Phys. Rev. B 81, 184508 (2010).

[4] M. A. Tanatar, et al., Phys. Rev. B 79, 180508(R) (2009)

[5] A. Subedi, D. J. Singh, and M. H. Du, Phys. Rev. B 78, 060506(R) (2008)

[6]M. A. Tanatar, E. C. Blomberg, A. Kreyssig, M. G. Kim, N. Ni, A. Thaler, S. L. Bud'ko, P. C. Canfield, A. I. Goldman, I. I. Mazin, and R. Prozorov, Phys. Rev. B 81, 184508 (2010)

[7] G.M. Zhang et al., EPL 86.3, p. 37006 (2009)

[8] R. Klingeler et al., Phys. Rev. B 81, 024506 (2010)

[9] Li Wei-Yong et al., Chinese Physics B 19.8, p. 087403 (2010)

[10] B. Xu et al., Phys. Rev. B 94, 085147 (2016)

[11] E. D. Mun, S. L. Bud'ko, N. Ni, A. N. Thaler, and P. C. Canfield, Phys. Rev. B 80, 054517 (2009)

[12] S. Arsenijevic, R. Gaál, A. S. Sefat, M. A. McGuire, B. C. Sales, D. Mandrus, and L. Forró, Phys. Rev. B 84, 075148 (2011).
[13] A. F. May, M. A. McGuire, J. E. Mitchell, A. S. Sefat, and B. C. Sales, Phys. Rev. B 88, 064502 (2013).
[14] Y. J. Yan, X. F. Wang, R. H. Liu, H. Chen, Y. L. Xie, J. J. Ying, and X. H. Chen, Phys. Rev. B 81, 235107 (2010).
[15] J.-H. Chu, J. G. Analytis, D. Press, K. De Greve, T. D. Ladd, Y. Yamamoto, and I. R. Fisher,
Phys. Rev. B 81, 214502 (2010)
[16] M. Matusiak, M. Babij, T. Wolf, Phys. Rev. B 97, 100506(R) (2018)
[17] J.M. Ziman, *Principles of the Theory of Solids*, (Cambridge University Press, 1972).
[18] I. Pallecchi, F. Bernardini, F. Caglieris, A. Palenzona, S. Massidda and M. Putti, Eur. Phys. J.B 86: 338 (2013).
[19] K. K. Huynh, Y. Tanabe and K. Tanigaki, Phys. Rev. Lett. 106, 217004 (2011).
[20] L. J. van der Pauw, *Philips Res. Rep.*, 16, 187-195 (1961).
[21] K. Behnia and H. Aubin, Rep. Prog. Phys. 79 046502 (2016).
[22] G. N. Grannemann and L. Berger, Phys. Rev. B 13, 2072 (1976).
[23] F. Caglieris, A. Braggio, I. Pallecchi, A. Provino, M. Pani, G. Lamura, A. Jost, U. Zeitler, E. Galleani D'Agliano, P. Manfrinetti, and M. Putti, Phys. Rev. B 90, 134421 (2014).
[24] M. Matusiak, T. Plackowski, Z. Bukowski, N. D. Zhigadlo, and J. Karpinski, Phys. Rev. B 79, 212502 (2009).
[25] H.Q.Yuan, L. Jiao, F. F. Balakirev, J. Singleton, C. Setty, J. P. Hu, T.Shang,L.J.Li, G.H.Cao, Z.A.Xu,B.Shen, and H.H.Wen, e-print arXiv:1102.5476.
[26] F. Caglieris, A. Leveratto, I. Pallecchi, F. Bernardini, M. Fujioka, Y. Takano, L. Repetto, A. Jost, U. Zeitler, and M. Putti, Phys. Rev. B 96, 104508 (2017).
[27] H.-H. Kuo, J.-H. Chu, S. C. Riggs, L. Yu, P. L. McMahon, K. De Greve, Y. Yamamoto, J. G. Analytis, and I. R. Fisher, Phys. Rev. B 84, 054540 (2011)
[28] T. Terashima, N. Kurita, M. Tomita, K. Kihou, C.-H. Lee, Y. Tomioka, T. Ito, A. Iyo, H. Eisaki, T. Liang, M. Nakajima, S. Ishida, S. I. Uchida, H. Harima, and S. Uji, Phys. Rev. Lett. 107, 176402 (2011).

[29] Y. Kim, H. Oh, C. Kim, D. Song, W. Jung, B. Kim, H. J. Choi, C. Kim, B. Lee, S. Khim, H. Kim, K. Kim, J. Hong, and Y. Kwon, Phys. Rev. B 83, 064509 (2011).
[30] P. Richard, K. Nakayama, T. Sato, M. Neupane, Y.-M. Xu, J. H. Bowen, G. F. Chen, J. L. Luo, N. L. Wang, X. Dai, Z. Fang, H. Ding, and T. Takahashi, Phys. Rev. Lett. 104, 137001 (2010).
[31] Z.-G. Chen, Luyang Wang, Yu Song, Xingye Lu, Huiqian Luo, Chenglin Zhang, Pengcheng Dai, Zhiping Yin, Kristjan Haule, and Gabriel Kotliar, Phys. Rev. Lett. 119, 096401 (2017).
[32] V. Oganesyan and I. Ussishkin, Phys. Rev. B 70, 054503 (2004).
[33] T. Morinari, E. Kaneshita, and T. Tohyama, Phys. Rev. Lett. 105, 037203 (2010).
[34] M. Matusiak, Z. Bukowski, and J. Karpinski, Phys. Rev. B 83, 224505 (2011).
[35] M. Matusiak, M. Babij, T. Wolf, Phys. Rev. B 97, 100506(R) (2018).
[36] Z. P. Yin, K. Haule, and G. Kotliar, Nat. Phys. 7, 294 (2011).
[37] Z. P. Yin, K. Haule, and G. Kotliar, Nat. Mater. 10, 932 (2011).
[38] M. Nakajima, M. Nagafuchi, S. Tajima, Phys. Rev. B 97, 094511 (2018).

4 Investigation of the strange metal regime of $Bi_2Sr_2CuO_{6+x}$: standard analysis and comparison with holographic theory

In Chapter 2 we introduced the complete set of transport coefficients, calculated by means of holographic techniques (section 2.7). We noticed that these results are amenable of direct experimental testing which can be performed by measuring all the transport properties of a strange metal as functions of temperature and magnetic field. The complete characterization consists of electrical resistivity, magnetoresistance, Hall effect, Seebeck, Nernst and thermal conductivity measurements. All these properties link directly to the theoretically derived coefficients σ_{xx}, σ_{xy}, α_{xx}, α_{xy}, κ_{xx} and κ_{xy}, giving the opportunity to compare experiments with the new ideas coming from holographic theories.

In this Chapter we will present the measurements of the whole set of transport properties performed on single crystals of $Bi_2Sr_2CuO_{6+x}$, a cuprate superconductor of the Bi-2201 family we describe in section 4.1. The collected data, presented and discussed in section 4.2, will be compared with the Boltzmann transport theory in section 4.3, focussing

on the limits of these formulae in reproducing all the anomalous features observed in the transport properties. In order to overcome these limits, a holographic-inspired data analysis will be performed in section 4.4.

4.1 The $Bi_2Sr_2CuO_{6+x}$ (Bi-2201) compound

Among the possible candidate materials, HTS are probably the most promising to test the holographic formulae. In particular, $Bi_2Sr_2CuO_6$ (Bi-2201) exhibits all the basic prerequisites, generally considered as signatures of the Fermi liquid breakdown: linear *T*-dependence of electric resistivity with the violation of the MIR limit [1] and, as a hole-doped cuprate, it shows a quantum critical region in the optimally doped part of its phase diagram [2] (see Chapter 1). Moreover, Bi-2201 is a single band, quasi 2D system. This simplifies the data analysis, avoiding complications due to multi-band nature that characterize other possible candidates. Indeed, in Chapter 3 we extensively discussed the case of $BaFe_2As_2$ as an example of the complications due to multiband effects which appear in iron-based materials.

In addition, Bi-2201 shows relatively low values of critical temperature T_c [3,4,5]. In fact, for Bi-2201 the carrier concentration can be widely changed by partially replacing Sr with La (to underdope) or Bi with Pb (to overdope); at optimal doping ($Bi_2Sr_{2-x}La_xCuO_6$ with $x \sim 0.4$), the maximum T_c is about 30 K [6]. By varying the oxygen concentration in $Bi_2Sr_2CuO_{6+x}$. the maximum T_c is around 11 K.

Due to such low T_c values, this compound is not interesting for applications. On the other hand, below T_c, electrical transport properties are short circuited from superfluid and fall down to zero. This means that the higher T_c, the smaller is the accessible temperature range for

transport measurements. Therefore, Bi-2201 system presents an ideal stage for the systematic study of the normal-state properties down to lower temperatures.

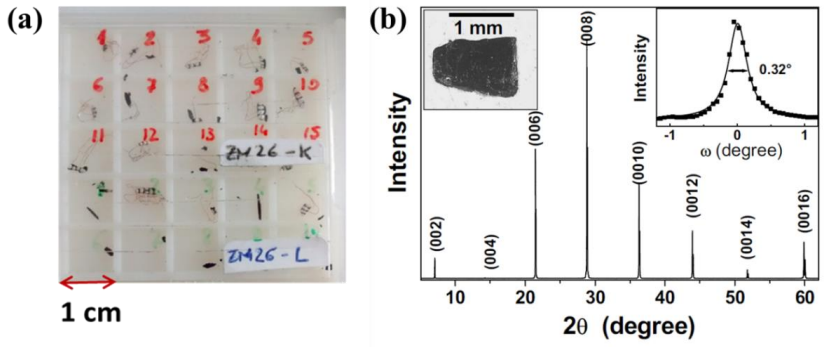

Figure 1: (a) Single crystals of pure Bi-2201; some of them show the contacts and the wires used for electric resistivity measurements. (b) X-ray diffraction pattern of one of the crystals (shown in the left-hand inset) oriented with the *c* axis parallel to the scattering vector. Right-hand inset: rocking curve exhibiting a full width at half maximum of 0.32°. After [5].

4.1.1 The Bi-2201 crystals

In the Bi-based series of superconducting cuprates, the single-layer compound $Bi_2Sr_2CuO_6$ is the less assiduously investigated because of its lower T_c (see previous paragraph). In addition, its pure superconducting phase is difficult to synthesize and this complication has fostered the study of the more easily processed La and/or Pb-doped Bi-2201, leaving pure Bi-2201 system quite unexplored. High purity and large crystals of this compound were grown by the group of Dr. Enrico Giannini (University of Geneva, Department of Quantum Matter Physics) and the details about the synthesis of the samples are reported in [5]. Figure 1a and inset of Figure 1b show some of the crystals that were cleaved from the core of a precursor rod with typical lengths of 1-5 mm and thickness of 0.1-0.2 mm [5]. The crystals are superconducting with an onset of the

magnetic susceptibility transition at 10 K and a transition width of about 4 K (see Appendix D). The quality of the crystals was checked by x-ray diffraction (XRD) and energy-dispersive x-ray microprobe (EDX). The XRD pattern measured in a Bragg-Brentano geometry is shown in Figure 1b. In this configuration, only the [00*l*] planes contribute to the pattern. The rocking curve of the [006] reflection is shown in the right inset of Figure 1b: the full width at half maximum is of 0.32° whereas that of the $I(2\theta)$ peaks is typically on the order of 0.05°. These XRD data prove the high crystallinity of the samples. The chemical composition of the crystals was checked by EDX. The average composition measured over large crystal areas is $Bi_{2.05}Sr_{1.98}Cu_{0.98}O_{6.04}$ with errors on the local deviations in formula units of Δ(Bi)=0.05, Δ(Sr)=0.05, and Δ(Cu)=0.02.

4.2 Transport properties measurements

The electrical measurements (resistivity, magnetoresistance, Hall effect) have been performed at the Physics Department in Genova, using a commercial system *Physical Property Measurement System* (PPMS) by Quantum Design (see Appendix C). This system allows to make (magneto)resistance and Hall effect measurements on samples of even less then millimetric sizes in a range of temperatures between 2K and 400 K and in magnetic fields from -9 T to 9 T. High-quality contacts of low resistance (tens of Ohm) were made by using an Ag paste which was cured in air at about 250°C. The electric resistivity was measured using a standard 4-probe technique, whereas we used a standard six-terminal method for simultaneous magnetoresistance and transverse resistivity measurements, in which the data are taken with a dc technique in the sweeping magnetic field *B* from -9 T to 9 T at fixed temperatures. We performed all the measurements with both positive

and negative *B* in order to separate the even (magnetoresistance) and odd (transverse resistivity) parts of the signal with respect to *B*.

The PPMS is also equipped with the *Thermal Transport Option* (TTO) which let perform thermal and thermoelectric measurements on samples of at least millimetric dimensions, since the experimental set up (heater, thermal mass and thermometers) needs to be hold by the sample itself. Therefore, the PPMS does not allow to perform such measurements on the $Bi_2Sr_2CuO_{6+x}$ crystals.

The thermoelectric and thermal characterization was performed at IFW Dresden (Germany) where the availability of home-made probes let measure thermal and thermoelectric properties of micrometric samples, in a temperature range 4-300 K and in magnetic fields up to 14 T (see Appendix C). The high magnetic field and the sensitivity of the apparatus help measuring the thermal Hall conductivity κ_{xy} which is a challenging quantity to detect since it can be as much as 1000 times smaller than κ and it is defined as $\kappa_{xy} = \kappa \frac{\nabla_y T}{\nabla_x T}$ (eq. 2.22 of Chapter 2). It is therefore necessary to measure the transverse thermal gradient $\Delta_y T/y$ (where y is the width of the crystal) which generates due to *B* applied perpendicularly to a longitudinal thermal gradient $\Delta_x T/x$ (where x is the length of the crystal). Typically $\Delta_x T/x$ and $\Delta_y T/y$ were of the order of magnitude of (0.1-1)×10^3 K/m and (0.1-1) K/m respectively. $\Delta_x T/x$.

We performed all the thermal and thermoelectric measurements with both positive and negative *B* in order to separate the even (Seebeck effect and longitudinal thermal conductivity) and odd (Nernst effect and transverse thermal conductivity) parts of the signal with respect to *B*. See Appendix C for the details of the sample mounting, the

experimental setup and the implemented corrections to the measured data in order to get rid of the spurious effects of the copper wires and the magnetic field calibrations of the thermocouples.

This activity has been rewarded and supported with a DAAD Scholarship, Research Grants Award – Short-term grants, 2017 (57314023).

4.2.1 Electrical measurements: resistivity, magnetoresistance and transverse resistivity

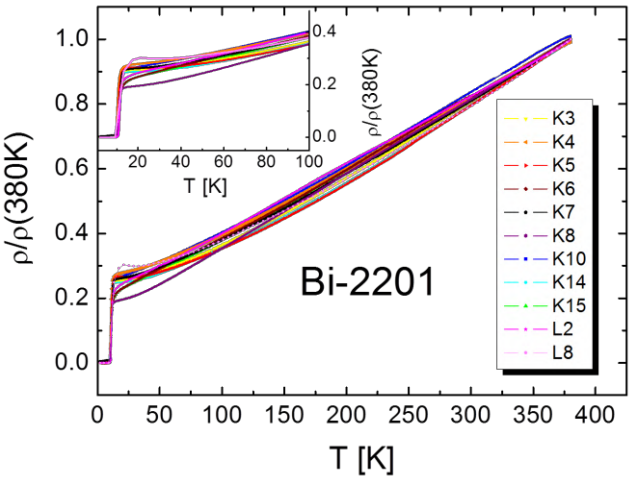

Figure 2: Temperature dependence of the normalized electric resistivity $\rho/\rho(380\text{K})$ in the range 4-380K. Inset: Enlarged view of $\rho/\rho(380)$ curves between 4 and 100 K.

Figure 2 shows $\rho(T)$ of the best eleven samples, measured in the temperature range 4-380 K. The curves are normalized to the value at 380 K ($\rho/\rho(380\text{K})$) to get rid of the geometrical factors when comparing the samples. All the crystals show a quite sharp

superconducting transition which occurs at $T_c \sim 11$ K (inset of Figure 2). All the $\rho(T)$ are almost T-linear at high temperatures and deviations from linearity can be observed for some samples, whose $\rho(T)$ curves show a saturation above T_c. Indeed, although all the Bi-2201 crystals are cut from the same batch, some samples can present more impurities. Furthermore the transport properties of Bi-2201 are quite non-reproducible even among crystals of nominally the same composition [7,8,9] and the residual in-plane resistivity is usually large [9,10]. Therefore, I performed the electric characterization on several samples and I report here the data relative to the best three crystals, namely L2, K8 and K14. In this context, with "best samples" I intend those whose $\rho(T)$ curves shows a T-linear behaviour in the widest investigated range of temperatures. Indeed, in Chapter 1 we discussed that this is the basic feature which characterizes the strange metal regime of cuprates.

Appendix D shows the magnetization and the magnetic susceptibility measurement of L2 sample, probing the normal and the superconducting state respectively. In particular, we find a quite narrow superconducting transition which evidences the good quality of the crystal.

Figure 3a displays the magnetoresistance, defined as $\left(\rho_{xx}(B) - \rho_{xx}(0)/\rho_{xx}(0)\right)$, of the L2 sample as a function of magnetic field up to 9 T applied in the out-of-plane direction perpendicular to the electric current for selected temperatures in the range 20-250K. Its *B*-dependence is almost quadratic, as shown by the solid lines in Figure 3a which are quadratic fits to experimental data (open symbols). Slight deviations from B^2 can be justified by the uncertainty due to the small magnitude of the signal, which at 20 K reaches 0.5% at 9T. The quadratic *B*-dependence is well reproduced also by K10 and K7 samples

(not reported). We do not report the measured magnetoresistance at 15 K since its B-dependence is almost linear rather than quadratic and this could be due to the proximity to T_c.

Figure 3b shows the bi-logarithmic plot of the magnetoresistance values at 9 T (MR@9T) as a function of temperature for the samples L2, K10 and K7. The data relative to the three samples almost overlap from 15 K to 40 K, where the MR@9T monotonically decrease with increasing temperature. However, it is important to notice that a sizeable magnetoresistance is measured up to 250 K. As evidenced by the bi-log scale, the low temperature reduction is as fast as $\sim T^{-4}$ (black dashed line in Figure 3b) up to 30 K. Above 40 K, the MR@9T of the three samples is almost constant, assuming values between $\sim 2 \cdot 10^{-4}$ and $\sim 10^{-3}$ (the orange dashed line in Figure 3b corresponds to a mean value of $7 \cdot 10^{-4}$).

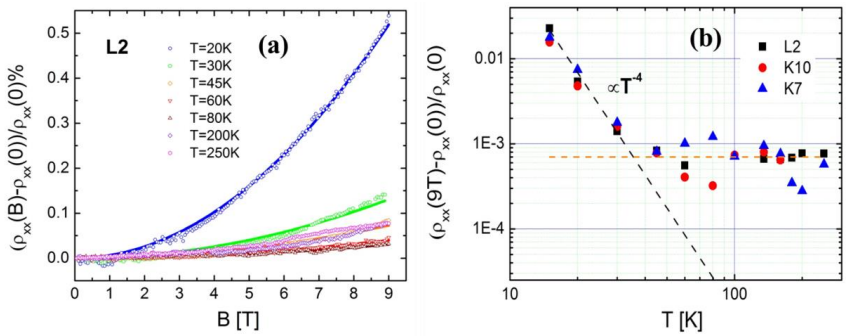

Figure 3: (a) *B*-dependence of the magnetoresistance $\left(\rho_{xx}(B) - \rho_{xx}(0)/\rho_{xx}(0)\right)$ of the L2 sample for selected temperature in the range 20-250K. Solid lines are quadratic fit to experimental data (empty symbols). (b) *T*-dependence of $\left(\rho_{xx}(9T) - \rho_{xx}(0)/\rho_{xx}(0)\right)$ for the L2, K10 and K7 samples.

Figure 4 shows the transverse resistivity ρ_{xy} of the L2 sample as a function of the magnetic field up to 9 T applied in the out-of-plane

direction perpendicular to the electric current for selected temperatures in the range 15-250 K. It is B-linear in the field and such behaviour has been also observed in K7 and K10 samples (not shown).

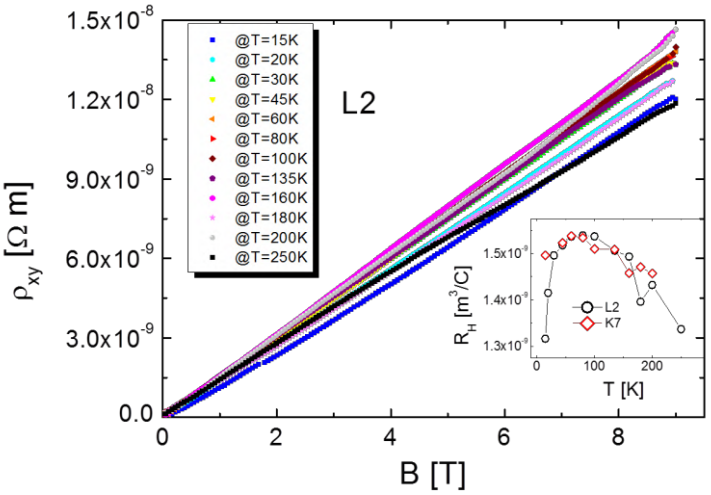

Figure 4: Magnetic field dependence of transverse resistivity ρ_{xy} of the L2 sample up to 9T for selected temperatures in the range 15-250 K. Inset: Hall coefficient R_H extracted from ρ_{xy} for the L2 sample (empty dots) and the k7 sample (empty squares).

The Hall coefficient R_H is obtained by the slopes of the ρ_{xy} curves at each temperature and its temperature dependence is reported in inset of Figure 4. We report the results for the L2 and K7 samples, which is positive indicating holes as dominant carriers. It displays a weak temperature dependence with a broad bump centred around 80 K. This behaviour is in agreement with the results reported in Chapter 1 for cuprates.

In Chapter 1 we also introduced the inverse Hall angle $\cot g\,\theta_H = \rho_{xx}/\rho_{xy}$ and we discussed that it has a peculiar temperature dependence. In ref. [11] it is reported that for La-doped Bi-2201 $\cot g\,\theta_H \sim A + BT^{\alpha}$ where α decreasing from 2 to 1.6-1.7 moving from the UD to the OD regime. Figure 5 shows the calculated $\cot\theta_H$ at B=9T

for the L2 and K7 samples as a function of $T^{1.66}$ and the data are well fitted by a straight line (blue line in Figure 5). The exponent 1.66 has been guessed by the bi-logarithmic plot of $\cot g\,\theta_H$, reported in inset of Figure 5.

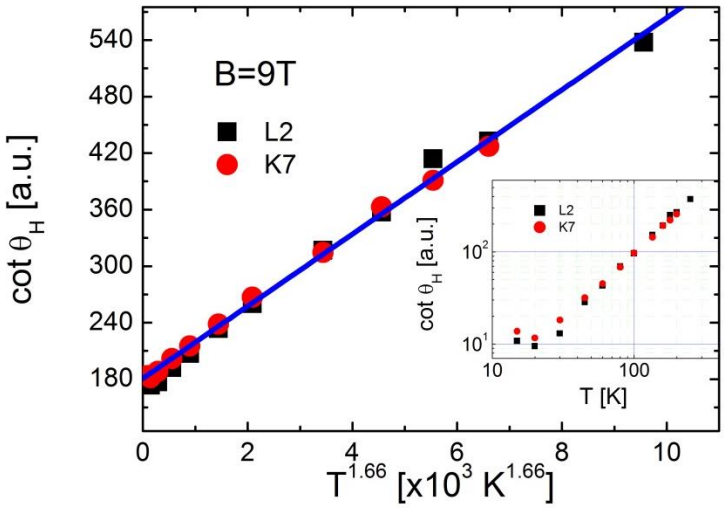

Figure 5: Inverse Hall angle $\cot\theta_H = \rho_{xx}/\rho_{xy}$ at B=9T of L2 (black squares) and K7 (red dots) samples as a function of $T^{1.66}$. The blue line is a linear fit to the data. Inset: Bi-logarithmic plot of $\cot\theta_H$.

4.2.2 Thermoelectric measurements: Seebeck and Nernst effect

Figure 6 shows the temperature dependence of the Seebeck effect S from 11 to 290 K. At low temperature, it is slightly positive (~0.3μV/K) and by increasing temperature it monotonically decreases reaching ~-18 μV/K at 290 K. S is markedly non-linear in the temperature range considered and the zero temperature extrapolated value S_0 is ~4μV/K. As already noted in Chapter 1, the peculiar in-temperature behaviour of the Seebeck effect of cuprates differs from the simple picture of conventional metals predicting a linear S with S_0 equal

to zero. Furthermore, no "phonon drag" peak is detected around $\theta_D/5$-$\theta_D/4$ (θ_D is estimated to be around 200 K in Bi-based cuprates [12]), as expected for a pure metal. It is also worth to notice that apart from the slightly positive values around 11 K, S is negative up to 290K, in contrast with the positive sign of the Hall coefficient (inset of Figure 4) and with the simple expectation that thermopower has the carriers' sign. On the other hand, Allen et al. [13] calculated the electronic energy bands of $La_{2-x}Sr_xCuO_4$ and $YBa_2Cu_3O_7$ from local density functional theory. They predicted that R_H should appear "holelike" when electrons orbit in metallic planes but S should appear "electronlike" for in-plane thermal gradients.

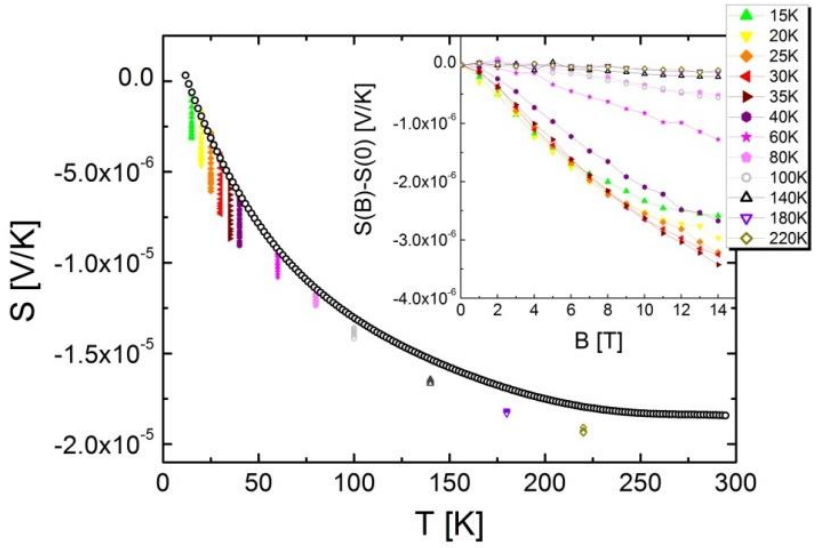

Figure 6: Temperature dependence of the Seebeck coefficient S as a function of temperature between 11 and 290 K (empty circles). The coloured symbols are isothermal measurements performed at selected temperatures in the range 15-220 K in a magnetic field from 0 to 14 T. Inset: Magnetic field dependence of $S(B) - S(0)$ from 0 to 14 T at same selected temperatures.

The coloured symbols in Figure 6 are isothermal measurements performed at selected temperatures varying the magnetic field from 0 to 14 T. The zero-field values of S (empty circles in Figure 6) are well reproduced by the isothermal data at 0 T up to 100 K and a slight difference occurs at higher temperatures, where almost no magnetic field dependence was detected. In Chapter 1 we also introduced the "universal" curve of T_c/T_c^{max}vs S (290 K) (OCT relation). Given the measured value of S(290 K) ∼-18 μV/K, it does not follow the OCT relation (which would predict S(290 K) ∼1μV/K for T_c/T_c^{max}∼1) and it is a factor ∼2 larger than the value measured in non-substituted Bi-2201 thin films (Figure 12 of Chapter 1).

In inset of Figure 6 we show the magnetic field dependence up to 14 T of $\Delta S = S(B) - S(0)$. We measured a significant magnetic field dependence from 15 40 K, with the maximum variation of ∼-3.4μV/K at 14 T when T=35 K (brown triangles in inset of Figure 6). By increasing temperature, ΔS progressively diminishes and becomes vanishing small above 80 K. It is worth to notice that no magnetic-field dependence of S is expected within the simple Mott formula (Eq. 2.56 in Chapter 2).

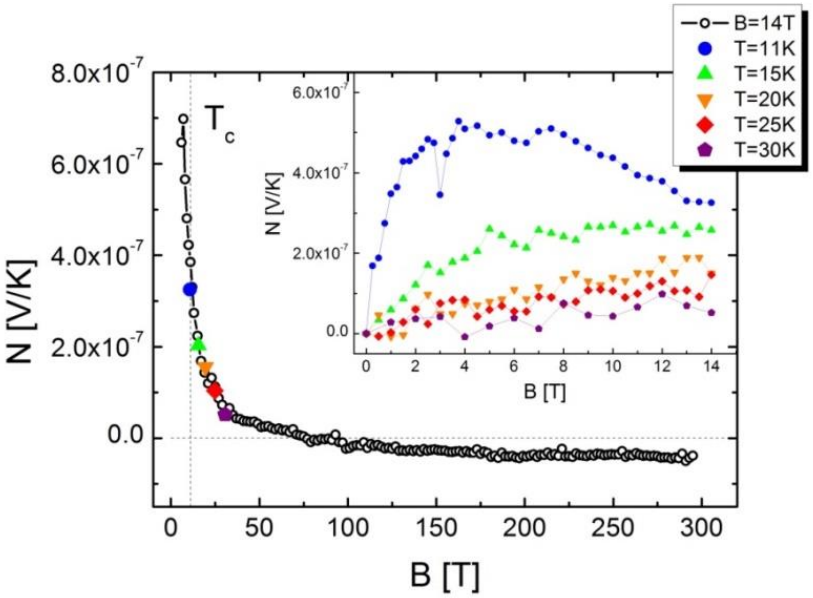

Figure 7: Temperature dependence of Nernst coefficient between 15 and 300 K, measured at B=14 T (empty bullets). The coloured filled symbols refer to the Nernst value at 14 T measured when performing isothermal measurements at T=11,15,20,25 and 30 K varying B from 0 to 14 T. Vertical dashed line signals the critical temperature T_c~11 K. Inset: B-dependence of the Nernst coefficient from 0 to 14 T at the selected temperatures.

Figure 7 shows the temperature dependence of the Nernst coefficient N between 15 and 300 K (empty bullets). At room temperature its value is negative ~-0.05 μV/K and it decreases in absolute value with lowering temperature, crossing zero at 75 K. Below this temperature N is positive and reaches ~ 0.7 μV/K at 7 K, that is 4 K below T_c. The inset of Figure 7 shows the magnetic field dependence of N from 0 to 14 T at T=11,15,20,25,30 K. At 11 K, just above T_c, N sharply rises with the field, reaching a broad maximum around 3T and slowly decreasing at higher fields. At T=15K, N decreases markedly and it almost saturates to ~$2.5 \cdot 10^{-7}$ μV/K at 14 T. For T≥20K it is linear in B with a slope mildly decreasing with increasing T. As discussed in Chapter 1, N of

hole-doped cuprates is the sum of the normal term N_n and an anomalous contribution N_a which below T_c is identified with the vortices contribution N_s we described in Chapter 2, whereas, above T_c, its origin remains controversial [14].

As shown in Chapter 2, the term. N_n is expected to be linear in B (eq. 2.66), whereas N_s has a characteristic "tilted-hill" profile as a function of B [14].We therefore suggest that $N \sim N_s$ below ~20 K. At this stage, we then observe that a (positive) anomalous contribution N_a is still present above 20 K.

4.2.3 Thermal transport: longitudinal and transverse conductivity

Figure 8 shows the temperature dependence of the longitudinal thermal conductivity κ between 6 and 280 K. For B=0 T, with decreasing temperature, it linearly decreases from 280 K to ~75 K, where κ starts to increase showing a peak of ~7.5 $Wm^{-1}K^{-1}$ around 25 K. Below this temperature κ goes to zero in the T→0 limit. By switching on a magnetic field B=14 T (red diamonds in Figure 8), the peak at 25 K reduces to ~6 $Wm^{-1}K^{-1}$ with a B-dependence which is shown in the Inset of Figure 8. The magnetic field dependence is maximum at 15 K ($\kappa(B)/\kappa(0)$~80%) and it decreases by increasing temperature being negligible above 80 K.

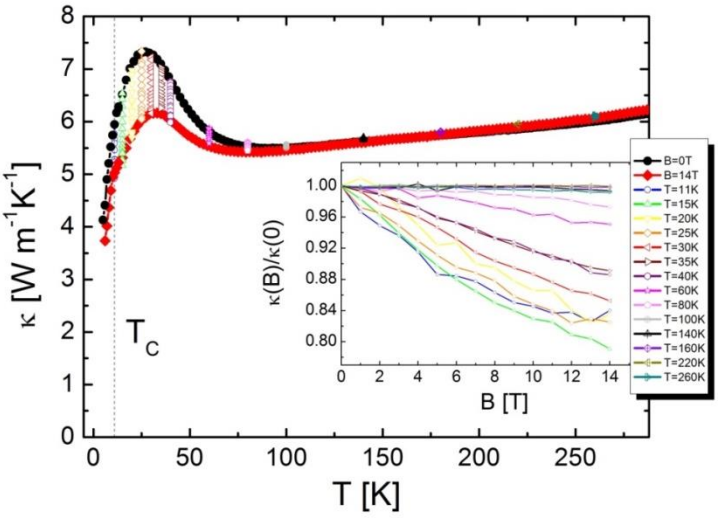

Figure 8: Temperature dependence of longitudinal conductivity κ from 6 to 280 K at B=0 T (black bullets) and B= 14 T (red diamonds). The dashed vertical line indicates the critical temperature T_c~11 K. Inset: magnetic field dependence of $\kappa(B)/\kappa(0)$ between 0 and 14 T at selected temperatures in the range 11-260 K.

In Chapter 1 we already showed that a distinctive feature of κ in-plane of cuprates is that it exhibits a large enhancement below T_c which culminates in a broad peak near $T_c/2$ [15]. This feature was discussed in terms of the BRT theory [16] whose essential point is that as the electrons condensate and the electronic thermal conductivity rapidly vanishes below T_c, the mean-free path of phonons may increase to such an extent that the lattice thermal conductivity more than compensates for the loss of the electronic contribution. Experiments show that the anomaly is readily suppressed applying the magnetic field [17] and this can be understood by considering that, in a *d*-wave superconductor, also nodal quasiparticles (QPs) contribute to the total thermal conductivity. Indeed, the magnetic field dependence of the broad peak below T_c is attributed to the QP scattering off vortices [18].

Interestingly, Figure 8 shows that the measured κ shows a peak which is above T_c and should be therefore of different origin than the broad peak common to the majority of cuprates which we described above. Indeed, a "knee" feature of κ around 10 K has been measured in Dy-doped Bi-2212 single crystals by Sun et.al [19]. Here they showed that upon doping Dy, the broad peak is strongly suppressed and a new peak at 10 K emerges. This low-T peak is the strongest in the x=30 sample (having T_C=45K) and survives in the non-superconducting samples, which clearly indicates that it originates from the phonon heat transport. Interestingly, in the undoped compound of other cuprates, the phonon heat transport shows a large phonon peak around 20 K, whose magnitude varies between ~20 and ~80 W/K m [19]. However, it is known that Bi-2201 system has much dirtier phonon heat transport than other cuprates, probably due to the strong disorder of the crystal lattice caused by the excess oxygen. For Dy-doped Bi-2212 in [19] is discussed that a moderate Dy doping can enhance the phonon conductivity rather strongly because the crystal structure is somewhat stabilized by doping an appropriate amount of Dy. They therefore linked the knee feature of κ(T) to the competition between the decrease of QP heat transport and the increase of phonon heat transport upon lowering temperature across 10 K. In addition, the measured field dependence of κ (Inset of Figure 8) is compatible with that measured in [19] and therefore, the peak observed around 25 K should be of the same phonon origin as described in [19]. The phonon peak was never observed before in Bi-2212 and to our knowledge it is the first time that it has been observed in Bi-2201.

As already discussed in section 4.2, κ_{xy} is a challenging quantity to detect since it can be as much as 1000 times smaller than κ and currently there are very few measurements for the cuprates [20,21].

Figure 9a shows the transverse thermal gradient $\Delta_y T/y$ (where y is the width of the crystal) which generates due to B applied perpendicularly to a longitudinal thermal gradient $\Delta_x T/x$ (where x is the length of the crystal). In order to calculate κ_{xy}, we considered the slope $\Delta(\Delta_y T/y)/\Delta B$ (Figure 9a). Figure 9b shows the temperature dependence of κ_{xy} calculated as $\kappa_{xy} = \frac{\Delta(\Delta_y T/y)}{\Delta B} B \frac{\kappa_{xx}}{\Delta_x T/x}$ at B=14T for selected temperatures in the range 20-40 K. As expected, it is small at low temperatures (~2× 10^{-3}W/m K at 20 K) and it decreases by rising temperature (Figure 9b).

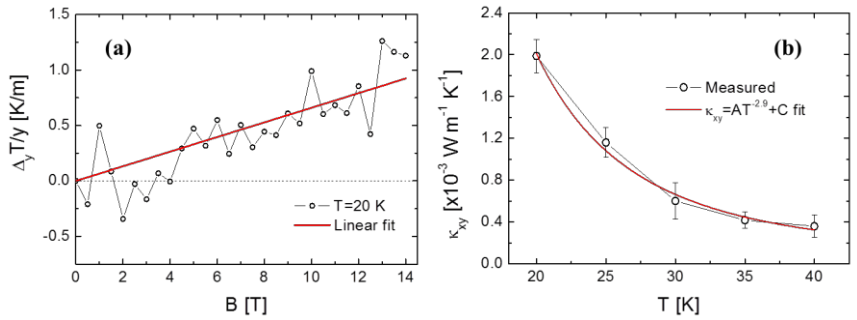

Figure 9: (a) Magnetic field dependence from 0 to 14 T of the transverse thermal gradient $\Delta_y T/y$ at T=20 K (empty dots). The red line is a linear fit to data. (b) Temperature dependence of κ_{xy} at B=14 T for selected temperatures in the range 20-40 K (empty dots). Red line is a fit to data with $\kappa_{xy} = AT^{-2.9} + C$ function.

4.3 Comparison with Boltzmann theory

With the set of data collected and presented in the previous paragraphs, we now perform the data analysis within the Boltzmann approach we introduced in Chapter 2.

4.3.1 Thermal conductivity and Wiedemann-Franz law

As already mentioned, the interpretation of longitudinal thermal conductivity κ in cuprates is complicated by the fact that the total thermal conductivity is given by $\kappa = \kappa_{el} + \kappa_{ph}$, where κ_{el} and κ_{ph} are the electron and phonon contribution to κ respectively. In cuprates, κ_{ph} can be the same order of magnitude of κ_{el} (e.g. in single crystals of YBCO [22] and Y-doped Bi-2201 [23]), or even 10-100 times larger (e.g. in polycrystalline samples of $REBa_2Cu_3O_7$ [24]). Figure 10 shows the comparison between the measured κ (black dots) and the κ_{el} estimated by means of the Wiedemann-Franz law ($\kappa_{el} = \frac{L_0 T}{\rho_{xx}}$ where L_0 =2.44× 10^{-8}WΩK^{-2} is the Lorenz number, see Chapter 2). One first observation is that the estimated κ_{el} is more than 20 times smaller than the measured κ and this implies that κ_{ph} is the main contribution to κ.

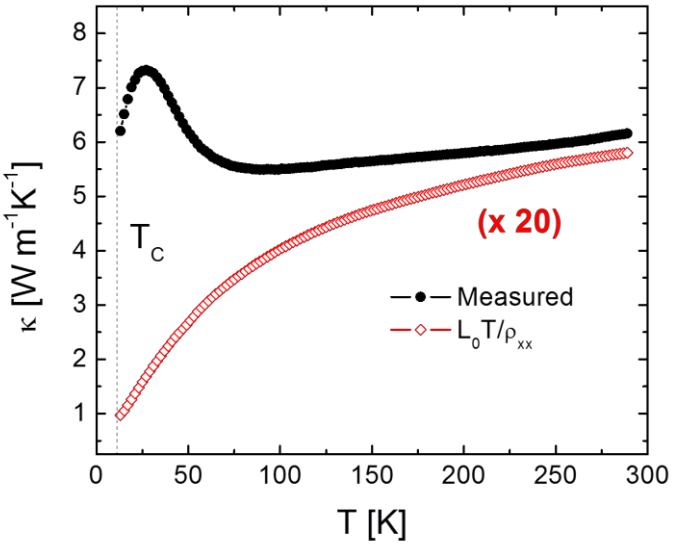

Figure 10: Measured longitudinal conductivity κ (black dots) compared with the electron contribution κ_{el} estimated with the Wiedemann-Franz law (red empty diamonds)

As discussed in Chapter 2, the thermal Hall effect is a useful tool to extract the electronic component from the total κ. In particular, we evaluate the Hall-Lorenz number $L_{xy} = \frac{\kappa_{xy}}{\sigma_{xy}T}$ (equation 2.68) which is regarded as a direct source of information about the electronic heat current [20]. Figure 11 shows the temperature dependence of the ratio L_{xy}/L_0 from 15 to 40 K. The results show an enhancement of L_{xy} above the L_0 value below 25 K, whereas, from above 25 K to 40 K L_{xy} is significantly smaller than L_0. Proust et al. [25] studied the (longitudinal) heat transport in $Bi_{2+x}Sr_{2-x}CuO_{6+\delta}$ at sub-Kelvin temperatures and in magnetic fields as high as 25 T. The zero-temperature limit of κ (κ_0) let them calculate the Lorentz number L and test the Wiedemann-Franz (WF) law. They reported values of L/L_0 between 2 and 3 for the optimally doped sample (in agreement with our low-temperature results) and L/L_0 results up to 6 in underdoped samples. In addition, they showed that the WF law is verified in the overdoped side of the phase diagram. In [25] they considered possible microscopic origins of the strong ($L/L_0 \geq 2$) and reproducible deviation measured for underdoped and optimally doped samples. A class of models are those invoking the breakdown of the Fermi liquid in the vicinity of a quantum critical point (QCP), where one may expect the emergence of non-Fermi-liquid properties, which may include a violation of the WF law. A value of Lorenz number which exceeds the Sommerfeld value for a factor around 2 has also been reported both in optimally doped $EuBa_2Cu_3O_7$ (EuBCO) single crystal [26] and optimally doped $YBa_2Cu_3O_{7-d}$ (YBCO) [21] by studying the transverse thermal transport. In ref. [21] the authors pointed out that an increase of L is expected if it is taken into account the opening of a pseudogap at the Fermi surface. This has been shown by Minami et al. in ref. [27], where it is shown that the ratio L/L_0 can reach a value of ~2.5

(depending on temperature and width of the pseudogap) and this agrees well with YBCO [21], EuBCO [26] and our low temperature results (Figure 11). On the other hand, Zhang et al. [20] reported in YBCO a L_{xy} which is significantly smaller than the Sommerfeld value, with the ratio L_{xy}/L_0 varying from 0.15 to 0.6 when temperature is increased from 95 to 320 K. They discussed that a suppressed L_{xy}/L_0 ratio may be expected in systems with dominant electron-electron (*ee*) scattering [20]. A discussion of this point illustrates how normal (*N*) and umklapp (*U*) scattering processes influence the L_{xy}/L_0 ratio. As in the case of lattice thermal conduction [28], *N* processes leave the total momentum of the electron gas unchanged, so that the charge current cannot relax without *U* processes. However (unlike lattice conduction), *N*-process *ee* scattering does relax the heat current because it causes a redistribution of energy between hot and cold electrons. This distinction implies that systems in which *ee* scattering is dominant have a strongly reduced Lorentz number. This may explain the measured L_{xy}/L_0 above 25K (see Figure 11).

The temperature dependence of the κ_{el} may be derived if we assume that $L \approx L_{xy}$. The results are shown in inset of Figure 11. With increasing temperature, κ_{el} decreases and this can be interpreted as a result of decrease in the effective concentration of charge carriers. Similarities between the behaviour of $\kappa_{el}(T)$ and the temperature dependence of the Hall concentration ($n_H = 1/(eR_H)$), that is shown in the same inset, support this conclusion. On the contrary, in YBCO κ_{el} and n_H both decrease with decreasing temperature from 300 to 100 K [21] and this is discussed in terms of a rapid change in the EDOS due to the pseudogap.

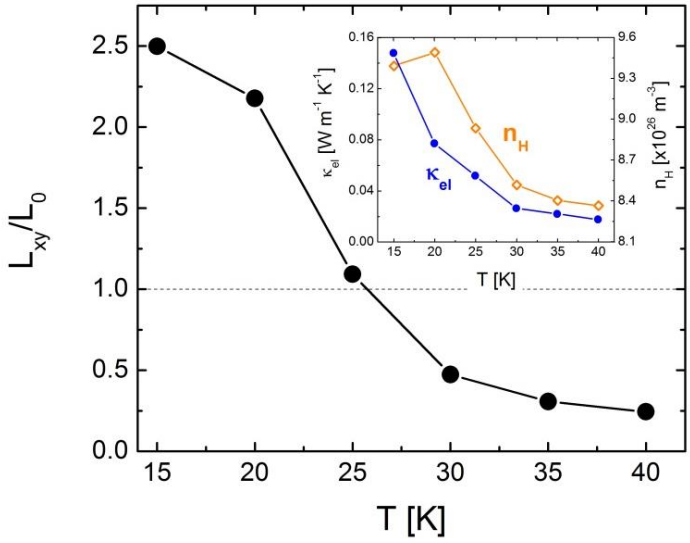

Figure 11: Temperature dependence of the ratio L_{xy}/L_0 from 15 to 40K. Inset: temperature dependence between 15 and 40 K of κ_{el} calculated as $\kappa_{el} = L_{xy}\rho/T$ and $n_H = 1/eR_H$.

In conclusion, from Figure 11 we would infer that the enhanced value of L_{xy}/L_0 could be due to a redistribution in the EDOS, although the temperature dependence of κ_{el} and $n_H$seem not to be compatible with the presence of a pseudogap. Above 25 K, the reduction of the L_{xy}/L_0 ratio down to 0.25 could be due to *ee* scattering.

4.3.2 Magnetoresistance analysis

As already presented, the magnetoresistance (MR) of the L2 sample (shown in Figure 3a) is quadratic in B. In Chapter 1 and Chapter 2 we argued that if ρ is proportional to $1/\tau_{tr}$, a plot of $\Delta\rho/\rho$ vs $(B/\rho)^2$ should fall on a straight line with a slope that is independent of T. This is known as Kohler plot and it is obeyed in a large number of standard

metals, provided that changes in temperature or purity simply alter $\tau_{tr}(T)$ by the same factor.

In Figure 12, we show the MR $(\rho(B) - \rho(0))/\rho(0) = \Delta\rho/\rho_0$ of the L2 sample as a function of B^2/ρ_0^2 with B between 0 and 9T. It is clear that Kohler's rule is violated below 45 K. Instead of a single curve, we obtain lines whose slope decreases with increasing T and only the T=45K, 60K and 80K almost overlap. Interestingly, this is the temperature region where magnetoresistance is constant with temperature (see Figure 3b).

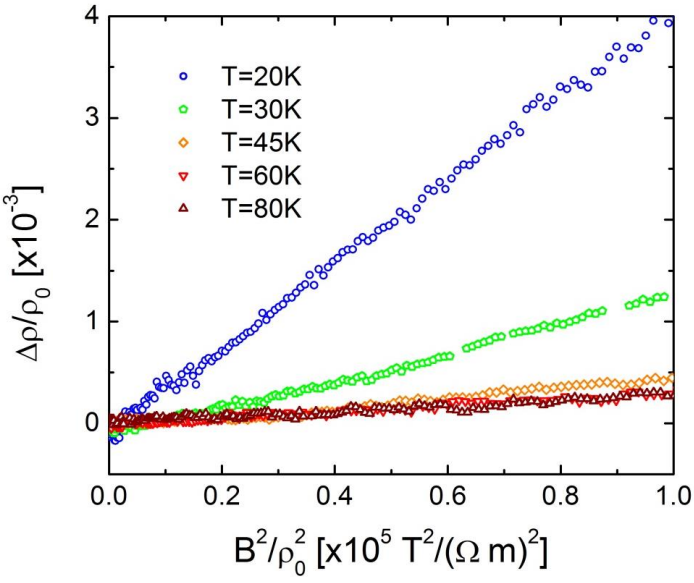

Figure 12: Kohler plot for the L2 crystal of Bi-2201 at temperatures between 20 and 80 K.

In ref. [29] it has been measured the normal-state MR of 90-K and 60-K YBCO and LSCO in the longitudinal and transverse geometries. In all cases, the orbital component of the MR displays a temperature dependence which strongly violates Kohler's rule. However, contrary to

the long-standing view that Kohler's rule is strongly violated in underdoped cuprates, in ref. [30] it is found that it is satisfied in the pseudogap phase of Hg-1201. Furthermore, Kimura et al. [31] focused on the in-plane MR of the overdoped and optimally doped regions of LSCO. By extending the MR measurements over a wide temperature range, they reported the validity of the classical Kohler's rule in the overdoped normal metal phase. In contrast to the Kohler scaling behaviour in the overdoped sample, MR for the optimally doped samples cannot be simply scaled by (B/ρ_0). At high temperatures the MR curves more or less fall onto the same single line whereas at low temperatures the MR curves deviate upwards from those at high temperatures. This deviation becomes more significant as the temperature approaches the optimal composition. The authors suggested that the violation of the Kohler's rule in superconducting LSCO is largely due to a superconducting fluctuation. Since the phenomenology reported in ref. [31] is similar to our results (Figure 12) it is reasonable to assume that superconducting fluctuations play a role also in Bi-2201. However in section 4.2.1 we discussed that we measured a *B*-linear magnetoresistance only at 15 K and that this could be related to the proximity to the superconducting transition. In addition, from the magnetic field dependence of N (see section 4.2.2) we confined the contribution of superconducting vortices below 20 K. At this stage we therefore suggest the presence of an (unknown) contribution which enhances the magnetoresistance in the range 20-40K.

4.3.3 Seebeck effect analysis

We already observed that the measured S is negative (Figure 6) whereas R_H is positive (inset of Figure 4). This is in contrast with the simple

prediction of the semiclassical theory (section 2.5 in Chapter 2) that the thermopower has the carrier sign. Nevertheless, in Figure 13 we report the measured S (black dots) compared with the calculated S from the Mott formula $S_{2D}{}^{(e/h)} = (-/+)\frac{1}{6}\frac{\pi^2}{e}\frac{k_B^2 T}{\epsilon_F}$ (eq. 2.56 in Chapter 2) for holes (red filled dots) and electrons (red empty dots). In particular, we consider the 2D expression of the Fermi energy $E_F = \pi\hbar^2 n_{2D}/m^*$ (inset of Figure 13), where $n_{2D} = n \cdot c_{axis}$ is the 2D density of carriers. We estimate the (volume) density of carriers n from R_H as $n = 1/R_H e$ and multiply it by c_{axis}=24.6 Å [32] to get n_{2D}. Furthermore, we considered that $m^* \sim 5m_e$ from quantum-oscillation experiments performed on single crystals of Tl-2201 [33]. Interestingly, Figure 13 shows that even if the measured S is not linear in T, its values are quite well reproduced by the Mott expression for electrons, in particular at low temperatures.

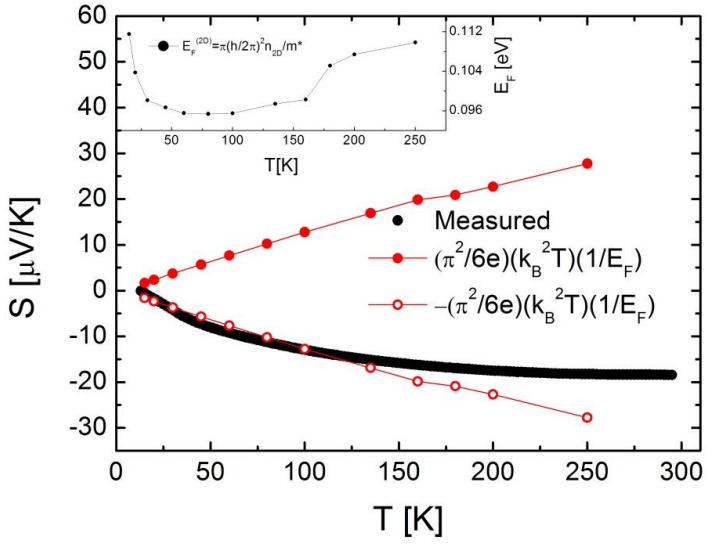

Figure 13: Temperature dependence of Seebeck effect from 13 to 300 K (black line). Red filled (empty) bullets represent the Mott expression for S for holes (electrons) carriers. Inset: calculated 2D expression for the Fermi energy E_F.

4.3.4 Nernst effect analysis

We already pointed out that in hole-doped cuprates the divergency of the Nernst signal N which occurs when $T \to T_c$ is due to the contribution of the superconducting vortices (N_s). N_s is futher characterized by its markedly non linear magnetic field dependence, in contrast to the signal of the charge carriers (N_n), which is expected to be B-linear ($N^{(e/h)} = B\frac{\pi^2}{3}\frac{k_B^2 T}{e}\frac{\mu}{\epsilon_F}$, eq. 2.66). From Figure 7 we confined the presence of N_s below 20 K and we discussed that the enhancement of N above 20 K should be due to another anomalous mechanism we identified with N_a. In order to investigate this effect, we estimate the Peltier coefficients. Given the measured temperature dependences of ρ_{xx}, ρ_{xy}, S and N, in analogy to the Ba-122 case (Chapter 3), we can estimate $\alpha_{xx} = \frac{S\rho_{xx} - N\rho_{xy}}{\rho_{xx}^2 + \rho_{xy}^2}$ and $\alpha_{xy} = \frac{S\rho_{xy} + N\rho_{xx}}{\rho_{xx}^2 + \rho_{xy}^2}$ (eq. 2.30 and 2.31 respectively) of our compound.

Figure 14a shows the temperature dependence of α_{xx} (black filled dots) and α_{xy} (empty black dots) from 15 to 250 K. It emerges that α_{xx} is negative in the temperature range considered, it reaches a maximum value of ~-1 V/K around 100 K and tends to zero for $T \to T_c$. α_{xy} (black empty dots) is more than 20 times smaller than α_{xx} and changes sign from negative to positive below 25 K. In ref. [34] it has already been discussed that α_{xy} may be written as a term α_{xy}^s due to the superconducting vortices that adds to a normal-state term α_{xy}^n. Therefore, we can relate the change of sign of α_{xy} (Figure 14a) to α_{xy}^s.

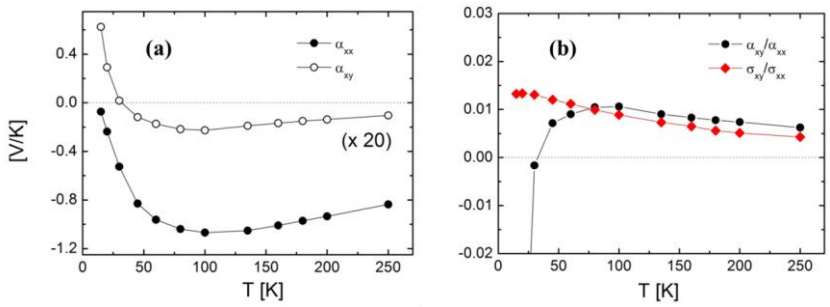

Figure 14: (a) Temperature dependence of the Peltier coefficients α_{xx} (black filled bullets) and α_{xy} (black empty bullets) from 15 to 250 K. α_{xy} is multiplied by a factor 20. (b) Temperature dependence of the Hall angle $\frac{\sigma_{xy}}{\sigma_{xx}}$ (red diamonds) and the thermal angle $\frac{\alpha_{xy}}{\alpha_{xx}}$ (black bullets) between 15 and 250 K.

Figure 14b shows the temperature dependence of the thermal angle $\frac{\alpha_{xy}}{\alpha_{xx}}$ (black filled bullets) and the Hall angle $\frac{\sigma_{xy}}{\sigma_{xx}}$ (red filled diamonds). They are nearly equal from 250 K down to 100 K, where we accordingly measured a small negative N (Figure 7). Below 75 K, the thermal and the Hall angles depart one from another, with the Hall angle almost saturating at ~0.01 whereas the thermal angle starts to diminish towards negative values. This behaviour is remarkable and evidences the presence of an anomalous contribution below 75 K.

In conclusion, with the analysis performed in this section we were able to discuss some features of the data presented in section 4.2. In particular: (i) from the values of L_{xy} we discussed a possible redistribution of the electronic density of states below 25 K (L_{xy}>L_0), supported by the similar T-behaviour of κ_{xy} and n_H.; (ii) the Kohler rule is violated below 40 K where the magnetoresistance decreases as T^{-4}; (iii) the low-temperature values of S are quite well reproduced by the Mott formula for the electrons; (iv) the Nernst effect exhibits the vortex contribution below 20 K, but it remains anoumalously enhanced also at higher temperatures; (v) the transversal Peltier coefficient α_{xy}

changes sign around 25 K from negative to positive by lowering *T* and this can be due to the vortices contribution; (vi) by comparing the Hall angle $\frac{\sigma_{xy}}{\sigma_{xx}}$ with the thermal angle $\frac{\alpha_{xy}}{\alpha_{xx}}$ we observed similar positive values from 250 K to 75 K. Below this temperature the Hall angle almost saturates at ~0.01, whereas the thermal angle rapidly diminishes towards negative values. This deviation is remarkable and could evidence the presence of an anomalous contribution in the Nernst effect below 75 K.

However, this analysis is not exhaustive for the Bi-2201 compound and many issues have still to be addressed. For instance, as discussed in Chapter 1, it is not possible to analyse the T-linear electrical resistivity (Figure 2) and the cotangent of the Hall angle (Figure 5) by means of the standard Boltzmann scenario.

In the next section we will try a completely different and innovative approach to the data analysis, starting right from the electrical reaistivity and the cotangent of the Hall angle.

4.4 Comparison with holographic formulae

For a highly correlated fluid, the interactions are large and so probably cannot be treated using any fundamentally perturbative approach which starts with a free particle description, as for the Fermi-Liquid theory. There is a well-developed and extremely successful theoretical solution of this problem applicable to one-dimensional and quasi-one-dimensional electron fluids based on “bosonization”, but no such approach exists in higher dimensions. In this context, it is important to seek new approaches – theories that honestly treat the strong correlation physics – even if the connection to the relevant microscopic physics is

unclear. This is where the mathematics of string theory may help: with the holographic duality, one can address the physics of strongly interacting finite density systems. Since 2007, the properties of matter at finite density have been central focus of this "holography" research [35]. In Chapter 2 we reported the dependence of transport coefficients (electric, thermal and thermoelectric) on temperature and magnetic field which have been predicted by mean of the holographic theory for those systems where the Fermi liquid picture fails [36, 37]. We already noted that the the six calculated transport coefficients depend only on four parameters: two thermodynamical variables ρ (charge density) and s (entropy density) and two dynamical parameters σ_Q (a characteristic quantum conductivity) and $\frac{\tau}{\mathcal{E}+P}$ (the ratio between the explicit momentum dissipation rate and the sum of the energy density and the pressure of the electronic plasma).

We therefore need four phenomenological entries to determine the transport properties of the system. In particular, we start the analysis considering the density of carriers obtained from the Hall coefficient R_H, the electric resistivity ρ_{xx}, the cotangent of the Hall angle $\cot\theta_H$ and the Seebeck effect S to get some information about the parameters ρ (density of charge), the ratio $\frac{\tau}{\mathcal{E}+P}$, σ_Q (quantum conductivity) and s (entropy density). We will then compare our predictions with the measured magnetoresistance, Nernst coefficient N and transverse thermal conductivity κ_{xy}.

As a first step, we would like to find which is the leading order for our parameters in the $T \to 0$ limit and to check if a coherent picture can be derived. Figure 15 shows the temperature dependence of the 2D carrier density we already calculated as $n_H^{(2D)} = (1/R_H)c_{axis}$ (see section 4.3.1) between 15 and 250 K. It can be noted that this quantity does not

change much in the range of temperature considered, showing a maximum variation of ~18% between 15 and 75 K. It is therefore reasonable to assume a constant density ρ (supposing that $\rho = n_H^{(2D)} e$, with e being the elementary charge).

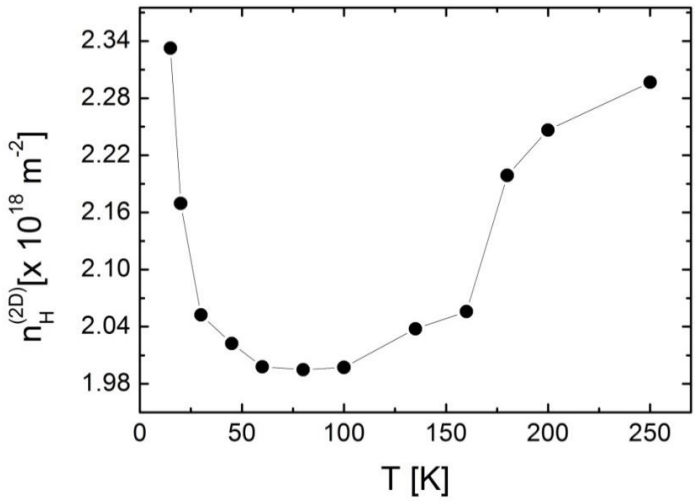

Figure 15: Temperature dependence of $n_H^{(2D)}$ from 15 to 250 K.

In section 4.2.1 we discussed that ρ_{xx} is T-linear in a broad temperature range above T_C, whereas by plotting cotgθ_H in a bi-log scale we observed that it is $\propto T^{1.66}$. Figure 16 reports ρ_{xx} (panel (a)) and cotg θ_H at B=9T (panel (b)) fitted with a linear and a power $T^{1.66}$ polynomyal, respectively (red curves). We see that both the linear part of ρ_{xx} and cotg θ_H tend to a constant $\neq 0$ when $T \to 0$.

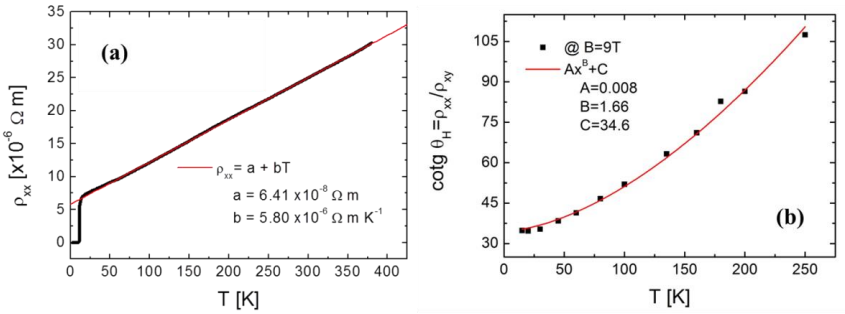

Figure 16: (a) Temperature dependence of the electric resistivity $\rho_{xx}$with the linear fit $\rho_{xx} = a + bT$ (red line). (b) Temperature dependence of the cotangent of the Hall angle $\text{cotg}\,\theta_H = \rho_{xx}/\rho_{xy}$ with the power fit $\text{cotg}\,\theta_H = AT^{1.66} + C$ (red line).

As already reported in Chapter 1, expanding the holographic formulae $\sigma_{xx} = \frac{\mathcal{E}+P}{\tau}\frac{\rho^2+\sigma_Q\left(B^2\sigma_Q+\frac{\mathcal{E}+P}{\tau}\right)}{B^2\rho^2+\left(B^2\sigma_Q+\frac{\mathcal{E}+P}{\tau}\right)^2}$ and $\sigma_{xy} = \rho B\frac{\rho^2+\sigma_Q\left(B^2\sigma_Q+\frac{\mathcal{E}+P}{\tau}\right)}{B^2\rho^2+\left(B^2\sigma_Q+\frac{\mathcal{E}+P}{\tau}\right)^2}$ (eq. 2.83)

at low B, we obtain:

$$\sigma_{xx} \sim \sigma_Q + \sigma_D, \qquad \sigma_{xy} \sim \frac{B\sigma_D}{\rho}(\sigma_Q + \sigma_D) \tag{4.1}$$

from which:

$$\text{cotg}\,\theta_H = \frac{\sigma_{xx}}{\sigma_{xy}} \sim \frac{\rho}{B\sigma_D} \tag{4.2}$$

and

$$\rho_{xx} = \frac{\sigma_{xx}}{\sigma_{xx}^2+\sigma_{xy}^2} \sim \frac{1}{\sigma_{xx}} \sim \frac{1}{\sigma_D+\sigma_Q} \tag{4.3}$$

where $\sigma_D = \frac{\rho^2\tau}{\mathcal{E}+P}$. Since we found that $\text{cotg}\,\theta_H \to C$ when $T \to 0$ (Figure 16b), from eq. 4.2 it follows that the leading order for σ_D is a constant value when $T \to 0$. With this in mind, from eq. 4.3 it comes out that also σ_Q has to tend either to a constant or to zero in order to fulfil that the linear part of ρ_{xx} tends to a constant when $T \to 0$ (Figure 16a).

We therefore fix that in the low field limit, for $T \to 0$, the leading order of σ_D should be a constant, while σ_Q can either tend to zero or a constant value.

We can also try to predict the temperature behaviour of the magnetoresistance and compare such prediction with our experimental data. Reminding the definition of the magnetoresistance $\frac{\Delta\rho_{xx}}{\rho_{xx}} = \frac{\rho_{xx}(B)-\rho_{xx}(0)}{\rho_{xx}(0)}$, from the holographic expressions of σ_{xx} and σ_{xy}, after some algebra it is possible to obtain:

$$\frac{\Delta\rho_{xx}}{\rho_{xx}} = B^2 \frac{\sigma_Q^3}{\sigma_D} \frac{1}{\rho^2+\rho^2\left(\frac{\sigma_Q}{\sigma_D}\right)^2+\rho^2\frac{\sigma_Q}{\sigma_D}+B^2\sigma_Q^2} \tag{4.4}$$

Eq. 4.4 shows that the magnetoresistance depends on σ_Q and σ_D. Therefore, it should tend either to a constant or to zero when $T \to 0$. Interestingly, from Figure 3b it emerges that $\frac{\Delta\rho_{xx}}{\rho_{xx}}$ at 9 T is constant in temperature above 40 K while it is quadratic in B, as predicted by eq. 4.4.

Therefore, we think about a scenario where there is a constant contribution satisfying the $T \to 0$ limit of eq. 4.4 and another (unknown) contribution which enhances the magnetoresistance below 40 K. We also recall that the Kohler rule is not fulfilled below this temperature, as discussed in section 4.3.2.

Let's now focus on the remaining parameter, namely the density of entropy s. Considering the Seebeck coefficient $S \sim \frac{\alpha_{xx}}{\sigma_{xx}}$, in order to obtain its low field expression, we first have to derive the expressions

for $\alpha_{xx} = \rho s \frac{\mathcal{E}+\mathrm{P}}{\tau} \frac{1}{B^2\rho^2+\left(B^2\sigma_Q+\frac{\mathcal{E}+\mathrm{P}}{\tau}\right)^2}$ (eq. 2.84) in the low field limit. It reads:

$$\alpha_{xx} \sim \frac{s\sigma_D}{\rho} \tag{4.5}$$

Reminding that $\sigma_{xx} \sim \sigma_Q + \sigma_D$, putting eq. 4.5 in $S \sim \frac{\alpha_{xx}}{\sigma_{xx}}$, we get the low field expression for S:

$$S \sim \frac{s\sigma_D}{\rho} \frac{1}{\sigma_D+\sigma_Q} \tag{4.6}$$

Therefore, in the $T \to 0$ limit, the temperature dependence of S should be the same of s. The inset of Figure 17 shows the temperature dependence of $-S$ in bi-log scale from 15 to 300 K. ($S(T)$ is shown in Figure 17 for reference). With increasing temperature, $-S$ shows a decreasing slope so that $S(T)$ cannot be reproduced by a single power of T in the considered temperature range. However, we see that at $T \to 0$, S tends to a positive value with a slope which is ~2. According to eq. 4.6, this should be the temperature dependence of s in the low T limit.

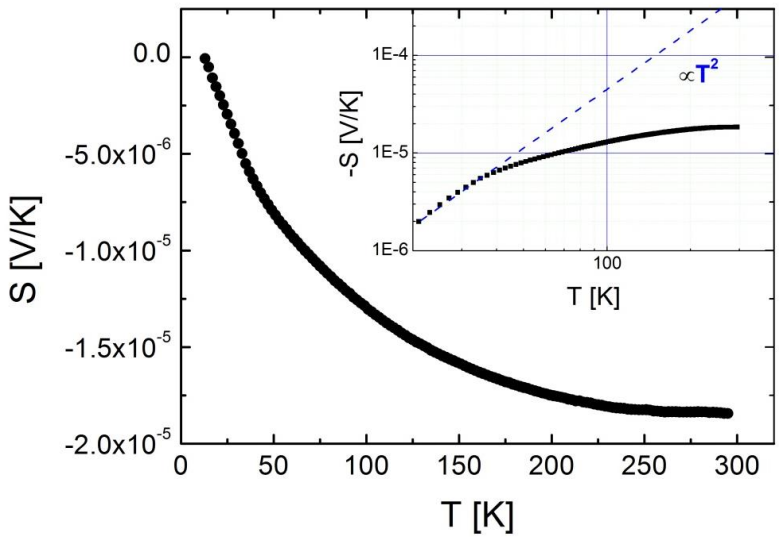

Figure 17: Temperature dependence of the Seebeck effect S from 10 to 300 K (black dots) Inset: bi-logarithmic plot of $-S$. The curve is compared with a dashed blue line which is proportional to T^2.

If our analysis is consistent, at this point we should be able to be predict the scaling of the Nernst coefficient N and the transverse thermal conductivity κ_{xy}. In the previous section we discussed that N is influenced by the superconducting vortices below 20 K and we will therefore consider it above this temperature. Given that

$$N = \frac{\alpha_{xy}}{\sigma_{xx}} - S\frac{\sigma_{xy}}{\sigma_{xx}} \sim \frac{\alpha_{xy}}{\sigma_{xx}} - \frac{\alpha_{xx}\sigma_{xy}}{\sigma_{xx}^2} \tag{4.7}$$

where the first equality is eq. 2.29 whereas the second follows from taking $S \sim \frac{\alpha_{xx}}{\sigma_{xx}}$, to obtain the low field expression for N, we first have to derive the expression of $\alpha_{xy} = sB\frac{\rho^2 + \sigma_Q\left(B^2\sigma_Q + \frac{\mathcal{E}+P}{\tau}\right)}{B^2\rho^2 + \left(B^2\sigma_Q + \frac{\mathcal{E}+P}{\tau}\right)^2}$ (eq. 2.84) in the low field limit. It reads:

$$\alpha_{xy} \sim sB\frac{\sigma_D}{\rho^2}(\sigma_D + \sigma_Q) \tag{4.8}$$

Putting eq. 4.1, 4.6 and 4.8 into eq. 4.7 we finally get the expression for N in the low field limit:

$$N \sim sB\frac{\sigma_D}{\rho^2}\left(1 - \frac{\sigma_D}{\sigma_D + \sigma_Q}\right) \tag{4.9}$$

From eq. 4.9, taking into account that σ_D tends to a constant and σ_Q either to a constant or zero in the $T \to 0$ limit, it follows that N has the same temperature dependence as s (and S) when $T \to 0$. On the contrary, the inset of Figure 18 reports N in a bi-log scale between 25 and 90 K (which is the range where $N > 0$ and it is then possible to put it in a bi-log scale). The data seem to be well reproduced by a power law $\propto T^{-2}$ (blue dashed line). This divergent behavior with decreasing temperature could not be accepted for the T-dependence of the entropy and in particular is not compatible with our prevision that $s \propto T^2$.

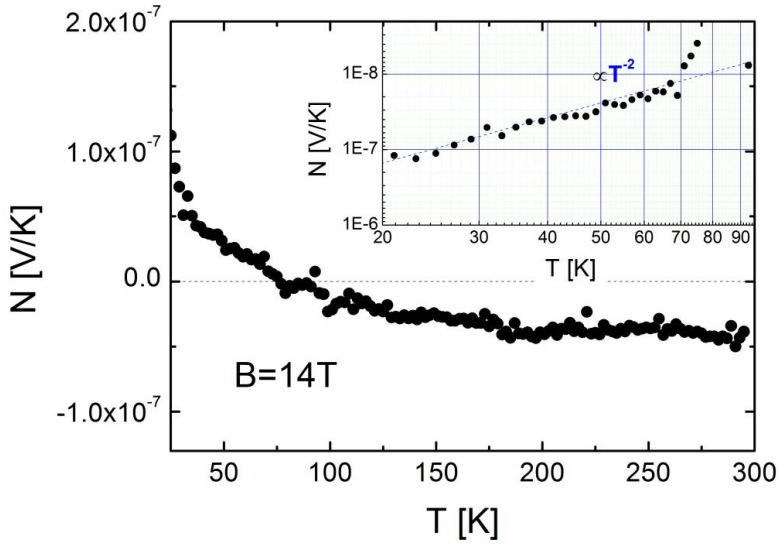

Figure 18: Temperature dependence of the Nernst coefficient N from 25 to 300 K (black dots). Inset: bi-logarithmic plot of $-S$. The curve is compared with a dashed blue line which is proportional to T^{-2}.

Considering Figure 14b, we already supposed that the divergent behaviour of N can be caused by an anomalous contribution which causes the thermal angle to depart from the Hall angle.

Let's finally consider the transverse thermal conductivity $\bar{\kappa}_{xy} = \frac{B\rho s^2 T}{B^2\rho^2+\left(B^2\sigma_Q+\frac{\mathcal{E}+P}{\tau}\right)^2}$ (eq. 2.85). Its low field expression reads:

$$\kappa_{xy} \sim \frac{BT}{\rho^3}\sigma_D^2 s^2 \tag{4.10}$$

where we supposed that $\bar{\kappa}_{xy} \sim \kappa_{xy}$. Remarkably, from Figure 9b it results that $\kappa_{xy} \propto T^{-2.9}$ and, taking into account that $\sigma_D \rightarrow$ constant when $T \rightarrow 0$, from eq. 4.10 we obtain $s \propto T^{-1.9}$ in the $T \rightarrow 0$ limit. Therefore, in order to fit κ_{xy}, we again find a divergent s when $T \rightarrow 0$. Interestingly, this is almost the same divergent temperature dependence we obtained from N ($\sim T^{-2}$). This could mean that κ_{xy} is affected by the same mechanism which causes N to be divergent at low temperatures. In addition, this contribution cannot be described within a holographic scenario, since it leads to a divergent s.

In conclusion, we found that, at leading order, σ_D should tend to a constant which is different from zero and that σ_Q has to tend to a constant which can be also zero. Such scenario leads to the prediction of a constant (or zero) magnetoresistance when $T \rightarrow 0$. This is compatible with the temperature dependence of the magnetoresistance measured above 40 K, whereas the experimental curve is $\propto T^{-4}$ below this temperature. Considering the Seebeck coefficient we found a density of entropy (s) which is $\propto T^2$ when $T \rightarrow 0$. However, such behaviour is not compatible with both the Nernst effect and the transverse thermal conductivity, from which it would emerge that s diverges as $\sim T^{-2}$ when $T \rightarrow 0$. At this stage, we suppose the presence of an unknown

contribution which (i) affects the magnetoresistance, (ii) causes N to be anomalously enhanced and this anomaly is compatible with the temperature dependence of the transverse thermal conductivity. This unknown contribution cannot be described within an explicit momentum-dissipation approach.

4.4.1 New insights: charge ordering in Bi-2201

In recent times, there have been strong experimental evidences that in cuprates the electrons tend to form superstructures unrelated to the underlying ionic lattice. Indeed, charge density wave orders have been observed in all the phase diagram of many different cuprates: early evidence of charge order (CO) had come from La-based cuprates, where charge "stripes" were observed near the doping level p=1/8 holes per Cu [38,39,40]. More recently, resonant X-ray scattering (RXS) experiments revealed incommensurate charge order competing with superconductivity also in $YBa_2Cu_3O_{6+x}$ (Y123) and in Hg- and Bi-based cuprates [41]. Furthermore, in [42] it is suggested that the behaviour of optical conductivity at optimal doping in strange metals could originate from quantum critical CDW modulations. It is questioned to what extent CO competes or intertwines with superconductivity, because the phenomenology is still incomplete.

Very recently, in ref. [43] experimental evidences of charge order (CO) have been reported in overdoped Sr-Bi-2201 with correlation length of 40-60 lattice units, that persist up to temperatures of at least 250 K. They performed resonant inelastic X-ray scattering (RIXS) that display sharp, incommensurate diffraction peaks in overdoped Bi-2201 over a wide range of doping levels. These peaks show properties similar to

those of the charge density modulation signal in RXS observed in underdoped cuprates; therefore, they had been assigned to CO. The continued decrease of the CO vector modulus versus increasing doping points to a picture where CO would be ubiquitous across the entire phase diagram of *p*-doped Bi-2201.

From the theoretical point of view the presence of charge modulation in the strange metal regime motivates studying quantum critical phases with spontaneously broken translations in addition to the explicit momentum-dissipation we discussed above. In this sense, Dr. A. Amoretti (University of Genova) is actively working to add possible electronic textures of the CO state to the holographic formulae discussed in the previous section. This could be relevant to understand the possible origin of the anomalous contribution we discuss in the previous section. In particular, we are thinking about a scenario where below a certain temperature, the explicit momentum dissipation is not enough to model the system due to the presence of CO. At the moment, only the electric conductivity is available and reads [44]:

$$\sigma_{xx} = \sigma_Q + \frac{\rho^2}{\epsilon+P}\frac{\Omega}{\Gamma\Omega+\omega_0} \tag{4.11}$$

where Γ is the explicit momentum dissipation rate (τ in eq. 2.83-2.85), whereas Ω and ω_0 are two characteristic frequencies due to the further spontaneous breaking of translations in presence of a CO. Interestingly, these two frequencies can be divergent in the $T \to 0$ limit without the violation of any physical law. Hence, there is hope that the divergence we found in s (from the Nernst coefficient and the thermal conductivity) might be reabsorbed by one of these quantities. To develop these ideas more quantitatively, we have to wait for the other transport coefficients to be calculated including the CO. When this will be completed, the

complete set of data collected on Bi-2201 will be of great help to test the formulae and this comparison could potentially constitute an alternative approach to confirm the presence of CO in the optimal doped region of Bi-2201.

References

[1] S. Martin, A. T. Fiory, R. M. Fleming, L. F. Schneemeyer, and J. V. Waszczak, Phys. Rev. B 41, Phys. Rev. B 41, 846(R) (1990)
[2]B. Keimer, S. A. Kivelson, M. R. Norman, S. Uchida & J. Zaanen, Nature volume 518, pages 179–186 (2015)
[3] M. Onoda, M. Sato, Solid State Commun., 67, p. 799 (1988)
[4] N. R. Khasanova, E. V. Antipov, Physica C: Superconductivity, 246, p. 241-252 (1995)
[5]A. Piriou, E. Giannini, Y. Fasano, C. Senatore, and Ø. Fischer, Phys. Rev. B 81, 144517 (2010)
[6] A. Maeda *et al.*, Phys. Rev. B 41, 6418 (1990)
[7] R. Jin, H.R. Ott, and D.P. Grindatto, Physica C **250**, 395 (1995)
[8] A.P. Mackenzie *et al.*, Phys. Rev. B **45**, 527 (1992)
[9] Y. Ando *et al.*, Phys. Rev. Lett. **77**, 2065 (1996); **79**, 2595 (E) (1997)
[10] S. Martin *et al.*, Phys. Rev. B **41**, 846 (1990)
[11] Yoichi Ando and T. Murayama, Phys. Rev. B 60, R6991(R) (1999)
[12] A. Mourachkine "Room-Temperature Superconductivity" (Cambridge International Science Publishing, (2004)
[13] P. B. Allen, W. E. Pickett, and H. Krankauer, Phys. Rev. B 37, 7482 (1988)
[14]Y. Wang, Lu Li, and N. P. Ong, Phys. Rev. B 73, 024510 (2006)
[15] Uher, C., Liu, Y. & Whitaker, J.F., J. Supercond. 7: 323 (1994)
[16]J. Bardeen, G. Rickayzen, and L. Tewordt, *Phys. Rev.* 113, 982 (1959)
[17] K. Krishana, N. P. Ong, Q. Li, G. D. Gu, and N. Koshizuka, Science 277, 83 (1997)
[18] Y. Ando, J. Takeya, Y. Abe, K. Nakamura, and A. Kapitulnik, Phys. Rev. B 62, 626 (2000)
[19] X. F. Sun, S. Ono, X. Zhao, Z. Q. Pang, Yasushi Abe, and Yoichi Ando, Phys. Rev. B 77, 094515 (2008)
[20] Y. Zhang, N. P. Ong, Z. A. Xu, K. Krishana, R. Gagnon, and L. Taillefer, Phys. Rev. Lett., vol. 84, (2000)

[21] Matusiak, M., Rogacki, K., and Veal, B. W., EPL, vol. 88, no. 4, p. 47005, (2009)
[22] Peacor S. D., Richardson R. A., Nori F. and Uher C., Phys. Rev. B, 44 9508 (1991)
[23] Allen P. B., Du X., Mihaly L. and Forro L., Phys.Rev. B, 49 9073 (1994)
[24] Ikebe M., Fujishiro H., Nakasato K. and Noto K., Physica C, 263 309 (1996)
[25] Cyril Proust, Kamran Behnia, Romain Bel, Duncan Maude, and S. I. Vedeneev, Phys. Rev. B 72, 214511 (2005)
[26] Matusiak M. and Wolf T., Phys. Rev. B, 72 054508 (2005)
[27] Minami H., Wittorff V. W., Yelland E. A., Cooper J. R., Changkang Chen and Hodby J. W., Phys. Rev.B, 68 220503(R) (2003)
[28] R.E. Peierls, "The Quantum Theory of Solids" (Oxford University Press, 1955)
[29] J. M. Harris, Y. F. Yan, P. Matl, N. P. Ong, P.W. Anderson, T. Kimura, and K. Kitazawa, Phys. Rev. Lett. 75, 1391 (1995)
[30] M. K. Chan, M. J. Veit, C. J. Dorow, Y. Ge, Y. Li, W. Tabis, Y. Tang, X. Zhao, N. Barišić, and M. Greven, Phys. Rev. Lett. 113, 177005 (2014)
[31] T. Kimura, S. Miyasaka, H. Takagi, K. Tamasaku, H. Eisaki, S. Uchida, K. Kitazawa, M. Hiroi, M. Sera, and N. Kobayashi, Phys. Rev. B 53, 8733 (1996)
[32]A. I. Beskrovnyi; I. G. Shelkova; S. Durčok; J. Hejtmánek; Z. Jirák; E. Pollert , Physica C: Superconductivity, 222, 3, 375-385 (1994)
[33] A. F. Bangura, P. M. C. Rourke, T. M. Benseman, M. Matusiak, J. R. Cooper, N. E. Hussey, and A. Carrington
Phys. Rev. B 82, 140501(R) (2010)
[34] Y. Wang, Z. A. Xu, T. Kakeshita, S. Uchida, S. Ono, Y. Ando and N. P. Ong, Phys. Rev. B 64, 224519 (2001)
[35] Zaanen, J., Sun, Y. W., Liu, Y.& Schalm, K. "Holographic Duality for Condensed Matter Physics" (Cambridge Univ. Press, 2015)
[36] S. A. Hartnoll and A. Karch, "Scaling theory of the cuprate strange metals," Phys. Rev.B, vol. B91, (2015)
[37] A. Amoretti, A. Braggio, N. Maggiore & N. Magnoli, Advances in Physics: X, 2:2, 409-427 (2017)
[38] Tranquada, J. M., Sternlieb, B. J., Axe, J. D., Nakamura, Y. & Uchida, S., *Nature* **375**, 561–563 (1995).
[39] Fujita, M., Goka, H., Yamada, K. & Matsuda, M. *Phys. Rev. Lett.* **88**, 167008 (2002).
[40] Abbamonte, P. et al., *Nat. Phys.* **1**, 155–158 (2005).
[41] 7. Chang, J. et al.*Nat. Phys.* **8**, 871–876 (2012); Blanco-Canosa, S. et al. *Phys. Rev. B* **90**, 054513 (2014); Gerber, S. et al., *Science* **350**, 949–952 (2015); Chang, J. et al.*Nat. Commun.* **7**, 11494 (2016); Tabis, W. et al., *Nat.*

Commun. **5**, 5875 (2014); Hashimoto, M. et al., *Phys. Rev. B* **89**, 220511(R) (2014).
[42] L. V. Delacretaz, B. Gouteraux, S. A. Hartnoll and A. Karlsson, SciPost Phys. 3 (2017) 025
[43] Y. Y. Peng, R. Fumagalli, Y. Ding, M. Minola, S. Caprara, D. Betto, M. Bluschke, G. M. De Luca, K. Kummer, E. Lefrançois, M. Salluzzo, H. Suzuki, M. Le Tacon, X. J. Zhou, N. B. Brookes, B. Keimer, L. Braicovich, M. Grilli & G. Ghiringhelli, Nature Materials 17, 697–702 (2018)
[44] A. Amoretti, D. Areán, B. Goutéraux, and D. Musso, Phys. Rev. Lett. 120, 171603 (2018)

Conclusions

The discovery of high-temperature (high-T_c) superconductors in 1986 demonstrated that there must be some – still unknown – mechanisms that underpin superconductivity other than phonon coupling. Rather, the coexistence and/or proximity of superconductivity to other states such as antiferromagnetism, charge order, pseudogapped or strange metal phase, is a fundamental point to start looking for what brings superconductivity out. In addition, these states are characterized by a plethora of emergent anomalous properties, ranging from the presence of Dirac fermions to the breakdown of Fermi liquid, which make them so fascinating and debated in modern condensed matter physics. In particular, I investigated the antiferromagnetic (AFM) phase of a parent compound of the 122 family of Iron based superconductors (IBS) and the strange metal regime of an optimal doped superconductor of the Bi-2201 family of cuprates (HTS) by means of electrical, thermal and thermoelectric transport properties measurements. Although in real materials the combined analysis of transport properties could be highly challenging due to multiband character, anisotropic electronic structure and physical mechanisms other than diffusive motion of carriers, each of these factors yields peculiar features in the temperature and magnetic field dependence of transport properties. This allows both the extraction of individual band parameters such as mobilities, effective masses, scattering times and to look for the main scattering mechanisms or signatures of exotic excitations like Dirac fermions. Moreover, from the detailed study of the electronic behaviour, the success or the failure of the Fermi liquid approach can be tested and discussed.

The magneto-transport, although very informative, is not very studied in literature, because of the tiny and elusive quantities which have to be investigated and the application of high magnetic fields allows to magnify them. During my PhD I had the opportunity to perform measurements in magnetic fields as high as 30 T at the High Magnet Laboratory of Nijmegen (The Netherlands) and up to 14 T at the IFW Dresden (Germany).The main aims of this work of thesis were two:

- to probe the electronic band structure of the IBS parent compounds by extracting meaningful quantities, namely the Peltier coefficients, which let disentangle the main transport mechanisms into play, despite the complexity of the multi-band nature which characterizes these compounds;
- to study the controversial strange metal phase of HTS in view of novel approaches developed in the context of emerging holographic theories, which address to and demand for the complete set of transport coefficient.

In Chapter 3 I discussed the investigation of the AFM phase of an annealed single crystal of $BaFe_2As_2$. Thanks to its exceptional quality and millimetric sizes, I could perform a complete characterization of its properties, both in-plane and out-of-plane. In order to access the Peltier coefficients α_{xx}, α_{xy} and α_{xz}, the complete set of transport properties is required. Hence, I performed longitudinal (ρ_{xx}) and transverse (ρ_{xy}, ρ_{xz}) resistivity, Seebeck (*S*) and Nernst (*N*) measurements as a function of magnetic field (*B*), for different field orientations, at selected temperatures. This characterization was performed at the Physics Department in Genova and the High Field Magnet Laboratory of Nijmegen. As remarkable results, I measured a large and anisotropic magnetic field dependence of *S* and a giant *N* in an extended temperature region. By combining all the transport coefficients, I

extracted α_{xy} and α_{xz}, obtained in the experimental configuration with B parallel or perpendicular to the crystalline c-axis, respectively. Interestingly, both α_{xy} and α_{xz} resulted anomalously large with $\alpha_{xy} \approx 2\,\alpha_{xz}$. Moreover, I found that their B-dependence is very well reproducible by a single-band model, which depends on the mobility μ and the Fermi energy E_F of the carriers, suggesting that one particular carrier species dominates the transport. I evaluated both μ and E_F as fit parameters of the α_{xy} curves, obtaining high values of μ (up to 10^3 $cm^2V^{-1}s^{-1}$) and small E_F ($\sim$11 meV). Similar values have been also extracted by fitting the α_{xz} curves. By comparing these numbers with quantum oscillations experiments on $BaFe_2As_2$, I identified the dominating band with an electron pocket (γ) located in a position of the band structure where Dirac cones had been experimentally confirmed by ARPES and infrared studies. In particular, the compatibility of both α_{xy} and α_{xz} with a Dirac-like dispersion pointed to a possible 3-dimensional nature of Dirac fermions in this compound, providing a clue in the still opened question whether Dirac fermions are 2- or 3-dimensional in the parent compounds of IBS.

Chapter 4 was dedicated to the transport properties of optimally doped single crystals of $Bi_2Sr_2CuO_{6+x}$, a cuprate superconductor of the Bi-2201 family. As a hole-doped cuprate, Bi-2201 shows a quantum critical region in the optimally doped part of its phase diagram characterized by a "strange metal" behaviour in its normal-state, which cannot be successfully described within the Fermi-liquid scenario. In addition, Bi-2201 shows relatively low values of critical temperature. Therefore, it presents an ideal stage for the systematic study of the normal-state properties down to lower temperatures.

In order to investigate the strange metal regime, I performed the electrical measurements at the Physics Department in Genova, whereas the thermoelectric and thermal characterizations were performed at IFW Dresden (Germany) with the support of a DAAD Scholarship (Research Grants Award – Short-term grants, 2017 (57314023)). This activity has been carried out in a strict collaboration with dr. A. Amoretti and prof. N Magnoli of the University of Genova.

As a first result, I observed some typical signatures of the Fermi-liquid breakdown, namely a *T*-linear ρ_{xx} in an extended temperature range and an anomalous *T*-dependence ($T^{1.66}$) of the cotangent of the Hall angle ρ_{xx}/ρ_{xy}. Remarkably, also the other transport properties showed a complex phenomenology with some anomalies explainable within a standard picture, such as the anomalous *B*-dependence of *N* for T<20 K and the sign change of α_{xy}, which are compatible with a contribution of the superconducting vortices below 20 K. However a comprehensive and exhausting explanation cannot be given within the Fermi liquid theory, which revealed to be inadequate to analyse the *T*-linear ρ_{xx}, the *T*-dependence of the Hall angle and the anomalous regime of *N* for *T*>20 K. Starting from these evidences, I tested a completely novel approach based on holographic formulae, which describes the transport coefficients of those strong correlated systems where the Fermi liquid fails. These formulae depend on four system-dependent parameters, which can be fixed by means of four experimentally measured properties. If the analysis is consistent, it should be then possible to predict the *T*-behaviour of the other transport coefficients. I fixed the $T \to 0$ limit of the parameters by means of the Hall coefficient, ρ_{xx}, the cotangent of the Hall angle and S. With these inputs, at low *T*, I predicted a constant magnetoresistance, $N \propto T^2$ and $\kappa_{xy} \propto T^4$. Unfortunately, in contrast to these outcomes, the magnetoresistance was

anomalously enhanced below 40 K and in the low temperature range also N and κ_{xy} give an unphysical divergent behaviour. The failure of this analysis led to the conclusion that the explicit momentum-dissipation approach implemented in the holographic model is probably not sufficient to describe the transport in the strange metal regime. Secondly, it is also suggestive that additional contributions, neglected in our treatment, could play an important role, such as the recently discovered charge ordering (CO) in Bi-2201. In this way, my findings also offer a fundamental experimental feedback to a completely novel theoretical method, whose potential is far to be completely explored and represents a pioneering attempt of testing new theories in order find a solution to unsolved problems in condensed matter physics, i. e. the strange metal regime in unconventional superconductors, where classical and standards theory failed.

In conclusion, simultaneous analysis of thermal, electric and thermoelectric properties is a powerful investigation tool of diffusive transport, which relies on, rather than being hindered by, the complex temperature and magnetic field dependence exhibited by real compounds, where multiple mechanisms may play a role, such as multiband character, presence of bands with different dispersion and dimensionality. Moreover, the complete set of transport properties provides a powerful test for new approaches to condensed matter physics.

A In-plane and out-of-plane properties of a $BaFe_2As_2$ single crystal

In Chapter 3 we showed and analysed the in-plane transport properties of a high quality 122 parent compound $BaFe_2As_2$ single crystal. Thanks to its millimetric dimensions it is further possible to probe its out-of-plane transport. In this Appendix we report in-plane and out-of-plane thermal, electric, thermoelectric and magnetic properties of the $BaFe_2As_2$ crystal. By comparing the electric properties with ab initio calculations, we discuss the observed anisotropies in the antiferromagnetic and non-magnetic phases in terms of electron, phonon and magnon band structures, as well as in terms of scattering mechanisms.

Experiment

To probe the in-plane and out-of-plane transport, the measurements were performed using two different configurations. In the in-plane set up (Figure A1a), we used a two-probe lead configuration with bar-shaped leads glued to the *yz* sides of the crystal to transfer a heat power *P* to the sample which creates a thermal gradient (ΔT_x) and a Seebeck voltage (ΔV_x) along the *x* direction. In the out-of-plane case (Figure A1b), we used a two-probe lead configuration with disk-shaped leads glued to the *xy* sides of the crystal. This set-up helps generating a

uniform thermal gradient along the *z* direction (ΔT_z) and we measured the Seebeck voltage (ΔV_z) along the same direction. Given the small size of the sample, the two probe configuration was affected by the thermal resistance of Cu leads connecting the thermometers to the sample which was in series with the sample thermal resistance. This caused an underestimation of thermal conductivity and Seebeck effect which are in inverse proportionality with the thermal gradient. The effect was quantitatively evaluated and the data corrected accordingly.

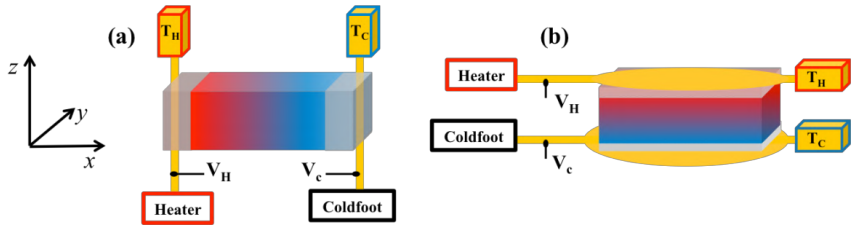

Figure A1: In-plane (a) and out-of-plane (b) measurement set-up. The heater, the hot thermometer (T_H) and the voltage probe (V_H) share one lead while the coldfoot, the cold thermometer (T_C) and the voltage probe (V_C) share the other lead. We used bar-shaped (a) and disk-shaped (b) leads glued to the *yz* sides and *xy* sides of the sample, respectively. (a) The thermal gradient $\Delta T_x=T_H-T_C$ and the voltage difference $\Delta V_x=V_H-V_C$ are measured along *x*. (b) The thermal gradient $\Delta T_z=T_H-T_C$ and the voltage difference $\Delta V_z=V_H-V_C$ are measured along *z*. The in-plane (out-of-plane) thermal conductivity $\boldsymbol{\kappa_x}$ ($\boldsymbol{\kappa_z}$) is defined as $\boldsymbol{\kappa_x = \frac{P}{\Delta T_x}\frac{x}{yz}}$ $\left(\boldsymbol{\kappa_z = \frac{P}{\Delta T_z}\frac{z}{xy}}\right)$, whereas the in-plane (out-of-plane) Seebeck coefficient $\boldsymbol{S_x}$ ($\boldsymbol{S_z}$) is defined as $\boldsymbol{S_x = \Delta V_x/\Delta T_x}$ ($\boldsymbol{S_z = \Delta V_z/\Delta T_z}$).

Magnetic susceptibility Figure A2 (upper panel) shows the temperature dependence of the in-plane (χ_x, black curve) and out-of-plane (χ_z, red curve) magnetic susceptibility between 5 and 300 K. In the magnetically disordered state ($T > T_N \sim$ 140 K), χ_x is larger than χ_z by a factor 1.2 and both curves increase linearly with temperature as widely reported for Ba-122 single crystals and pnictides in ref. [1] and

ref. therein. The different magnitude of χ_x and χ_z is ascribed to the anisotropic nature of Ba-122 system. Around T_N, both χ_x and χ_z decrease abruptly within less than 2 K. The remarkable sharpness of this transition is the fingerprint of the very high quality of the crystal under test. Both χ_x and χ_z diminish rapidly below T_N, almost saturate to $\sim 1.1\times10^{-4}$ at about 100 K and increase with decreasing temperature with a tiny Curie-like term. This contribution could be ascribed to a very low percentage of highly diluted paramagnetic impurities (i.e. well below the x-ray scattering detection threshold).

Electric resistivity Figure A2 (bottom panel) shows the temperature dependences of the in-plane and out-of-plane resistivities (ρ_x and ρ_z respectively). In the high temperature paramagnetic (PM) phase, $\rho_x(T)$ decreases with decreasing temperature, while $\rho_z(T)$ monotonically increases down to T_N. Below T_N, both ρ_x and ρ_z show a significant decrease. The small values of the residual resistivities (~15 μΩcm for ρ_x and ~35 μΩcm for ρ_z) indicate the high purity of the sample. In the inset of the bottom panel of Figure A2 the temperature dependence of the anisotropy ρ_z/ρ_x is reported. It is ~4 at room temperature, increases with decreasing temperature and reaches a maximum value of ~6 at T_N. Below T_N, the anisotropy starts to decrease and becomes ~2 at low temperatures.

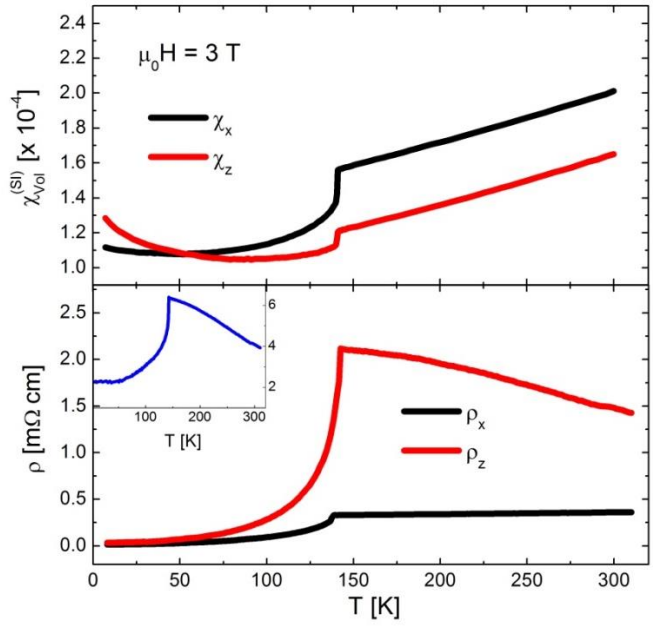

Figure A2: Upper panel: temperature dependence of the in-plane ($\boldsymbol{\chi_x}$, black curve) and out-of-plane ($\boldsymbol{\chi_z}$, red curve) magnetic susceptibility between 5 and 300 K with an applied field $\boldsymbol{\mu_0 H}$=3T. Bottom panel: temperature dependence of $\boldsymbol{\rho_x}$ (black curve, left axis) and $\boldsymbol{\rho_z}$ (red curve, right axis) between 5 and 300 K. Inset: temperature dependence of the anisotropy $\boldsymbol{\rho_z/\rho_x}$ in the same temperature range.

In ref. [2] ρ_x and ρ_z measured in a crystal of $BaFe_2As_2$ which underwent the same annealing process as our sample are reported. The data are in overall agreement with our measurements, apart from the low-temperature ρ_z/ρ_x which is around 1.6. In addition, optical spectroscopy experiments in ref. [3] reported plasma frequency and scattering time measurements from which a low temperature anisotropy ρ_z/ρ_x~1.4 can be estimated.

Thermal conductivity Figure A3 shows the temperature dependence of the measured in-plane (κ_x, upper panel) and out-of-plane (κ_z, bottom

panel) thermal conductivity. Interestingly, the two curves show almost the same temperature dependence, with κ_z being smaller than κ_x by a factor around 3 in the considered temperature range. In the PM state, both curves do not show significant temperature dependence. By lowering T, two features are present in both curves. Specifically, in correspondence of T_N the κ curves increase and exhibit a quite broad bump centred around 120 K extending down to 80 K. Below this temperature, a second bump centred around 50 K is evident and by further lowering T, the curves tend to zero.

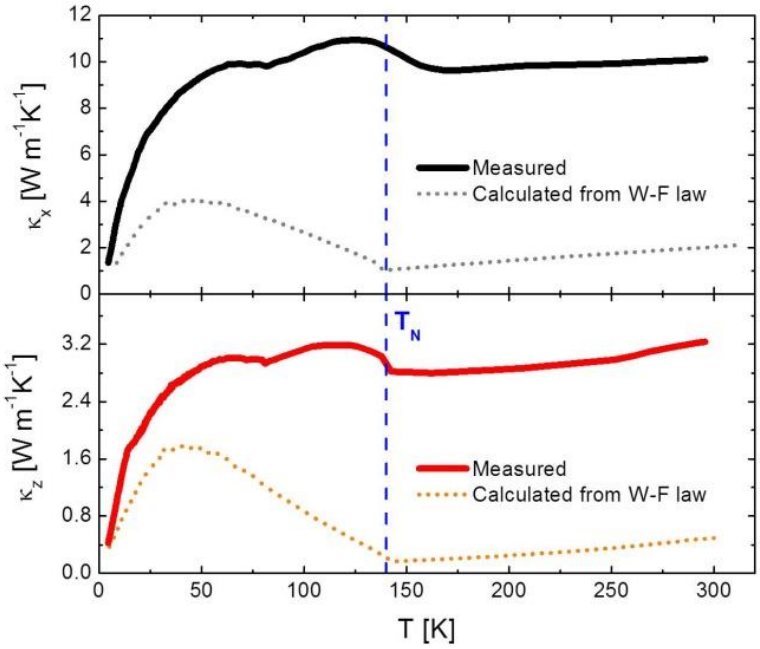

Figure A3: Temperature dependence of $\boldsymbol{\kappa_x}$ (black curve, upper panel) and $\boldsymbol{\kappa_z}$ (red curve, lower panel) between 5 and 300 K. The dotted curves represent the electronic contribution $\boldsymbol{\kappa_{el}}$ to $\boldsymbol{\kappa_x}$ (grey dotted curve, upper panel) and to $\boldsymbol{\kappa_z}$ (orange dotted curve, lower panel), estimated from the Wiedemann-Franz law from 5 to 300 K. The dashed blue line indicates $\boldsymbol{T_N}$, evaluated from magnetic susceptibility and electric resistivity (Figure A2).

The magnitude and the temperature dependence of κ_x above T_N is in substantial agreement with data reported for a single crystal of $BaFe_2As_2$ in ref. [5]. However, in the AFM phase, κ_x in ref. [5] does not show any significant change in the temperature dependence at T_N and only displays a single broad bump centred at 20 K. In addition, to our knowledge, no κ_z data have ever been reported for $BaFe_2As_2$.

Seebeck coefficient. Figure A4 (upper panel) shows the temperature dependence of S_x and S_z (black curve and red curve respectively). S_x increases almost linearly with negative sign from room temperature down to T_N, where an abrupt change of regime occurs. Here, it strongly diminishes and crosses zero around T=120 K. For T=90 K, S_x becomes again negative and it exhibits a broadened minimum centred around 40 K. On the other hand, S_z is negative at room temperature, but it decreases by lowering the temperature and crosses zero around T=186 K, reaching $\sim 16 \mu VK^{-1}$ immediately just above T_N. At T_N, it drastically falls down to $\sim -28 \mu VK^{-1}$ and the transition at T_N is much sharper than in S_x case. In the AFM state no broadened peaks exist and S_z goes monotonically to zero with temperature. In addition, it is worth to notice that the absolute value of S_z is generally larger than the absolute value of S_x. The temperature behaviour of S_x is in substantial agreement with previous reports on $BaFe_2As_2$ [4,5,6], whereas, we are not aware of previous S_z measurements in this compound.

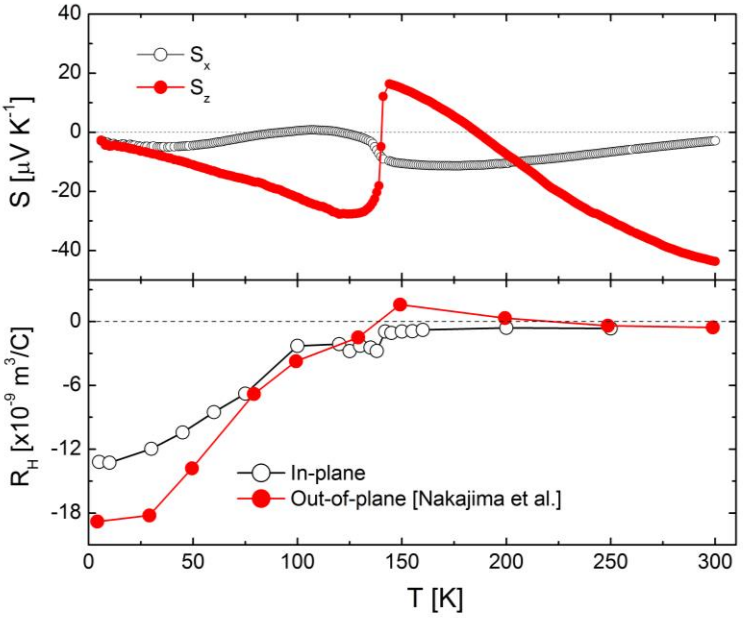

Figure A4:Upper panel: temperature dependence between 5 and 300 K of $\boldsymbol{S_x}$ (black empty dots) and $\boldsymbol{S_z}$ (red filled dots). Bottom panel: temperature dependence between 5 and 250 K of the in-plane (black empty dots, data taken from [33]) and out of plane (red filled dots, data taken from [2]) Hall coefficient $\boldsymbol{R_H}$.

Ab-initio calculations: resistivity

The calculations were performed using the VASP [7] package within the generalized gradient approximation [8] (GGA) to density functional theory, and the projected augmented wave (PAW)[9] scheme. Transport coefficients were obtained within the Relaxation Time Approximation (RTA) according to Boltzmann's theory [10]. Calculations were performed for different magnetic alignment (checkerboard, antiferromagnetic-stripe tetragonal ($a=b=(a_{exp}+b_{exp})/2$ and orthorhombic ($a=a_{exp,}$ $b= b_{exp}$) structure and for the non-magnetic structure (body central tetragonal). Calculations did not include correlation effects. We

find that the structural orthorhombic distortion does not change considerably the in-plane anisotropy of the transport coefficients showing that this is essentially related to the magnetic ordering. On the other hand we find that the magnetic ordering, e.g. checkerboard versus AFM-stripe, results in major variations.

In order to make a meaningful comparison between experimental and ab-initio results we must consider that the latter do not take into account effects of spin density waves and/or fluctuations that are expected to occur as the PM-AFM transition is approached; therefore, a meaningful comparison holds only at low temperature and well above the transition where magnetic alignment is either long range or absent.

With this in mind, we start comparing our results for the in-plane and out-of-plane resistivity. As calculations are performed within RTA, we plot in Figure A5 the $\rho\tau$ product, the product of the resistivity with the relaxation time which, within RTA, results to be independent on the carriers life time. The temperature dependence comes from the temperature dependence of the Fermi Dirac statistic.

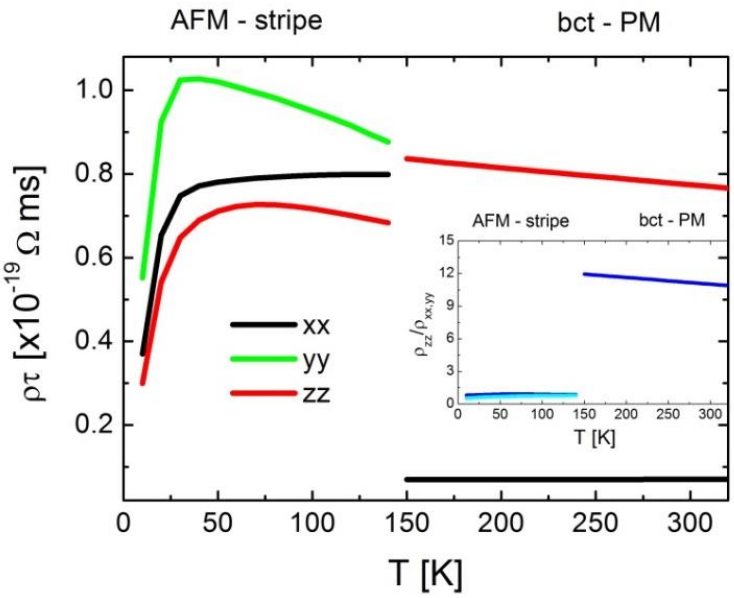

Figure A5: Temperature dependence of the diagonal elements of the resistivity tensor as obtained by first principle calculations from 10 to 320 K. Black, green and red curves refer to the xx, yy, zz components, respectively. Please note that the x, y axes refer to the *a* (longer, AFM stripe direction), *b* (shorter, FM alignment) axes of the in plane orthorhombic cell respectively, while the z-axis is directed along the orthorhombic *c* lattice parameter. Inset: Temperature dependence of the anisotropy ρ_{zz}/ρ_{xx} (blue curve) in the same temperature range. Light blue curve refers to the anisotropy ρ_{zz}/ρ_{yy} in the AFM phase.

Discussion

A straightforward numerical comparison between experimental and theoretical calculation of resistivity is not possible as the ab-initio results do not take into account scattering processes, being based just on the band contribution. Nevertheless, it is possible to observe that the calculated anisotropy (inset of Figure A5) is present in both phases and that in the non-magnetic phase the resistivity along the z-axis is much

larger than the in plane one, as also found in experiment (bottom panel of Figure A2).

Calculations show that the anisotropy can be traced back to the band velocity associated with the carrier states involved. Carriers at the Fermi level of the bct-structure occupy cylindrical-like Fermi surface states showing quite a flat dispersion along the c-axis of the Brillouin zone; thus, the corresponding calculated squared velocity results to be one order of magnitude lower than in the in-plane directions. In addition, at energies very close to the Fermi level, the out-of-plane velocity v^2_{zz} rapidly increases with energy while it is constant in the in-plane directions: this explains the decreasing behaviour predicted as a function of temperature which, within the ab-initio framework, is strictly due to the Fermi-Dirac statistics. This argument of course does not take into account other possible mechanisms related to the incoming transition: Hall measurements in fact reveal a change from incoherent electron-like (higher T) to more efficient hole-like transport that, according to Nakajima et al.[2] would be responsible for the non-metallic behaviour of the out-of-plane resistivity.

The situation in the AFM-stripe phase looks more complex: here, the calculated band velocity is much more isotropic resulting in a more isotropic resistivity (Figure A5), as experimentally measured (bottom panel of Figure A2). However, from calculations it emerges that without taking into account anisotropic scattering processes, the resistivity is larger for in-plane than out-of-plane directions ($\rho_{zz}/\rho_{xx,yy} < 1$ in the AFM phase, see inset of Figure A5).

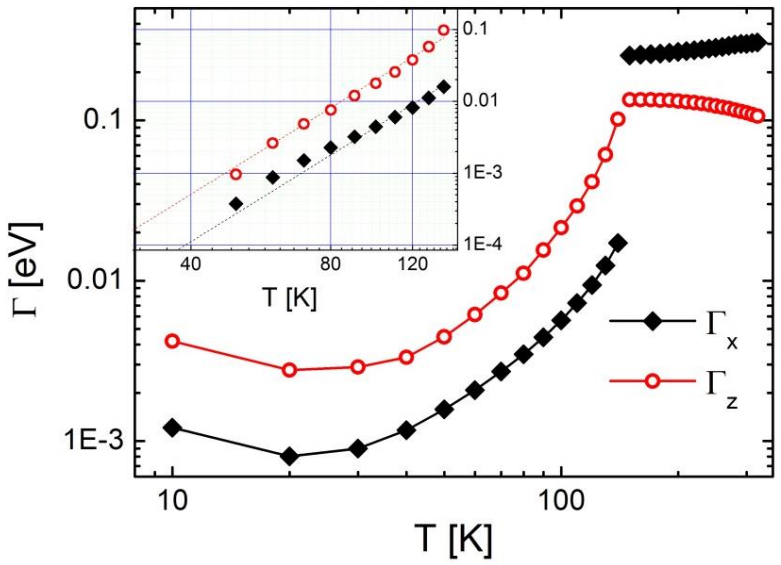

Figure A6: Bi-logarithmic plot from 10 to 300 K of in-plane (black filled squares) and out-of-plane (red empty bullets) scattering rate obtained as $\boldsymbol{\Gamma = \rho_{EXP}/(\rho\tau)_{DFT}}$. Inset: Same data in the AFM phase after subtracting an appropriate constant in order to evaluate the temperature dependence of $\boldsymbol{\Gamma_x}$ and $\boldsymbol{\Gamma_z}$. Dotted lines refer to a $\boldsymbol{T^{-4}}$ temperature behaviour.

In Figure A6 we tentatively plot the scattering rate for the in-plane (Γ_x) and out of plane (Γ_z) directions. For each direction, it was evaluated as $\Gamma = \rho_{EXP}/(\rho\tau)_{DFT}$ where ρ_{EXP} is the measured electric resistivity (bottom panel of Figure A2) and $(\rho\tau)_{DFT}$ is the DFT result in Figure 5. It is worth to notice that we obtain reasonable values of Γ_x and Γ_z in the range 1-10 meV and 100-400 meV for the AFM and PM phase respectively.

In the AFM phase, we find that Γ_z/Γ_x ~3 at 10 K and the anisotropy interestingly increases up to ~5 when approaching T_N (Figure A6). This could suggest an anisotropic scattering mechanism in the AFM state, which becomes much more important when approaching T_N.

It is known that at low temperature $BaFe_2As_2$ is characterized by the presence of anisotropic magnetic excitations [5,11,12,15]. In particular, neutron polarization analysis performed by Li et al [12] detects the presence of anisotropic spin excitations in the AFM state, being those polarized along the c-axis much more pronounced than the in-plane ones [12]. Moreover, anisotropic spin-wave velocities, have been reported in ref. [15], with the in-plane spin-wave velocity (∼280 meV Å) larger than the c-axis spin-wave velocity (∼57 meV Å) and an isotropic energy gap is Δ∼9.8 meV. In addition, in ref. [11] it is shown that also Δ is anisotropic, being larger for the in-plane excitations (∼19 meV) than out-of-plane excitations (∼12 meV). Assuming in the ordered state a dominating scattering mechanism of electrons by magnons, the above evidences would suggest a scattering rate along *c* larger than the in-plane (*ab*) one, in agreement with data reported in Figure A6.

In addition, in the inset of Figure A6 we report the bi-logarithmic plot of Γ_x and Γ_z after subtracting a residual contribution in order to emphasize the temperature dependence. It turns out that the data are quite well described by a power law T^4 (dashed lines). This is the temperature dependence for the (antiferromagnetic) magnon-electron scattering rate, estimated by replacing the magnon spectrum for the ferromagnet ($\omega(q) \propto q^2$) with the spectrum ($\omega(q) \propto q$) [13,14] expected for an antiferromagnet neglecting the energy gap. Given Δ ∼10 meV [11,15] this means for $T \gtrsim 100$ K.

In contrast with the AFM phase, in the PM phase it results that Γ_x/Γ_z ∼2 (Figure A6). In this phase, inelastic neutron scattering [12,15] on $BaFe_2As_2$ detects anisotropic spin fluctuations. Short-range antiferromagnetic fluctuations are also believed to be the source of the

unusual linear temperature increase of the magnetic susceptibility above the AFM transition [16, 17, 18], which we observe to be anisotropic (upper panel in Figure A2).

In addition, in ref. [12] it is reported that spin fluctuations in the PM state are anisotropic (with in-plane fluctuations larger than those out-of-plane) immediately above T_N, but become isotropic already at 160 K.

In this scenario, the in-plane short-range spin fluctuations could increase Γ_x with respect to Γ_z near T_N but this mechanism cannot explain why the anisotropy survives up to 300 K (Figure A6).

However, at higher temperature, other mechanisms come into play such as phonons and correlations effects [19] which are not included in the present calculations.

The thermal conductivity is given by $\kappa = \kappa^{el} + \kappa^{ph}$,with κ^{el} and κ^{ph} being the electron and the phonon contribution, respectively. κ^{el} can be estimated from the Wiedemann-Franz law $\kappa^{el} = L_0 T/\rho$, where $L_0 = 2.44 \times 10^{-8} \mathrm{W\Omega K^{-2}}$ is the Lorentz number and ρ the electric resistivity.

It is worth to notice that the Wiedemann-Franz law is expected to be valid in the limit of low and high temperatures [20], namely when inelastic scattering can be neglected. This was already shown by means of transverse thermal conductivity measurements in $CaFe_2As_2$ [21], $Fe_{1+d}Te_{1-x}Se_x$ [22] and $Ba(Fe_{1-x}Co_x)_2As_2$ [23]. We will therefore limit our discussion to low and high temperature limits.

In Figure A3 we compare the measured thermal conductivity κ (solid lines) with the contribution from electrons κ^{el} (dotted lines). It turns out that κ^{el}/κ at low temperature is up to 50% and 60% for the in-plane and

out-of-plane case, respectively. This differs from what was measured in other iron-based compounds: in polycrystalline LaFeAsO [24,25] and SmFeAsO [26], it was observed that thermal conductivity is dominated by phonons and the same result was reported for $Ba(Fe_{1-x}Co_x)_2As_2$ single crystals in ref. [5]. Since κ^{el} is limited by the collisions with defects and impurities [30], κ^{el} is indeed expected to be higher in our single crystal, where the annealing process remarkably removed crystal defects and lattice dislocations [27]. Interestingly, Figure A3 shows that the low-temperature bump of κ could be due to κ_{el} which shows a broad peak around 40 K, both for the in-plane (upper panel) and out-of-plane (lower panel) measurement.

Let's now consider the feature observed at T_N in both κ_x and κ_z (Figure A3) and the corresponding bump at 120 K. Since at high temperature κ^{el}/κ reduces to 20%, we see that the leading contribution to κ is κ^{ph} in the PM phase. When approaching T_N, as already discussed in [26], an abrupt rise of κ_{ph} is expected in correspondence to the gap opening at the Fermi surface, due to carrier condensation and consequent suppression of electron-phonon scattering. We therefore ascribe the bump at 120 K to an enhancement of κ^{ph} due to the SDW gap opening at T_N. Interestingly, the feature at T_N is more abrupt for κ_z than for κ_x.

In Figure A7 the temperature dependence of the anisotropy κ_x/κ_z is reported. As already mentioned, κ_x is a factor ~3 larger than κ_z. In order to separate the anisotropy of the phonon contribution from those of the electron contribution, we calculate $\kappa_{x,z}^{ph} = \kappa_{x,z} - \kappa_{x,z}^{el}$ (see the inset of figure 7). This estimation depends on the validity of the Wiedemann-Franz law, thus it is expected to be valid in the limit of low and high temperatures (unhatched region). The ratio $\kappa_x^{ph}/\kappa_z^{ph}$ (red symbols) between 30 and 300 K is reported in Figure A7. At high

temperature, as expected from the small contribution of electrons (see Figure A3, $\kappa_{el} \ll \kappa$), the anisotropy $\kappa_x^{ph}/\kappa_z^{ph}$ almost reproduces κ_x/κ_z, reaching 2.9 at 300 K. At low temperatures, $\kappa_x^{ph}/\kappa_z^{ph}$ increases, reaching a value around 5 at 30K.

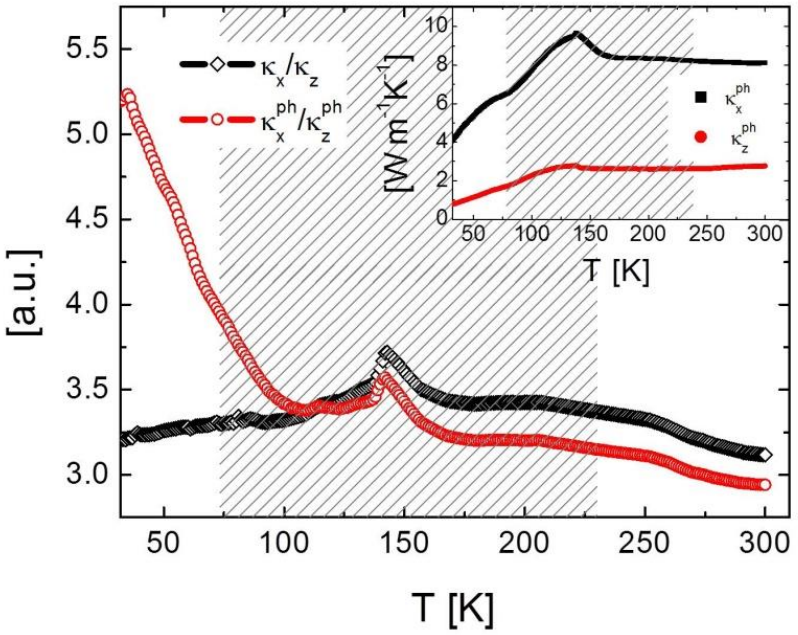

Figure A7: Temperature dependence of the anisotropy $\boldsymbol{\kappa_x/\kappa_z}$ (black symbols) and $\boldsymbol{\kappa_x^{ph}/\kappa_z^{ph}}$ (red symbols) between 30 and 300 K, where $\boldsymbol{\kappa^{ph}}$ is the phonon contribution to thermal conductivity, estimated as $\boldsymbol{\kappa_{x,z}^{ph} = \kappa_{x,z} - \kappa_{x,z}^{el}}$. Inset: phonon contribution to $\boldsymbol{\kappa_x}$ ($\boldsymbol{\kappa_x^{ph}}$, black curve) and to $\boldsymbol{\kappa_z}$ ($\boldsymbol{\kappa_z^{ph}}$, red curve). The dashed region of temperature indicates where the Wiedemann-Franz law is not reliable.

A complete model for κ^{ph} is reported in [28,29]. However, it is qualitatively expected that $\kappa^{ph} \propto Cvl$, where C is the heat capacity, v is the sound velocity and l is the phonon mean free path [30]. Although

this formula is an approximation, it gives hints of the main mechanisms into play.

At high temperature, the phonon-phonon scattering is expected to be dominant and, if we assume as first approximation that this mechanisms is isotropic, we expect that $\kappa_x^{ph}/\kappa_z^{ph}$ reflects the anisotropy of the sound velocities v_x/v_z.

On the other hand, at low temperatures phonons should mainly relax with the sample boundaries and l becomes comparable with the sizes of the sample. Therefore, l is limited by the width a (the thickness c) when measuring in-plane (out-of-plane) [30]. One would then expect that the ratio $\kappa_x^{ph}/\kappa_z^{ph}$ becomes $\propto (v_x/v_z)(a/c)$. Remarkably, for the measured crystal the ratio $(a/c)\sim 2$. Considering that at high temperature we evaluated $v_x/v_z\sim 3$, it is reasonable to predict an enhanced $\kappa_x^{ph}/\kappa_z^{ph}$ up to ~ 6, which is in good agreement with our low temperature data in Figure A7.

We conclude that our thermal conductivity data suggest an anisotropy of the sound velocities, with the in-plane sound velocity bigger by a factor ~ 3 than the out-of-plane one. Qualitatively, from calculations in ref. [31], we could infer that the sound velocity is predicted to be anisotropic but, to our knowledge, sound velocity values have never been reported for $BaFe_2As_2$ compounds.

In this regard, it might be interesting to notice that phonon contribution to thermal expansion along c-axis is measured to be a factor 2 larger than that along a-axis [32]. This would be correlated with a larger in-plane sound velocity as compared to the out-of-plane as emerged from our experiment.

We finally move to the Seebeck coefficient, reported in Figure A4 (upper panel). We measured an remarkable anisotropy of this property, both in magnitude and sign. As already mentioned, S_z has never been reported before and we can compare our Seebeck data with Hall coefficient (R_H in bottom panel of Figure A4), whose in-plane value was measured on the same crystal [33] and whose out-of-plane value was reported in ref. [2].

Indeed, both Seebeck and Hall effect are carrier-sign-sensitive transport properties and we can therefore discuss the changes of sign of S in terms of R_H.

It is interesting to notice that whereas the in-plane R_H is negative from 5 to 300 K (bottom panel of Figure A4), in ref. [2] it is reported that the out-of-plane R_H shows a sign change from negative to positive around 200 K and it becomes negative again below T_N (bottom panel of Figure A4). Remarkably, S_x is mostly negative (being slightly positive just for a small temperature range around 100 K) whereas we measured that S_z changes in sign from negative to positive in almost the same temperature range as the out-of-plane R_H (see Figure A4).In the PM phase, in ref. [2] it was proposed that, the contributions of electrons and holes are nearly balanced, and the prevailing carrier changes from electrons at high temperatures to holes between 200 K and T_N. Instead, upon entering the AFM phase, the negative values of both S_z and R_H indicate that electrons dominate the out-of-plane conduction below T_N.

These considerations lead to the conclusion that multiband effects can play a role in qualitatively understanding the anisotropy of the Seebeck coefficient. However a quantitative comparison with ab initio calculations is challenging and requires further studies.

References

[1] S. L. Skornyakov, V. I. Anisimov, and D. Vollhardt, Phys. Rev. B 86, 125124 (2012)
[2] M. Nakajima, M. Nagafuchi, and S. Tajima, Phys Rev B 97, 094511 (2018)
[3] Z.G. Chen, T. Dong, R. H. Ruan, B. F. Hu, B. Cheng, W. Z. Hu, P. Zheng, Z. Fang, X. Dai, and N. L.Wang, Phys. Rev. Lett. 105, 097003 (2010).
[4] S. Arsenijević, R. Gaál, A. S. Sefat, M. A. McGuire, B. C. Sales, D. Mandrus, and L. Forró, Phys. Rev. B 84, 075148 (2011).
[5] A. F. May, M. A. McGuire, J. E. Mitchell, A. S. Sefat, and B. C. Sales, Phys. Rev. B 88, 064502 (2013).
[6] Y. J. Yan, X. F. Wang, R. H. Liu, H. Chen, Y. L. Xie, J. J. Ying, and X. H. Chen, Phys. Rev. B 81, 235107 (2010).
[7]G. Kresse and J. Furthmuller, Phys. Rev. B 54, 11169 (1996), and Comput. Mater. Sci. 6, 15 (1996).
[8] J. P. Perdew, K. Burke, and M. Ernzerhof, Phys. Rev. Lett. 77, 3865 (1996).
[9]P. E. Blochl, Phys. Rev. B 50, 17953 (1994).
[10] Zhi-Guo Chen et al., Phys Rev. Lett 119, 096401 (2017)
[11]N. Qureshi, P. Steffens, S. Wurmehl, S. Aswartham, B. Büchner, and M. Braden
Phys. Rev. B 86, 060410(R) (2012)
[12] Yu Li, Weiyi Wang, Yu Song, Haoran Man, Xingye Lu, Frédéric Bourdarot, and Pengcheng Dai, Phys. Rev. B 96, 020404(R) (2017)
[13] N. V. Volkenshtein, V. P. Dyakina, V. E. Startsev, Phys. Stat. sol. (b) 57, 9 (1973)
[14]C. Ferdeghini, F. Canepa, M.R. Cimberle, G. Grassano, S. Gariglio, D. Marrè, F. Napoli and M. Putti, *Intermetallics*, **7**, 12, (1389), (1999)
[15] K. Matan, R. Morinaga, K. Iida, and T. J. Sato, Phys. Rev. B **79**, 054526 (2009).
[16] X. F.Wang, T.Wu, G.Wu, H. Chen, Y. L. Xie, J. J. Ying, Y. J. Yan, R. H. Liu, and X. H. Chen, Phys. Rev. Lett. 102, 117005 (2009)
[17] G. M. Zhang, Y. H. Su, Z. Y. Lu, Z. Y. Weng, D. H. Lee, and T. Xiang, Europhys. Lett. 86, 37006 (2009)
[18] M. M. Korshunov, I. Eremin, D. V. Efremov, D. L. Maslov, and A. V. Chubukov, Phys. Rev. Lett. 102, 236403 (2009)
[19] L. de' Medici, G. Giovannetti, and M. Capone, Phys. Rev. Lett. 112, 177001 (2014)
[20] J.M. Ziman, "Electrons and Phonons. ", Oxford University Press (1960)

[21] M. Matusiak, Z. Bukowski, and J. Mucha, JPS Conf. Proc. 3, 015002 (2014)
[22] Matusiak, M. , Babij, M. , Pomjakushina, E. and Conder, K., Phys. Status Solidi B, 253: 1607-1611 (2016)
[23] M. Matusiak and T. Wolf, Phys. Rev. B 92, 020507 (2015)
[24]Michael A. McGuire, Andrew D. Christianson, Athena S. Sefat, Brian C. Sales, Mark D. Lumsden, Rongying Jin, E. Andrew Payzant, David Mandrus, Yanbing Luan, Veerle Keppens, Vijayalaksmi Varadarajan, Joseph W. Brill, Raphaël P. Hermann, Moulay T. Sougrati, Fernande Grandjean, and Gary J. Long, Phys. Rev. B 78, 094517 (2008)
[25] Athena S. Sefat, Michael A. McGuire, Brian C. Sales, Rongying Jin, Jane Y. Howe, and David Mandrus, Phys. Rev. B **77**, 174503 (2008)
[26] M. Tropeano, A. Martinelli, A. Palenzona, E. Bellingeri, E. Galleani d'Agliano, T. D. Nguyen, M. Affronte, and M. Putti, Phys. Rev. B 78, 094518 (2008)
[27]S. Ishida, T. Liang, M. Nakajima, K. Kihou, C. H. Lee, A. Iyo, H. Eisaki, T. Kakeshita, T. Kida, M. Hagiwara, Y. Tomioka, T. Ito, and S. Uchida, Phys. Rev. B 84, 184514 (2011).
[28]L. Tewordt and T. Wolkhausen, Solid State Commun. 70, 839 (1989); **75**, 515 (1990)
[29]S. Castellazzi, M. R. Cimberle, C. Ferdeghini, E. Giannini, G. Grasso, D. Marrè, M. Putti, and A. S. Siri, Physica C **273**, 314 (1997)
[30] C. Kittel, "Introduction to Solid State Physics", John Wiley & Sons, Inc. (2005)
[31]L. Boeri, M. Calandra, I. I. Mazin, O. V. Dolgov, and F. Mauri Phys. Rev. B 82, 020506(R) (2010)
[32]C. Meingast, F. Hardy, R. Heid, P. Adelmann, A. Böhmer, P. Burger, D. Ernst, R. Fromknecht, P. Schweiss, and T. Wolf, Phys. Rev. Lett. 108, 177004 (2012)
[33]M. Meinero, F. Caglieris, G. Lamura, I. Pallecchi, A. Jost, U. Zeitler, S. Ishida, H. Eisaki, and M. Putti, Phys. Rev. B 98, 155116 (2018)

B In-plane anisotropy of Seebeck and Nernst coefficients of $BaFe_2As_2$ parent compound

As the Seebeck effect is a powerful tool to explore effects related to Fermi surface and scattering mechanisms, it turns out to be more sensitive than resistivity to nematicity, the spontaneous symmetry breaking of planar crystalline directions, driven by magnetic or orbital degree of freedom. Nematicity is observed in transport, magnetic and optical properties of 122 compounds at the boundary between tetragonal and orthorhombic phases, but universal consensus has not yet been achieved about its origin. Nematicity of the Seebeck effect is investigated in detwinned crystals of $BaFe_2As_2$ and $CaFe_2As_2$ [1]. In Figure B1 (panels (a) and (b)) are displayed the temperature behaviours of $S_a(T)$ and $S_b(T)$ the Seebeck coefficients along the in-plane *a*- and *b*-axes. In either case, the anomaly at T_{SDW} is more pronounced along the *b*-axis, but both S_a and S_b seem to share the same characteristic features. Nevertheless, the thermoelectric power measured along the *a*-axis differs significantly from that measured along the *b*-axis and the anisotropy in the SDW phase is much more pronounced than that observed for the resistivity (Figure B1c) [1]. Figure B1d compares the normalized anisotropy of the thermoelectric power $\Delta S = (S_b -$

$S_a)/(S_{max} - S_{min})$ for both samples. ΔS in $BaFe_2As_2$ is similar to that reported for $EuFe_2(As_{1-x}P_x)_2$ [2], i.e., it is slightly negative just above T_{SDW} and rapidly turns positive just below the transition. However, ΔS in $BaFe_2As_2$ clearly changes sign back to negative at low temperatures, which is not the case for $EuFe_2(As_{1-x}P_x)_2$. This does also not happen in $CaFe_2As_2$, where ΔS stays positive in the entire SDW phase and, in agreement with resistivity data, there is no sign of anisotropy above T_{SDW}.

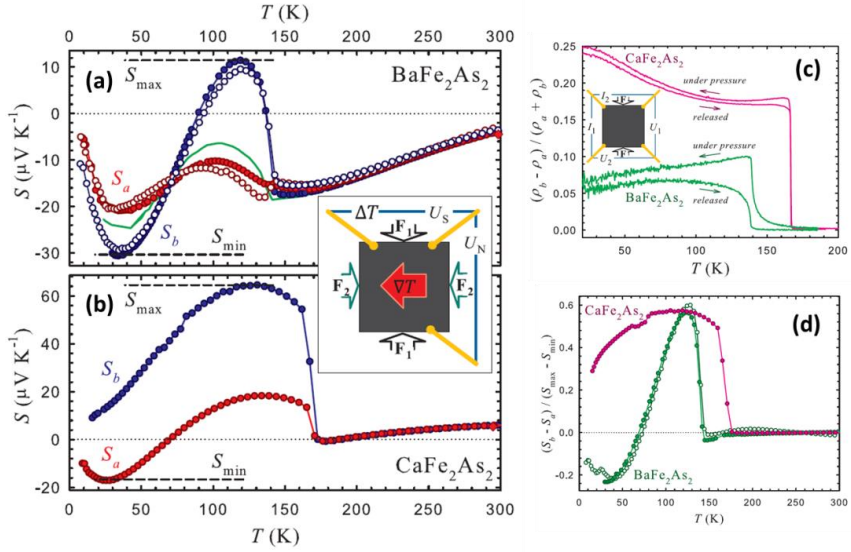

Figure B1: Temperature dependences of the thermoelectric power in $BaFe_2As_2$ (solid points: sample No. 1; open points: No. 2) (a) and $CaFe_2As_2$ (b) along the orthorhombic *a* and *b* axes. Inset presents the schematic diagram of the experimental set up for the thermoelectric measurements. (c) Temperature dependences of the normalized resistivity anisotropy. Inset presents the schematic diagram of the experimental setup for resistivity measurements. (d) Temperature dependences of the normalized thermopower anisotropy in $BaFe_2As_2$ (solid points: sample No. 1; open points: No. 2) and $CaFe_2As_2$. After [1].

Similarly to the Seebeck effect, in [1] it has also been measured the in-plane anisotropy of the Nernst effect of the $BaFe_2As_2$ and $CaFe_2As_2$ crystals. Their results are shown in Figure B2a, where it is evident that

the Nernst effect also shows a sizable anisotropy, with ν_a and ν_b exhibiting the large anomaly below T_{SDW} attributed to the possible influence of highly mobile Dirac fermions. It is worth noting that the Nernst coefficient at the maximum is about an order of magnitude larger in $BaFe_2As_2$ than in $CaFe_2As_2$.

The normalized anisotropy of the Nernst coefficient $\Delta\upsilon = (\upsilon_b - \upsilon_a)/(\upsilon_{max} - \upsilon_{min})$ presented in Figure B2b is substantial in the SDW phase. $\Delta\upsilon(T)$ in $BaFe_2As_2$ is positive $(\upsilon_b > \upsilon_a)$ and roughly proportional to the average Nernst signal, whereas $\Delta\upsilon(T)$ in $CaFe_2As_2$ is negative just below T_{SDW}, then $\Delta\upsilon$ becomes positive at low temperature, i.e. $\upsilon_b > \upsilon_a$. Analogously to the resistivity and thermopower, there is no anisotropy of the Nernst effect in the tetragonal phase of $CaFe_2As_2$, whereas in $BaFe_2As_2$ a contribution from fluctuations appears below ~200 K.

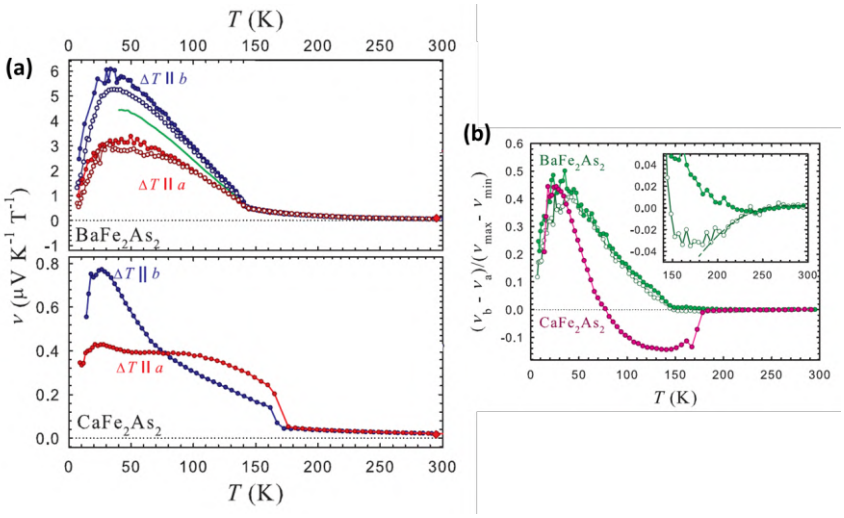

Figure B2: Temperature dependences of the Nernst coefficient along the orthorhombic *a* and *b* axes for $BaFe_2As_2$ and $CaFe_2As_2$. After [1].

By considering the band model of [3] and the anisotropy of both resistivity and Nernst effect, the authors of [1] concluded that the Dirac band is rather isotropic in-plane, whereas anisotropy should be attributed to the regular holelike carriers.

References

[1]M. Matusiak, M. Babij, T. Wolf, Phys. Rev. B 97, 100506(R) (2018)
[2] S. Jiang, H. S. Jeevan, J. Dong, and P. Gegenwart, Phys. Rev. Lett. 110, 067001 (2013)
[3] T. Morinari, E. Kaneshita, and T. Tohyama, Phys. Rev. Lett. 105, 037203 (2010)

C Experimental details

PPMS The zero-field and low field (B<9T) transport measurements have been performed using a commercial *Physical Property Measurement System* (PPMS) by Quantum Design (Figure C1). This system allows to make (magneto)resistance, Hall effect, thermal conductivity, Seebeck effect and Nernst effect measurements in a range of temperature between 2 and 400 K and applying a magnetic field from -9T to 9T. The system can work in high vacuum (10^{-6} torr) in order to create the best conditions for thermoelectric measurements.

Figure C1: Quantum Design Physical Property measurements system (PPMS)

Resistivity and Hall effect measurements were performed using a standard four-probe technique. In Figure C2a the general scheme for electric transport measurements is shown. It consists of two current

leads at the extremities of the sample, two electrodes to pick up the longitudinal difference of potential ΔV_x and two electrodes for the transverse difference of potential ΔV_y. For the magnetoresistance and Hall effect measurements a magnetic field B was applied perpendicularly to the current flow.

Figure C2b shows the practical realization of the experimental setup in case of a sample of millimetric dimensions where the electrodes are copper wires glued on the sample with a silver epoxy. This is the setup used for resistivity, magnetoresistance and Hall effect measurements both on Ba-122 single crystal (Chapter 3) and Bi-2201 single crystals (Chapter 4). The operative definition for resistivity and Hall coefficient are the following:

$$\rho_{xx} = \frac{\Delta V_x}{I}\frac{l\,s}{\Delta x} \tag{1}$$

$$R_H = \frac{R_{xy}}{B}\frac{l\,s}{\Delta y} \tag{2}$$

where l is the width of the sample, Δx (Δy) is the distance between the two longitudinal (transverse) voltage probes (see Figure C2a). $R_{xy} = \Delta V_y / I$ is the Hall resistance.

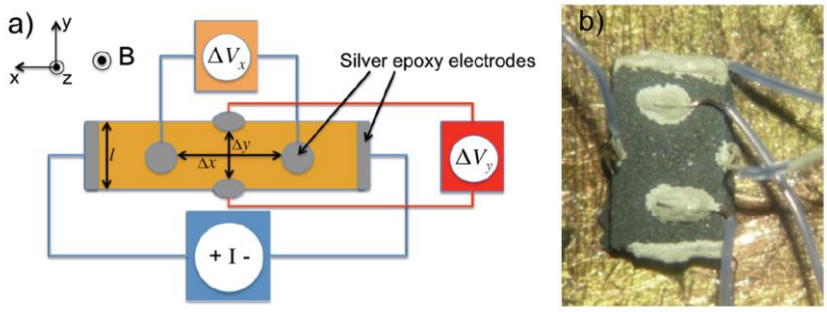

Figure C2: (a) Measurement configuration for (magneto)resistance and Hall effect measurements; (b) Practical realization on a bar-shaped sample.

The Hall effect measurement is often characterized by spurious voltages ΔV_{sp} that are added to ΔV_y, principally due to a misalignment between the transverse electrodes which causes Δy being not perpendicular to the current flow direction. Therefore the measured signal is $\Delta V_{meas} = \Delta V_y + \Delta V_{sp}$. In order to delete the spurious part of the signal, it is sufficient to invert the direction of B, since we have $\Delta V_y(B) = -\Delta V_y(-B)$, whereas the spurious signals are symmetric ($\Delta V_{sp}(B) = \Delta V_{sp}(-B)$). So that:

$$\Delta V_y = \frac{\Delta V_{meas}(B) - \Delta V_{meas}(-B)}{2} \quad (3)$$

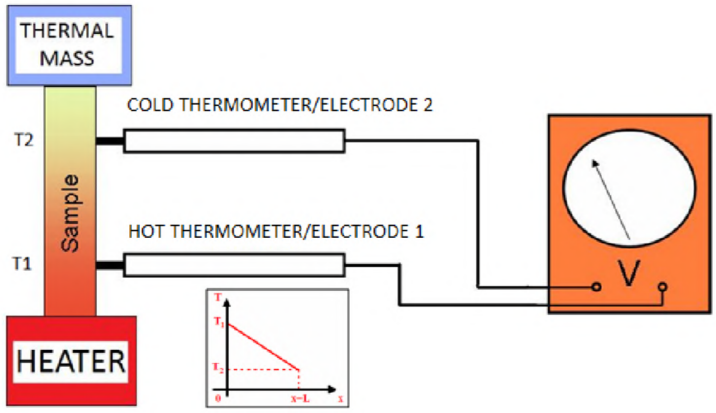

Figure C3: Seebeck effect measurement configuration. Inset: ideal temperature distribution along the sample.

Unlike electric transport measurements, thermoelectric measurements require high vacuum conditions in order not to dissipate heat to the environment. Figure C3 shows the general scheme of a Seebeck effect measurement. It includes: (i) a heater and a thermal mass put at the extremities of the sample in order to create a longitudinal gradient of temperature $\Delta_x T$; (ii) two thermometers to measure the difference of

temperature and (iii) two electrodes to measure the Seebeck voltage ΔV_S (we set them at the same positions of the thermometers). An usually allowed approximation is to consider a constant gradient of temperature trough the sample (inset of Figure C3), so that:

$$\nabla_x T = \frac{\Delta T}{\Delta x} \tag{4}$$

where ΔT is the difference between the temperatures measured by the two thermometers. ΔT is set to be a fraction of the sample average temperature T. In particular the heater power is set in order to keep $\frac{\Delta T}{\Delta x}$~0.02÷0.03 (see Figure C4). Moreover the heating pulse must have a defined shape (typically a square wave or a sine function) in order to distinguish the response to the heater excitation from the spurious signals caused by the fluctuations of the background.

The Seebeck coefficient is then:

$$S = -\frac{\Delta V_S}{\Delta T} \tag{5}$$

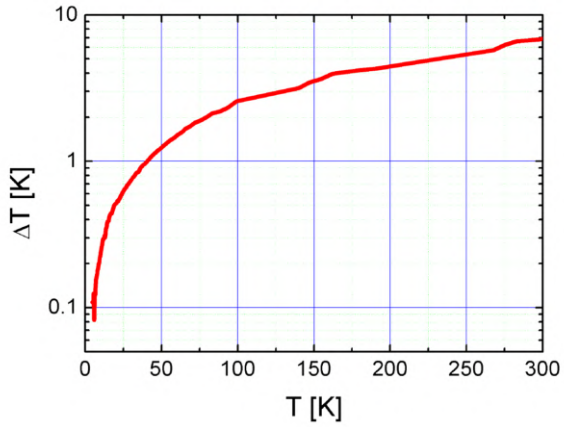

Figure C4: $\Delta \boldsymbol{T}$ vs $\boldsymbol{T}$ curve, where $\Delta \boldsymbol{T}$ is the difference of temperature measured by the two thermometers mounted on the sample for a Seebeck effect measurement according to the configuration of Figure C3.

Figure C5 shows the practical realization of the measurement scheme of Figure C3 in the *Thermal Transport Option* (TTO) of the PPMS: four high quality copper bars are glued to the sample through silver paste (Figure C5a); then the heater and two "Cernox 150" thermometers (which also play the role of electrodes) are connected to three bars while the fourth ("cold foot") is clamped to the thermal mass (Figure C5b) in order to obtain the complete set up (Figure C5c). Note that in this set up the minimum sample dimension has to be at least 1 mm [1] in order to support the copper bars. In our case it was then possible to perform thermoelectric measurements on the Ba-122 crystal but not on the Bi-2201 crystals, whose thickness is around 150 μm (see Chapter 4).

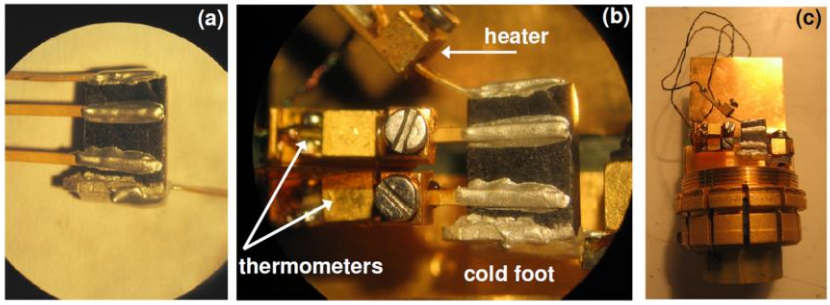

Figure C5: (a) Sample preparation for a Seebeck effect measurement: high purity copper bars on a millimetric sample to let the connection of the heater and thermometers; (b) heater and thermometers mounted on the sample; (c) TTO sample holder of the PPMS.

Figure C6a shows the general scheme of a Nernst effect measurement. The measurement is performed in an external magnetic field B, applied perpendicular to the gradient of temperature (along the z axis in Figure C6a). The experimental setup is almost the same as for the Seebeck effect described above. The main difference is that the voltage $\mathbf{\Delta V_N}$ is measured transversally (i.e. along the y-direction in Figure C6a) with respect to the gradient of temperature. The Nernst coefficient is then:

$$N = \frac{\Delta V_N}{\Delta T}\frac{\Delta x}{\Delta y} \tag{6}$$

In analogy to the Hall effect measurement, also a Nernst effect measurement is characterized by spurious signals due to the misalignment of the electrodes, that causes an additional Seebeck voltage component S_{mis}. Moreover another source of spurious signals are the copper wires used for electric connections that contribute with a Seebeck voltage S_{Cu} due to the fact that their extremities are in principle at different temperatures.

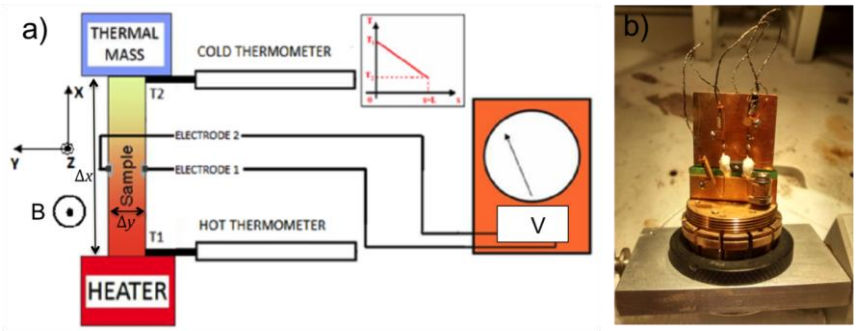

Figure C6: (a) Nernst effect measurement scheme; Inset: Ideal temperature distribution along the sample; (b) practical realization of the measurement scheme in Figure C6a on the TTO sample holder of the PPMS

Therefore the measured signal is $N_{meas} = N + S_{sp}$ where $S_{sp} = S_{mis} + S_{Cu}$. Again, in order to delete the spurious part of the signal, it is sufficient to invert the magnetic field direction, because N is antisymmetric ($N(B) = -N(-B)$) as respect to B, while the spurious Seebeck signals are symmetric ($S_{sp}(B) = S_{sp}(-B)$), so that:

$$|N| = \left|\frac{N_{meas}(B) - N_{meas}(-B)}{2}\right| \tag{7}$$

HFML (Nijmegen) High field characterization on Ba-122 (see Chapter 3) has been performed at the international facility High Field Magnet Laboratory (HFML) of Nijmegen (The Netherlands). All the experiments were carried out in a work-station (Figure C7a) set with a water-cooled copper magnet capable to create DC magnetic fields in a range between -30 and 30 T. We performed all the measurements with both positive and negative B in order to separate the even (Seebeck) and odd (Nernst) part of the signal with respect to B.

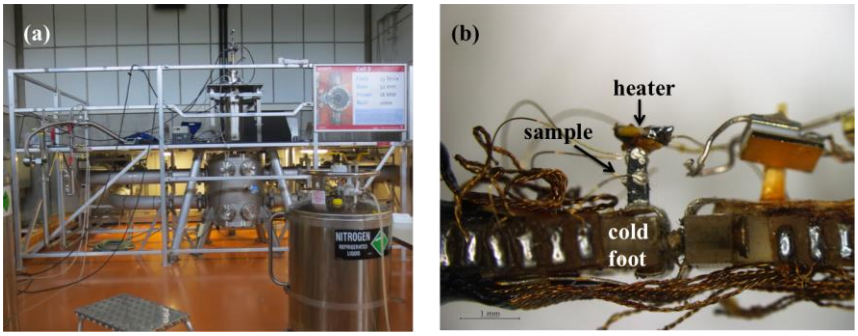

Figure C7: (a) High Field Magnet Laboratory work-station; (b) Ba-122 sample mounted for thermal transport on the sample stage of the probe.

The Seebeck and Nernst measurement schemes (shown in Figure C3 and C6 respectively) were practically realized on a homemade probe at the HFML (Figure C7b). In this case the sample and the resistive heater were directly glued with a thermal conducting varnish respectively on the probe (cold foot) and on the top of the sample (see Figure C7b). Six electrodes were put on the sample using manganin wires welded on the sample with silver paste, in order to collect the Seebeck and the Nernst signals at the same time.

IFW (Dresden) The thermal and thermoelectric transport properties on the single crystals of Bi-2201 have been measured using an experimental setup consisting of:

- A liquid-He cryostat from Oxford Instruments endowed with 15/17 T superconducting magnet.
- A homemade probe sketched in Figure C8. The probe supporting parts are stainless steel capillaries that contain the copper wires for the electrical connection between the plugs at the top of the probe and the sample stage at the bottom. The probe is inserted in a stainless-steel tube directly sinking in the He bath. The thermal exchange between the He bath and the probe is realized through a brass cylinder pressing on copper plates, thermally connected to the copper sample stage at the bottom of the probe. The cooling power supplied by the He bath is balanced by a heater cup which allows a high precision temperature stabilization from 4.2 K to room temperature. Two Cernox temperature sensors are glued at the bottom of the probe in the positions indicated in the inset of Figure C8. The sample temperature sensor is our reference for the experimental data. All the measurements have been realized in condition of high vacuum by pumping inside the stainless-steel tube.
- The required electronic devices: #1 Lakeshore 340 temperature controller connected to the heater-cup of the probe to change and stabilize the temperature for the measurements; #1 Keithley 2400 source meter to supply the heating current to the sample heater for thermal and thermoelectric measurements; # 3 Keithley 2182 A/E nanvoltmeter to pick up the sample heater voltage, thermocouple signal and the Seebeck/Nernst signal respectively.

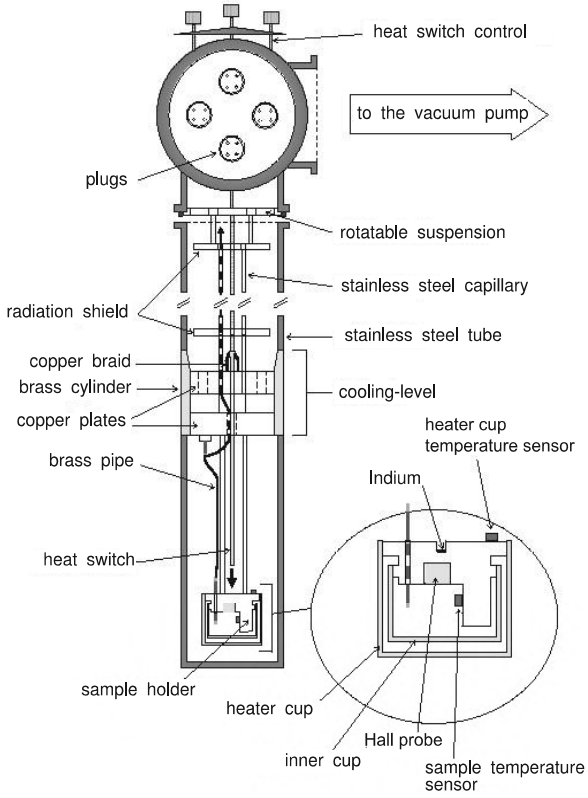

Figure C8: sketch of the home-made probe for transport measurements [2]

The sample stage offer an area of 2 cm x 1 cm to mount the sample with a vertical extension around 1 cm. Figure C9 shows a photo of a Bi-2201 sample prepared for thermal conductivity measurements. The thermal circuit is realized by gluing the bottom of the sample to the copper sample stage, which plays the role of thermal mass (stabilized by the balance of the cooling power of the He-bath and the heater cup). The sample is glued using a tested electrical insulating glue, with high performance in heat conduction (the blue glue in Figure C9). A 3 KΩ-resistive heater is glued on the top of the sample in order to create a temperature gradient across the samples (see Figure C9).

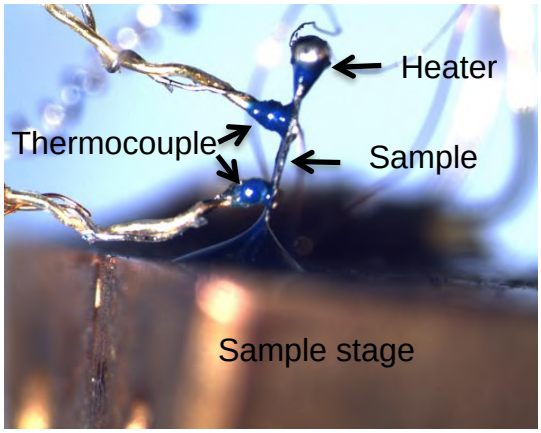

Figure C9: Bi-2201 sample mounted for thermal transport on the sample stage of the probe.

The temperature gradient is estimated using a Chromel-Au differential thermocouple, whose tips are glued to the sample using again the thermal *blue* glue. The thermocouple principle is based on the Seebeck coefficient at the Chromel-Au junction. The thermocouple calibration (Seebeck coefficient vs temperature) is shown in Figure C10a. Since many of our measurements have been realized in relatively high magnetic fields (up to 15 T), the field-effect on the thermocouple has to be considered.

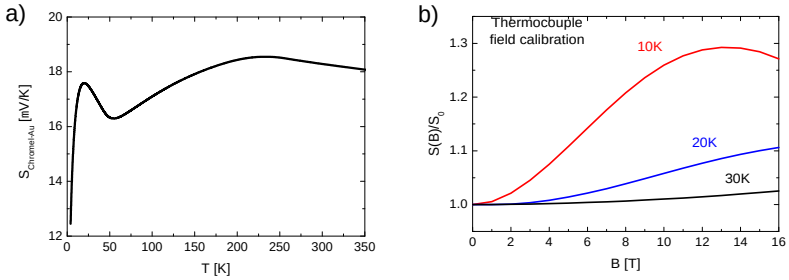

Figure C10: a) Seebeck coefficient of the Chromel-Au thermocouple as a function of temperature. b) Magnetic field dependence of the the Seebeck coefficient of the Chromel-Au thermocouple divided by its zero field value $S(B)/S_0$

Figure C10b exhibits the calibration of the thermocouple for three selected temperatures. In particular the graph shows the field-dependence up to 16 T of the Seebeck coefficient divided by its zero field value $S(B)/S_0$, evidencing a non-negligible correction for T<30K. The electrodes to pick up the Seebeck and/or the Nernst signals consists of calibrated copper wires attached to the sample through silver paste in the preferred position.

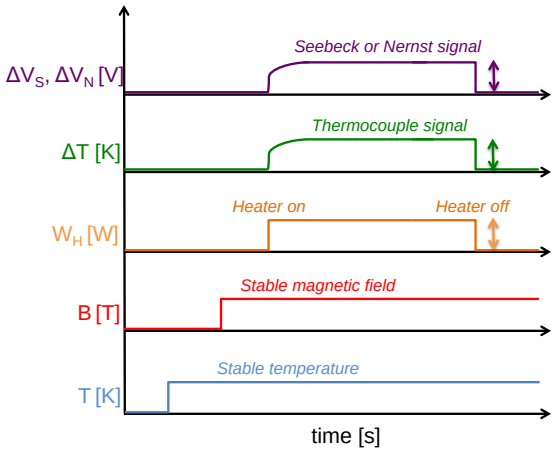

Figure C11: Schematic of the measurement procedure as a function of time

All the measurements have been carried out in conditions of temperature and magnetic field stability. Figure C11 shows a scheme of the measurement procedure: once the temperature T and the field B are stable, the sample heater is switched on in order to apply the heating power W_H to the sample. The thermocouple reacts measuring the temperature difference ΔT and the corresponding Seebeck (Nernst) voltage ΔV_S (ΔV_N) is also measured until they both get stable. The stability values are used to calculate the transport coefficients:

$$S = (\Delta V_S/l_S)/(\Delta T/l_T),$$
$$N = (\Delta V_N/l_N)/(\Delta T/l_T),$$

$k = (W_H/A)/(\Delta T/l_T)$,

where l_S, l_N, l_T and A are the distance between the Seebeck electrodes, the distance between the Nernst electrodes, the distance between the thermocouples tips and the sample cross section. As usual, we performed the measurements from -14 T to 14 T and we symmetrized the signal to get the even contributions (Seebeck and longitudinal thermal conductivity), whereas we antisymmetrized it to extract the odd effects (Nernst and transverse thermal conductivity).

References

[1] Physical Property Measurement System – Thermal Transport Option User's Manual, Quantum Design, San Diego USA (2002)
[2] Figure adapted from C. Hess, *Thermischer Transport in Übergangsmetalloxiden mit niedrigdimensionalen Ladungs- und Spinstrukturen*, Ph.D. thesis, University of Köln (2002).

D Magnetization and magnetic susceptibility measurement of Bi-2201 L2 sample

The field dependent magnetization M and the temperature dependent volume magnetic susceptibility $\chi_{Vol}^{(SI)}$ were measured by a commercial dc-SQUID magnetometer (MPMS2 by Quantum Design) in a temperature range from 2 to 300 K by applying a magnetic field up to 5.5 T.

Figure D1 shows the T-dependence of $\chi_{Vol}^{(SI)}$ measured between 2 and 30 K in an applied magnetic field $\mu_0 B$ = 1 mT, parallel to the c-axis. The measurement is performed in order to measure the magnetic shielding, performed by first cooling the sample to a low temperature (2 K) below T_C, then turning on the magnetic field (ZFC curve, black empty bullets in Figure D1). The superconducting transition is narrow, with an onset temperature T_c~11 K and the saturation value ~ -0.9 reached at ~8 K. This is a proof of the good quality of the crystal.

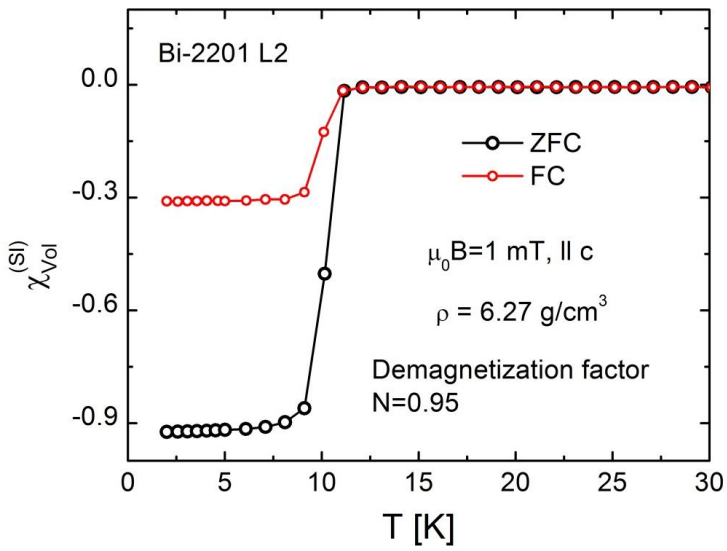

Figure D1: Temperature dependence of the volume magnetic susceptibility $\boldsymbol{\chi_{Vol}^{(SI)}}$ between 2 and 30 K in an applied magnetic field $\boldsymbol{\mu_0 B}$= 1 mT. The zero-field cooled (ZFC) curve (black empty bullets) has been measured cooling down the sample below $\boldsymbol{T_C}$, then turning on the magnetic field. After reaching 30 K the sample has been in-field cooled down and the measurement was repeated by heating again up to 30 K (FC curve, red empty bullets).

The low temperature saturation value $\chi_{Vol}^{(SI)} \sim -0.9$ corresponds to a 90% Meissner fraction which implies that almost all the sample is superconducting. This value has been obtained taking into account the demagnetization factor. We approximate our sample to a disk which may be considered the limiting case of a very flattened oblate ellipsoid with c/a~0.05 (c~90μm is the thickness of the sample, a~1.75 mm is the average in-plane dimension). From [1] it has been estimated that to this c/a correspond $N_\perp$ ~0.02 and $N_\parallel$ ~0.95, where $N_\perp(N_\parallel)$ is the demagnetization factor when $\mu_0 B$ is applied in-plane (out-of-plane). Since we applied $\mu_0 B$ out-of-plane to obtain $\chi_{Vol}^{(SI)}$, we corrected the measured susceptibility χ_{exp} as [1]:

$$\chi_{Vol}^{(SI)} = \chi_{exp}/(1 - N_{\parallel}\chi_{exp})$$

Figure D2 shows the magnetization M measured in the normal state at a temperature just above (12 K) and well above (300 K) T_C~11 K, varying the applied field from 0 to 5.5 T. M is linear for both temperatures, as expected for a paramagnet. A slight deviation from linearity can be observed in the T=300 K curve and this could be due to a small ferromagnetic impurity which is well saturated for fields above 0.5 T.

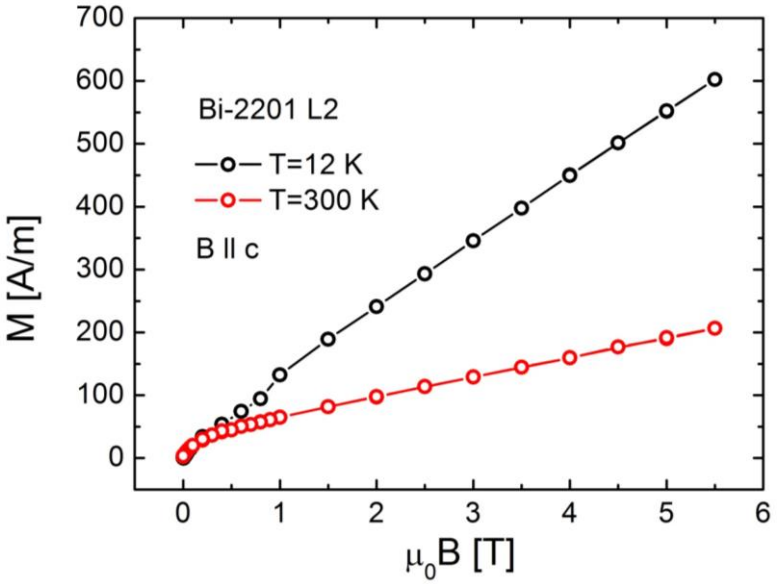

Figure D2: Magnetic field dependence of the magnetization ***M*** from 0 to 5.5 T, at T=12 K (black empty bullets) and T=300 K (red empty bullets).

References

[1] C. P. Poole, H. A. Farach, R. J. Creswick, "Superconductivity" (Academic Press, 1995)

E

Published articles related to this work of thesis

M. Meinero, F. Caglieris, I. Pallecchi, G. Lamura, S. Ishida, H. Eisaki, A. Continenza, and M. Putti, **In-plane and out-of-plane properties of a $BaFe_2As_2$ single crystal**, Journal of Physics: Condensed Matter, article in press (2019)

M. Meinero, F. Caglieris, G. Lamura, I. Pallecchi, A. Jost, U. Zeitler, S. Ishida, H. Eisaki, and M. Putti, **Unusual thermoelectric properties of $BaFe_2As_2$ in high magnetic fields**, Physical Review B **98,** 155116 (2018)

Conference communications related to this work of thesis

Oral presentations

M. Meinero, F. Caglieris, G. Lamura, I. Pallecchi, S. Ishida, H. Eisaki, A.Jost, U.Zeitler and M. Putti, **Unusual thermoelectric properties of $BaFe_2As_2$ in high magnetic fields**, International conference on Superconductivity and Functional Oxides (SuperFOx2018), Fisciano Campus, University of Salerno (Italy), September 13-15, 2018

M. Meinero, F. Caglieris, G. Lamura, I. Pallecchi, S. Ishida, H. Eisaki, A.Jost, U. Zeitler and M. Putti, **Unusual thermoelectric properties of $BaFe_2As_2$ in high magnetic fields**, invited speaker at Institute of Low Temperature and Structure Research, Polish Academy of Sciences, Wroclaw (Poland), June 7-8, 2018

M. Meinero, F. Caglieris, G. Lamura, I. Pallecchi, S. Ishida, H. Eisaki, and M. Putti, **Anisotropy of transport properties in parent compound $BaFe_2As_2$**, Third conference on superconductivity and

functional oxides (SuperFOx), Politecnico di Torino, Turin (Italy), September 19-21, 2016

Posters

M. Meinero, F. Caglieris, G. Lamura, I. Pallecchi, F. Bernardini, A. Jost, M. Shahrokhvand, U. Zeitler and M. Putti, **Low temperature transport in 1111 IBS parent compounds**, DPG Spring Meeting 2018, Technishe Universtiät Berlin (Germany), March 11-16, 2018

M. Meinero, F. Caglieris, G. Lamura, I. Pallecchi, S. Ishida, H. Eisaki, and M. Putti, **Transport properties in parent compound $BaFe_2As_2$ of iron based superconductors**, WE Heraeus Seminar on "Superconducting materials on their way from Physics to Applications", Physikzentrum, Bad Honnef (Germany), February 17-20, 2016